Modelling Stable Atmospheric Boundary Layers over Snow

H. A. M. Sterk

Thesis committee

Promotor
Prof. Dr A.A.M. Holtslag
Professor of Meteorology
Wageningen University

Co-promotor
Dr G.J. Steeneveld
Assistant professor, Meteorology and Air Quality Group
Wageningen University

Other members
Prof. Dr S.E.A.T.M. van der Zee, Wageningen University
Dr B.J.H. van de Wiel, Eindhoven University of Technology
Prof. Dr M.R. van den Broeke, Utrecht University
Dr A.C.M. Beljaars, European Centre for Medium-Range Weather Forecasts, Reading, UK

This research was conducted under the auspices of the Graduate School for Socio-Economic and Natural Sciences of the Environment (SENSE).

Modelling Stable Atmospheric Boundary Layers over Snow

H. A. M. Sterk

Thesis
submitted in fulfilment of the requirements for the degree of doctor
at Wageningen University
by the authority of the Rector Magnificus
Prof. Dr M.J. Kropff,
in the presence of the
Thesis Committee appointed by the Academic Board
to be defended in public
on Wednesday 29 April 2015
at 1.30 p.m. in the Aula.

H.A.M. Sterk
Modelling Stable Atmospheric Boundary Layers over Snow,
192 pages.

PhD thesis, Wageningen University, Wageningen, NL (2015)
With references, with summaries in Dutch and English

ISBN 978-94-6257-226-3

Contents

Chapter 1

Introduction

The Arctic is the Earth's northern polar region. One formal definition that covers the region, is 'the area North of the Arctic Circle'. The latter represents the latitude north of which the sun does not rise during winter solstice and does not set during summer solstice. The Arctic can also be defined as the area north of the Arctic tree line, which indicates the boundary between boreal forest and tundra, or defined as the area at high latitudes where temperatures remain below 10° C (NSIDC, 2014a).

With these low temperatures and the area being mostly covered by sea ice and snow during the winter, the Arctic's climate is known for its harsh environment, and life has to be uniquely adapted to these conditions. However, the relatively short growing season and small variety of species compared to lower latitudes, make that Arctic life is vulnerable. Moreover, the highly variable climate could cause sudden storms or frost episodes which can kill large parts of a population (ACIA, 2005).

Besides these challenges, Arctic life faces a more gradual threat, namely climate change. With global temperatures increasing, the spatial extent of the Arctic region decreases, which endangers the unique biodiversity. An evident proof for the changing climate is the decline of sea-ice extent and mass during its minimum (Figure 1.1). Especially during the recent years, these minima are on the lower end of, or even reaching below the 1981 - 2010 average sea-ice extent. Other changes that are already occurring are retreating glaciers, thawing permafrost, which could release carbon and methane (NSIDC, 2014a), coastal erosion, and an altered distribution of species (ACIA, 2005).

According to observations, climate change is more profound in the Arctic regions compared to other latitudes, a phenomenon called 'Arctic Amplification'. In particular, observations and reanalysis data indicate that the Arctic near-surface temperature increases more rapidly than the global mean temperature (e.g. Johannessen *et al.*, 2004; Serreze and Francis, 2006; Serreze *et al.*, 2009), while it is also seen higher in the atmosphere (Graversen *et al.*, 2008; Screen and Simmonds, 2010). Often the ice-albedo feedback (Curry *et al.*, 1995) is hypothesised as main contributor to the Arctic Amplification. With decreasing ice and snow surface, less short wave radiation is reflected back towards space so that more energy is absorbed, heating the surface even further, which causes even more ice to melt. However, also in months without sunshine, this enhanced warming is found, indicating that other processes are important as well.

Alterations in cloud cover and water vapour play a role as these influence the surface energy balance. Using satellite derived products, Francis and Hunter (2007)

found that the increase in downward long wave radiation is related to the increase in water vapour content and cloud fraction. This was confirmed in climate model simulations by Graversen and Wang (2009). They also found that in seasons with sunlight, the presence of clouds can somewhat counteract the increased long wave impact, by forming a higher albedo and hence reflecting short wave radiation. This effect reduces the ice-albedo feedback, and indicates that the ice-albedo feedback may not be as important as previously thought.

Variations in atmospheric circulations and/or transport can cause more heat and moisture being transported towards the Arctic. This increases the downward long wave radiation at the surface, thereby amplifying the warming (Alexeev *et al.*, 2005; Graversen, 2006; Graversen *et al.*, 2008). Also, increased heat advection due to changed oceanic circulations/transport can impact the sea-ice distribution and the Arctic temperatures (Spielhagen *et al.*, 2011). Additionally, with weak vertical mixing, the near surface warming is less easily spread aloft and captured at the surface, amplifying the surface temperatures even more (Alexeev *et al.*, 2005; Graversen and Wang, 2009; Bintanja *et al.*, 2011a, 2011b). Not only vertical mixing, but also the degree of horizontal mixing, determines the effectiveness of the distribution of the local signal to adjacent areas (Serreze *et al.*, 2011).

All these processes interact with each other, sometimes with positive feedbacks such that changes accelerate and perhaps become irreversible. This can have severe consequences for the Arctic, as well as for the entire world. I.e. Overland and Wang (2010) report a change in large-scale atmospheric circulations with Arctic sea-ice loss, the North Atlantic storm tracks may be affected (Lu *et al.*, 2004), and with melting ice-sheets of Greenland the sea level rises (Van den Broeke *et al.*, 2009; Graversen *et al.*, 2011). Therefore, scientists try to explain the observed climate changes, and try

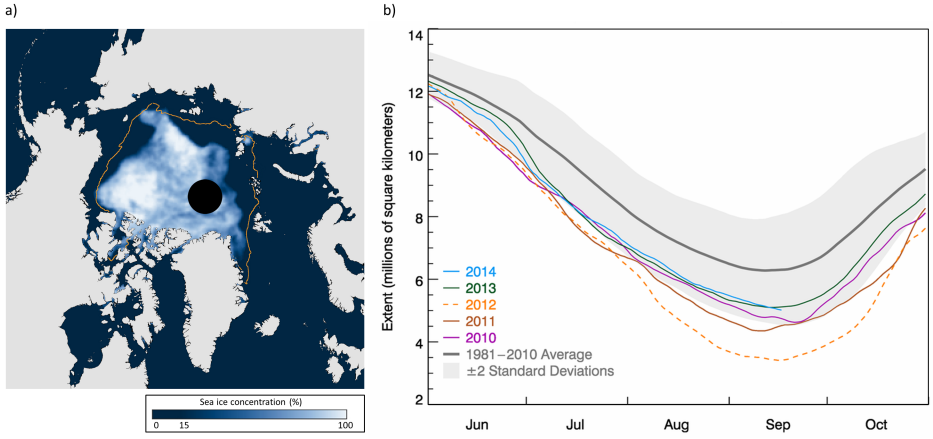

Figure 1.1: a) The 2013 minimum sea-ice concentration (13 September) versus the 1981 - 2010 median extent (orange line), and b) the Arctic sea-ice extent (area of ocean with at least 15% sea ice) throughout the year. (a) adapted from: NOAA Climate.gov; b) from: NSIDC, 2014b, Boulder CO.)

to explore future trends using global and regional climate models.

Unfortunately there is still a lot of uncertainty in modelling the Arctic climate, which follows from a large disagreement between model results and observations, as well as from the large variation between model results (Holland and Bitz, 2003; Rinke *et al.*, 2006; Walsh *et al.*, 2008; Boé *et al.*, 2009). For example, when comparing the ensemble mean of several regional climate models with the ECMWF (European Centre for Medium-Range Weather Forecasts) reanalysis data, modelled 2 m temperatures remain up to 5 K too low (Rinke *et al.*, 2006). Walsh *et al.* (2008) compared surface air temperatures of 15 global climate models with ERA40 reanalysis data, and found their area-averaged annual root mean square errors to range from 3 up to almost 14 K north of 60°N. Furthermore, Holland and Bitz (2003) analysed the zonally averaged 2 m temperature increase of several coupled atmosphere-ocean-sea-ice-land models, where simulations for doubled CO_2 concentrations indicated a range of warming between 1.7 and 4.3 times the global average. The differences with observations and between the models, underlines the need for further understanding of the physical processes at hand.

The Arctic Amplification seems to be most profound during the winter months (e.g. Screen and Simmonds, 2010; Bintanja *et al.*, 2011b; Pithan and Mauritsen, 2014). The atmospheric boundary layer (the lowest part of the atmosphere which is in direct contact with the surface), is then often stably stratified, which is referred to as a stable boundary layer (SBL, further explained below). Proper modelling of the SBL is difficult due to the weak mixing and the interaction of many small-scale processes (Holtslag *et al.*, 2013). This thesis aims to enhance our understanding on the role of some of the small-scale processes in the SBL. In this introduction the SBL is further explained, as well as why knowledge on the SBL is important besides for climate understanding. Furthermore, the processes studied in this thesis are explained briefly, followed by the research methodology as well as the aim and research strategy.

1.1 Stable boundary-layer phenomenology

The atmospheric boundary layer (henceforth called 'boundary layer' or 'BL') is typically turbulent, which makes that exchanges of heat, momentum, humidity and scalars (e.g. CO_2) can take place. Turbulence is generated either by 'buoyancy' or mechanically by 'wind shear'. Buoyancy is the force that is caused by vertical density differences, e.g., when the sun heats the surface and the surface becomes warmer than the environment, the air just above the surface expands and obtains a lower density than the surroundings (it becomes positively buoyant), so that this air parcel will rise. Turbulence can also be generated by friction of the flow near the surface, which occurs when air is forced past an obstacle such as trees, buildings or mountains. This results in variation of mean wind with height, known as wind shear. The latter can also occur higher aloft in the atmosphere, which can be experienced as unpleasant during air travel.

In unstable atmospheric conditions, buoyancy is the most dominant forcing mech-

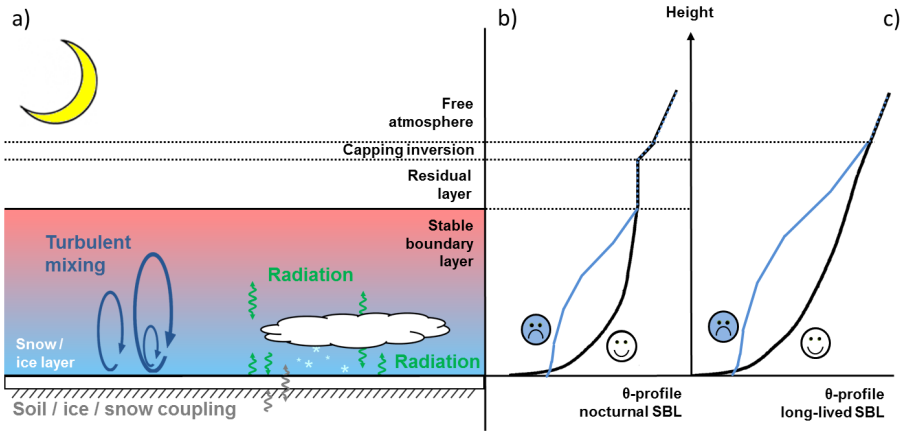

Figure 1.2: a) Sketch of the idealized stable boundary layer over a snow/ice-covered surface (not to scale, only the processes studies in this thesis are indicated), and some examples of potential temperature profiles (θ) for b) the nocturnal stable boundary layer, and c) the long-lived stable boundary layer. The profiles are adapted from Vogelezang and Holtslag (1996) and Zilitinkevich (2002). See also the text for further explanation. Concave up (happy/up face) potential temperature profiles are typical for low wind speeds, concave down (frowny/down face) potential temperature profiles are typical for high wind speeds. Mnemonics after Pleacher (2014).

anism for turbulence. This typically results in decreasing potential temperature[1] profiles just above the surface and rather uniform profiles of potential temperature higher in the BL. In neutral conditions, the potential temperature gradient with height is very small, and turbulence is mostly generated by wind shear. In stable conditions, vertical motions are suppressed due to a negative buoyancy, and turbulence is only produced mechanically. In very stable conditions with very strong potential temperature gradients, the negative buoyancy can be sufficiently large to overcome the mechanically driven turbulence, so that turbulence becomes very weak. This calm state can be interrupted by sudden turbulence, which is then referred to as intermittent turbulence (e.g. Van de Wiel *et al.*, 2003; 2007).

The SBL often develops at night, when after sunset or just prior to that, radiative cooling at the surface leads to the development of a stable stratification in the atmosphere, and heat will be transferred from the atmosphere to the surface (Mahrt, 2014). This stratification can become more profound with low wind speeds and clear skies, when the additional downward long wave radiation from clouds is absent, and the net radiative cooling is larger. With a stronger insulating underlying medium (e.g. snow), the transport of heat through the underlying medium to the surface is also reduced, which in its turn results in cooler surfaces as well.

On top of these nocturnal SBLs, often the remainder of the well-mixed BL of the

[1]Potential temperature is defined as the temperature an air parcel would have when brought adiabatically to the surface or reference pressure of 1000 hPa, so without heat exchange with the environment.

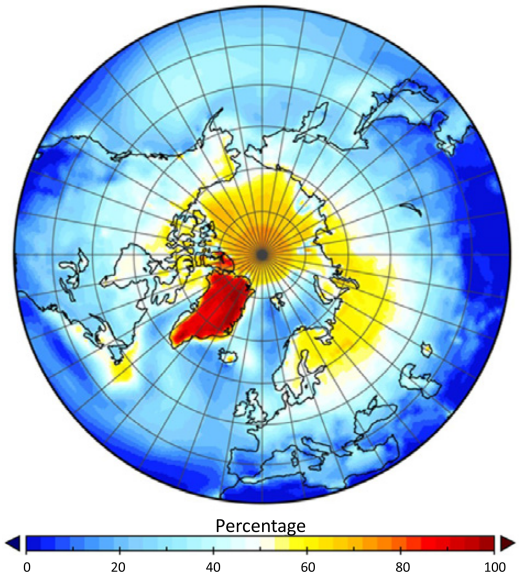

Figure 1.3: The percentage of days with a stable boundary layer from ERA-Interim data from 1979 - 2010. From: Esau *et al.* (2012).

previous day, the so-called residual layer, is found (see Figure 1.2b). The residual layer is bounded at the top by the capping inversion, which indicates the transition of the well-mixed layer and the free atmosphere. SBLs can also be present during (the start of) the day, when the incoming solar radiation is insufficient to balance the net radiative cooling, and can develop when warm air is advected over a colder surface.

Polar BLs are often characterized by a prolonged stable stratification, especially in winter when incoming solar radiation is limited. For a long-lived SBL, the SBL can then connect with the air of the free atmosphere, and there is neither a residual layer nor a capping inversion present (Zilitinkevich, 2002; Figure 1.2c). Tower measurements from the SHEBA (Surface Heat Budget of the Arctic Ocean Experiment) campaign, indicated that the mean near-surface conditions were strongly stable from November - April, and near-neutral or weakly stable for the remainder of the year, though hourly data suggested neutral conditions for 25% of the time in winter (Persson *et al.*, 2002). The SHEBA soundings revealed a stable stratification 61% and 53% of the time for autumn and winter respectively (Tjernström and Graversen, 2009). Figure 1.3 shows the percentage of days with a SBL for the northern hemisphere, using ERA-Interim reanalysis data (Esau *et al.*, 2012). However, reanalysis data may have some deficiencies as it is a combination of observations and model results, but observations in the Arctic are relatively scarce such that the impact of the model (which may have limited skills in these regions) on the reanalysis is relatively large (Tjernström and Graversen, 2009).

The classification of the SBL is rather complicated, as the development of the

SBL is influenced by many independent forcings as will be discussed later. Typically a distinction is made between the weakly stable and very stable boundary layer. The weakly SBL is characterized by continuous turbulence and is more likely to occur in windy and/or cloudy conditions (Mahrt *et al.*, 1998; Mahrt, 1999; Van de Wiel *et al.*, 2012). Often then the potential temperature profile becomes better mixed, and is concave-down shaped (blue profiles in Figure 1.2) (André and Mahrt, 1982; Van Ulden and Holtslag, 1985; Vogelezang and Holtslag, 1996). The very stable BL is characterized by strong potential temperature gradients close to the surface, and turbulence is very weak (Mahrt *et al.*, 1998; Mahrt, 1999; Van de Wiel *et al.*, 2012). This is often found with weak winds and clear-sky conditions. The potential temperature then becomes more concave-up shaped (black profiles in Figure 1.2). Note that since there is a variety of different scenarios for the SBL, many vertical structures are possible and a unique conceptual picture is insufficient (Mahrt, 2014).

Since SBLs occur rather frequently, it is important that they are represented properly in numerical weather prediction models as many end-users depend on these forecasts. Knowledge on the BL wind shear and its development in time is relevant for the gaining of wind energy (Storm *et al.*, 2009; Floors *et al.*, 2013). Awareness of possible surface frost, minimum temperatures and fog is important for agricultural purposes (Prahba and Hoogenboom, 2008; Baas, 2009). Strong (cross) winds (Van Dinther *et al.*, 2013), wind shear and fog formation are of interest for aviation and road traffic (Bergot *et al.*, 2005; Gultepe *et al.*, 2009; Van der Velde *et al.*, 2010). Furthermore, since the exchange of scalars in stable conditions is small, the development of SBLs is of importance for air quality studies (Hanna and Yang, 2001; Salmond and McKendry, 2005), as pollutants may be trapped in the SBL (Karppinen *et al.*, 2001).

The above gives just a few examples of why research on the SBL is necessary. Another important reason to learn more about SBLs, is for climate modelling and understanding, as discussed at the start of this introduction.

1.2 Stable boundary-layer processes

The fact that many processes act simultaneously and interact with one another, is one of the reasons of the difficulty in SBL modelling. Several small-scale processes play a role in the SBL, for example the turbulent mixing mentioned earlier, but also the coupling of the atmosphere and the surface (Holtslag and de Bruin, 1988; Duynkerke, 1991; Van de Wiel *et al.*, 2002; Steeneveld *et al.*, 2006a) and radiation (Savijärvi, 2006; 2013; Hoch *et al.*, 2007; Edwards 2009a; 2009b) are among the more important processes. Furthermore, the presence of clouds or fog impact the SBL, as do subsidence, advection, gravity waves, and drainage and katabatic flows (Delage, 1997; Mahrt *et al.*, 1998; Mahrt, 1999; Steeneveld *et al.*, 2006b).

Processes are represented in a simpler form in models, and sometimes the processes and/or the interactions are not completely understood. Additionally, the resolution both horizontally and vertically in the models may be insufficient to properly resolve the SBL, i.e. the grid boxes may be too large for the small-scale processes, which partly explains the incorrect representation (Byrkjedal *et al.*, 2008). Moreover, the large variety of SBL archetypes hampers a straightforward solution. The type

of SBL influences the SBL depth and the efficiency of the exchange of quantities horizontally and vertically. For each situation, processes may play a relatively more or less important role.

In this thesis, SBLs over snow-covered surfaces are studied. The main focus is on the small-scale processes of turbulent mixing, the coupling between the atmosphere and the snow-covered surface, and long wave radiation effects. These processes are considered to mostly control the SBL evolution and structure (André and Mahrt, 1982; Beljaars and Holtslag, 1991; Steeneveld *et al.*, 2006b; Bosveld *et al.*, 2014b). Therefore we will briefly discuss these three processes.

1.2.1 Turbulent mixing

Atmospheric turbulence can be seen as the chaotic or irregular motion of air. Short term fluctuations of the mean wind are related to small-scale motions of eddies which exist in different sizes, varying from a millimetre up to the depth of the BL. The superposition of these different scale eddies make up the turbulence spectrum (Stull, 2000). The friction caused by eddies, reduces the intensity of the turbulence and decreases the eddy size until it is totally dissipated by molecular viscosity.

The process of turbulent mixing was already discussed earlier in this introduction, by that it can be generated both by buoyancy and by mechanical production, and by that it is an important factor in transport of heat, momentum, humidity, and other scalars. This transport is evident, not only in the atmosphere, but it is also important for the exchange of sensible and latent heat between the surface and the atmosphere. This in turn affects the further SBL development, which makes a more exact representation of turbulence in models essential. In the SBL, the turbulence is suppressed by buoyancy effects, and turbulence is only produced by wind shear. Therefore, turbulence is very sensitive to changes in the wind speed and temperature profile (e.g. Steeneveld, 2007; 2014).

Due to the small-scale nature of turbulence, there is always an impact of turbulence on the mean flow from scales that are smaller than the grid scale that is used in models (Holtslag *et al.*, 2013). To represent the effects of the smaller scales on the model grid scales, these relatively small-scale processes are parametrized, contrary to the larger scale processes that are explicitly resolved in the model. Atmospheric models solve the basic governing equations such as the equation of state (the ideal gas law), the conservation of mass (the continuity equation), and the conservation of momentum, heat and moisture, and possibly conservation of other scalars.

To distinct between the larger and smaller scales, the local or instantaneous value of a variable C is decomposed in a mean part $\overline{C}$ and a turbulent part c'. When for example this is averaged over the entire grid box, this implies that the average turbulent part $\left(\overline{c'}\right)$ equals zero. This fact is taken into account when averaging the governing equations, as average terms including only 1 turbulent component, drop out (so-called Reynolds averaging). Average terms including 2 turbulent components, are not necessarily zero and are kept in the equation. The equation of conservation of variable C then becomes (e.g. Stull, 1988; Stensrud, 2007; Holtslag, 2015):

$$\frac{\partial \overline{C}}{\partial t} = -\overline{U_j}\frac{\partial \overline{C}}{\partial x_j} - \frac{\partial(\overline{U_j' c'})}{\partial x_j} + S\,. \tag{1.1}$$

Here U_j represents the component of the wind speed vector in direction j (j = 1,2,3), and S represents several other sources and sinks for C (see also Chapter 4). The term on the left hand side represents the storage, and the first term on the right hand side represents advection, while the second term on the right represents the turbulent effects. This equation shows that turbulence partly determines the forecast of the mean variable, while furthermore especially wind speed is important for variables unrelated to wind speed, so that the budget equations for momentum, heat, humidity and other scalars are closely coupled.

Though the basic principle of how to design the parametrization for turbulence is similar, the implementation in models developed both for research and for operational services can vary substantially, which is likely due to differences in tuning that have evolved from the past, and differences in preferences for complexity (Holtslag *et al.*, 2013). Furthermore, from operational viewpoint, it has proven beneficial for e.g. the representation of near-surface temperatures and synoptic cyclones to artificially enhance the mixing in models (Beljaars and Viterbo, 1998; Viterbo *et al.*, 1999; Sandu *et al.*, 2013). Though beneficial for the large-scale model performance, this can be detrimental for an accurate SBL forecast. For example: the SBLs tend to become too deep, with too weak low-level jets (LLJ, when layers of air no longer 'feel' the presence of the surface, they can start to accelerate, resulting in a wind maximum, the so-called LLJ), and the surface drag is overestimated (Cuxart *et al.*, 2006; Holtslag, 2006). Also the surface temperatures can now be overestimated (Steeneveld *et al.*, 2006a), and the angle between the surface wind speed and wind speeds aloft is too low which has implications for the direction and speed of mass transport and cyclone filling within the BL (Svensson and Holtslag, 2009). Sometimes also the stable stratification in the free atmosphere is affected, affecting the atmospheric flow aloft as well, by weakening the upper tropospheric jets and/or inversion layers (Sandu *et al.*, 2013). This can result in a reduction of low cloud cover (Köhler *et al.*, 2011).

Further information on turbulence parametrizations and how this was done in the model that was used in this thesis, is provided in Chapter 2.

1.2.2 Land-surface coupling

The thermal coupling of the atmosphere and the surface can also play an important role in the SBL development. This process represents the effect of heat conduction throughout the underlying medium and how then the surface temperature is affected, which is considered as the lower boundary for the atmosphere. With a high conductivity, more heat is transported from the lower soil/ice/snow layers towards the surface (that is, in stable conditions, otherwise heat is more effectively transported away from the atmosphere-surface interface). This heat transport becomes more difficult for an underlying medium with a low conductivity, e.g. when a snow layer is present.

Generally, the heat transport (G) between the underlying medium and the surface is determined with:

$$G = -\lambda \frac{\partial T}{\partial z}\,, \tag{1.2}$$

for which λ equals the conductivity, and $\partial T/\partial z$ the temperature gradient. The conductivity in its turn is very dependent on the type of the underlying medium.

For soil, the conductivity is determined by the soil material, the texture, and the density, but also soil moisture impacts the soil conductivity. Furthermore, when vegetation is present, an isolating layer is included since air is trapped between the vegetation. Fresh snow also has a relatively low conductivity, though the density increases in time as does the conductivity.

As with turbulent mixing, the difference in scales between the process scale and the grid scale in the model can be of importance. The conductivity of a certain small area can change substantially in space and in time, while furthermore the land surface varies in temperature, soil moisture, and also roughness (Fernando and Weil, 2010; Stoll, 2012). Thus surfaces can be very heterogeneous, which makes representing the real world surface in models more difficult, as this has an impact on the transfer of momentum, heat and moisture (Beljaars *et al.*, 2006).

Therefore in modelling practice, a representative average for the grid cell needs to be taken into account to determine the average transport of heat, momentum and moisture needed to determine the state at the first model level (Ronda and De Bruin, 1999; Batchvarova *et al.*, 2001). Some studies claim that the enhanced mixing mentioned in the previous section, is necessary to account for contributions to turbulence due to the surface heterogeneity (Sandu *et al.*, 2013).

Over the years, the schemes to parametrize the atmosphere-surface interaction (the land-surface model, LSM) have gradually evolved. At the ECMWF for example, the LSM has changed from a climatological deep soil boundary condition with 2 layers, to a prognostic 4-layer model with 6 surface tiles which calculate separate energy balances for 6 fractions of the gridbox (Van den Hurk *et al.*, 2000; Beljaars *et al.*, 2006). In that sense there is now the possibility to account for partial snow cover and snow under high vegetation, as well as different types of vegetation (if any) in the different subgrids. The sea-ice model has also improved from a single slab to

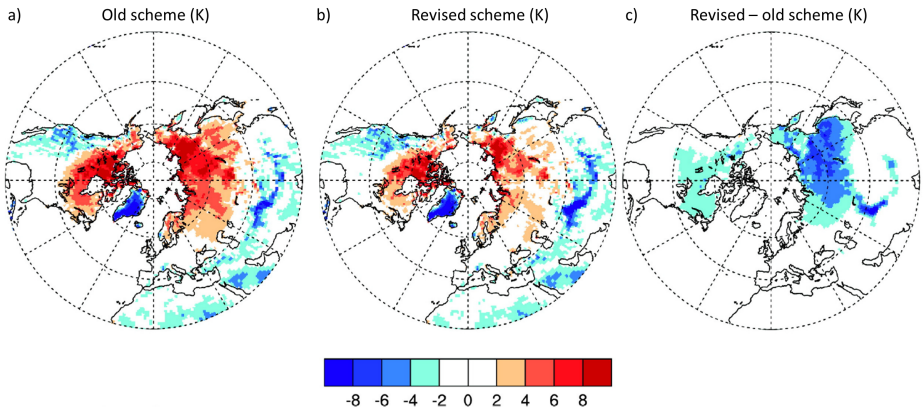

Figure 1.4: The 2 m temperature bias of the ECMWF model with a) the old snow scheme, b) the revised snow scheme, and c) the difference between the two, compared with observation based climate produced at the Climate Research Unit of the University of East Anglia, for the December, January and February climate. From: Balsamo *et al.*, 2014.

a 4-layer sea-ice temperature model with tiles for open water and sea ice (Beljaars *et al.*, 2006). Also some models now incorporate a global vegetation database which has a wide variety of vegetation types to implement in the model (Van den Hurk *et al.*, 2000). Other improvements are on the land-surface hydrology to have a better representation of infiltration and runoff with a dependency on the soil texture for example (Balsamo *et al.*, 2009). In 2009 also a new snow scheme was introduced in the ECMWF model, which has a different snow density parametrization, includes a liquid water representation with freeze/thaw periods, and has altered formulations for the snow cover fraction and snow albedo, which also impacts the snow conductivity for example (Dutra *et al.*, 2010; Balsamo *et al.*, 2014). The improvement on the modelled winter 2 m temperature compared with observation based climate after the introduction of the new snow scheme is shown in Figure 1.4. However, it is still clear that winter time temperature biases remain substantial and that further research is needed.

Chapter 2 explains more on how the coupling is taken into account in the model used for this thesis, i.e. the Weather Research and Forecasting model.

1.2.3 Long wave radiation

The third process that is taken into account in this thesis is that of long wave radiation. Every object with a temperature above 0 K emits some radiation. The amount of radiation that is emitted per wavelength, is strongly determined by the objects temperature (Liou, 1980). For very warm objects, such as the sun, the peak in emission is found at short waves, therefore solar radiation is referred to as 'short wave radiation'. The Earth-atmosphere system is a lot cooler, and hence emits more in the long wave part of the spectrum, which is thus called 'long wave radiation'.

Besides temperature, the amount of emitted energy depends on the emissivity, or the effectiveness of the energy emission (value ranging from 0 to 1) of the object. For a perfect radiator (black body) the emissivity equals 1 and all energy from all wavelengths is absorbed, so there is no reflection nor any transmission. Furthermore, a black body emits the maximum amount of energy possible for each wavelength (Stensrud, 2007). However, most objects have an emissivity lower than 1, and the emissivity varies per wavelength and per object.

The emissivity of the atmosphere depends on the concentrations of absorbing gases (e.g. water vapour, CO_2 and O_3). Also the presence of clouds are critical in the emitted long wave radiation, since they also absorb radiation in the range of 8 - 11 μm, whereas a clear-sky atmosphere does not (therefore this range in the spectrum is called the 'atmospheric window') (Liou, 1980). This also explains that cloudy nights compared to clear-sky night are relatively warmer at the surface, since there is more incoming long wave radiation at the surface. Due to the more negative net radiation during night-time clear-sky conditions, the atmosphere is likely to become more stably stratified.

Because the temperature and emissivity varies per atmospheric layer, the emitted long wave radiation also varies between the layers, which therefore results in a net radiative flux (Steeneveld, 2007). The net radiative flux at the surface, determined by the incoming minus the outgoing radiation, has a strong impact on the determination of the surface temperature (Edwards, 2009a). However, also the divergence

of the long wave radiative flux over the different atmospheric layers can affect the development of the SBL. Hoch *et al.* (2007) report that the mean radiative cooling in winter for Greenland is about 11 K day^{-1}, though cooling rates of 30 K day^{-1} can occur for several days, which clearly indicates its importance on the SBL evolution.

Hence, the transport of long wave radiation needs to be parametrized in models. Parametrization schemes include thermal radiation that is absorbed and emitted by gases and water species, while the upward long wave radiation at the surface is determined by the skin temperature and the emissivity of the surface which depends on the land-use type. In a line-by-line approach, the absorption and emission are calculated for each wave length. However, this is computationally very expensive, and therefore often a broadband method is used (where intervals are taken to include the long wave absorption/emission spectrum (Stensrud, 2007)) or correlated-k method (where wavelengths with similar spectral properties are grouped (West *et al.*, 2010)) is applied.

As mentioned previously, both the incoming long wave radiation at the surface and the long wave radiative flux divergence should be parametrized. For example, Tjemkes and Duynkerke (1989) showed that including radiative cooling from this divergence, can help to reduce the inversion strength, making the SBL less stable which increases the SBL height by 25%. Also recent model studies show the importance of radiative cooling in the atmosphere, and indicate that with very strong temperature gradients close to the surface, even radiative warming can occur (Savijärvi, 2006; 2013). However, a model study by Steeneveld *et al.* (2010) showed a model underestimation of the radiative cooling compared with observations. This could be related to the relatively coarse resolution in models, as for example Ha and Mahrt (2003) have shown that the long wave fluxes are very sensitive to the temperature and moisture profiles close to the surface and should therefore be carefully resolved. Other possibilities for the underestimation are a deficiency in the long wave radiation scheme, or a poor input into the long wave radiation scheme (Steeneveld, 2014).

Another deficiency is that often the incoming long wave radiation is underestimated by models for cold conditions. Niemelä *et al.* (2001) found this to be the case for clear-sky winter conditions in Sodankylä (northern Finland), especially for strong inversions. Wild *et al.* (2001) also reported that general circulation models typically underestimate the incoming long wave radiation, and particularly so at sites with cold and dry conditions where there is little downward long wave radiation emission. They expect this not to be due to errors in the forecasted temperature and humidity profiles that are signalled into the radiation schemes, but the radiation schemes themselves, as an accurate simulation of thermal emission from the cloud-free, cold and dry atmosphere is difficult. Barton *et al.* (2014) also suspect other reasons than the modelled temperature and humidity for this bias, as several models were forced with the same profiles of temperature and humidity and still a large spread in clear-sky downward long wave radiation was found.

In this thesis we study the relative impact of the incoming long wave radiation on the SBL evolution. Several long wave radiation schemes were used. The principles behind the determination of the long wave radiative transport of the mainly used scheme is given in Chapter 2.

1.3 Research methodology

As mentioned previously, SBL modelling remains challenging and many model results differ from observations and from one-another. This might be explained by the presence of many interacting processes and feedbacks, lack of fundamental understanding of these processes, and the existence of contrasting SBL regimes. Moreover, model results are also deteriorated by insufficient resolution, the simplified model representation of physical processes, and by compensating errors.

The aim of this thesis is to improve our understanding of the SBL, with special focus on the challenging boundary condition of a snow-covered surface. Due to the many processes and feedbacks that are at hand, we try to better isolate some of the processes. To do so, the Weather Research and Forecasting (WRF) single-column model (SCM, also sometimes called a 1D-model) is used. A SCM consists of only one column of atmosphere with its physics included, and hence horizontal interaction with other atmospheric columns is prohibited, and interaction is only found in the vertical. In this way, feedbacks from large-scale dynamics which would be present in a 3D-model (e.g. a moving pressure system, and effects from other terrain types and/or orography) are excluded. Studies in a SCM set-up can hence provide useful information on specific parametrizations, which could later give more insight when implemented in the more complete 3D-model as this in essence consists of many single columns that include the interactions and feedbacks with one-another. Another advantage of a SCM model is that simulations are computational relatively fast compared to larger models, which enables us to perform simulations with a higher vertical resolution as well.

Besides the WRF-SCM, the full 3D WRF model is used in this thesis for evaluation of several stably stratified case-studies (see also Section 1.4), while additionally it is used to determine the forcings needed for the SCM. The full 3D WRF model is a mesoscale model, where mesoscale refers to meteorological phenomena on the scale of a few kilometres up to several hundreds of kilometres. Whereas climate models cover the entire globe, mesoscale models focus on a smaller region, such that a higher resolution is possible. LES (large eddy simulation) and DNS (direct numerical simulation) models have an even higher resolution and as such can resolve much smaller scales of atmospheric motion than a mesoscale model (for DNS the parametrization of turbulence is not even necessary). However, this makes them computationally extremely expensive, which makes them not directly suitable for weather and climate modelling.

The WRF model is maintained and supported by a wide community: evaluation studies are performed in the form of e.g. case-study analyses and model intercomparison studies, while furthermore other attributes are developed (such as new parametrization schemes) and included in a newer model version, while also other improvements and bug fixes are incorporated (Klemp, 2006). As such, WRF is widely used for weather forecasting as well as atmospheric research in the field of for example BL research, air quality studies, fog, cloud micro-physics, regional climate studies, and wind energy research (Klemp, 2006).

The SCM has also been a valuable tool for SBL research in the past. Delage (1974) studied the structure of the nocturnal SBL using a 1D model, though at that time the surface temperature was prescribed as a function of time with a constant

geostrophic wind speed. Nieuwstadt and Driedonks (1979) used a similar model and found that important characteristics such as the nocturnal SBL height can be modelled reasonably well, though advection would be more important higher up in the BL and was now left out. The importance of advection was also recognized by Carlson and Stull (1986) when studying the impact of subsidence on the SBL. Delage (1997) studied several turbulence schemes in the 1D model, though still with prescribed surface temperature. Later, a SCM was developed which included interaction with the surface, including a vegetation layer, to study the SBL and radiation fog (Duynkerke, 1991; 1999). Including vegetation helped the skin temperature to develop to lower temperatures than was suggested by the higher soil temperatures.

SCMs are also often used for model intercomparisons where many research institutes and operational weather centres cooperate. A good example is the GABLS programme, where GABLS stands for the GEWEX (Global Energy and Water Cycle Experiment) Atmospheric Boundary Layer Study. The purpose of GABLS is to enhance the understanding and representation of the atmospheric BL in regional and climate models (Holtslag *et al.*, 2013). So far three GABLS experiments have been carried out, where SCMs and LES models are compared, while a fourth GABLS experiment is ongoing.

The first GABLS experiment analysed a weakly SBL over ice with an academic setup and with special focus on the turbulence (Beare *et al.*, 2006; Cuxart *et al.*, 2006). Surface temperatures and radiative cooling were prescribed. It was found that many operational models showed enhanced mixing, together with the deficiencies that accompany this feature, as was already discussed in section 1.2.1. The second GABLS experiment included idealized forcings based on observations to enable a more straightforward comparison between the models. The emphasis was now on the diurnal cycle for which a large variation was found between the models, which is thought to be related to the prescribed surface temperature forcing (Svensson *et al.*, 2011). Therefore, a SCM study on the impact of the surface forcing was performed (Holtslag *et al.*, 2007), from which followed that the range in model output regarding sensible heat flux, and potential temperature and wind speed profiles for stable conditions was decreased when an interactive surface scheme is included in the model. Thus, the third GABLS intercomparison study used full coupling with the surface for the SCMs, while furthermore radiation is included. In order to compare model results with observations, it was found that the SCM forcings need to be carefully prescribed (Bosveld *et al.*, 2014a). One of the main results (Bosveld *et al.*, 2014b) was that the thermal coupling greatly influenced the spread in 2 m minimum temperatures between SCMs. Variations in incoming downward long wave radiation were mostly due to different thermodynamic profiles and not as much due to the difference in parametrization schemes. The impact of the turbulent mixing on the 2 m temperature was considered relatively small as well. This indicates that indeed the focus should be also on the other processes, while in previous GABLS exercises the focus was mostly on the turbulent mixing. Therefore, it is important to include the interactions of the various processes in the model.

The above studies are just a limited sample of the many studies that have been executed with SCMs. This shows the practical strength and feasibility of using a SCM for research. Subsequently, the gained knowledge can be implemented in the

larger-scale models.

1.4 Aim and research strategy

This thesis follows several earlier theses about SBLs composed at Wageningen University. For example Van de Wiel (2002) studied the intermittent behaviour in the SBL using a relatively simple bulk model, where the interaction is described between the bulk of the SBL and the underlying surface including a vegetation layer. Surface evaporation is ignored and a dry atmosphere is assumed. A simple radiation scheme is applied. This course of action facilitates an analytical approach to study the intermittency. It was shown that the role of a vegetation layer was critical for the SBL modelling. Due to the low heat capacity and isolating effects, the surface temperature may change rapidly with varying turbulent heat fluxes, which has an effect on the radiation and turbulent heat budget and causes an important feed-back mechanism which may induce the intermittency (Van de Wiel *et al.*, 2002).

The latter thesis was followed by the work by Steeneveld (2007) on the understanding and prediction of SBLs over land, where more complex SCM and 3D models were used. Again the importance of including interaction with the surface and a vegetation layer was evident. Amongst others it was shown that the SBL development is very sensitive to the selected resolution in both soil and atmosphere. Furthermore, alternatives for defining the turbulent mixing were investigated, and the role of gravity wave induced terrain drag to possibly replace the enhanced turbulent mixing in models was studied.

Subsequently, Baas (2009) focused on the turbulence and low-level jets in the SBL. The LLJ characteristics are distinguished for the different SBL regimes, making use of the observational dataset at Cabauw (The Netherlands). Additionally, two different closure assumptions to model atmospheric turbulence were studied. Moreover, a single-column model was applied to investigate how the LLJ representation in the model depends on the formulation of the turbulence, while also a method to determine the forcings needed for the SCM was explained.

Despite the research progress made by the above cited authors and others, still problems exist when modelling the SBL, in particular for stable conditions over snow. The aim of this thesis is to improve our understanding of the SBL with the additional complexity of a snow-covered surface. Here we incorporate the findings of previous studies in that a coupled model should be used, with a high vertical resolution.

The first part of this thesis focusses on the relative role of snow-surface coupling, radiation, and turbulent mixing for an Arctic clear-sky SBL over sea-ice. To better isolate these processes from larger scale feedbacks, the WRF-SCM is used for this particular study. As such we try to answer the following research questions in Chapter 3:

> ***Question 1:*** *What is the variety in model outcome regarding potential temperature and wind speed profiles that can be simulated with one model by using different parametrization schemes?*
>
> ***Question 2:*** *Which of the three governing processes is most critical in determining the SBL state in various wind regimes?*

Question 3: *Can we identify compensation mechanisms between schemes, and thus identify where possible compensating model errors may be concealed?*

With WRF, several parametrization schemes for the different physical processes can be selected, such that with one model a substantial variation in output can be acquired (Question 1). With Question 2 it is studied which processes are responsible for a similar spread in model results. An idealized case study is carried out with a certain reference set up, for which the intensity of the different processes is adjusted, and this is repeated for various wind speeds. So-called process diagrams (Bosveld *et al.*, 2014b) are used for the sensitivity analysis. In a process diagram 2 parameters are studied and a line connects the reference state with the perturbed state. By comparing the change of the different perturbed processes with respect to the reference state (i.e. comparing the relative length of the lines) for the different wind regimes, one can learn about the relative importance of these processes. When under a certain wind regime, a process is relatively more important, more care should be taken in the process parametrization under these conditions. Subsequently, this analysis shows where future research should be focused on.

Furthermore, the process diagrams can assist in identifying compensating processes (Question 3). When a change in perturbed state with respect to the reference state of different processes is similar (i.e. lines overlap), it implies that errors in either process parametrization can remain hidden by compensating errors in the parametrization of the other process. This would hamper the understanding whether the model is physically realistic.

Since the research for the first study was carried out in an idealized setting, we do not know how this analysis compares to observations. Therefore, this sensitivity analysis is repeated for observed cases, and it is studied whether an adjustment of process intensity may bring the model output closer to the observed values, if prior in disagreement. This requires first an evaluation of the WRF-SCM which is done in Chapter 4 where the subsequent questions are investigated:

Question 4: *What is the performance of WRF in stable conditions with low wind speeds for three contrasting snow-covered sites?*

Question 5: *How should we prescribe the single-column model forcings, using WRF-3D?*

We have chosen to focus on low wind speed conditions, as these are considered as particularly difficult to model (Edwards *et al.*, 2011; Tastula and Vihma, 2011; Holtslag *et al.*, 2013) and a better understanding is desirable. Three different observational sites were selected to cover a variety of land-surface types and for which both surface and tower observations were available. The first site is that of Cabauw in The Netherlands, with a case with snow overlying the grass. The second site is that of Sodankylä in Northern Finland, with snow in an evergreen needle-leaf forest. The third site is located at Halley, Antarctica, with snow over an ice shelf. Figure 1.5 depicts photos representative of the different sites.

For each site first briefly the WRF-3D model results are compared with the observations. Next, the WRF-SCM is evaluated for which realistic forcings of the 3D

Figure 1.5: Photos of sites representative of the study cases in Chapter 4 and 5, a) snow over grass at Hoogblokland (about 11km south of Cabauw, The Netherlands), b) snow in a needle-leaf forest at the Pallas-Sodankylä measurement station (Finland, from Ylitalo, 2014), and c) the measurement site on an ice shelf at Halley (Antarctica, from NERC-BAS, 2014).

atmospheric field are necessary (Baas *et al.*, 2010; Bosveld *et al.*, 2014a). Therefore, secondly this study emphasizes on the SCM forcings, by testing various forcing sets using WRF-3D (Question 5), and subsequently comparing the different obtained WRF-SCM simulations with the observations. Since the research in Chapter 3 indicated that the coupling process plays a more distinct role in low wind speed conditions, extra care was taken in prescribing the surface characteristics.

Using the optimal forcing strategy as a reference state, a similar sensitivity analysis as carried out for Question 2 is applied on the three case studies in Chapter 5. Here the questions are:

> ***Question 6:*** *How do the model results with various process intensities compare with observations?*
>
> ***Question 7:*** *Are any differences in relative process impacts found for the three contrasting sites?*
>
> ***Question 8:*** *Does the model sensitivity vary between two different BL schemes?*

In addition to the issue addressed by Question 2, we can now compare the process sensitivity with observations. Also the orientation of the process sensitivity lines in the process diagrams obtained by varying the process intensity hints which process is mostly responsible for a deviation from observations. Since the three sites have various surface characteristics (e.g. grass, needle-leaf forest, ice shelf; all with snow, see Figure 1.5), we can also compare whether this sensitivity varies per site. Furthermore, we have repeated the sensitivity analysis with two different BL schemes to study any variation in sensitivity between the schemes.

For this thesis, several physical parametrization schemes were used. To increase our understanding in the parametrizations, the frequently used schemes are discussed in Chapter 2 with particular emphasis on the aspects important for the SBL. Furthermore, to vary the intensity of the three processes as part of the sensitivity analyses performed, some alterations had to be made within the parametrization schemes. These are also explained in Chapter 2. A summary of the thesis work is given in

Chapter 6 and a discussion together with recommendations and a few notes on unfinished work is given in Chapter 7.

Chapter 2

WRF model background and small-scale process representations

The research tool used in this thesis, is the 3.2.1 version of the Weather Research and Forecasting (WRF) model (Skamarock *et al.*, 2008), which is widely used as already illustrated in Section 1.3. For the model evaluation in Chapter 4, the 3D version is applied, while for the model evaluation and sensitivity analyses in Chapters 3 to 5 the single-column model (SCM) version is employed. The WRF-3D fields are also used to determine the magnitude of advection prescribed into the SCM in Chapter 4 and 5, as well as to prescribe the initial profiles.

The WRF model is a non-hydrostatic model with a fully compressible atmosphere. A vertically stretched terrain-following vertical coordinate is used with the model top at a constant pressure. In WRF-3D the horizontal resolution can be chosen by selecting the grid sizes. With relatively small grid sizes, the model is able to resolve relatively small scale processes. Within WRF-3D, nested grids are possible, with a domain with higher resolution only present in part of the outer domain. The model equations that are used to describe the evolution of the state of the atmosphere are the equation of state, the conservation of mass (continuity equation) and the conservation of momentum, heat and moisture. The model equations are based on the Reynolds-averaged Navier-Stokes method.

The impact of processes with a scale that is smaller than the grid size, cannot be resolved explicitly, and are therefore represented by parametrization schemes. In WRF, several parametrization schemes are available for the boundary- and surface-layer physics, the land-surface physics, atmospheric radiation, micro-physics, and cumulus parametrization. The advantage of a SCM, is that horizontal physical interactions are neglected, and a full focus on the vertical exchange is obtained. In the column all physical parametrizations are represented so that these can be studied more straightforwardly when kept in isolation from the large-scale dynamics. Therefore, with the WRF-SCM, the evolution of the vertical atmospheric profiles is represented by the land-atmosphere coupling and the exchanges of energy and momentum in the vertical (Tardif and Hacker, 2006). By prescribing large-scale forcings such as geostrophic wind speed and advection, it is possible to represent the horizontal interaction with adjacent columns in a simplified manner (Baas, 2009). Furthermore,

it is beneficial that simulations can be performed relatively fast. This makes a higher vertical resolution computationally affordable, where this becomes computationally very expensive with numerical weather models and climate models. Also, the knowledge obtained from SCM studies, can provide insight when implemented in the larger scale 3D model.

Though many processes play a role in the SBL, the main focus in this thesis is on the processes of turbulent mixing, thermal coupling between the atmosphere and the surface, and the incoming long wave radiation. Each of their representation can vary substantially between schemes, e.g. due to different theories that are used, and differences in complexity. As such, some of the physical packages for the relevant processes during stable conditions are discussed in this chapter, with special elaboration on the schemes that were more frequently used in this thesis.

Two Boundary Layer (BL) schemes are discussed in Section 2.1, which represent the turbulent mixing. Since the surface-layer scheme links the interaction between the surface and the first model level in the BL scheme, the determination of the fluxes and exchange coefficients is also explained for the two surface-layer schemes that run in conjunction with the two BL schemes in Section 2.2.

No distinction has been made between the land-surface models; only one was used in this thesis, which is explained in Section 2.3. This discussion provides insight in how the sensible and latent heat fluxes are estimated and how this is related with the surface-layer schemes. Also, for the model evaluation and sensitivity analyses over contrasting snow-covered terrains (Chapter 4 and 5), understanding the representation of the snow layer is essential.

Regarding the long wave radiation parametrization schemes, two were used as a reference in this thesis, for which one is the follow-up of the other. Hence only one is described in Section 2.4, though the differences are indicated as well.

To study the relative importance of these three processes for different wind regimes (Chapter 3), and for different terrains in low wind speed regimes (Chapter 5), a reference set of parametrization schemes was selected, for which simulations were repeated with an adjusted process intensity. Therefore, a final section explains which variables were adjusted to achieve an altered process intensity.

2.1 Boundary-layer schemes

The boundary-layer schemes parametrize the sub-grid scale turbulent fluxes of heat, momentum and moisture throughout the atmospheric column (so not only for the BL) and hence the turbulent mixing. The schemes can be categorized as either "local" or "non-local". With local schemes, thermodynamic properties of a layer only interact with directly neighbouring layers. In non-local schemes, the effect of mixing by larger eddies is also taken into account as properties of a layer may mix with those of layers further away than just the adjacent layers.

Often local gradient mixing, or K-theory, is used to determine the turbulent fluxes (Holtslag, 1998; 2015). Here a relation is assumed between the turbulent fluxes and the resolved spatial gradients of the variable C in the vertical direction z:

$$\overline{w'c'} = -K_c \frac{\partial \overline{C}}{\partial z}\,, \tag{2.1}$$

where w' is the fluctuation of the vertical wind speed, $\overline{w'c'}$ is the turbulent flux for C in the vertical, and K_c is the eddy diffusivity coefficient for C. K_c is often a function of a representative length scale, a velocity scale, and stability, though these parametrizations are dependent on the state of the boundary layer, and differ per boundary-layer scheme.

Furthermore, the boundary-layer schemes used in this thesis are either a relatively simple first or a more complex one-and-a-half order closure. A first order closure uses the prognostic equations for zero-order mean variables such as mean temperature, moisture and wind, so that the second moments, or turbulent fluxes (e.g. the terms $\overline{w'c'}$), remain unknown.

The one-and-a-half order closure also uses the prognostic equations for mean variables for temperature, moisture and wind, while additionally the prognostic equation for the turbulent kinetic energy (TKE, ($\overline{e}$)) is applied, with:

$$\overline{e} = \frac{1}{2}\left(\overline{u'^2} + \overline{v'^2} + \overline{w'^2}\right) . \tag{2.2}$$

Therefore with one-and-a-half order closure, besides the turbulent fluxes, also the dissipation term from the TKE equation and the turbulent transport of $\overline{w'e}$ remain unknown (see Section 2.1.2). Sometimes with one-and-a-half order closure, also an equation for the potential temperature variance is used (e.g. Stull, 1988), but that was not the case in this thesis.

Though by applying one-and-a-half order closure the amount of unknowns increases compared to first-order closure, the hope is to obtain a more physically realistic eddy diffusivity as more physics of the atmosphere are taken into account (Holt and Raman, 1988). The K coefficients in equation 2.1 are then a function of an empirical length scale and the TKE. For more information on these closures, see for instance Stull (1988), Stensrud (2007), and Holtslag (2015).

2.1.1 YSU boundary-layer scheme

One of the schemes that we use in this thesis is the Yonsei University (YSU) BL scheme (Hong *et al.*, 2006, Hong, 2010; Skamarock *et al.*, 2008), developed after Troen and Mahrt (1986) and Holtslag and Boville (1993). This is a non-local scheme which applies a counter-gradient flux contribution for θ and momentum to include the contribution of the large-scale eddies to the total flux. This is applied only during unstable conditions, for the stable boundary layer the counter-gradient term is excluded. Furthermore, YSU is a first-order closure model, for which the eddy diffusivity for momentum in the boundary layer is determined with:

$$K_m = 0.001\Delta z + \kappa w_s z \left(1 - \frac{z}{h}\right)^p , \tag{2.3}$$

with κ the von Kármán constant of 0.4, z the height above the surface, and p the profile shape exponent of 2. Note that the first part of this equation ($0.001\Delta z$, where Δz is the thickness of the model layers) is actually not mentioned in Hong *et al.* (2006) or Hong (2010), but this is present in the WRF code. A minimum K_m of 0.01 $m^2\ s^{-1}$ is applied.

The boundary-layer height h is determined by linearly interpolating between the two heights just below and above where the critical bulk Richardson number ($\mathrm{Ri_{b,cr}}$) is reached. The actual bulk Richardson number (Ri_b) is defined as:

$$Ri_b = \frac{g\left(\overline{\theta}_v(z) - \overline{\theta}_{vs}\right) z}{\overline{\theta}_{va}\overline{U}(z)^2}\,, \tag{2.4}$$

for which $\overline{\theta}_v(z)$ and $\overline{U}(z)$ are the virtual potential temperature and total wind speed at height z respectively, $\overline{\theta}_{va}$ is the virtual potential temperature at the lowest model level, $\overline{\theta}_{vs}$ the virtual potential temperature near the surface (technically also at the first model level), and g is the acceleration due to gravity. The Richardson number gives the ratio of turbulence determined by buoyancy effects over the mechanical shear term (Stull, 2000). Therefore, for large Ri_b values, buoyancy effects strongly suppress turbulence generated by wind shear. In stable conditions, $\mathrm{Ri_{b,cr}}$ is set to 0.25 over land. Note that some alternatives for equation 2.4 are discussed by Vogelezang and Holtslag (1996) and Kleczek *et al.* (2014).

For stable conditions the velocity scale w_s in equation 2.3 is a function of mechanical forcing only (in the form of the friction velocity u_*), for unstable conditions also a convective velocity scale is included. Hence for stable conditions w_s is defined as:

$$w_s = \frac{u_*}{\phi_m}\,, \tag{2.5}$$

with ϕ_m being the stability function for momentum, which is equal to the stability function for heat ϕ_h in stable conditions (after Businger *et al.* (1971) and Dyer (1974)):

$$\phi_m = \phi_h = 1 + 5\frac{z_1}{L}\frac{z}{z_1}\,. \tag{2.6}$$

Here L indicates the Obukhov length, and z_1 the first model level. For $\frac{z_1}{L}$, this is consistent with the Monin-Obukhov similarity in the surface layer (see Section 2.2.1), and it follows that:

$$\frac{z_1}{L} = Ri_{b,s}\frac{\left[\ln\left(\frac{z_1}{z_{0m}}\right) - \Psi_m\left(\frac{z_1}{L}\right)\right]^2}{\left[\ln\left(\frac{z_1}{z_{0h}}\right) - \Psi_h\left(\frac{z_1}{L}\right)\right]}\,, \tag{2.7}$$

where $Ri_{b,s}$ is Ri_b in the surface layer, calculated as in equation 2.4 with temperatures at the first model level and the surface. The roughness length for momentum and heat are given by z_{0m} and z_{0h} respectively, and Ψ_m and Ψ_h are the similarity stability functions for momentum and heat in the surface layer (see Section 2.2.1).

To determine the eddy diffusivity for heat, use is made of the Prandtl number, $Pr = K_m/K_h$, where K_h is the eddy diffusivity for heat. In stable conditions Pr equals 1, such that the eddy diffusivity of heat equals that of momentum. Additionally, the eddy diffusivity for moisture K_q is set equal to K_h, so that all eddy diffusivities are equal in stable conditions.

Note that the ϕ_m function in equation 2.6 was erroneously implemented in the original 3.2.1 version of YSU (Sukanta Basu and Wayne Angevine, personal communications, summer 2012; Hu *et al.*, 2013) by:

$$\phi_m = 1 + 5\frac{z}{L}\frac{h'}{h}\,, \tag{2.8}$$

where h' is a first estimate of the boundary-layer height for which an erroneous $\mathrm{Ri_{b,cr}}$ of 0 was used to determine the boundary-layer height. This lead to a too small value of ϕ_m and thus a too large eddy diffusivity. This stability function was corrected from WRF version 3.4.1 onwards. In the YSU-BL scheme used in this thesis (with WRF 3.2.1), we have corrected this also, making the YSU-BL scheme more compatible with WRF 3.4.1. Furthermore, as in WRF 3.4.1, the lower limit on w_s of $u_*/5$ was removed and replaced with 0.001 m s^{-1}.

The eddy diffusivity for heat in the free atmosphere is determined by (Hong *et al.*, 2006):

$$K_{h\ fa} = l^2 f\left(R_{ig}\right)\sqrt{\left(\frac{\partial\overline{u}}{\partial z}\right)^2 + \left(\frac{\partial\overline{v}}{\partial z}\right)^2}\,, \tag{2.9}$$

with l the mixing length, and $f\left(R_{ig}\right)$ the stability function which for a stably stratified free atmosphere is defined as:

$$f\left(R_{ig}\right) = \frac{1}{\left(1 + 5R_{ig}\right)^2}\,, \tag{2.10}$$

with R_{ig} the local gradient Richardson number:

$$R_{ig} = \frac{g}{\overline{\theta}_v}\frac{\frac{\partial\overline{\theta}}{\partial z}}{\left(\frac{\partial\overline{u}}{\partial z}\right)^2 + \left(\frac{\partial\overline{v}}{\partial z}\right)^2}\,. \tag{2.11}$$

To determine the eddy diffusivity for momentum in the free atmosphere, the Prandtl number is applied which is now defined as:

$$Pr_{fa} = \frac{K_{m\ fa}}{K_{h\ fa}} = 1 + 2.1R_{ig}\,, \tag{2.12}$$

where R_{ig} is the local gradient number as defined in equation 2.11 for cloud-free conditions, otherwise a modification has to be made to account for the smaller stability in the cloud layer (see Hong *et al.*, 2006). Now the Prandtl number is larger than unity to account for momentum transport due to pressure fluctuations which becomes more important with increasing stability (Kim and Mahrt, 1992).

The impact of the revision in the boundary-layer stability function turned out to be substantial for the YSU behaviour. Previously during the night time, often an overestimation of the low-level-jet height was found with too low wind speeds (Storm *et al.*, 2009). Hu *et al.* (2013) compared the two YSU versions and also found a clear improvement regarding the prediction of wind speed and the simulation of stronger low-level-jet at a lower height. Also the temperature profiles in the BL were improved, and surface temperatures were in better agreement with the observations.

Kleczek *et al.* (2014) noted as well that the typical overestimation of mixing that was found with the previous version is not visible in their simulations with the revised version. During the night, the model even underestimated the near-surface air temperature, with the low-level jet at a too low height, though with the correct speed. Sun and Barros (2013) find that for weakly stable conditions the mixing properties may now be underestimated.

2.1.2 MYJ BOUNDARY-LAYER SCHEME

In addition to the YSU-BL scheme, the Mellor-Yamada-Janjic (MYJ) BL scheme (Mellor and Yamada, 1982; Janjic, 2001) is used here. The MYJ scheme is a local, 1.5 order closure model and is considered as appropriate for stable and slightly unstable flows, but the errors can increase when the atmosphere becomes more convective (Hu *et al.*, 2010). The Level $2\frac{1}{2}$ Model version of MYJ is used in this thesis, for which the prognostic equation of the potential temperature variance is omitted, and only the prognostic equation for TKE is used on top of the prognostic equations for the mean variables of e.g. temperature, moisture, and wind. The governing equation for TKE ($\overline{e}$) that is solved within MYJ is:

$$\frac{\partial \overline{e}}{\partial t} = -\overline{U_j}\frac{\partial \overline{e}}{\partial x_j} - \frac{1}{\overline{\rho}}\frac{\partial \overline{w'p'}}{\partial z} - \frac{\partial \overline{w'e}}{\partial z} - \left(\overline{w'u'}\right)\frac{\partial \overline{u}}{\partial z} - \left(\overline{w'v'}\right)\frac{\partial \overline{v}}{\partial z} + \beta g\left(\overline{w'\theta_v'}\right) - \epsilon\,. \quad (2.13)$$

Here the term on the left hand side represents the storage or tendency of TKE. The first term on the right hand side represents the advection, the second term represents the redistribution of TKE due to pressure perturbations, while the third term describes the turbulent transport. The fourth and fifth term on the right hand side combined describe the production or loss of TKE due to wind shear, while the sixth term represents the production or loss due to buoyancy effects. Here β is usually $1/\overline{\theta_v}$, but is set to $1/273$ K^{-1} in the MYJ code. Finally, ϵ represents the viscous dissipation.

Note that to determine the eddy diffusivity for stable conditions in first order closure, it is assumed that the production and destruction of turbulence due to mechanical shear and buoyancy effects, balances the dissipation (Holtslag, 1998). However, in reality this is not always the case, and as such from a conceptual point of view it is preferable to use the full TKE equation, though as will be seen below, some simplifications were also made here.

The turbulent transport of $\overline{w'e}$ was chosen to be a function of the turbulent kinetic energy gradient in the form of $-lqS_q\frac{\partial \overline{e}}{\partial z}$, where q equals $\left(\overline{u_i'^2}\right)^{0.5}$, and S_q is a constant of 0.2 which was found to have the optimal agreement between model results and data (Mellor and Yamada, 1982). A similar relation can be assumed for $\overline{w'p'}$, however, then the constant was set to zero to reduce nomenclature and since the model would not distinct between the pressure and velocity diffusion. Alternatively, $\overline{w'p'}$ was set to zero by Mellor (1973), as this term is only small according to Hanjalic and Launder (1972). Furthermore, ϵ is parametrized as:

$$\epsilon = \frac{q^3}{\Lambda_1} = \frac{q^3}{B_1 l_M}\,, \quad (2.14)$$

for which Λ_1 is the dissipative length scale determined with the constant B_1 and the master length scale l_M.

The turbulent flux terms of $\overline{w'u'}$, $\overline{w'v'}$, and $\overline{w'\theta'}$ are defined as in equation 2.1. However, the expressions for K_m and K_h are more complex than for the YSU first-order scheme. In their simple form they are defined as:

$$K_m = l_M q S_m \,, \tag{2.15}$$

$$K_h = l_M q S_h \,, \tag{2.16}$$

where S_m and S_h are dimensionless stability functions (Bianco *et al.*, 2011). With the following equations representing the turbulence production by shear (G_m) and by buoyancy (G_h):

$$G_m = \frac{l_M^2}{q^2}\left[\left(\frac{\partial \overline{u}}{\partial z}\right)^2 + \left(\frac{\partial \overline{v}}{\partial z}\right)^2\right] , \tag{2.17}$$

$$G_h = -\frac{l_M^2}{q^2}\beta g\left(\frac{\partial \overline{\theta_v}}{\partial z}\right) , \tag{2.18}$$

the equation for TKE in 2.13 can be rewritten as:

$$\frac{\partial \overline{e}}{\partial t} + \overline{U_j}\frac{\partial \overline{e}}{\partial x_j} - \frac{\partial}{\partial z}\left[l_M q S_q \frac{\partial \overline{e}}{\partial z}\right] = \left[S_m G_m + S_h G_h - \frac{1}{B_1}\right]\frac{q^3}{l_M} \,. \tag{2.19}$$

The set of equations that determines S_m, S_h, G_m and G_h is:

$$S_m\left(6A_1A_2G_m\right) + S_h\left(1 - 3A_2B_2G_h - 12A_1A_2G_h\right) = A_2 \,, \tag{2.20}$$

$$\begin{aligned} S_m\left(1 + 6A_1^2G_m - 9A_1A_2G_h\right) - S_h\left(12A_1^2G_h + 9A_1A_2G_h\right) = \\ A_1\left(1 - 3C_1\right) \,. \end{aligned} \tag{2.21}$$

The constants A_1, A_2, B_1, B_2, and C_1 are determined using experimental data and internal relations. Note that a full account on how these equations have been derived and on the closing of this system is given in Mellor and Yamada (1982) and Janjic (2001).

The master length scale in the boundary layer is defined following Blackadar (1962):

$$l_M = l_0\frac{\kappa z}{\kappa z + l_0} \,, \tag{2.22}$$

such that the mixing length approaches κz close to the surface, and is about l_0 for large values of z. Here l_0 is defined as:

$$l_0 = \alpha\frac{\int_0^h |z| q dz}{\int_0^h q dz} \,, \tag{2.23}$$

where h is the BL height, which is now determined as the highest model level below a prescribed upper bound of TKE (Janjic, 2001), and α is a constant value of 0.3.

Finally, the eddy diffusivity for moisture is set equal to that of heat (Xue *et al.*, 2014).

2.2 Surface-layer schemes

The BL scheme runs in close connection with the surface-layer scheme. This scheme determines the friction velocities and the exchange coefficients that are used to calculate the fluxes in the land-surface model, as well as the surface stress in the BL scheme (Skamarock *et al.*, 2008). Over water surfaces, the surface layer itself calculates the surface fluxes and surface diagnostic fields. In WRF, each BL scheme has a particular surface-layer scheme tied to it. For YSU this is the MM5 surface scheme, while for MYJ the ETA surface-layer scheme is applied.

2.2.1 MM5 surface-layer scheme

The MM5 surface-layer scheme parametrizes the sensible heat (H), latent heat ($L_v E$) and momentum (τ) fluxes as follows:

$$H = -\overline{\rho} c_p u_* \theta_* = -\overline{\rho} c_p C_h \overline{U}_a (\overline{\theta}_a - \overline{\theta}_0)\,, \tag{2.24}$$

$$L_v E = L_v \overline{\rho} M u_* q_* = -L_v \overline{\rho} M C_q \overline{U}_a (\overline{q}_a - \overline{q}_0)\,, \tag{2.25}$$

$$\tau = \overline{\rho} u_*^2 = \overline{\rho} C_d \overline{U}_a^2\,, \tag{2.26}$$

where $\overline{\rho}$ is the air density, c_p the specific heat of dry air, and C_h, C_q, and C_d are the exchange coefficients for heat, moisture and momentum respectively. $\overline{\theta}$ is the potential temperature, $\overline{q}$ the specific humidity, and $\overline{U}$ is the wind speed magnitude. The subscript a indicates the first model level, the subscript *0* represents the surface. The latent heat of vaporization for water is given by L_v. Note that in the land-surface model, an adjustment is made for this parameter to also account for the latent heat flux of sublimation. M is the soil moisture availability (between 0 and 1). The friction velocity and the temperature and humidity scales are indicated with u_*, θ_* and q_* respectively.

In this surface-layer scheme, the Monin-Obukhov similarity theory is applied (Monin and Obukhov, 1954). Based on dimensional analysis, the parameters that govern the surface layer (z, ρ, g, τ, H, and E, De Bruin, 1998), must be a function of the dimensionless length of z/L, such that for the dimensionless potential temperature gradient and wind shear it holds that (e.g. Stull, 1988; De Bruin, 1998; Jiménez *et al.*, 2012):

$$\frac{\partial \overline{U}}{\partial z} \frac{\kappa z}{u_*} = \phi_m \left(\frac{z}{L} \right)\,, \tag{2.27}$$

$$\frac{\partial \overline{\theta}}{\partial z} \frac{\kappa z}{\theta_*} = \phi_h \left(\frac{z}{L} \right)\,, \tag{2.28}$$

$$\frac{\partial \overline{q}}{\partial z} \frac{\kappa z}{q_*} = \phi_q \left(\frac{z}{L} \right)\,. \tag{2.29}$$

It is more convenient in observations and models to determine the absolute differences than the derivatives. Hence, these equations are integrated with respect to height between the roughness length and the first model level and it follows that:

$$\overline{U}_a = \frac{u_*}{\kappa} \left[\ln \left(\frac{z_a}{z_{0m}} \right) - \Psi_m \left(\frac{z_a}{L} \right) + \Psi_m \left(\frac{z_{0m}}{L} \right) \right]\,, \tag{2.30}$$

$$\overline{\theta}_a - \overline{\theta}_0 = \frac{\theta_*}{\kappa}\left[\ln\left(\frac{z_a}{z_{0h}}\right) - \Psi_h\left(\frac{z_a}{L}\right) + \Psi_h\left(\frac{z_{0h}}{L}\right)\right], \tag{2.31}$$

with z_{0m} and z_{0h} the roughness lengths for momentum and heat respectively. In the MM5 surface-layer scheme z_{0h} equals z_{0m}. Now Ψ_m and Ψ_h are the integrated similarity stability functions for momentum and heat respectively, which is done according to (Panofsky, 1963):

$$\Psi_{m,h} = \int_0^{z/L}\left[\frac{1-\phi_{m,h}\left(\frac{z}{L}\right)}{\frac{z}{L}}\right] d\left(\frac{z}{L}\right). \tag{2.32}$$

The relations in equations 2.30 and 2.31 are also used to determine the relation in equation 2.7. In the YSU BL scheme and MM5 surface-layer scheme then the third term in the squared brackets of equations 2.30 and 2.31 is omitted, as this is generally very small compared to the other terms (though it becomes relatively more important for rough surfaces) and this saves computational time. Then the following relations are found for u_* and θ_*:

$$u_* = \frac{\kappa \overline{U}_a}{\ln(\frac{z_a}{z_{0m}}) - \Psi_m\left(\frac{z_a}{L}\right)}, \tag{2.33}$$

$$\theta_* = \frac{\kappa(\overline{\theta}_a - \overline{\theta}_0)}{\ln(\frac{z_a}{z_{0h}}) - \Psi_h\left(\frac{z_a}{L}\right)}. \tag{2.34}$$

An analogous approach was followed for q_*:

$$q_* = -\frac{\kappa(\overline{q}_a - \overline{q}_0)}{\ln(\frac{\kappa u_* z_a}{C_s} + \frac{z_a}{z_l}) - \Psi_h\left(\frac{z_a}{L}\right)}, \tag{2.35}$$

though now the term z_l is included for the assumption of a viscous sublayer from the ground to height z_l, while a turbulent layer where Monin-Obukhov theory is applicable is assumed from z_l to z_a (Jiménez *et al.*, 2012). Over land, z_l is set to 0.01 m, over water surfaces this equals z_0. The term $\frac{\kappa u_* z_a}{C_s}$ is included as a scaling height to represent an effective roughness length for heat (Carson and Boland, 1978). C_s is taken as a background molecular diffusivity set to $2.4{\cdot}10^{-5}$ m^2 s^{-1} (Grell *et al.*, 1994).

Combining equations 2.33 - 2.35 with equations 2.24 - 2.26, gives for the exchange coefficients:

$$C_d = \frac{\kappa^2}{\left[\ln(\frac{z_a}{z_{0m}}) - \Psi_m\left(\frac{z_a}{L}\right)\right]^2}, \tag{2.36}$$

$$C_h = \frac{\kappa^2}{\left[\ln(\frac{z_a}{z_{0m}}) - \Psi_m\left(\frac{z_a}{L}\right)\right]\left[\ln(\frac{z_a}{z_{0h}}) - \Psi_h\left(\frac{z_a}{L}\right)\right]}, \tag{2.37}$$

$$C_q = \frac{\kappa^2}{\left[\ln(\frac{z_a}{z_{0m}}) - \Psi_m\left(\frac{z_a}{L}\right)\right]\left[\ln(\frac{\kappa u_* z_a}{c_s} + \frac{z_a}{z_l}) - \Psi_h\left(\frac{z_a}{L}\right)\right]}. \tag{2.38}$$

The integrated similarity stability functions are dependent on the stability regime. The MM5 surface-layer scheme uses 4 stability regimes based on Zhang and Anthes (1982). The first regime is for stable conditions where $Ri_b \geq 0.2$:

$$\Psi_m = \Psi_h = -10 \ln \left(\frac{z_a}{z_0} \right) . \tag{2.39}$$

This was determined to be zero by Zhang and Anthes (1982) as above the critical Richardson number here set at 0.2, it was assumed that there is no more turbulence. In the MM5 implementation this is set at a constant value to allow for some mixing. The second regime is for $0 < Ri_b < 0.2$, and represents damped mechanical turbulent conditions:

$$\Psi_m = \Psi_h = -5 Ri_b \frac{\ln(\frac{z_a}{z_0})}{1.1 - 5Ri_b} , \tag{2.40}$$

where now in the denominator, it is stated 1.1 - $5Ri_b$ instead of 1 - $5Ri_b$, to avoid a division by zero for $Ri_b = 0.2$. This division of the two regimes for stable conditions is somewhat peculiar as now for very stable conditions the stability function is independent on the stability. Assuming a constant density and wind speed, but varying the temperature gradient, this implies that at first H increases with increasing temperature gradient, after which a decrease in H is seen with increasing temperature gradient. This is indeed representative of the two regimes where at some point the increase in H due to increasing temperature gradient is counteracted by the strongly reduced exchange coefficient (Holtslag *et al.*, 2007). However, as soon as an Ri_b of 0.2 is reached, the exchange coefficient cannot decrease further such that the magnitude of H starts to increase again with the increasing temperature gradient. Hence this behaviour seems to be physically incorrect.

The two other stability regimes represent forced convection conditions for $Ri_b = 0$, and for unstable conditions with $Ri_b < 0$. As this thesis focusses only on stable conditions, these are not discussed here.

Over land, the surface-layer scheme provides the exchange coefficients to the land-surface model, where the surface heat and moisture fluxes are calculated. Additionally, u_* is provided to the BL scheme to represent the surface stress. Interestingly, in the surface-layer model, there are different exchange coefficients for heat and moisture, but only one exchange coefficient is read into the land-surface model. This exchange coefficient C_H in m s^{-1} is defined as:

$$\begin{aligned} C_H &= \frac{u_* \kappa}{\ln(\frac{\kappa u_* z_a}{c_s} + \frac{z_a}{z_l}) - \Psi_h \left(\frac{z_a}{L} \right)} = \\ &= \frac{\kappa^2 \overline{U}_a}{\left[\ln(\frac{z_a}{z_0}) - \Psi_m \left(\frac{z_a}{L} \right) \right] \left[\ln(\frac{\kappa u_* z_a}{c_s} + \frac{z_a}{z_l}) - \Psi_h \left(\frac{z_a}{L} \right) \right]} = C_q \overline{U}_a . \end{aligned} \tag{2.41}$$

2.2.2 ETA surface-layer scheme

The ETA surface-layer scheme runs in conjunction with the MYJ-BL scheme. The surface sensible heat and moisture fluxes are determined similarly as in the MM5

surface-layer scheme (see equations 2.24 - 2.26). For the exchange coefficients, here all three terms in the square brackets of equations 2.30 and 2.31 are taken into account, and the exchange coefficient of moisture is set equal to that of heat. Therefore the exchange coefficients are determined with:

$$C_d = \frac{\kappa^2}{\left[\ln\left(\frac{z_a}{z_{0m}}\right) - \Psi_m\left(\frac{z_a}{L}\right) + \Psi_m\left(\frac{z_{0m}}{L}\right)\right]^2}, \tag{2.42}$$

$$C_H = \frac{\kappa^2 \overline{U}_a}{\left[\ln\left(\frac{z_a}{z_{0m}}\right) - \Psi_m\left(\frac{z_a}{L}\right) + \Psi_m\left(\frac{z_{0m}}{L}\right)\right]\left[\ln\left(\frac{z_a}{z_{0h}}\right) - \Psi_h\left(\frac{z_a}{L}\right) + \Psi_h\left(\frac{z_{0h}}{L}\right)\right]}, \tag{2.43}$$

where C_H is also the exchange coefficient read into the land-surface model. Contrary to the MM5 surface-layer scheme, the ETA surface-layer scheme does explicitly distinct between z_{0m} and z_{0h}, where z_{0h} is determined following Zilitinkevich (1995):

$$z_{0h} = z_{0m} \exp\left(-\kappa C_{zil}\sqrt{Re_*}\right). \tag{2.44}$$

Here C_{zil} is a constant, and Re_* is the roughness Reynolds number defined as $\frac{u_* z_{0m}}{\nu}$ with ν being the kinematic molecular viscosity. As such, z_{0h} is a function of the atmospheric flow (Stensrud, 2007). The thermal roughness length is included to account for the transport of heat by molecular diffusion.

The similarity stability functions Ψ_m and Ψ_h are dependent on the stability regime. For the stable surface layer ($\frac{z}{L} \geq 0$) a somewhat similar equation is used as in Holtslag and De Bruin (1988, according to Tardif and Hacker (2006). Note that what is written in the code for stable conditions (as stated below), differs from what is stated in Tardif and Hacker (2006) to be the stability function in the ETA surface-layer scheme. In the code this is:

$$\Psi_m = \Psi_h = -0.7\frac{z_a}{L} - 0.75\frac{z_a}{L}\left(6 - 0.35\frac{z_a}{L}\right)\exp\left(-0.35\frac{z_a}{L}\right). \tag{2.45}$$

In this way a smooth transition for all stable values of z/L is simulated instead of the abrupt transition that was seen with the MM5 surface-layer scheme for the stable regime. The Obukhov length L is calculated with (Tardif and Hacker, 2006):

$$L = -\frac{\rho c_p \theta_a u_*^3}{\kappa g H} = \frac{\theta_a u_*^3}{\kappa g C_H (\theta_a - \theta_0)}. \tag{2.46}$$

Since L is a function of C_H and u_*, and both these terms are a function of L, this set of equations is solved by several iterations.

2.3 Land-surface model

The land-surface model (LSM) determines the surface heat and moisture fluxes over land and sea ice. It also determines the conductive heat flux through the soil and possibly snow cover and updates certain variables such as the surface temperature,

temperature and moisture of the soil, snow cover, and canopy properties (if present) (Skamarock *et al.*, 2008). Also for the 3D-WRF model, there is no horizontal interaction between soil columns, such that it can be regarded as a single-column model for each grid cell.

In this thesis only the Noah LSM has been used, which is therefore the only scheme discussed here. The determination of the sensible (H) and latent heat (LE) fluxes will be addressed, using the exchange coefficients provided by the surface-layer scheme, as well as the conductive heat flux (G). For the latter, knowledge on how the fraction and depth of the snow cover is defined is necessary. Furthermore, this gives more insight in the model behaviour when the snow conductivity is adjusted to study the relative impact of snow-surface coupling on the SBL evolution.

The sensible heat flux H is determined with:

$$H = -c_p \overline{\rho} C_H (\overline{\theta}_a - T_0)\,, \tag{2.47}$$

which is similar as equation 2.24, but now the wind speed is included in the exchange coefficient, and T_0 is the effective skin temperature, contributing for the ground, canopy and snow pack. While for H there is a direct relation between the temperature difference and the exchange coefficient, this is more advanced for the latent heat flux LE. LE is determined using the sign of the potential evaporation (LE_p), according to:

$$LE = \begin{cases} L_v E_{dir} + L_v E_c + L_v E_{tt} + L_s E_{snow}, & \text{for } LE_p > 0\,, \\ LE_p, & \text{otherwise}\,. \end{cases} \tag{2.48}$$

The potential evaporation is the amount of evaporation that would occur if there are no restrictions on the water supply, for example over a water surface. Then the evaporation is only determined by the atmospheric conditions (Mahrt and Ek, 1998). Also when LE is directed downwards, the state of the surface does not impact the latent heat flux, and hence LE equals LE_p and occurs in the form of dew or rime. When the flux is directed upwards, the actual evaporation is dependent on e.g. the soil moisture availability in the soil (E_{dir}, the direct soil evaporation), the intercepted canopy water content and the capacity of the vegetation to hold this (E_c, the canopy water evaporation), and the resistance of the vegetation (E_{tt}, the total plant transpiration), as well as the amount of sublimation from the snow pack if present (E_{snow}) (Chen and Dudhia, 2001). Furthermore, the individual terms are multiplied with either L_v or L_s, which are the latent heat of vaporization ($2.50 \cdot 10^6$ J kg^{-1}) and sublimation ($2.83 \cdot 10^6$ J kg^{-1}) respectively, to determine the evaporation in W m^{-2}.

Since in this thesis during the stable conditions in general a downward directed latent heat flux is found, only LE_p is explained in more detail here. This is calculated with:

$$LE_p = \left((1 - \sigma_{snow})\, L_v + \sigma_{snow} L_s\right) E_p\,, \tag{2.49}$$

with σ_{snow} being the snow cover fraction. To determine E_p, the energy balance is used:

$$(1 - \alpha) SW\downarrow + LW\downarrow - \epsilon \sigma T_0^4 = G + H + LE_p\,, \tag{2.50}$$

for which α is the surface albedo, and $SW\downarrow$ and $LW\downarrow$ are the incoming short wave and long wave radiation respectively. The surface emissivity is indicated with ϵ, and σ is the Stefan Boltzmann constant ($5.67 \cdot 10^{-8}$ W m^{-2} K^{-4}). Since several terms are so far unknown (i.e. T_0, which is also part of H), this equation is reorganized and solved for LE_p as:

$$LE_p = \left(\frac{\left[\frac{R_n}{\rho c_p C_H} + \left(\overline{\theta}_a - \overline{T}_a \right) \right] \Delta + (r+1)\, A}{\Delta + r + 1} \right) \overline{\rho} c_p C_H \,, \tag{2.51}$$

making use of the following equations (which are also used to make the code more insightful):

$$\begin{aligned} R_n &= (1-\alpha) SW\downarrow + LW\downarrow - \epsilon\sigma \overline{T}_a^4 - G \,, \\ \Delta &= \frac{d\overline{q}^*}{d\overline{T}} \frac{L}{c_p} \,, \\ r &= \frac{4\epsilon\sigma \overline{T}_a^4 R_d}{p_{sfc} c_p C_H} \,, \\ A &= \left(\overline{q}_a^* - \overline{q}_a \right) \frac{L}{c_p} \,. \end{aligned} \tag{2.52}$$

Here R_d is the gas constant for dry air, and dq_*/dT is the derivative of the saturation specific humidity with respect to T. For this the Tetens' formula is applied (Stull, 2000), where a distinction is made regarding the constants for either water saturation or ice saturation properties. A full account on how equation 2.51 is attained is given by Ek and Mahrt (1991).

As mentioned previously, during stable conditions, the atmospheric temperatures are higher than the surface temperature. Then also the temperature of the underlying medium is higher than the skin temperature, such that the conductive heat flux, or soil heat flux (G), is also directed towards the surface. G is determined as:

$$G = -\lambda \frac{\Delta T}{\Delta z_{tot}} \,. \tag{2.53}$$

Here ΔT represents the temperature difference throughout the depth of the top layer Δz_{tot}, which is determined as the sum of the depth to the centre of the first soil layer (Δz_{soil}) and the snow depth (Δz_{snow}). The determination of the different layers is also indicated in Figure 2.1. The conductivity of the top layer is represented by λ and determined with (Ek *et al.*, 2003):

$$\lambda = \sigma_{snow} \lambda_{snow+soil+veg} + (1 - \sigma_{snow}) \lambda_{soil+veg} \,, \tag{2.54}$$

$$\lambda_{snow+soil+veg} = \frac{\Delta z_{snow}}{\Delta z_{tot}} \lambda_{snow} + \frac{\Delta z_{soil}}{\Delta z_{tot}} \lambda_{soil+veg} \,, \tag{2.55}$$

$$\lambda_{soil+veg} = \lambda_{soil} \exp(-\beta_{veg} \sigma_{veg}) \,. \tag{2.56}$$

The conductivity for the soil layer including snow and vegetation ($\lambda_{snow+soil+veg}$) is determined with the relative layer thickness of the individual layers times the conductivity of the associated layer (λ_{snow} and $\lambda_{soil+veg}$, representing the conductivity

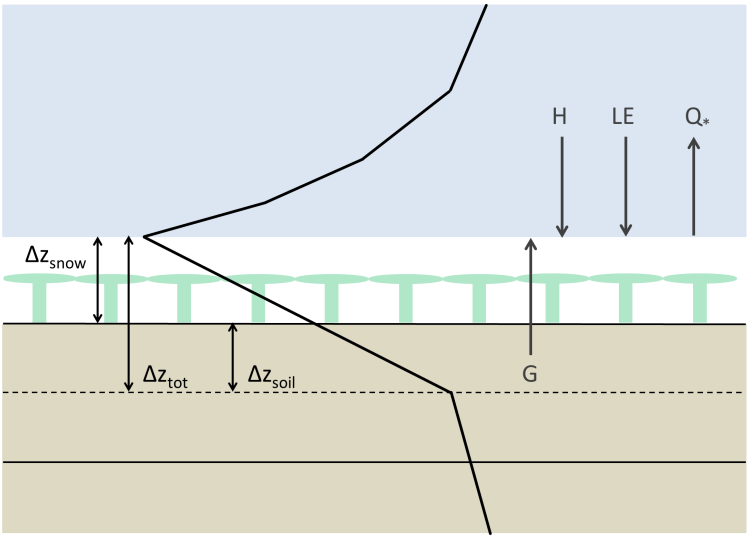

Figure 2.1: Sketch of the idealized temperature profile in the underlying medium and the stable boundary layer, and indications of the different soil / snow layers, as well as the direction of the fluxes. The dashed line indicates the centre of the soil layer for which calculations are performed, the total thickness of the first soil layer is given by the full lines.

of the snow layer, and the conductivity of the soil layer including vegetation effects respectively). Furthermore, $\lambda_{soil+veg}$ is determined as the conductivity of the bare soil times an exponential function of an empirical coefficient (β_{veg}) and the vegetation fraction (σ_{veg}).

When the snow cover is larger than 97%, the top layer conductivity is set equal to the snow conductivity. Furthermore, in the case of sea ice, the conductivity of underlying ice layers is set equal to the top layer conductivity.

2.4 Long wave radiation

In this thesis, mostly the RRTM (Rapid Radiative Tranfer Model, Mlawer *et al.*, 1997) and the follow-up RRTMG (Iacono, 2011; where G stands for General circulation model) long wave radiation schemes are used. The RRTMG model uses the same physics as RRTM, and as such the RRTM scheme will be discussed here. The radiation schemes in WRF are applied in a single-column mode, and within WRF-3D the radiation calculations of all columns are treated independently. Therefore horizontal homogeneity is assumed, which is considered a good approximation when the thickness of the vertical levels are relatively thin compared to the horizontal resolution (Skamarock *et al.*, 2008), as is also the case in this thesis.

The long wave radiation schemes in general parametrize the transport of energy by long wave radiation. As such, the incoming and outgoing long wave radiation at the surface necessary for the surface energy balance are determined, as well as the radiative flux divergence in the atmosphere which determines the atmospheric

heating/cooling by:

$$\frac{\partial \overline{T}}{\partial t} = -\frac{1}{\overline{\rho} C_p} \frac{\partial \overline{Q}^*}{\partial z}\,, \tag{2.57}$$

where $\overline{Q}^*$ is the net radiation and in the absence of short wave radiation equal to the incoming minus the outgoing long wave radiation. Therefore, for each layer the incoming and outgoing long wave radiation have to be known.

At the top of the atmosphere, the incoming long wave radiation is zero. However, between the top of the atmosphere and the surface, each layer of atmosphere emits radiation. The emission occurs in all directions, so towards and away from the surface. Therefore each layer also receives the emitted radiation from the layer above and below plus possibly from further away when certain layers transmit some of the received radiation instead of absorbing it. The outgoing long wave radiation of a certain atmospheric layer is determined by its temperature and its emissivity ϵ as:

$$LW \uparrow = \epsilon \sigma T^4\,, \tag{2.58}$$

with σ being the Stefan-Boltzmann constant ($5.67{\cdot}10^{-8}$ W m^{-2} K^{-4}).

As mentioned already in Chapter 1, the amount of radiation emitted varies per wavelength (λ_w) for a given temperature. This follows Planck's law, which determines the amount of energy emitted at a single wave length, B^*_λ, assuming a black body, by (Stull, 2000):

$$B^*_\lambda = \frac{c_1}{\lambda_w^5 \left(\exp\left(\frac{c_2}{\lambda_w T}\right) - 1\right)}\,, \tag{2.59}$$

with c_1 and c_2 being constants of $3.74{\cdot}10^{-16}$ W m^{-2} and $1.44{\cdot}10^{-2}$ m K. Again, as many objects are not a black body, the actual emitted energy per wavelength is determined by the emissivity at that wavelength: $B_\lambda = \epsilon_\lambda B^*_\lambda$.

Besides that a layer emits the radiation that it absorbed (though be it with a different temperature), it also transmits that part of received radiation that it does not absorb. This is also dependent on the density of the absorbing gas (ρ), and given by:

$$E_{\lambda\ transmitted} = E_{\lambda 0} \exp\left(-k_\lambda \rho \frac{\Delta z}{\cos(\phi)}\right)\,. \tag{2.60}$$

Here $E_{\lambda 0}$ is the incoming amount of energy, k_λ the absorption coefficient at a certain wavelength, Δz the thickness of the layer, and ϕ the angle of the optical path (zero when exactly overhead). This equation is often called Beer's law, and the part with $k_\lambda \rho \Delta z$ is sometimes written as τ_λ, being the optical depth of the layer (Stensrud, 2007). Note that radiation transport can also take place in the form of scattering. However, this is negligible for the long wave range and hence not taken into account (Liou, 1980).

So far the discussion on outgoing radiation only concerns a single wavelength. That is because the absorption coefficient which is equal to the emissivity and which also influences the transmission efficiency, varies per wavelength. This is due to the

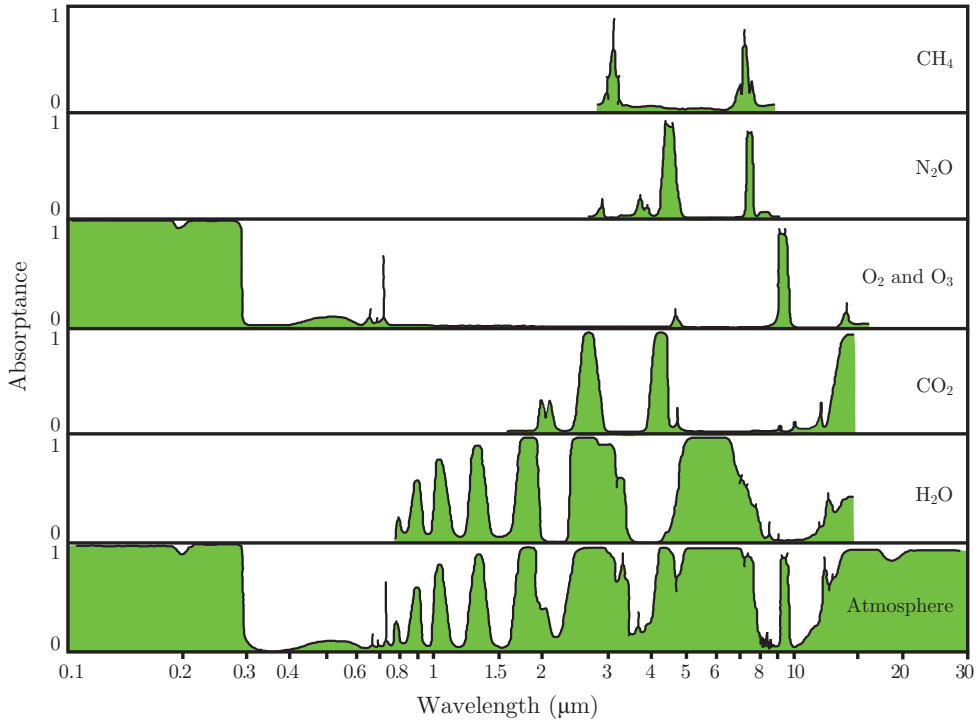

Figure 2.2: The absorptivity of radiation due to different gases in the atmosphere and the atmosphere as a whole. Adapted from Fleagle and Businger (1963).

fact that the atmosphere consists of water species and several gases. As is indicated with Figure 2.2, different gases in the atmosphere absorb differently for different wave lengths. E.g. O_2 and O_3 are very effective in absorbing the short wave radiation, while other gases are more effective in absorbing radiation in the long wave range. Due to Kirchhoffs law, which states that the emissivity is equal to the absorption (Stull, 2000), also the emissivity differs per wavelength for the different gases. The figure also shows that the gases can be associated with specific wavelength bands (Stensrud, 2007). As such, in the RRTM long wave radiation scheme, the long wave region is divided in series of spectral bands, which contain strong absorption/emission bands due to a limited number of gases (Mlawer *et al.*, 1997).

RRTM treats the following molecular species: water vapour, CO_2, O_3, N_2O, CH_4, $CFC-11$, $CFC-12$, $CFC-22$, and CCl_4. The selection of bands was such that each spectral band only has a maximum of 2 species with a substantial absorption/emission, the so-called key-species, and that the range in emitted energy obtained for the various wavelengths was not too extreme, while keeping the amount of bands at a minimum. An overview of the 16 bands used in RRTM is given by Mlawer *et al.* (1997). A distinction for the key species is also made for the lower part and middle/upper part of the atmosphere, since the presence of species can vary

with height.

Concerning only one band for a given atmospheric layer, the spectral absorption coefficient k of a gas species varies irregularly for the wave numbers in the spectral band, which makes it difficult to determine representative values for the absorption coefficient (Mlawer *et al.*, 1997). Therefore, these varying absorption coefficients are rearranged in ascending order, such that a smooth cumulative function is obtained. For each spectral band, this cumulative function is again divided in 16 intervals. RRTM has many k_j stored for a set of reference pressures in combination with a set of reference temperatures, combined with several fixed relative contributions of the key species. These stored values are obtained from a line-by-line radiative transfer model (LBLRTM) and validated with observations. From these tables, linear interpolation is applied to obtain an accurate value for k_j for the simulated atmospheric layer in RRTM.

More details on the precise calculation of the radiance with RRTM at a single atmospheric layer are out of the scope of this thesis and described in Mlawer *et al.* (1997). In order to achieve the downward radiation, the calculations are started at the top, going down layer by layer (ECMWF, 2013). Then the incoming long wave radiation at the surface is known, such that the outgoing long wave radiation at the surface can be calculated from:

$$LW \uparrow_s = \epsilon_s \sigma T_s^4 + (1 - \epsilon_s)\, LW \downarrow \ . \tag{2.61}$$

Here the subscript s denotes the surface, and ϵ_s is the emissivity (or absorptivity) of the surface. The last term in equation 2.61 is included to represent reflection of the long wave radiation at the surface, which is equal to the fraction that is not absorbed (1 - ϵ_s).

From the now known upward radiation at the surface, subsequently the upward radiation at the atmospheric layers can be calculated, going up layer by layer (ECMWF, 2013).

The RRTM long wave radiation scheme was used as the reference long wave radiation scheme in Chapter 3. In Chapters 4 and 5, the follow-up RRTMG long wave radiation scheme was used. The RRTMG uses the same physics and absorption coefficients as RRTM, though several modifications were made to improve its computation efficiency for use in global climate models for example (Iacono *et al.*, 2008; Iacono, 2011). In particular, the amount of intervals in the long wave bands, has been reduced for several long wave bands, such that the total number of intervals is reduced from 256 (16 x 16) to 140. Also, with RRTMG it is possible to have cloud fractions at a certain atmospheric layer, where with RRTM the layer is either cloud-free or has a full cloud cover, however, this is not of relevance for the clear-sky conditions studied in this thesis.

2.5 Code adjustments for the sensitivity analyses

The essential parts of the parametrization schemes most frequently used in this thesis have just been discussed. As explained in Section 1.4, sensitivity analyses were performed to a) obtain which of these processes is most critical in determining the SBL state for various wind regimes (Chapter 3), and b) study the relative impact of these

processes for contrasting terrains (Chapter 5). For these sensitivity analyses, the intensity of the different processes was varied, and simulations for the different cases were repeated with this renewed intensity. This section describes the adjustments in the parametrization schemes to alter the process intensity.

To adjust the turbulent mixing within the boundary-layer schemes, the eddy diffusivities for heat, momentum, and moisture were multiplied by a certain amplification factor F. To consistently link the boundary layer and the surface layer, also the exchange coefficients in the surface layer were adjusted with the same factor.

For the YSU-BL scheme which runs in conjunction with the MM5 surface-layer scheme, the eddy diffusivities K as calculated in equation 2.3 have been multiplied with F. The same was done for the exchange coefficients for heat and moisture in equation 2.41. The exchange coefficient of momentum C_d is not directly calculated. Hence, u_* in the surface-layer was adjusted (equation 2.33), as it can be seen from equations 2.33 and 2.36 that:

$$u_* = \sqrt{C_d}\overline{U}_a \,. \tag{2.62}$$

As such, u_* is multiplied with $\sqrt{F}$. However, as is seen in equations 2.3 and 2.5, u_* is also used to determine the already adjusted K. Therefore, the terms containing u_* that were used for the eddy diffusivity equations in the YSU-BL scheme were corrected by dividing them with $\sqrt{F}$ to avoid a double impact on the K's. The same holds for the terms needed to derive the exchange coefficient for heat and moisture in equation 2.41, which is also dependent on u_*.

With the MYJ-BL scheme that runs in conjunction with the ETA surface-layer scheme, u_* was not used to determine K, so that adjustments on this were not necessary. Then u_* is only used to calculate the turbulent kinetic energy at the first model level being the top of the surface layer. Thus u_* in equation 2.33 was multiplied with $\sqrt{F}$, and the exchange coefficient for heat and moisture in equation 2.43 was multiplied with F, as were the K's calculated with equations 2.15 and 2.16. The set of equations in the surface-layer scheme is solved iteratively. Therefore the adjustments were only made after the finalization of the iterative process.

To study the relative impact of the snow-surface coupling compared to the impact of the other processes, the snow conductivity λ_{snow} that is used in equations 2.53 - 2.55, was multiplied with varying factors F. Since over sea ice the snow cover is set to 100%, this implies that for sea ice cases the conductivity of the entire underlying medium is adjusted, while for surfaces with snow cover over soil, only the snow conductivity is changed.

Finally, to analyse the relative impact of incoming long wave radiation, two approaches were chosen. The first is that the initial profile of the specific humidity q was adjusted with a certain factor F. This is because according to Svensson and Karlsson (2011), the clear-air $LW\downarrow$ in cold and dry conditions is very sensitive to a change in the q-profile and in lesser extent to a change in the temperature profile. Therefore the atmospheric water content is very important for the radiation balance of the surface. Zhang *et al.* (2001) also showed that a change in precipitable water has a higher impact on $LW\downarrow$ than a change in mean atmospheric temperature for similar conditions. Therefore this approach was used to adjust $LW\downarrow$ in Chapter 3.

Changing q may also affect the surface evaporation and thus the surface energy

balance and temperature in the air. Therefore the change in model behaviour may not only be related to a change in $LW\downarrow$ (though a change in $LW\downarrow$ of course also affects the surface energy balance). As such, in Chapter 5 an alternative approach, besides an altered q-profile, was taken to adjust $LW\downarrow$, namely by multiplying the CO_2 gas concentration prescribed in the RRTMG long wave radiation scheme with a certain factor.

Note that several multiplication factors F have been applied, either increasing or decreasing the process intensities (ranging from 0.25 - 4), and that the factors may differ for the different processes. The exact multiplication factors, and how this compares with observed/modelled uncertainties, are given in the separate chapters.

Chapter 3

The role of snow-surface coupling, radiation, and turbulent mixing in modelling a stable boundary layer over Arctic sea ice

Abstract

To enhance the understanding of the impact of small-scale processes in the polar climate, this study focuses on the relative role of snow-surface coupling, radiation and turbulent mixing in an Arctic stable boundary layer. We extend the GABLS1 (GEWEX Atmospheric Boundary-Layer Study, 1^{st}) model intercomparison for turbulent mixing with the other relevant physical processes in the stable boundary layer over sea-ice. We use the Single Column Model (SCM) version of the Weather Research and Forecasting (WRF) mesoscale meteorological model, and run different combinations of boundary-layer and radiation schemes, using a state of the art land-surface scheme. With this intercomparison of schemes, we confirm a wide variety in the state of the atmosphere and the surface variables for the selected parametrization schemes.

To understand this variety, a sensitivity analysis for one particular combination of parametrization schemes is performed, using a novel analysis method of process diagrams. The variation between the sensitivity runs indicates a relative orientation of model sensitivities to variations in each of the governing processes and these can explain the variety of model results obtained in the intercomparison of different parametrization schemes.

Moreover, we apply the same method for several geostrophic wind speeds to represent a large range of synoptic conditions. Results indicate a shift in process significance for different wind regimes. For low wind regimes, the model sensitivity is larger for surface coupling and radiation, while for high wind speeds, the largest sensitivity is found for the turbulent mixing process. An interesting non-linear feature was found for turbulent mixing for frequently occurring wind speeds and low wind speed cases, where the 2 m temperature increases for decreased amounts of mixing.

This Chapter has been published as Sterk HAM, Steeneveld GJ, Holtslag AAM. 2013. The role of snow-surface coupling, radiation, and turbulent mixing in modeling a stable boundary layer over Arctic sea ice, *J. Geophys. Res. Atmos.* **118**: 1199–1217, doi: 10.1002/jgrd.50158.

3.1 Introduction

Modelling the atmospheric stable boundary layer (SBL) is a challenging task. Many global and regional climate model outputs diverge from one another, as well as from observations for near surface variables such as temperature, wind speed and humidity (see also Section 3.2). These features underline the lack of understanding of the governing mechanisms related to the SBL. Furthermore, SBL modelling may be hampered by computational limitations such as resolution. The relatively coarse resolution that is often used in operational models is typically not sufficient to represent the SBL properly (e.g. Steeneveld *et al.*, 2006b; Svensson and Holtslag, 2009). However, a good representation of the SBL is important for numerical weather prediction (Beljaars and Viterbo, 1998; Viterbo *et al.*, 1999; Atlaskin and Vihma, 2012), air quality studies (Hanna and Yang, 2001; Salmond and McKendry, 2005), understanding polar biogeochemistry (Hunke and Meier, 2012), and climate modelling (Tjernström *et al.*, 2005; Holtslag *et al.*, 2007).

The SBL is affected by many small-scale physical processes, such as turbulent mixing, the coupling of the atmosphere and the underlying medium, radiation, the presence of clouds or fog, subsidence, advection, gravity waves and drainage and katabatic flows (Delage, 1997; Mahrt et al,. 1998; Mahrt, 1999; Steeneveld *et al.*, 2006b). The ongoing challenges in SBL modelling are related to the physical processes and their interactions, which are either not completely understood, or are represented incompletely. To enhance the understanding and representation of the SBL in regional and large-scale models, so far three GABLS (GEWEX Atmospheric Boundary Layer Study) experiments have been organized (Holtslag, 2006; Holtslag *et al.*, 2012).

We build upon the GABLS1 experiment for which a large eddy simulation (LES) (Beare *et al.*, 2006) and a single column model (SCM) intercomparison study (Cuxart *et al.*, 2006) have been performed, set on a weakly SBL over ice. These studies indicated that LES models and most SCMs are able to simulate a weakly SBL, but that operational models typically have too much mixing. Both studies were performed with a prescribed surface temperature and surface cooling. However, in reality, the surface temperature, sensible heat flux and ice/soil heat flux are strongly interdependent (Derbyshire, 1999) and the surface temperature will be affected through a coupled surface energy budget (Holtslag and de Bruin, 1988; Duynkerke, 1991; Van de Wiel *et al.*, 2002; Steeneveld *et al.*, 2006a). Therefore, it is important to consider the coupling between the surface and the lower atmosphere in SBL modelling.

In addition to the feedbacks in this non-linear coupled system, the surface temperature and sensible heat flux are strongly dependent on the geostrophic wind regime (Steeneveld *et al.*, 2006a, 2006b; Holtslag *et al.*, 2007). Roughly speaking, we can distinguish between two SBL types. Type I represents the very stable case where the system is dominated by radiative cooling and low wind speeds and has a more exponentially (or concave up) shaped potential temperature (θ) profile ($\partial^2\theta/\partial z^2 < 0$), while type II is typical for larger wind speeds, and therefore has a well-mixed (or concave down) vertical θ profile ($\partial^2\theta/\partial z^2 > 0$) (Van Ulden and Holtslag, 1985; Vogelezang and Holtslag, 1996). Considering the Arctic SBL, the ERA-Interim reanalysis data for the years $1979 - 2010$ indicates that a wide variety of the 850 hPa wind field (as a proxy for the geostrophic wind speed) occurs for the regions above 75°N for the NH winter (Figure 3.1), and it is likely that both SBL regimes can be

found. We will study the different wind regimes in this chapter.

The overall aim of this study is to examine which of the governing processes in the Arctic SBL are most dominant in explaining the SBL state for different wind regimes. Here we focus on the processes of snow-surface coupling (also known as conductive heat flux), radiation and turbulent mixing, since these processes are controlling the evolution and structure of the SBL the most (André and Mahrt, 1982; Beljaars and Holtslag, 1991; Steeneveld *et al.*, 2006b; Bosveld *et al.*, 2012). Utilizing the WRF (Weather Research and Forecasting) SCM, first the model will be run with different parametrization schemes for the representation of the SBL and the long wave radiative effects. In this way, the model output variability between parametrization schemes within one mother model can be explored. Secondly, after selecting one permutation of schemes, a sensitivity analysis will be performed for the main processes, using novel process diagrams as introduced by Bosveld *et al.* (2012) for GABLS3. This approach illustrates for which processes the model is more sensitive and which physical processes can explain the model variability and hence where future research efforts should be focused. Finally, we investigate whether errors in the boundary-layer (BL) schemes can remain hidden by compensating errors in another part of the model such as the land-surface scheme. Hence, this study is not a validation study of the WRF parametrization schemes, but a strategic study to determine possible focus points for future research. Therefore, apart from adjusting an incorrectly implemented stability function as well as a limitation for the friction velocity in the YSU BL scheme, we apply the schemes in the WRF 3.2.1. model without any modifications or tuning, despite that these schemes might have produced some biases in earlier model evaluations for both homogeneous or complex terrain. For instance, the 2 m temperatures (T_{2m}) have been reported as either too warm or too cold

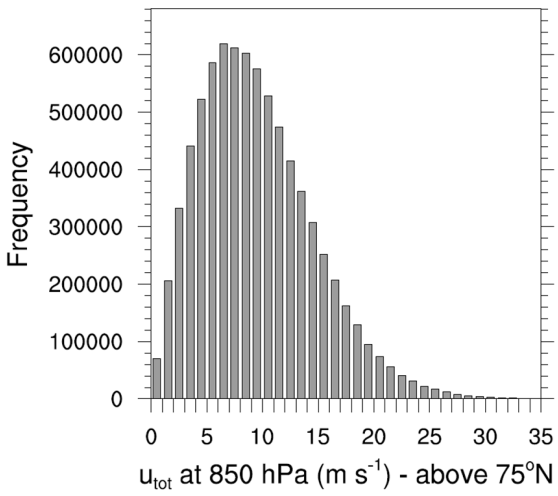

Figure 3.1: Histogram of ERA-Interim 850 hPa wind speeds (m s^{-1}) for latitudes > 75°N, based on 6-hourly data from the months of December, January and February of years 1979-2010.

(Hu *et al.*, 2010; Tastula and Vihma, 2011; Mäkiranta *et al.*, 2011; Shin and Hong, 2011). Also wind speed was found to be either overestimated (Tastula and Vihma, 2011; Shin and Hong, 2011) or underestimated (Mäkiranta *et al.*, 2011), while the overall correlation coefficients for wind speed are rather low, especially under low wind speeds (Tastula and Vihma, 2011; Mäkiranta *et al.*, 2011). Furthermore, some complications can occur with the surface layer formulation which can only handle a limited range of stabilities, e.g. by a lower limit for the friction velocity u_* (Jiménez *et al.*, 2012). However, these uncertainties in the model performance underline the need for a sensitivity analysis within WRF.

As mentioned before, our study is based on the GABLS1 benchmark (Beare *et al.*, 2006; Cuxart *et al.*, 2006), but extended to coupling with the land/snow surface and by comparing the importance of the processes for different geostrophic wind speeds. To exclude vertical resolution as a limiting factor, we will use a vertical resolution in the atmosphere which is much higher than in GABLS1.

The chapter is organized as follows: Section 3.2 provides more background information for this study, particularly on the challenges in modelling the Arctic stable boundary layer. Section 3.3 gives a model description with an overview of the utilized parametrization schemes. Section 3.4 describes the GABLS1 case as we use it, and this is applied in the model intercomparison in Section 3.5 and the sensitivity analysis in Sections 3.6 and 3.7. This is followed by the conclusion and discussion in Section 3.8.

3.2 Background

The last few decades the Arctic region seems subject to rapid changes. Available observations report an increase of the surface air temperature in a large part of the Arctic (Johannessen *et al.*, 2004). At the same time, the sea-ice cover decreases rapidly, e.g., in 2007 the observed sea-ice autumn minimum was 38% smaller than the climatological mean of 1979 - 2007 (Comiso *et al.*, 2008). Additional changes such as retreating glaciers and the thawing of permafrost are reported (ACIA, 2005).

The mentioned observations indicate that the Arctic climate system is more sensitive to climate change than the lower latitudes, a feature known as 'Arctic amplification' (AA) (Serreze and Francis, 2006; Bony *et al.*, 2006), of which the physical origin is so far not completely understood. A possible explanation for the AA is that several feedbacks in the polar climate system may enhance the initial response. The ice-albedo feedback (Curry *et al.*, 1995), for example, enhances the Arctic warming. Secondly, changes in cloud cover and water vapour can contribute to AA (Graversen and Wang, 2009). Other contributors are, e.g., changes in oceanic and atmospheric circulation and the weak vertical mixing in the Arctic lower atmosphere (Alexeev *et al.*, 2005; Graversen *et al.*, 2008; Graversen and Wang, 2009). Furthermore, the amount of horizontal and vertical mixing affects the efficiency at which the effects of local warming diffuses to adjacent regions (Serreze *et al.*, 2011). Bintanja *et al.* (2011a, 2011b) found that with a stronger surface inversion, the surface warming signal dilutes less easily aloft and thus remains at the surface, consequently further enhancing the temperature. This feature is important especially in the Arctic winter where strong surface inversions occur frequently and indicates the significance of the

θ profile.

Using SHEBA tower data, Persson *et al.* (2002) found that the mean near-surface conditions are strongly stable from November - April, though hourly data did reveal neutral stratifications occurring 25% of the time in winter with clouds and higher wind speeds. From the same data, Grachev *et al.* (2005, 2007) found bulk Richardson numbers (Ri_B) mostly greater than 0, frequently greater than the critical Ri_B and sometimes even greater than 1. Furthermore, the stability parameter z/L could reach up to 100. SHEBA soundings indicated near surface stratified conditions 61% and 53% of the time in autumn and winter respectively (Tjernström and Graversen, 2009).

Despite earlier research efforts, SBL modelling remains challenging, which particularly arises during model intercomparison and evaluation studies. As an illustration, the ensemble mean of regional climate models in Rinke *et al.* (2006) provides T_{2m} that are up to 5 K too cold compared to the European Centre for Medium-Range Weather Forecasts (ECMWF) reanalysis data in winter, while the scatter between the models was $1-5$ K over land. Holland and Bitz (2003) compared several coupled atmosphere-ocean-sea-ice-land models. The simulations for doubled CO_2 concentrations showed a range of warming for the Arctic between 1.7 and 4.3 times the global average, with some up to even 9 K warmer. Moreover, Walsh *et al.* (2008) report area-averaged annual root mean square errors of surface air temperature of 15 global climate models compared to ERA40 reanalysis data of 3 to almost 14 K for the Arctic region. Note that though these reanalysis data are used as a reference in these studies, they can have some inefficiencies of their own, since due to limited observations in these regions the reanalyses are mostly based on model parametrizations (e.g. Tjernström and Graversen, 2009), but these can have serious problems in dealing with the physical processes in this region.

In addition to the T_{2m} biases, deficiencies are found in the modelled inversion strengths. Boé *et al.* (2009), defining the inversion strength between 850 and 1000 hPa, compared 15 CMIP3 models which showed an average inversion strength in the range of $2.1-7.4$ K for November to February. On the contrary, defining the inversion strength as the temperature change across the BL gives a mean inversion strength of about 13 K for the SHEBA data in stably stratified cases in autumn and winter (Tjernström and Graversen, 2009). Though the results from observations represent surface based inversion layers ánd have a higher vertical resolution, the differences with the models do indicate that these inversion strengths are not captured properly by the models (which also follows from the differences between the models), although in cases of surface pressure higher than 1000 hPa the actual inversion strength can be stronger than mentioned in the study of Boé *et al.* (2009).

To gain further understanding in modelling the Arctic SBL, we examine the relative strength of the governing processes in the SBL during cooling conditions and under various wind regimes. First we consider the coupling between the snow surface and the lower atmosphere which plays a distinct role in the SBL (Holtslag and De Bruin, 1988; Duynkerke, 1991; Van de Wiel *et al.*, 2002; Steeneveld *et al.*, 2006a; Holtslag *et al.*, 2007). The surface temperature (T_{surf}), sensible heat flux and soil/ice/snow heat flux are strongly interdependent (Derbyshire, 1999) and can influence the SBL evolution. The soil heat flux is determined by the soil's thermal

heat conductivity and temperature gradient, and influences the energy flux to the atmosphere. Implementing a skin layer in the surface model does improve the model performance substantially (Holtslag and De Bruin, 1988; Steeneveld *et al.*, 2006a, 2006b), since it allows T_{surf} to react more easily to sudden changes in the surface cooling (Van de Wiel *et al.*, 2002; Steeneveld *et al.*, 2006a). In our study, the underlying medium is ice, which is covered by a snow layer which will act as an insulation layer. The area of the snow cover and its depth control the land-atmosphere coupling, and affects the air and the soil/ice temperature (Dutra *et al.*, 2011). They should thus be accounted for.

Secondly we study the relative impact of long wave radiation, which has two distinct effects on the SBL (Edwards, 2009a). The first is that the net radiation at the surface dominates T_{surf} and is greatly influenced by conditions in and above the SBL, for example by clouds (e.g. Intrieri *et al.*, 2002; Stramler *et al.*, 2011). Moreover, the divergence of long wave radiative flux across the SBL can affect its development (Edwards, 2009a), and also takes place in clear-sky nighttime conditions, because of the presence of absorbing gases, e.g. water vapour, CO_2, O_3 and aerosols (Garratt and Brost, 1981; André and Mahrt, 1982). Tjemkes and Duynkerke (1989) found that including radiative cooling in the atmosphere acts to reduce the inversion strength across the BL, making the BL less stable, and increasing the SBL height by 25%. Also Hoch *et al.* (2007) note the importance of the long wave radiative flux divergence during the ETH Summit Greenland experiment, and reported radiative cooling of typically 10 - 20 K day^{-1}.

Finally, we also study turbulent mixing, which is in principle determined by the stratification and wind shear. Especially in clear-sky conditions, the stratification suppresses the buoyancy and turbulence is solely produced by wind shear. Therefore, the vertical structure of both wind and θ strongly influences the SBL state. In the very stable case with very little turbulence, turbulent transport between the surface and the overlying atmosphere vanishes, and the net radiation equals the soil heat flux. This can result in a so-called 'decoupled' state of the SBL and is also seen in observations (Derbyshire, 1999; Grachev *et al.*, 2005). From a modellers perspective, then the SBL's decoupled state may result in unrealistically cold surface temperatures (Derbyshire, 1999; Jiménez *et al.*, 2012). To circumvent this model phenomenon, some large-scale models utilize artificial enhanced mixing or enhanced thermal diffusion for very stable situations (e.g. Viterbo *et al.*, 1999).

3.3 Model description

The single column model (SCM) in our study is based on the WRF-3D model version 3.2.1. The WRF-SCM uses the same physics and dynamics as the WRF-3D model (Skamarock *et al.*, 2008), and a few features will be highlighted here. The model utilizes a vertically stretched σ coordinate, with the model top defined at a constant pressure surface.

The WRF model has a wide range of parametrizations for several physical processes, which differ in their degree of complexity and computation time. In our study we examine the relative importance of the coupling with the surface, the radiative effects and the turbulent mixing. The following sections will briefly describe the

selected land/snow-surface, the long wave radiation, and the BL parametrizations.

3.3.1 Snow-surface coupling

The land-surface models (LSMs) provide the fluxes of the energy balance: the sensible, latent and soil heat flux, and the upward long wave and short wave radiation. As such, the LSMs provide the lower boundary condition for the vertical transport in the BL scheme. Additionally, they determine the skin temperature (T_{skin}), the temperature and moisture profiles in the soil, as well as the snow cover and canopy properties (Skamarock *et al.*, 2008).

In this study we use the Noah LSM as a reference (Chen and Dudhia, 2001; Ek *et al.*, 2003). This model uses four layers to represent the dynamics in the soil (ice). The layer thicknesses in our setup are from top to bottom 1, 2, 4 and 8 cm (see Section 3.4). The Noah LSM can handle soil, ice and fractional snow cover effects, and considers surface emissivity properties (Skamarock *et al.*, 2008). Snow effects are included in just the top soil layer. Thus the thickness of the top layer is defined as the thickness of the top soil/ice layer plus the snow depth. The thermal conductivity of the top layer is then defined as the weighted sum of the product of the thermal conductivity and layer thickness of the individual layers (Ek *et al.*, 2003).

3.3.2 Long wave radiation

In addition to the land-surface physics, the long wave radiative transport needs to be parametrized. The radiation schemes represent the atmospheric cooling due to radiative flux divergence, and determine the amount of downward long wave and short wave radiation at the surface (Skamarock *et al.*, 2008). In our study, a 9 h run during polar night time is performed and therefore we study only long wave radiation (LW_{rad}). The LW_{rad} scheme considers thermal radiation that is absorbed and emitted by gases, water species and the land/snow surface (e.g. Rodgers, 1967). To determine LW_{rad}, the scheme takes the model-forecasted cloud and water vapour distributions into account, as well as specified concentrations of CO_2, O_3 and optionally trace gases.

Ideally, radiative transfer models can use the line-by-line approach, where the absorption and emission is calculated for each wavelength. This approach, however, is computationally expensive and more often the broad band or correlated-k method is used. The latter uses several bands of wavelengths for which averaged values of absorption and emission are employed. This approach limits the computation time and is within 1 % accuracy compared to the line-by-line approach (Stensrud, 2007).

Three different LW_{rad} schemes are used in this study. The first scheme is the Rapid Radiative Transfer Model (RRTM) (Mlawer *et al.*, 1997), which is used as the reference scheme. This is a spectral-band scheme with 16 different bands (Skamarock *et al.*, 2008). The scheme treats several molecular species, namely water vapour, CO_2, O_3, CH_4, N_2O, and the common halo-carbons, and accounts for cloud optical depth.

The second LW_{rad} scheme is the Eta Geophysical Fluid Dynamics Laboratory (GFDL) scheme. For this scheme the radiation spectrum is divided into 14 bands, which treat water vapour, CO_2 and O_3 in its calculations (Skamarock *et al.*, 2008).

The last LW_{rad} scheme that has been selected is the spectral-band scheme used in the NCAR Community Atmosphere Model (CAM). CAM has only 2 bands in the

long wave range. As well as the RRTM and the GFDL scheme it treats water vapour, CO_2 and O_3. Furthermore, the CAM scheme accounts for several trace gases (Collins *et al.*, 2004; and Skamarock *et al.*, 2008).

3.3.3 Turbulent mixing

The boundary-layer (BL) schemes parametrize the sub-grid scale turbulent fluxes of heat, momentum and moisture throughout the atmospheric column. The schemes that are used in this study are either a relatively simple first or a more complex one-and-a-half order closure.

The first scheme that we have selected is the so-called YSU BL scheme (Hong *et al.* 2006; Skamarock *et al.*, 2008). This is a first-order scheme that uses profiles for the eddy diffusivities of heat, momentum and moisture in terms of friction velocity and the BL depth following Troen and Mahrt (1986) and Holtslag and Boville (1993) among many others. The BL top depends on the buoyancy profile by using a critical bulk Richardson number (Rib_{cr}) to determine the BL height. In stable conditions, $Rib_{cr} = 0.25$ is applied over land. It appears that in this way, enhanced mixing is allowed under weak geostrophic winds (Mauritsen *et al.*, 2007; Hong and Kim, 2008). Note that in the YSU scheme as implemented in WRF 3.2.1, the stability function ϕ was not correctly implemented (Sukanta Basu and Wayne Angevine personal communications, summer 2012). As such we have replaced the erroneous function by the intended version: $\phi = 1 + 5\ z/L$ (as in the original Troen and Mahrt (1986) description), which leads to less enhanced mixing compared to the original YSU scheme. This implementation also makes the runs compatible with WRF 3.4.1.

In addition, we consider the Mellor-Yamada-Janjic (MYJ) BL scheme (Mellor and Yamada, 1982). The MYJ scheme is a local, 1.5 order closure model and is considered appropriate for stable and slightly unstable flows, but the errors can increase when the atmosphere becomes more convective (Hu *et al.*, 2010).

The third BL scheme that we consider is the Quasi-Normal Scale Elimination (QNSE) scheme (Sukoriansky *et al.*, 2006). The eddy diffusivities for heat, momentum and moisture are estimated using an alternative approach, which accounts for the combined effects of turbulence and waves. Moreover, this scheme accounts for anisotropy, which is especially relevant in the SBL where vertical motions are suppressed. In addition, the scheme does not have a Ri_{cr} at which turbulence is suppressed, and turbulence can thus exist even at very high Ri. In practice, QNSE was implemented as a modification of the MYJ-scheme and is also a local, 1.5 order closure model. Good agreement was found between the QNSE scheme and observations for cases of moderate and strong stable stratification (Sukoriansky *et al.*, 2006).

Together with the BL scheme, the surface-layer scheme is used. This scheme determines the friction velocities and the exchange coefficients, which are provided both to the land-surface model and the BL scheme to enable the calculation of the fluxes of the energy balance at the surface and the surface stress respectively (Skamarock *et al.*, 2008). In WRF, each BL scheme has a particular surface-layer scheme tied to it. For YSU this is the MM5 surface scheme, which makes use of Monin-Obukhov similarity theory. For MYJ the ETA surface-layer scheme is applied, which is also based on the Monin-Obukhov similarity theory (Tastula and Vihma, 2011). Also for the QNSE BL scheme its analogue surface-layer scheme has been

utilized (Sukoriansky, 2008).

3.4 Case description

Our study has been inspired by the GABLS1 SCM intercomparison study which is based on the LES study of the Arctic SBL by Kosovic and Curry (2000), but with some modifications. They used the Beaufort Sea Arctic Stratus Experiment observational dataset to define the initial and boundary conditions. These were chosen such that a clear-sky SBL with moderate surface cooling could be numerically simulated. The case was also used for an LES and 1D intercomparison study (Beare *et al.*, 2006, Cuxart *et al.*, 2006) to analyse the reliability of LES and 1D models for the SBL. For these experiments the cooling rate was prescribed, which is a limiting boundary condition, and the radiation schemes were switched off.

We adopt the same initial profiles of potential temperature (θ) and wind speed as in the GABLS1 case study. The θ profile consists of a 100 m thick mixed layer of $\theta = 265$ K. Above this layer θ increases at a rate of 0.01 K m^{-1}. The geostrophic wind speed (u_{geo}) was chosen as 8 m s^{-1} for the u-component and 0 m s^{-1} for the v-component. Below 100 m the wind speed decreases logarithmically to 0 m s^{-1} at the surface (z_{0m}). Figure 3.1 reveals that an u_{geo} of 7 - 8 m s^{-1} indeed occurs most frequently in the Arctic. The specific humidity profile (q) has a uniform value of $q_0 = 0.5$ g kg^{-1} up to a height of 4 km. This is comparable to what was found from observations, e.g., Serreze *et al.* (1995) found a value of $q_0 \sim 0.8$ g kg^{-1} during winter above 70°N, while near surface q_0 from SHEBA winter data was found to range between 0.1 and 0.7 g kg^{-1} (Tjernström *et al.*, 2005; Stramler *et al.*, 2011). Above 4 km to the model top, which is at about 12 km, q decreases exponentially according to $q_0 \cdot \exp(-\alpha(z - 4000\text{m}))$, where $\alpha = 10^{-3}$. To overcome a large amount of degrees of freedom and because we want to focus on the interaction of the snow surface and the SBL, we decided to keep the atmosphere clear from clouds and turned the micro-physics off. The impact of the micro-physics might also be important since cloudy conditions also frequently occur in the Arctic which can affect the Arctic surface energy balance (e.g. Intrieri *et al.*, 2002; Shupe and Intrieri, 2004). Therefore this impact needs to be studied on its own in a subsequent study.

The GABLS1 case uses a rather large roughness length (z_0) for snow/ice of 0.1 m for momentum and heat. Although we are aware that usually the thermal roughness length is smaller than the roughness length for wind speed (Andreas, 1987), a thermal roughness parametrization is not included in this WRF model, and we apply a roughness length of $5 \cdot 10^{-4}$ m for both momentum and heat, since this is more in agreement with observed roughness lengths. E.g. from the ASFG tower at SHEBA z_0 was found to be about $3.1 - 10.8 \cdot 10^{-4}$ m (Persson *et al.*, 2002), while Schröder *et al.* (2003) report an average z_0 of $5 \cdot 10^{-4}$ m for a wide range of sea-ice conditions. z_0 Measured at 6 SHEBA winter sites (Andreas *et al.*, 2010) ranged from $10^{-7} - 10^{-1}$ m.

The WRF model uses a lower limit on u_* of 0.1 m s^{-1} in the YSU BL scheme to prevent a vanishing heat flux in very stable conditions (Jiménez *et al.*, 2012). Otherwise, this could possibly cause a decoupling between the atmosphere and the surface resulting in too low temperatures at the surface. However, in very stable

conditions, this u_* minimum is rather high, therefore we set it to 0.001 m s^{-1} to reduce the restriction, but still preventing the heat flux from becoming zero and therefore avoid runaway cooling (Jiménez *et al.*, 2012). Finally, the case runs at 73°N latitude with a time step of 10 s, has a duration time of 9 hours and is performed in wintertime to ascertain the total absence of solar heating at the surface.

In the current study the SBL is modelled with a very high vertical atmospheric resolution. In this way we can focus on the relative significance of the representation of the physical processes without a limiting vertical resolution playing a role. We chose 200 vertical levels in the atmosphere, which were stretched so that the thinnest layer is closest to the surface, and the layer thickness increases with height. The first model level is located at about 0.55 m. Since now the first model level is below the 2 m level, we had to interpolate T_{2m} from the temperature profile, as the standard WRF T_{2m} uses T_{skin} in combination with the exchange coefficients (see equation 3.4) as determined at the 2 m level and not the temperature difference between the model level above and below 2 m, which is in disagreement with the profile.

Steeneveld *et al.* (2006a) showed that the model results are very sensitive to the vertical resolution in the ice when the atmosphere and surface are coupled. In order to obtain a better interaction with the ice, the thickness of the layers as in the original Noah LSM is reduced. The ice slabs are now respectively from the top to bottom layer 1, 2, 4 and 8 cm thick. The initial temperature profile for the ice layers is set to a uniform value of 265 K. The ice is fully covered by a 5 cm snow layer which is the snow depth as in the WRF-SCM for sea-ice. Since during the winter night this snow depth might be a bit low, we reran the model with 20 cm snow depth and will briefly comment on that as well. The emissivity of a fresh snow surface is 0.98 as is comparable to what was found in observations (Kondo and Yamazawa, 1986; Claffey *et al.*, 1999; Persson *et al.*, 2002; Andreas *et al.*, 2010). The total ice thickness is 3 m for multi-year sea-ice, and the lower boundary condition for temperature at the ice-water interface is 271.16 K in the Noah LSM in WRF.

3.5 Model intercomparison

In this section, the boundary-layer (BL) and long wave radiation (LW_{rad}) schemes are varied (see Section 3.3). As such, the spread between the permutations is quantified, which reflects the uncertainties that can occur within one model.

First we compare the forecasted θ profiles after 9 hours (Figure 3.2a, the initial profile is given as well). This figure shows the profound difference in shape of the θ profiles. The runs with the MYJ scheme indicate an exponentially shaped profile, while the YSU and QNSE runs provide some mixing as is also seen from the inflection point in the profile, though they do show a strong inversion. For the YSU scheme this inversion is more smooth, while for the QNSE a strong inversion is seen on top of the shallow "mixed" layer. Consequently, the figure reveals that both SBL "archetypes" as mentioned in the introduction can be obtained by choosing different BL schemes, even with the same wind forcings, where YSU and QNSE can be allocated the type II SBL, and MYJ type I. The difference between MYJ and QNSE is explained by the allowed turbulent mixing under extreme stable conditions in QNSE, while this is absent in MYJ (Sukoriansky *et al.*, 2006).

Examining the first model level temperatures, MYJ runs cool the least with a cooling from 265 K to $\sim$ 250.5 K, while YSU runs cool to $\sim$ 249 K. The coldest first model level temperatures are found for the QNSE runs, with $\theta \sim 248.8$ K. Thus after 9 hours the model runs produce a spread of almost 2 K near the surface.

While the differences between the BL schemes can be clearly distinguished, the differences between the three $\mathrm{LW_{rad}}$ schemes are small for the θ profiles. E.g., the incoming long wave radiation ($L\downarrow$) for similar BL schemes differs $\sim$ 3 W m^{-2} after 9 hours, on a total amount of $L\downarrow$ of about 168 W m^{-2}.

Due to the large differences in θ profiles, it might be more meaningful to compare the amount of integrated cooling (IC) as a measure for the temperature differences, since for a better mixed profile the cooling at the surface might not be as strong, but aloft more cold air is found. The IC is defined as (Steeneveld *et al.*, 2006a):

$$IC = \int_{z=0}^{z=200m} (\theta_{start} - \theta_{final}) dz \,. \tag{3.1}$$

Here we only calculate the IC up to 200 m, since this is the height where the model runs converge. Table 3.1 presents the IC for the model intercomparison runs. Though the MYJ runs show the least cooling at the first model level, the IC is the largest, because of the relatively colder air above $\sim$ 33 m compared to the other BL schemes. The YSU and QNSE runs show a similar cooling at the first model level, but the integrated cooling is larger for the QNSE runs, which reflects a more effective mixing of cold air into the atmosphere.

The wind profiles also show some differences (Figure 3.2b), especially between the MYJ runs and the other BL schemes. The MYJ runs forecast a more smooth wind profile and a low-level jet at $\sim$ 85 m. The YSU and QNSE runs do not show such a clear low-level jet and reach their maximum wind speed at a lower altitude. As for the θ profile and the IC, also for the wind profiles the largest differences occur between the BL schemes. Thus, at first sight, the BL scheme seems to be most important in explaining the differences between the model runs. However, in the next section we

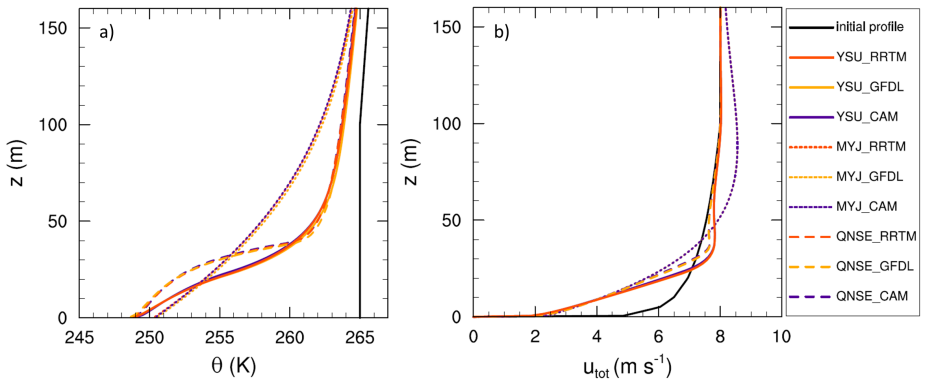

Figure 3.2: Vertical structure of a) the potential temperature θ (K) and b) the total wind speed u_{tot} (m s^{-1}) for various WRF-SCM runs, initially and after 9 hours.

Table 3.1: Integrated cooling for the model intercomparison runs.

BL scheme	LW_{rad} scheme	*IC* (K m)
YSU	RRTM	-653
YSU	GFDL	-633
YSU	CAM	-665
MYJ	RRTM	-925
MYJ	GFDL	-896
MYJ	CAM	-931
QNSE	RRTM	-734
QNSE	GFDL	-716
QNSE	CAM	-745

will analyse whether there may be complementary processes at hand which can show a similar spread.

3.6 Sensitivity and process analyses

To analyse and quantify which of the three governing processes of snow-surface coupling, radiation and turbulent mixing is most critical in determining the state of the SBL, we perform an extensive sensitivity and process analysis. To do so, we chose the YSU BL scheme as a reference, because this scheme is a first-order scheme and allows for some enhanced mixing, while for the LW_{rad} scheme RRTM was chosen. Both schemes are close to operational practice in weather forecasts and climate modelling (Iacono *et al.*, 2000; Morcrette *et al.*, 2001; Roeckner *et al.*, 2003; Collins *et al.*, 2004; Cuxart *et al.*, 2006; Inoue *et al.*, 2006; ECMWF, 2009, 2012).

The amount of coupling of the surface to the atmosphere is affected by adjusting the snow/ice conductivity λ. The amount of incoming long wave radiation ($L\downarrow$) is changed by adjusting the initial specific humidity profile (q). Svensson and Karlsson (2011) found that it is primarily the q profile and not the temperature profile that determines the clear-air $L\downarrow$ in very cold and dry conditions and hence that the atmospheric moisture content is very important for the radiation balance at the Arctic surface. Results by Zhang *et al.* (2001) also indicated that changes in the atmospheric precipitable water have a higher impact on $L\downarrow$ than the change in mean atmospheric temperature. Finally, the amount of turbulent mixing is varied by both adjusting the eddy diffusivity coefficient K for heat, momentum and moisture in the BL scheme, and the exchange coefficients C for heat, momentum and moisture in the LSM to adjust the mixing in the surface layer. Note that in Bosveld *et al.* (2012) only the activity of turbulent mixing above the lowest level was adjusted. However, it is more physical to consistently link the surface layer and the BL as was also recognized by Svensson and Holtslag (2009). To more easily compare our results with those of Bosveld *et al.* (2012), we also show the mixing sensitivity analysis while only adjusting K in the BL scheme.

To study how the changes in process strengths compare to one another, we will show a series of plots as introduced by Bosveld *et al.* (2012) for the GABLS3 intercomparison study. In this chapter we refer to these plots as 'process diagrams'. A

process diagram plots two variables against each other, which are either a time average of variable X over 9 hours, or a change of variable X in 9 hours time. Therefore, each model run is represented by one point in the process diagram. The points for the model intercomparison runs performed in the previous section give the spread within the WRF-SCM. From the point for the reference run with the YSU-RRTM scheme combination, we will add the points for the sensitivity analysis runs. By drawing lines from the reference point to these sensitivity points, we can compare the direction of the sensitivity for a certain process and indicate whether this might explain the spread within the WRF-SCM. Furthermore, we can compare the orientation and length of these lines under different geostrophic wind regimes (u_{geo}) to learn how the relative significance of the physical processes shifts. To compare the significance of the three processes for varying u_{geo} in a more convenient way, the axes of the process diagrams representing different u_{geo} are kept identical. Finally, we extend Bosveld *et al.* (2012) by carrying out *two* perturbations in each 'direction' (e.g. two runs with increased mixing, two runs with decreased mixing) to detect whether the change in process intensity gives a linear response (straight line) or a non-linear response (curved line).

Below we study the sensitivity for a prescribed amplification of the coefficients described above, while in Section 3.7 we compare runs with a similar change in the net surface energy budget. The extended GABLS1 case with $u_{geo} = 8$ m s^{-1} will be used as a reference case when we compare the competition between the physical processes for different ranges of u_{geo}. Figure 3.1 shows that this wind speed is often found at latitudes north of 75°N. The case is repeated for an u_{geo} of 3 and 20 m s^{-1} to cover a wide variety of wind speeds in the Arctic (see also Figure 3.1).

3.6.1 Amplification strategy

In the first part of the sensitivity analysis we prescribe the amplification of the governing processes. These multiplication factors were chosen to get a significant effect in the sensitivity analysis. To increase the amount of coupling, we multiplied the ice/snow conductivity (λ) with 2.0 and 4.0. To decrease the amount of coupling, a multiplication factor of 0.5 and 0.25 was applied. These runs are referred to as *coupling*. The rationale behind these multiplication factors are the large uncertainties observed in λ_{snow} and λ_{ice}, which can vary in space (both horizontally and vertically) and time due to density and texture differences for example. Sturm *et al.* (2002) report in situ measurements of λ_{snow} during the SHEBA experiment ranging from 0.078 to 0.574 W m^{-1} K^{-1} with the lowest values for fresh snow and the highest value for a layer of snow-ice. From these probe measurements they found an average bulk λ of 0.14 W m^{-1} K^{-1}, while when they used measured ice growth to deduce the heat extraction from the ice and hence determine the bulk λ, values of 0.1 to 0.7 W m^{-1} K^{-1} were found with an average of 0.34 W m^{-1} K^{-1}, but this also includes the effect of heterogeneity. Huwald *et al.* (2005) calculated an effective λ_{snow} at the snow-ice interface by using the SHEBA internal snow and ice temperature data and found hourly values that ranged from 0.1 - 1.0 W m^{-1} K^{-1}, while the average values ranged from 0.4 - 0.5 W m^{-1} K^{-1}. Other studies also show a range of 0.02 - 0.3 W m^{-1} K^{-1} for various sites (Gouttevin *et al.*, 2012) and 0.06 - 0.4 W m^{-1} K^{-1} for various depths (Domine *et al.*, 2012). With a set λ of about 0.22 W m^{-1} K^{-1} in

the WRF-SCM, λ in our sensitivity analysis ranges from 0.055 to 0.88 W m^{-1} K^{-1} when we use the multiplication factors of 0.25 to 4.0.

Large variations are also found in the modelled incoming long wave radiation ($L\downarrow$). Svensson and Karlsson (2011) revealed that the median for $L\downarrow$ during the Arctic winter (DJF) ranged from about 140 - 190 W m^{-2} for 9 global climate models. Though this contains all sky conditions, the range in variation for $L\downarrow$ in clear-sky conditions was also found to be over 20 W m^{-2}. When we would use identical multiplication factors as for λ to vary the initial q profiles (*radiation* runs), the initial specific humidity profile would range up to 2 g kg^{-1} which is rather high for an Arctic winter (see also Section 3.4). Therefore we decided to multiply with 0.5, 0.67, 1.5 and 2.0. In this way we can still compare the 0.5 and 2.0 perturbations in a systematic approach with the other sensitivity analyses, while representing typical Arctic conditions better. The $L\downarrow$ after 9 hours now ranges between 155.2 - 180.3 W m^{-2} compared to the 167.4 W m^{-2} of the reference run.

To alter the amount of mixing, the eddy diffusivity K in the BL scheme and the exchange coefficient C in the LSM are again multiplied with 0.25 - 4.0. These runs are referred to as *mixing*. For the mixing sensitivity analysis as was applied in Bosveld *et al.* (2012) only K in the BL scheme was varied. Since the maximum eddy diffusivities for heat and momentum that were found in the SCM intercomparison study by Cuxart *et al.* (2006) ranged from less than 1 to over 5 m^2 s^{-1} (see their Figure 6), we anticipate that the range of the multiplication factors covers the typical uncertainty in K.

3.6.2 Vertical profiles

We start discussing the sensitivity analysis for $u_{geo} = 8$ m s^{-1} (a frequently occurring wind speed, see Figure 3.1). Figure 3.3a and b show the θ and wind speed profile after a 9 h forecast for the YSU-RRTM reference run and for the sensitivity analysis runs for this u_{geo}. Also the initial profiles are presented for comparison. The labels *K_Chm*, K, λ and q represent the processes of mixing in both BL and surface layer, mixing in only the BL, snow-surface coupling and radiation respectively and the numbers indicate the amount by which each process is multiplied.

An increase in mixing leads to higher temperatures at the surface, since there is more entrainment of potential warmer air from the overlying layers and cold air from the surface is more easily lifted aloft so that there is a more efficient redistribution of heat in the boundary layer. This also results in deeper and better mixed boundary layers. Similar results were found for increasing the amount of snow-surface coupling. An increased λ means that heat from the underlying and relatively warmer ice layers is more efficiently transported to the surface and thus more energy is added to the atmosphere. An increased q results in a higher amount of $L\downarrow$. This again leads to higher temperatures and deeper boundary layers compared to the YSU-RRTM reference run. Also we observe that applying a multiplication factor of 0.5 and 2.0 for both coupling and radiation forecasts comparable profiles. When the physical processes are decreased in intensity, results change in opposite directions.

Some differences can be observed between both types of mixing runs. When we increase the amount of mixing, the boundary layers are deeper and better mixed when the amount of mixing is also increased in the surface layer (*K_Chm* runs). This

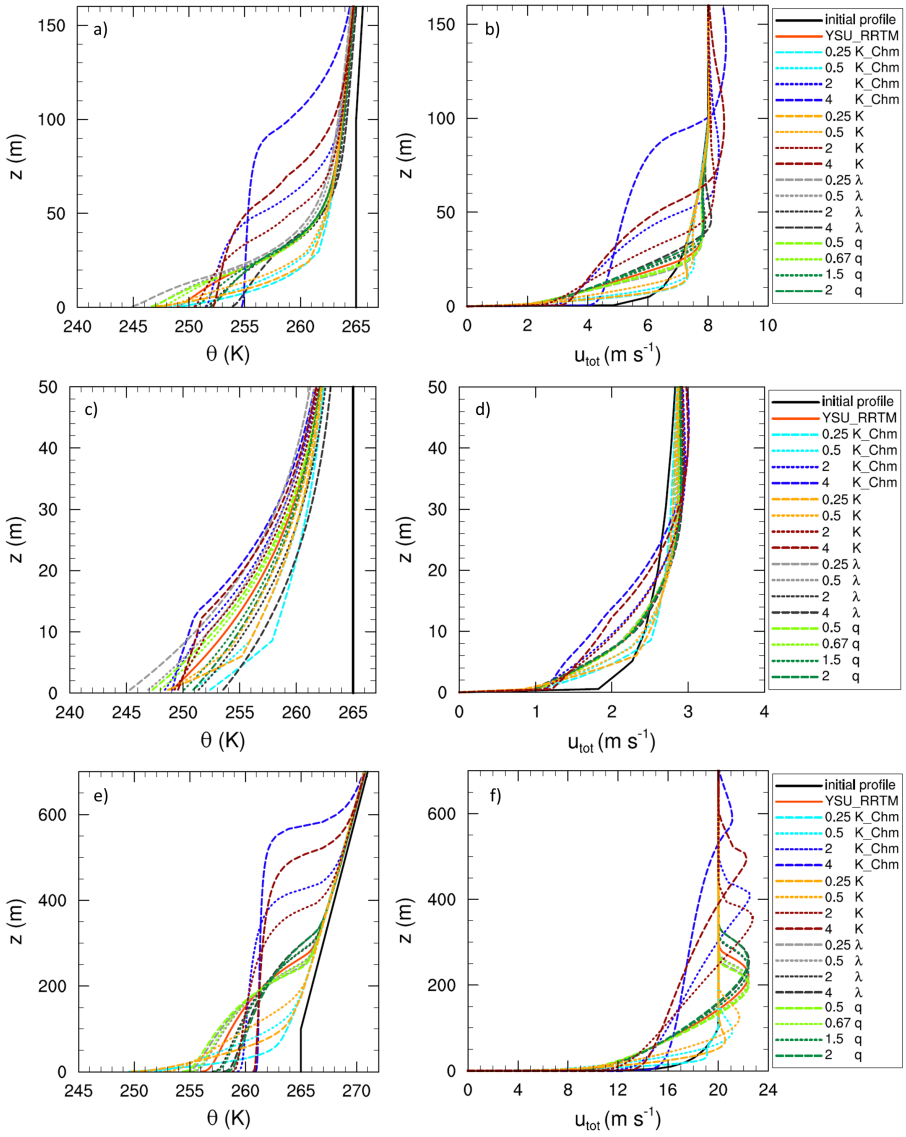

Figure 3.3: Vertical profiles for potential temperature θ (K) (a, c and e) and wind speed u_{tot} (m s^{-1}) (b, d and f) initially and after 9 hour forecasts for the runs of the sensitivity analysis using geostrophic wind speeds of 8 m s^{-1} (a, b), 3 m s^{-1} (c, d) and 20 m s^{-1} (e, f). *K_Chm* represents the eddy diffusivity and exchange coefficients and therefore the change in mixing in both boundary and surface layer, K represents the eddy diffusivity and therefore change in mixing in the boundary layer only, λ represents the ice conductivity and thus the coupling and q represents the specific humidity profile and therefore the incoming long wave radiation. YSU-RRTM is the reference run.

Table 3.2: Overview of the amount of integrated cooling (IC), the 2 m temperature ($T_{2m\ 9h}$) and skin temperature ($T_{skin\ 9h}$) after 9 hours for a geostrophic wind speed of 8 m s^{-1}, and the changes in net radiation over 9 hours (ΔQ^*, see equation 3.5) for the three wind regimes for the sensitivity analysis runs with the specified multiplication factors.

Param.	**Multipl. factor**	***IC*** **(K m)**	$T_{2m\ 9h}$	$T_{skin\ 9h}$	ΔQ^*(Wm^{-2}) u_{geo} 8 ms^{-1}	ΔQ^*(Wm^{-2}) u_{geo} 3 ms^{-1}	ΔQ^*(Wm^{-2}) u_{geo} 20 ms^{-1}
K_Chm	0.25	−479	250.7	245.5	7.6	4.8	25.7
	0.5	−532	249.5	245.8	5.2	3.4	16.2
	2.0	−893	251.7	250.6	−11.1	−4.2	−11.7
	4.0	−1160	254.8	254.3	−23.4	−8.2	−16.6
K	0.25	−513	248.8	245.9	5.2	2.4	17.5
	0.5	−564	248.8	246.4	3.2	1.3	9.0
	2.0	−793	250.7	248.7	−4.6	−1.4	−6.8
	4.0	−977	252.3	250.1	−9.8	−3.0	−10.9
λ	0.25	−787	245.6	243.1	14.0	15.4	4.0
	0.5	−727	247.3	245.0	8.0	8.6	2.3
	2.0	−580	251.9	250.1	−9.1	−9.4	−2.6
	4.0	−521	254.2	252.6	−17.3	−18.3	−5.3
q	0.5	−678	247.3	244.8	−5.0	−5.2	−6.2
	0.67	−669	248.2	245.8	−2.8	−3.0	−3.6
	1.5	−628	251.0	249.1	2.4	3.0	3.3
	2.0	−601	252.3	250.5	3.6	4.9	5.3

more effective mixing also follows from the higher amount of integrated cooling for *K_Chm* runs compared to runs with only mixing in the BL (*K* runs) (see Table 3.2). However, when we decrease the amount of mixing, we also find higher atmospheric temperatures for the *K_Chm* runs compared to the *K* runs. On the other hand, T_{skin} remains colder for the *K_Chm* runs compared to the *K* runs, resulting in large temperature gradients between the surface and the lowest model level for the *K_Chm* runs (see also Table 3.2). This is explained by the smaller sensible heat flux in the *K_Chm* runs which hampers the transport of heat to the surface.

Also when we study the two 'decreased mixing' lines of the *K_Chm* runs, we see that when mixing is increased from 0.25*K_Chm* to 0.5*K_Chm*, the temperatures in the atmosphere just above the surface decrease. This behaviour is contrary to the expectation that when mixing increases, more warm air is entrained, which would result in higher atmospheric temperatures. It appears that, when the amount of mixing is decreased sufficiently, the cold air from the surface is not effectively lifted and therefore the layers above the surface do not cool as much, while at the same time the warmer air aloft cannot reach the surface. Indeed, we find lower surface temperatures for the 0.25*K_Chm* run compared to the 0.5*K_Chm* run (see Table 3.2).

Table 3.2 summarizes the amount of integrated cooling (*IC*) for the sensitivity analysis runs. The *IC* of the YSU-RRTM reference run amounts up to -653 K m. When we decrease the amount of mixing, the *IC* decreases, because cold air from the surface is not efficiently mixed into the atmosphere. Indeed we find a stronger *IC* for decreased mixing for the *K* runs compared to *K_Chm*, where the exchange

coefficients in the surface layer are kept identical to the YSU-RRTM reference run so that there is a more efficient mixing of cold air away from the surface. Decreasing the coupling leads to increased IC, because of the less efficient heat transport from the deeper ice layers to the surface enabling the surface to cool more, while the mixing remains strong enough to bring this signal to higher atmospheric layers. Decreasing the amount of $L\downarrow$ also leads to lower T_{skin} and again a stronger integrated cooling. Opposite results are found for increasing the process strengths.

The vertical profiles for an u_{geo} of 3 m s^{-1} and 20 m s^{-1} are given in Figure 3.3c-f. Note that the axes are different from the figures for $u_{geo} = 8$ m s^{-1}. Increasing u_{geo} results in more developed and deeper SBL heights and overall higher θ as more warm air is mixed towards the surface, and cold air is mixed away from the surface.

Reducing u_{geo} results in smaller SBL heights, and strongly affects the θ profile. The YSU-RRTM θ profile now has an exponential, or type I, shape. The profile shape remains similar for increased and decreased amounts of $L\downarrow$ and coupling, though this does respectively increase and decrease θ. With increased mixing, the θ profile shape becomes somewhat more mixed, though this only happens in a shallow layer. When the mixing decreases in intensity, a pronounced exponential profile is forecasted. As was the case with the smallest amounts of mixing for $u_{geo} = 8$ m s^{-1}, again we note that the mean SBL temperatures remain higher when the mixing is decreased, but also now the mean SBL temperatures decrease when the amount of mixing increases. This is likely caused by the small sensible heat flux which prevents the transport of warm air towards the surface and transport of cold air away from the surface.

As mentioned in the introduction we can distinguish between two types of SBLs. Type I has a more exponential (or concave up) profile and is dominated by radiative cooling and low wind speeds. Type II is typical for larger wind speeds and better mixed (or concave down) vertical temperature profiles (Van Ulden and Holtslag, 1985; Vogelezang and Holtslag, 1996). In Figure 3.3c the different profile shapes can be observed, though this is not necessarily followed by the lower and higher wind speeds for type I and II respectively in Figure 3.3d. However, this sensitivity analysis does indicate the importance of parameter choice for the vertical profile for cases of low u_{geo}, since it affects the vertical profile shape significantly.

3.6.3 Process diagrams: Snow-surface coupling

Figure 3.4a depicts the process diagram for the T_{2m} cooling that occurs in 9 hours and the soil heat flux (G) averaged over 9 hours for $u_{geo} = 8$ m s^{-1}. As such, this figure represents the time integrated interaction between the surface and the atmosphere. The spread within the WRF-SCM results (the runs with sets of different parametrizations shown by the first 9 symbols in the legend) shows a small but clear correlation: the stronger the amount of surface cooling, the larger G is. This is explained by the fact that G depends on the ice conductivity (λ) and the temperature difference between the surface and the lower ice layers (dT/dz, where z increases downwards):

$$G = -\lambda \frac{dT}{dz}\,. \tag{3.2}$$

With a stronger atmospheric cooling and a stronger decrease in T_{skin}, the upper ice temperature difference increases and that results in a stronger G. This in turn tends to increase T_{skin} which leads to a smaller G. Hence the process of snow-surface coupling has a negative feedback.

The results of the sensitivity analysis are indicated with the lines. The line of the coupling sensitivity is oriented perpendicular to the orientation of the model intercomparison runs. The reason for this perpendicular orientation is that λ is adjusted to generate more and less coupling. To increase the amount of coupling, λ is increased, which causes a stronger G. Also now more heat from the ice is brought

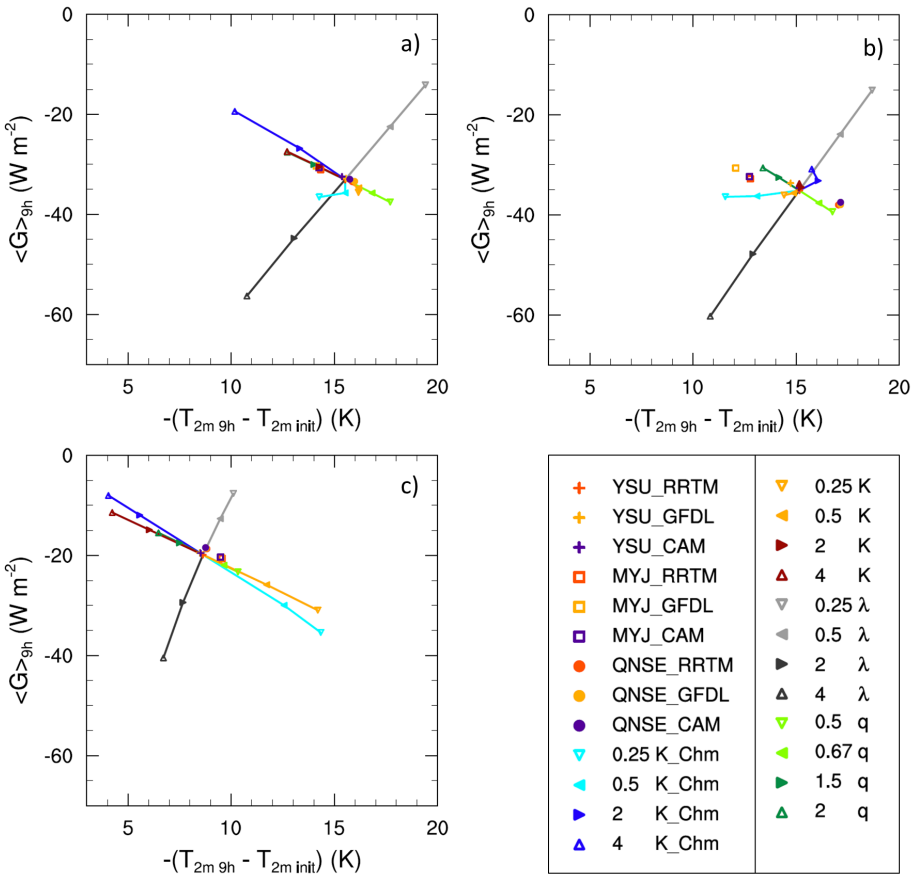

Figure 3.4: Cooling of the 2 m temperature (-($T_{2m\ 9h} - T_{2m\ init}$) (K)) over the 9 hour run versus the soil heat flux ($< G >_{9h}$ (W m^{-2})) averaged over 9 hours for a geostrophic wind speed of a) 8 m s^{-1}, b) 3 m s^{-1} and c) 20 m s^{-1}. *K_Chm* represents the eddy diffusivity and exchange coefficients and therefore the change in mixing in both boundary and surface layer, K represents the eddy diffusivity and therefore change in mixing in the boundary layer only, λ represents the ice conductivity and thus the coupling and q represents the specific humidity profile and therefore the incoming long wave radiation. YSU-RRTM is the reference run.

to the surface into the atmosphere resulting in higher T_{skin}, which is reflected in higher T_{2m} and less cooling at this level.

The processes of turbulent mixing and radiation only affect the temperatures at the surface and do not influence λ. When the amount of turbulence increases, more heat is transported to the surface and cold air is transported aloft. An increase in $L\downarrow$ also results in higher T_{skin}. Thus both these enhanced process strengths reduce the temperature difference in the ice and result in smaller G. The opposite occurs for a decrease in $L\downarrow$ and for the decreased K runs.

A non-linear feature is observed for the decreased K_Chm runs, where there is also less mixing in the surface layer, and for runs with K decreased from 0.5 to 0.25. We will come back to this later. The overall direction of the sensitivity lines is comparable with the results of Bosveld *et al.* (2012) for GABLS3, though the direction of our K and q runs show more overlap.

Since the lines of radiation, and partially mixing, are oriented in the same direction as the spread within the model, they explain mostly the spread within the model for these plotted variables. Furthermore, the overlap indicates that the radiation and mixing processes can compensate each other for this set of variables. The coupling can also compensate these processes as far as T_{2m} is concerned. In a way this graph is rather straightforward, because to obtain the spread within the models, several BL schemes were used for which the mixing is calculated differently, and several $\mathrm{LW_{rad}}$ schemes were used including therefore differences in $L\downarrow$. However, Figure 3.4 also indicates that surface coupling has a strong influence on the T_{2m} cooling and G. The difference between the K_Chm and K runs do indicate the sensitivity of the model to the description of the surface layer and its link to the BL in the parametrization schemes.

Figure 3.4b shows a similar process diagram, but for $u_{geo} = 3$ m s^{-1}. We see that the orientation of the model intercomparison runs is similar as those for $u_{geo} =$ 8 m s^{-1}, but with a larger spread. Furthermore, the orientation of the radiation and coupling processes as well as their length, is comparable with those for the standard u_{geo}. The line representing turbulent mixing however, has a different orientation for multiplication factors of 0.5 - 2.0 and shows a change in direction for the amount of cooling in time as was also seen in the line from 0.5 - 0.25 K_Chm for $u_{geo} = 8$ m s^{-1}. For both types of mixing runs a decrease in mixing results in less T_{2m} cooling and a larger G. A possible explanation for this will be given later on. The line does not change direction regarding G. Increasing the amount of mixing does increase T_{skin} (because the cold air is mixed to the air just above the surface). Therefore the temperature difference between the skin layer and the deeper ice layers decreases, followed by a decrease in G. Furthermore, the model is more sensitive for mixing when this process is also adjusted in the surface layer, since the line for the K_Chm runs is considerably longer than for the K runs.

As far as the orientation of the points is concerned, it is seen that radiation plays a large role in explaining the differences between the model intercomparison runs. This does not come as a large surprise. As can be seen in Figure 3.3c, the θ profiles resemble a type I profile as in Vogelezang and Holtslag (1996), which represents mainly radiation dominated boundary layers.

Figure 3.4c presents the results for a wind regime of 20 m s^{-1}. The orientation

of the model intercomparison runs is similar to the 3 and 8 m s^{-1} runs and again follows the alignment of the radiation and mixing (K runs) sensitivity as for the 8 m s^{-1} case. However, the line representing coupling has decreased in length and is now more 'steep': it still covers a large range in the change in average G (which is directly linked to the change in λ), but this does not have as strong an impact on the 2 m cooling. The radiation line is similar in length, but the line representing turbulent mixing is now relatively larger and plays a more important role. This is also seen from the stronger change in G and 2 m cooling when multiplying both mixing processes by 0.5 and 2.0 compared to multiplying the radiation process with the same factors. The difference in line length for both increased and decreased mixing indicates that the model is more sensitive for decreasing turbulent mixing than an increase in mixing. This is probably related to the fact that if there already is sufficient mixing, an increase in mixing only causes the change in the system to be divided over a deeper BL and the signal may not be as clearly detectable.

In order to study the sensitivity of our results for snow thickness, we repeated the runs for a thicker snow cover of 20 cm. Although the forecasts for the three geostrophic wind speeds resulted in overall colder solutions, the relative orientation of the sensitivity lines remained approximately similar. Especially the insensitivity to coupling at higher wind regimes was now even more pronounced, with a line hardly deviating from the reference run. The same holds for the process diagrams in sections 3.6.4 and 3.6.5.

Next, we still need to explain the non-linearity in the *K_Chm* sensitivity analysis runs for the 3 and 8 m s^{-1} case regarding the amount of cooling at 2 m. Intuitively, one would expect that, when increasing the amount of mixing, more warm air is redistributed towards the surface. Thus the amount of cooling in time should decrease for increased mixing and vice versa for a decreased amount of mixing. This is indeed the case for an u_{geo} of 20 m s^{-1} and partly for the 3 and 8 m s^{-1} regime, but for the other cases opposite results are found.

In fact, similar results were found by McNider *et al.* (2012) in their model study. As they used 2 different models than the WRF-SCM, this gives more confidence in the non-linear behaviour. For low wind speed regimes they obtained colder atmospheric solutions when the wind speed was increased. In their study also the two states of the SBL were found. McNider *et al.* (2012) explain that for very light wind speeds, there is so little mixing that the boundary layer is very shallow and weak and only a little amount of cold air is mixed from the surface to the first model level. When now the wind speed increases, more cold air is mixed away from the surface and brought to higher levels thus leading to lower temperatures in the atmosphere above the surface. They find this to be the case for solutions with exponential (concave up), or type I, θ profiles. As the wind speed increases even further, the air close to the surface begins to warm with increased wind speeds as now more warm air is able to reach the surface. McNider *et al.* (2012) found these solutions for concave down, or type II, θ profiles.

In the current study we also find the different behaviour of the SBL for either increasing or decreasing the wind speed (see Figure 3.5). We find that for the wind regimes left of the T_{2m} minimum, T_{2m} *decreases* when the wind speed increases. The θ profiles (not shown here) then show a concave up, or more exponential shape

(e.g. as in Figure 3.3c for the reference run and decreased mixing runs for a u_{geo} of 3 m s^{-1}). In these cases, when mixing or wind speed increases, the change in temperature for a fixed distance downward is larger than the change in temperature for an identical fixed distance upward. Therefore a turbulent eddy centred at this given height will bring up cold air that more than compensates for the warm air brought down by the sinking part of the eddy. Hence, there will be a net cooling with enhanced mixing at this level. The opposite is true for a concave down θ profile which is found when wind speeds have increased sufficiently and are on the right of the T_{2m} minimum for the standard (1 K_Chm) and increased mixing runs (e.g. as in Figure 3.3c for the increased mixing runs). Then there will be net warming with enhanced mixing and wind speed.

Note that the difference in profile shape is not as profound for the decreased amount of mixing runs, where the θ profiles resemble a more exponential shape also on the right of the T_{2m} minimum, but they do show a weaker curvature for these wind speeds, which makes it easier for the mixing to overcome the temperature gradient close to the surface. Also when the wind speeds increase further, though the θ profile remains exponential, eddies with larger sizes can now reach the surface and bring warmer air from higher levels downward which can compensate for the cold air that is brought upwards from the surface. For the lower wind speeds, the eddies are relatively smaller so that the amount of downward transported warm air is not sufficient to compensate for this effect.

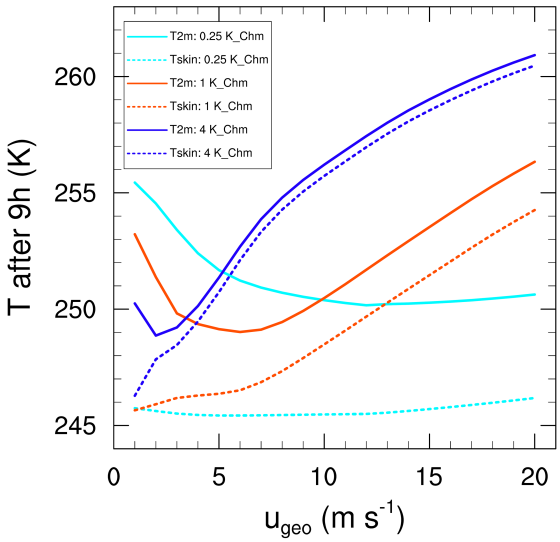

Figure 3.5: The modelled skin and 2 m temperature (K) after 9h for different geostrophic wind speeds (u_{geo} (m s^{-1})) using varying turbulence intensities where mixing is adjusted in both boundary and surface layer. The solid lines refer to the 2 m temperatures, the dotted lines refer to the skin temperatures.

It is furthermore seen that the change in behaviour shifts earlier (at lower u_{geo}) when the mixing is enhanced. Also, we see that for a more efficient mixing, the temperature difference between the surface and the 2 m level is smaller. In this way T_{2m} is indeed lower for higher amounts of mixing when u_{geo} is kept constant at a low value since the lower amount of mixing cannot mix away the large temperature gradient.

T_{skin} always increases when the amount of wind speed is increased for both the reference and the increased amount of mixing runs. Only for the $0.25K\_Chm$ runs we detect a very small decrease in T_{skin} when the wind speed is increased from 1 to 6 m s^{-1}. The reason for this is that due to the small sensible heat flux the cold air at the surface is not efficiently lifted and the mean SBL temperature remains relatively high. This results in an increase in $L\downarrow$ from the layers above the surface towards the surface which, when mixing or wind speeds decrease sufficiently, overcomes the radiative cooling resulting in less cooling of the surface.

For an $u_{geo} = 3$ m s^{-1} we detect a change from an exponentially shaped θ profile to a concave down shaped profile when the amplification of mixing increases to 2.0 (see Figure 3.3c). Now the temperatures in the SBL decrease. When the amount of mixing increases further to 4.0 K_Chm, T_{2m} is still lower than T_{2m} for 1 K_Chm, but has increased compared to 2.0 K_Chm, indicating that there is more effective mixing with higher (and warmer) levels. For decreasing the amount of mixing for $u_{geo} = 8$ m s^{-1}, also the θ profile shifts from mixed to more exponentially shaped. The non-linear effect is more profound for the K_Chm runs than the K runs. This is extended knowledge after Bosveld *et al.* (2012). The decreased K runs, which have a similar altered mixing as in the study of Bosveld *et al.* (2012) over land, still have the normal amount of mixing in the surface layer and thus are more efficient in transporting cold air away from the surface and warmer air towards the surface so that this non-linear effect is not as strongly visible.

Note that this non-linear behaviour is also found from observations over sea-ice and in the nocturnal SBL over land. Lüpkes *et al.* (2008) found that the minimum 10 m temperature observed during the SHEBA experiment in winter months is not observed for very calm conditions, but for a wind speed of ~ 4 m s^{-1}. Moreover, they found decreasing snow temperatures for increasing wind speeds up to ~ 4 m s^{-1} due to the reduced $L\downarrow$ from the colder air as was also found in our study. The non-linearity was also detected by Acevedo and Fitzjarrald (2003) from measurements in the Albany region. They found that wind gusts below a certain threshold (in their data 1.5 m s^{-1}) only mix the air downwards to the colder ground, hence cooling the surface layer, while higher wind speeds cause mixing with higher levels as well and thus warming the surface layer. The existence of two different wind regimes with a threshold at wind speeds of 2 - 4 m s^{-1} was furthermore reported by Rinke *et al.* (2012) from observations over the Antarctic.

3.6.4 Process diagrams: Radiation impacts

Next we study which processes influence the temperature and radiative cooling at and near the surface. There is a tight coupling between the incoming and outgoing long wave radiation at the surface and the temperatures in the SBL and at the surface respectively (Bosveld *et al.*, 2012). Therefore, Figure 3.6 shows the process diagrams

of the 2 m temperature and the net radiation (Q^*), both averaged over 9 hours. Again we will first study the runs with a geostrophic wind speed of 8 m s^{-1}.

The spread within the WRF-SCM shows a strong correlation: when T_{2m} is high, a more negative Q^* can be found. This indicates that $L\uparrow$ dominates in the variation within the model intercomparison runs, since the extra $L\uparrow$ due to higher temperatures overcompensates the extra $L\downarrow$ resulting in a more negative Q^*.

When studying the lines that are obtained with the sensitivity analysis, we find that the processes of increased mixing (K runs) and increased/decreased coupling are oriented in the same direction as the model intercomparison runs. For example

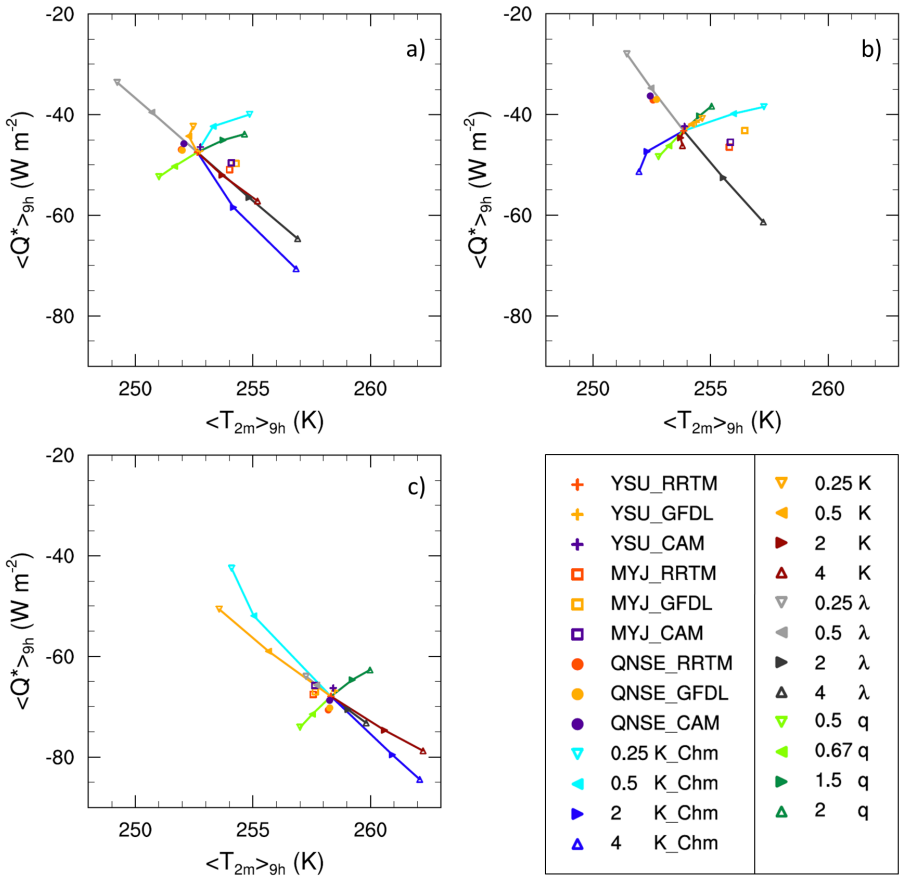

Figure 3.6: The 2 m temperature ($< T_{2m} >_{9h}$ (K)) versus the net radiation ($< Q^* >_{9h}$ (W m^{-2})), both averaged over 9 hours for a geostrophic wind speed of a) 8 m s^{-1}, b) 3 m s^{-1} and c) 20 m s^{-1}. *K_Chm* represents the eddy diffusivity and exchange coefficients and therefore the change in mixing in both boundary and surface layer, K represents the eddy diffusivity and therefore change in mixing in the boundary layer only, λ represents the ice conductivity and thus the coupling and q represents the specific humidity profile and therefore the incoming long wave radiation. YSU-RRTM is the reference run.

when the amount of mixing or coupling is increased, a higher T_{2m} is found as well as a more negative Q^*. This is not the case when we look at the process of radiation. For increased $L\downarrow$ indeed a higher T_{2m} is found, but also a less negative Q^*, and the opposite occurs for a decreased amount of $L\downarrow$. Apparently for the radiation sensitivity the change in $L\downarrow$ dominates over the change in $L\uparrow$. For both mixing runs, we again see the non-linearity as was explained in the previous subsection. The spread within the model can mostly be explained by increasing the mixing strength (K runs) and increasing/decreasing the coupling strength, so that mixing and coupling appear to be complementary processes for these considered variables. Again the overall orientation of the K, λ and q runs is similar as in Bosveld *et al.* (2012) without the non-linear effect.

Figure 3.6b gives the process diagram for $u_{geo} = 3$ m s^{-1}. Studying the lines representing coupling, we see a slight change in orientation, the lines are more 'steep': the change in T_{2m} is smaller for a similar change in Q^*, however, they are not too different from the 8 m s^{-1} case. The orientation of the mixing lines however, has changed orientation and direction, as was also the case in figure 3.4b. The average T_{2m} decreases when the amount of mixing increases. As explained in the previous subsection this phenomenon can occur when the BL is very weak and shallow and increased turbulence mixes cold air from the surface upward which is not sufficiently compensated by the downward transported warm air. Q^* does decrease with increased mixing. This is because $L\uparrow$ is determined by T_{skin}, and these do increase for increased mixing (see also Figure 3.5). For $u_{geo} = 3$ m s^{-1} it is further observed that the model is more sensitive to mixing when also the amount of mixing in the surface layer is adjusted and not very sensitive to mixing only in the BL. The spread of the model intercomparison runs is now mostly found by a combination of increase in radiation, decrease in mixing and a change in snow-surface coupling.

The process diagram for T_{2m} and Q^* for $u_{geo} = 20$ m s^{-1} (Figure 3.6c) again indicates that the effect of snow-surface coupling has decreased significantly, while the effect of mixing is relatively larger compared to the 8 m s^{-1}, as was also observed in Figure 3.4. The model intercomparison runs show less spread than for the other wind speeds and cannot clearly be explained by one unique process modification.

3.6.5 Process diagrams: Turbulent mixing

We continue with the process diagrams representing atmospheric mixing in showing the temperature difference between the lowest model level and the surface (ΔT), versus the sensible heat flux (H), both averaged over 9 hours (Figure 3.7). H in the BL is determined by the eddy diffusivity for heat (K_h) and the potential temperature gradient ($\partial\theta/\partial z$) via:

$$H = -\rho c_p K_h \frac{\partial \theta}{\partial z}\,. \tag{3.3}$$

Again we first focus on the case with $u_{geo} = 8$ m s^{-1} in Figure 3.7a. When λ increases, more energy is added from the deeper ice layers to the atmosphere resulting in higher surface temperatures and hence a smaller ΔT, which consequently lowers the magnitude of H. The opposite occurs for decreasing the amount of coupling. If the amount of incoming radiation increases, the temperature difference becomes

slightly smaller, and a similar orientation is found as for the coupling process.

The amount of mixing in the K runs is adjusted by altering the eddy diffusivity coefficient in the BL scheme. The amount of mixing in the K_Chm runs is adjusted similarly, but includes an adjustment in the exchange coefficient in the land-surface model. When the amount of mixing in both the K_Chm runs and the K runs is increased, H increases due to the increased K_h. However, the orientation regarding ΔT differs, causing the orientation of the two mixing lines to be perpendicular. When the mixing increases, the temperature gradient decreases for the K_Chm runs, while

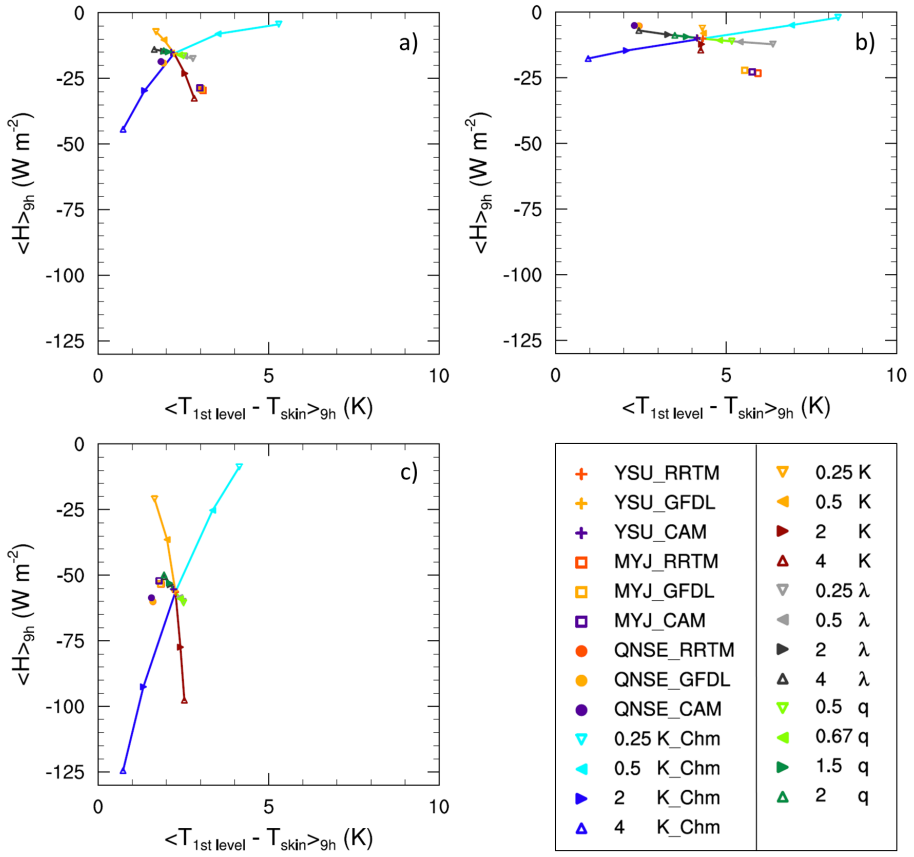

Figure 3.7: The temperature difference between the first model level and the surface ($< T_{1st\ level} - T_{skin} >_{9h}$ (K)) versus the sensible heat flux ($< H >_{9h}$ (W m^{-2})), both averaged over 9 hours for a geostrophic wind speed of a) 8 m s^{-1}, b) 3 m s^{-1} and c) 20 m s^{-1}. K_Chm represents the eddy diffusivity and exchange coefficients and therefore the change in mixing in both boundary and surface layer, K represents the eddy diffusivity and therefore change in mixing in the boundary layer only, λ represents the ice conductivity and thus the coupling and q represents the specific humidity profile and therefore the incoming long wave radiation. YSU-RRTM is the reference run.

an increase in temperature gradient is found for the K runs. The first behaviour is what we would expect. When there is more mixing, the heat exchange between the surface and the atmosphere occurs more efficiently resulting in smaller temperature differences. That the temperature gradient increases with increased mixing for the K runs can be explained by the constant flux approach for which H in the surface layer equals H at the first model level. For the surface layer H is determined with:

$$H = -\rho c_p C_H u(\theta_1 - \theta_s)\,, \tag{3.4}$$

where C_H is the exchange coefficient for heat, u the wind speed and θ_1 - θ_s represents the temperature difference between the first model level and the surface. In the constant flux approach this equation should be equal to equation 3.3. When the amount of mixing in the surface layer is not adjusted, it follows from the equations that for an increase in K_h, there should be an increase in θ_1 - θ_s and vice versa. In other words, an increase of K in the BL increases θ_1, but has little direct effect on θ_s, therefore ΔT increases and vice versa. This is indeed seen in figure 3.7 for the K runs.

When we compare the lines of the sensitivity analysis with the model intercomparison runs, we find that the orientation of the intercomparison runs can be explained by a combination of the K mixing process and coupling process. The model intercomparison runs are better represented by the K runs compared to the K_Chm runs. We expect this is due to the spread between the model intercomparison runs being dominated by the different BL schemes, and not the surface-layer schemes, since these are rather similar (Skamarock *et al.*, 2008).

Figure 3.7b gives the same process diagram for $u_{geo} = 3$ m s^{-1}. Again, the orientation of the radiation and coupling lines is identical compared to those of a geostrophic wind speed of 8 m s^{-1}. The effect of change in coupling appears to be slightly more important than the effect of a change in radiation, since the 0.5 and 2.0 perturbation are equally oriented and the coupling line is longer. The length of the mixing line of the K_Chm runs is longer than the coupling line, though not in the orientation of the model intercomparison runs. The length of the mixing line for the K runs is very short as seen previously for this wind speed.

Figure 3.7c presents the process diagram for $u_{geo} = 20$ m s^{-1}. The orientation of the lines is comparable to the 8 m s^{-1} case without the strong non-linear effect, but the changes in H are now more profound, while the changes in ΔT at the surface are smaller for the coupling and radiation sensitivity runs. The latter can be explained by the already better mixed temperature profile. Again the line for snow-surface coupling is rather short, a perturbation of 0.25 and 4.0 for coupling leads to similar results as perturbating radiation by 0.5 and 2.0, implying the insensitivity to snow-surface coupling in this wind regime. The radiation line points more in the direction of the orientation of the model intercomparison runs, but as for the other process diagrams, the largest sensitivity is found for the turbulent mixing process.

3.7 Rescaled sensitivity analyses

In the previous section we perturbed each process by multiplying the coefficients with a prescribed amplification factor. However, multiplying for example the eddy

Table 3.3: Overview of the changes in net radiation over 9 hours (ΔQ^*) for $u_{geo} = 8$ m s^{-1} and the factor by which both the eddy diffusivity and exchange coefficient (K_Chm), only the eddy diffusivity (K), the ice conductivity (λ) and the initial specific humidity profile (q) are multiplied to obtain this net radiation change.

Parameter	**ΔQ^* (W m^{-2})**	**Multiplication factor**
K_Chm	7	0.305
	3.5	0.683
	−3.5	1.292
	−7	1.599
K	7	0.065
	3.5	0.462
	−3.5	1.716
	−7	2.769
λ	7	0.551
	3.5	0.752
	−3.5	1.311
	−7	1.708
q	3.5	1.935
	−3.5	0.612
	−7	0.383

diffusivity or the conductivity by such a factor, may not necessarily have a similar impact on the atmospheric system in terms of energy and thus we would not compare the processes in a 'fair' way. Therefore we repeat the sensitivity analyses by varying the process strengths such that the change in surface net radiation (ΔQ^*) for the new run compared to the reference run is similar:

$$\Delta Q^* = \frac{1}{\Delta t}\left(\int Q^*_{SA}dt - \int Q^*_{ref}dt\right). \tag{3.5}$$

Here Q^*_{SA} is the net radiation for the sensitivity analysis run and Q^*_{ref} is the net radiation for the YSU-RRTM reference run. Δt is the total time difference (9h) and dt represents the smaller time steps to calculate the integral. Table 3.3 gives an overview of the amount by which K_Chm, K, λ and q were multiplied to achieve the desired ΔQ^* for $u_{geo} = 8$ m s^{-1}. These prescribed ΔQ^*s are within the range of the ΔQ^*s that were found for the sensitivity analysis runs with the prescribed multiplication factors (see Table 3.2). We were unable to adjust the radiation process to a ΔQ^* of 7 W m^{-2}, because the model did not reach this parameter range.

Note that the choice of these multiplication factors might be time scale dependent, since ΔQ^* does not necessarily occur at the same rate for each physical process. Since we will examine ΔQ^* over the entire 9h run, it is justified to adjust the parameters such that the surface energy change at 9h is similar. Figure 3.8 depicts the same process diagrams as discussed in the previous section, for $u_{geo} = 8$ m s^{-1}. We adjusted the axis, but kept them in the same proportion as Figures 3.4, 3.6 and 3.7 for better comparison.

When we compare Figure 3.8a, b and c with Figures 3.4, 3.6 and 3.7 a, in general

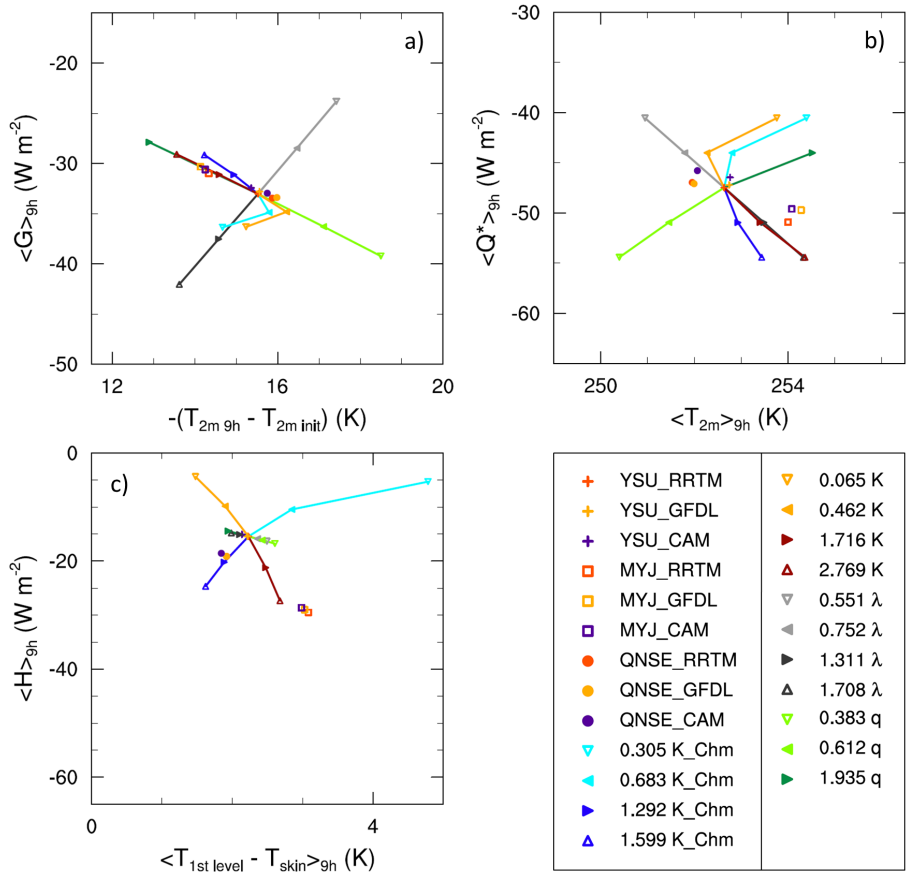

Figure 3.8: Process diagrams for a geostrophic wind speed of 8 m s^{-1} of a) the cooling of the 2 m temperature (-($T_{2m\ 9h} - T_{2m\ init}$) (K)) over the 9 hour run versus the soil heat flux ($< G >_{9h}$ (W m^{-2})) averaged over 9 hours, b) the 2 m temperature ($< T_{2m} >_{9h}$ (K)) versus the net radiation ($< Q^* >_{9h}$ (W m^{-2})), both averaged over 9 hours, and c) the temperature difference between the first model level and the surface ($< T_{1st\ level} - T_{skin} >_{9h}$ (K)) versus the sensible heat flux ($< H >_{9h}$ (W m^{-2})), both averaged over 9 hours. In all cases ΔQ^* is kept similar, i.e. $\Delta Q^* = 7$, 3.5, -3.5 and -7 W m^{-2}. YSU-RRTM is the reference run.

we see a similar orientation, but a decrease in line length for the K_Chm and λ runs and for the increased K runs. The line length of reduced K runs has increased due to the stronger perturbation factor that was applied to achieve a ΔQ^* of 7 W m^{-2} than the multiplication factors as applied in the previous section. These differences with the previous Figures indicate the importance of the choice for the multiplication factors of the parameters.

To get a ΔQ^* of 3.5 W m^{-2} for $u_{geo} = 3$ m s^{-1}, the K_Chm run had to be multiplied by 0.488, the K run by 0.103, the λ run by 0.763 and the q run by 1.628. These findings indicate that for low wind speeds the model is not that sensitive to

mixing, and especially to mixing in the BL scheme only, while being more sensitive to coupling and radiation. This is supported by the ΔQ^*s that were found when the prescribed amplification factors were applied in the previous section (see Table 3.2). For an u_{geo} of 3 m s^{-1} we find smaller changes in ΔQ^* for the mixing runs, especially the K runs, and larger changes for the coupling runs compared to the u_{geo} = 8 m s^{-1} runs. The radiation runs only show minor differences between the ΔQ^*.

For u_{geo} = 20 m s^{-1} we had to multiply K_Chm by 0.861, K by 0.756, λ by 0.312 and q by 1.542 to obtain a ΔQ^* of 3.5 W m^{-2}. When we compare ΔQ^* for u_{geo} = 20 m s^{-1} with 8 m s^{-1} while keeping the multiplication factor for each process equal in Table 3.2, we see stronger changes for the mixing runs, and smaller changes for the coupling runs. The changes are stronger when the amount of mixing is decreased, since the signal is mixed over a more shallow boundary layer. The radiation runs do show a somewhat larger difference in ΔQ^* as well.

3.8 Conclusions and discussion

This study focuses on identifying the dominant governing processes in the Arctic stable boundary layer for different wind regimes. We consider three physical processes, i.e. snow-surface coupling, radiation and turbulent mixing. First we perform a 1D model intercomparison within the WRF framework, by varying the boundary-layer and long wave radiation schemes for the GABLS1 case (Beare *et al.*, 2006; Cuxart *et al.*, 2006). Hence, we quantify the spread between the different model schemes. To explain this spread, we perform a sensitivity analysis for the three governing processes.

Overall we notice a shift in significance of the different processes for varying wind regimes. In situations with high wind speeds, model output is most sensitive to turbulent mixing, while the effects of radiation and especially the snow-surface coupling are small (as one could anticipate), as seen from the strongest change in potential temperature and wind speed profile, and from the relatively long sensitivity lines in the process diagrams (Bosveld *et al.*, 2012) for the mixing process.

Considering situations with low wind speeds, we reveal that the model is most sensitive to snow-surface coupling and radiation in the SBL structure and evolution. Then, the impact of turbulent mixing is minor except when the mixing strength is also adjusted in the surface layer. This stresses the significance of consistently linking the surface layer with the boundary layer.

For the cases with a geostrophic wind speed of 8 and 20 m s^{-1}, we find a relatively mixed boundary layer profile topped by a strong inversion, though when we decrease the amount of mixing by 0.25 and 0.5 (for 8 m s^{-1}) and 0.25 (for 20 m s^{-1}), this becomes more exponential. For a low wind speed of 3 m s^{-1}, a more exponential profile shape for the reference run is found though this becomes better mixed for a higher turbulent mixing strength. Thus, even though choosing a different mixing parameter may not significantly affect the surface variables, it does strongly influence the vertical profiles and thus possibly other variables away from the surface. Therefore, it is recommended that when evaluating and optimizing a model, the vertical structure should be considered as well. If the model is optimized for 2 m temperatures, as often occurs in operational studies, it is likely that the model results deviate aloft.

Furthermore, an intriguing non-linear behaviour regarding the effects on temperature just above the surface is found, as was also seen in observations (Acevedo and Fitzjarrald, 2003; Lüpkes *et al.*, 2008; Rinke *et al.*, 2012). The 2 m temperature *decreases* for increased mixing strength and vice versa. The skin temperature, however, does increase for increased mixing strength and vice versa. This suggest that mixing occurs only in a shallow layer close to the surface and cold air that is mixed upward is not fully compensated by downward mixed warm air. These findings do have an implication for the understanding of the Arctic climate, since apparently the behaviour at the 2 m level is not straightforward, while the 2 m temperature is often used in research.

Moreover, this 'counter-intuitive' behaviour was found for low wind speeds with exponential (or concave up) potential temperature shapes (McNider *et al.*, 2012), when relatively more cold air is mixed towards the 2 m level than warm air is transported downwards. For higher wind speeds, we find better mixed (or concave down) potential temperature profiles, where there is a more efficient redistribution of heat and 2 m temperatures increase with increased wind speeds. Keeping the wind speed constant, this non-linear behaviour can also occur for better mixed boundary layer profiles when the mixing strength is decreased and the temperature inversion at the surface increases greatly.

The process diagrams indicate that some process sensitivity lines can overlap, which implies that variations due to these processes can compensate each other. This further implies that errors in either process parametrization can remain hidden by the parametrization of the other process, keeping it unclear if the model is less physically realistic. Unfortunately, the two overlapping processes are not the same for various sets of variables. Hence, in order to proceed in model development, processes should not be studied in isolation. This requires coordination of many different types of measurements which poses a challenge for observationalists.

This study explored the relative significance of the governing physical processes for a cooling Arctic SBL compared to each other under different wind regimes. Moreover, future work is calling for observational confirmation of the current work. In this way we would know how to improve the model. However, this study is for an idealized set-up and we were unable to directly compare our model results with observations.

Overall, the representation of small scale processes in the Arctic SBL remains challenging. Though there is not one single process absolutely governing the evolution and structure of the SBL, we were able to indicate a shift in their relative significance for changing wind regimes and we confirmed the non-linear behaviour of turbulent mixing regarding the temperatures close to the surface for frequently occurring wind speeds. Therefore, in regimes with high wind speeds we think it is worthwhile to focus on improving the turbulent mixing schemes, while for low wind speed regimes better investments can be made in land-surface and radiation schemes. However, due to the non-linearity effects that we detected, choosing the amount of turbulent mixing should be done wisely, not only for proper forecasting of temperatures close to the surface but for the entire atmospheric profile and hence transports aloft.

Acknowledgements

The authors are grateful to Dr. Fred Bosveld for inspiring us to use the process diagrams and discussions with him were greatly appreciated. The ERA-Interim data used in this study have been obtained from the ECMWF data server. We also thank Kevin Manning for providing us a better insight in how the snow cover is implemented in the Noah land-surface model. We acknowledge the support from NWO (The Dutch Science Foundation) with grant number 829.09.005 ("Quantifying contributions of surface climate feedbacks to the Arctic amplification of greenhouse warming" in the Sustainable Earth program). The contribution by G.J. Steeneveld has partly been sponsored by the NWO contract number 863.10.010 ("Lifting the fog"). We also thank the 2 anonymous reviewers for their valuable suggestions.

Chapter 4

Clear-sky stable boundary layers with low winds over snow-covered surfaces. Part 1: WRF model evaluation

Abstract

In this article, we evaluate the Weather Research and Forecasting (WRF) mesoscale meteorological model for stable conditions in clear skies with low wind speeds. Three contrasting terrains with snow covered surfaces are considered, namely Cabauw (The Netherlands, snow over grass), Sodankylä (Finland, snow over a needle-leaf forest) and Halley (Antarctica, snow over an ice shelf). We used the full 3D model and the single-column versions of the WRF model. The SCM was driven by realistic forcings of the WRF-3D field. Several sets of SCM forcings were tested: A. no advection, B. varying geostrophic wind in time, C. momentum advection in addition to B, D. temperature and moisture advection in addition to C, and E. forcing the SCM field to the 3D field above a threshold height.

The WRF-3D model produced good results overall for wind speed, but the near-surface temperatures and specific humidity were overestimated for Cabauw and Sodankylä, and underestimated for Halley. Prescribing advection for momentum, temperature and moisture gave the best results for the WRF-SCM, and simulations deviated strongly from reality without advection. Nudging the SCM field to the 3D field above a threshold height lead to an unrealistic behaviour of the variables below this height and is not recommended. Detailed prescription of the surface characteristics, e.g. adjusting the snow cover and vegetation fraction, improved the 2 m temperature simulation. For all three sites, the simulated temperature and moisture inversion were underestimated, though this improved when prescribing advection.

Overall, in clear-sky conditions, the stable boundary layer over snow and ice can be modelled to a good approximation if all processes are taken into account at high resolution, and if land surface properties are carefully prescribed.

This Chapter has been slightly updated from the paper published as Sterk HAM, Steeneveld GJ, Vihma T, Anderson PS, Bosveld FC, Holtslag AAM. 2015. Clear-sky stable boundary layers with low winds over snow-covered surfaces. Part 1: WRF model evaluation, *Q. J. R. Meteorol. Soc.*, doi: 10.1002/qj.2513.

4.1 Introduction

The evolution of the stable boundary layer (SBL) is mostly determined by turbulent mixing, the coupling between the atmosphere and the surface, and radiative effects. Additionally, the presence of clouds or fog, subsidence, geostrophic wind speed, advection, gravity waves, and drainage and katabatic flows may play a role (Delage, 1997; Mahrt *et al.*, 1998; Mahrt, 1999; Steeneveld *et al.*, 2006a; Williams *et al.*, 2013). The reason why SBL modelling remains complex, could be related to the large amount of relatively small-scale processes which may act simultaneously and interactively, while on top of that the physical processes and their interactions are also not completely understood and are represented incompletely in models.

Furthermore, a large variety of SBL types exists, e.g. there can be continuous or intermittent turbulence, or even laminar flow, which influences the SBL depth and the vertical and horizontal exchanges of quantities (e.g. Holtslag *et al.*, 2013). A relatively coarse resolution (e.g. in operational models) can also hamper proper SBL modelling (e.g. Steeneveld *et al.*, 2006a; Tardif, 2007; Byrkjedal *et al.*, 2008; Svensson and Holtslag, 2009; Svensson and Karlsson, 2011; Savijärvi, 2013). Especially over snow-covered polar surfaces where atmospheric conditions can become very stable, modelling the SBL is challenging. For example in the Arctic and Antarctic, many global and regional climate model outputs diverge from one another, as well as from observations (e.g. Holland and Bitz, 2003; Rinke *et al.*, 2006; Walsh *et al.*, 2008; Rinke *et al.*, 2012; Valkonen *et al.*, 2013). Though simplified model representation of SBL processes may not be the only cause of these model biases, we will focus on the SBL processes in this paper.

Single-column models (SCMs) are convenient to evaluate the physical processes in the boundary layer (BL) and can therefore be used to improve the understanding of SBL processes (Baas *et al.*, 2010; Sterk *et al.*, 2013; Bosveld *et al.*, 2014b). Therefore in this study the SCM version of the Weather Research and Forecasting (WRF, Skamarock *et al.*, 2008) mesoscale meteorological model is evaluated for stable conditions over snow-covered surfaces. To evaluate the model performance against observations, the SCM needs to be driven by realistic forcings of the 3D atmospheric field (Baas *et al.*, 2010; Bosveld *et al.*, 2014a). A complete observational dataset at high temporal resolutions is typically not always available, e.g. due to a low temporal data coverage, possible equipment failure with low temperatures, and measurement stations may be limited spatially and not measure all required quantities. Therefore we rely on 3D model results to determine the SCM large-scale forcings, which is also advantageous since some aspects of the forcings are difficult to measure. We perform WRF-3D runs to determine the SCM forcings, and evaluate the WRF-3D runs briefly.

In part 1 of this study we evaluate the model for stable conditions with approximately the same low wind speeds for 3 contrasting terrains with snow, i.e. from the Cabauw site in the Netherlands, the Sodankylä site in northern Finland and the Halley station on Antarctica. These sites are characterized by snow over grass/crop-land, snow in an evergreen needle-leaf forest, and snow on an ice sheet respectively. For all terrain types, a case is selected with little to no cloud cover, as then stable stratifications are more likely to develop, while additionally this reduces the complexity of the radiative transfer. This makes the interpretation when studying the interaction of the snow surface and the SBL less difficult. Furthermore, because models often

have problems simulating stable cases with relatively low wind speeds (Edwards *et al.*, 2011; Tastula and Vihma, 2011; Holtslag *et al.*, 2013), the selected study periods have low wind speeds as well. Such SBLs are typically referred to as so-called type I SBLs for which, with very stable temperature stratifications and low wind speeds, radiative cooling is the dominating process and the vertical potential temperature (θ) profile is more exponentially (or concave up, $\partial^2\theta/\partial z^2 < 0$) shaped (Van Ulden and Holtslag, 1985; Vogelezang and Holtslag, 1996). Van de Wiel *et al.* (2012), report on a minimum wind speed under clear-sky conditions below which sustainable, continuous turbulence is unlikely and a very stable boundary layer is more likely. At the so-called crossing level of 40 m at Cabauw (the height where wind is relatively stationary compared to other levels), this minimum wind speed is $\sim$ 5 - 7 m s^{-1}.

Apart from the WRF-SCM evaluation for SBLs over snow for various land use types under low wind regimes, we will discuss how to determine the required forcings for running the SCM. We compare runs where only initial profiles are given, as well as where advection is prescribed, and report on experiences with a straightforward nudging approach above the BL.

SCMs are also a convenient tool for sensitivity analyses, because parameters can be controlled without introducing strong 3D effects. Focusing on the Arctic, Sterk *et al.* (2013) performed a sensitivity analysis to the snow-surface coupling, radiation, and turbulent mixing, since these mostly control the SBL evolution and structure (André and Mahrt, 1982; Beljaars and Holtslag, 1991; Steeneveld *et al.*, 2006a; Bosveld *et al.*, 2014b). Due to their idealized setup a direct comparison with observations was not possible. Therefore we extend their sensitivity analysis in Part 2 of this study, using the real-world cases defined in the current paper as a reference. In this way, we study how the importance of the processes shifts and whether the model sensitivity varies between certain processes over different terrains. As such we hope to gain more insight in where future research efforts should be focused.

This paper is organized as follows: in Section 4.2 an overview of the case studies and observational data is presented together with their accompanying synoptic settings. Section 4.3 gives an explanation of the WRF model, after which the methodology is described in Section 4.4. This is followed by the results in Section 4.5, and the conclusions and discussions in Section 4.6.

4.2 Observational data

The three locations and selected cases are described below. The first criterion for the case selection was that no clouds were observed. We checked this from either the observed cloud fraction, and/or the downwelling long wave radiation. The second criterion was that the tower observations indicated strongly stable conditions. Furthermore, near surface wind speeds had to be relatively low (less than 5 m s^{-1}), while soundings indicated relatively low wind speeds up to at least 1.5 km as well. Table 4.1 summarizes the characteristics during the SCM study periods.

4.2.1 Cabauw

The first dataset that we will study, has been obtained from the Cabauw Experimental Site for Atmospheric Research (Cesar) observatory, located in a flat area in the

Table 4.1: Characteristics of the Cabauw, Sodankylä and Halley sites during the SCM study periods, both from observations and settings in the WRF-SCM simulations. Observed are: latitude and longitude (lat/lon), land use, snow depth (not at Halley), near-surface wind speed ($U_{tot\ near-sfc}$), wind speed at the top of the mast ($U_{tot\ top-mast}$), minimum 2 m temperature ($T_{2m\ min}$), observed temperature gradient along the mast at the end of the SCM study period (ΔT_{mast}). Model-based characteristics are: roughness length that was applied in the WRF-SCM (z_0, from observations at Halley), geostrophic wind speeds applied for the WRF-SCM ($U_{geo\ 3D-WRF}$, from WRF-3D).

	Cabauw	**Sodankylä**	**Halley**
Lat/lon	51.97° N, 4.93° E	67.36° N, 26.63° E	75.58° S, 26.65° W
Land use	Grass	Forest, bogs, shrubland	Ice shelf
Snow depth	3.5 cm	62 cm	Gradual transition to ice in reality 6.2 cm in WRF-3D
$U_{tot\ near-sfc}$	0.7-3.5 m s^{-1} (at 10 m)	0-1.5 m s^{-1} (at 10 m)	2.5-4.7 m s^{-1} (at 8 m)
$U_{tot\ top-mast}$	2.6-7.6 m s^{-1} (at 200 m)	0-2.7 m s^{-1} (at 47 m)	2.1-4.7 m s^{-1} (at 32 m)
$T_{2m\ min}$	253.4 K	244 K	240.5 K
ΔT_{mast}	11.6 K (2-200 m)	9 K (3-48 m)	14 K (1-32 m)
z_0	1 mm	0.5 m	0.056 mm
$U_{geo\ 3D-WRF}$	2.6-5.9 m s^{-1} (obs. 2.3-6 m s^{-1})	0.4-2.6 m s^{-1}	3.5-7.3 m s^{-1}

western part of the Netherlands (51.97° N, 4.93° E). At this site, profiles of wind speed and wind direction from the Cabauw tower at 10, 20, 40, 80, 140 and 200 m height were available. At these heights and at the 2 m level, also temperature and relative humidity were measured. Furthermore all components of the surface radiation and energy budget were available from this measurement site. Further details on the

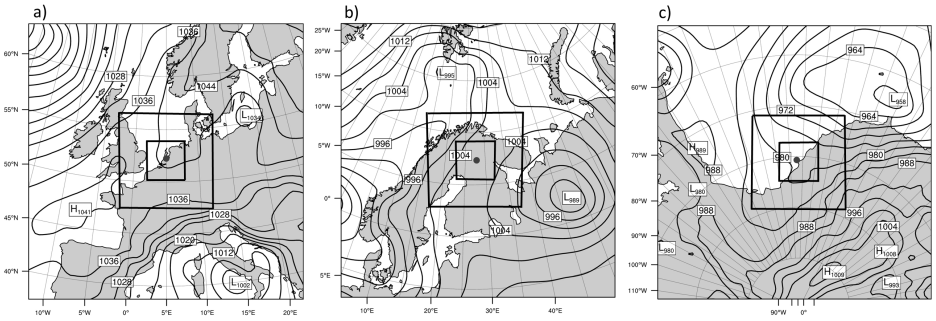

Figure 4.1: Mean sea level pressures in contours (hPa) for a) the Cabauw case, 4 February 2012, 0 UTC, b) the Sodankylä case, 27 March 2009, 0 UTC, and c) the Halley case, 18 May 2003, 12 UTC. The study sites are indicated with the dot. The outer and inner domain for the WRF-3D runs are indicated with the squares.

measurement site, and information on the different instruments used, are found in Van Ulden and Wieringa (1996), Beljaars and Bosveld (1997) and CESAR (2013).

The cloud-free night of 3 - 4 February 2012 was selected, since very low temperatures were reached over the fresh snow cover that had fallen in the morning and afternoon of 3 February. The prevailing weather was determined by a blocking high pressure system located over Scandinavia and North West Russia reaching to the British Isles (KNMI, 2012, see Figure 4.1a). This indicated winds coming from the East to North. Wind speeds at 10 m ($U_{tot\ 10m}$) were about 0.7 - 3.5 m s^{-1}, at 200 m this varied between 2.6 and 7.6 m s^{-1}. The surface geostrophic wind speed obtained from analysing surface pressure data from 18 stations within 100 km of Cabauw (Bosveld *et al.*, 2014a), ranged from 2.4 - 6 m s^{-1} during the SCM study periods. Furthermore, at the crossing level of 40 m as defined by Van de Wiel *et al.* (2012), wind speeds during the SCM study period were below the minimum 5 m s^{-1} to maintain continuous turbulence, so that the development of a very SBL is more likely. 2 m Temperatures (T_{2m}) decreased to 253.4 K, while at the 200 m level the diurnal cycle was hardly visible with temperatures of about 265 K, showing an absolute temperature gradient of almost 12 K over the 200 m. The snow depth in Cabauw was about 3.5 cm (averaged from the 2 stations closest by: Groot-Ammers, about 9 km from Cabauw (3 cm) and Benschop, about 6 km from Cabauw (4 cm)).

The snow heat flux was determined with $G = -\lambda\ \mathrm{d}T/\mathrm{d}z$, where we took the difference in temperature from the snow skin temperature determined from the long wave radiation components, and the observed ground surface temperature below the 3.5 cm snow pack, over the 3.5 cm snow layer. For the conductivity λ the value 0.021 W m^{-1} K^{-1} for fresh snow with a density of 100 kg m^{-3} was used following Stull (1988). Note that with this method, G can be underestimated for a large $\mathrm{d}z$, since the temperature gradient in the snow is highly non-linear and can be steeper close to the snow surface (Luce and Tarboton, 2001; Oldroyd *et al.*, 2013).

4.2.2 Sodankylä

The second case study is built on observations from the Arctic Research Centre of the Finnish Meteorological Institute (FMI-ARC, 2013), located at Sodankylä in northern Finland (67.36^{o} N, 26.63^{o} E). The area is fairly flat, though the land use is rather heterogeneous with coniferous and deciduous forests (49%) alongside more open areas of peat bogs and shrub lands and a river close by (Batchvarova *et al.*, 2001; Atlaskin and Vihma, 2012).

A 48-m-high micro-meteorological mast in a Scots pine forest, having a moderate density of trees 10 - 12 m tall, measured temperature and relative humidity at the heights of 3, 8, 18, 32 and 48 m, and wind speed at the heights of 18, 30, 38 and 47 m. An automatic weather station (AWS) in a more open land located some 500 m from the weather mast provided data on air temperature and relative humidity at the height of 2 m, wind speed and direction at 10 m, as well as surface pressure. Comparing data from the two sites for our study period, the air temperatures at 2 and 3 m heights typically agreed within 0.5 K, and the wind speeds at 10 and 18 m within 0.2 m s^{-1}. Furthermore, soundings were launched twice a day (0 and 12UTC) at the AWS site, and provided additional data on temperature, relative humidity, wind speed and direction in the vertical direction. Also the surface radiation fluxes

(at the AWS site) and sonic anemometer based turbulent fluxes (at the mast) were measured.

The case study covered the night of 26 - 27 March 2009 when a low pressure system was located east of Finland, as well as just north of the British isles with a weak pressure gradient over Finland (Figure 4.1b) resulting in weak wind speeds. Cloud free conditions were observed with very low wind speeds of 0 - 1.5 m s^{-1} at the 10 m level (so somewhat intermittent), and between 0 and 2.7 m s^{-1} at 47 m at the top of the mast. The wind direction was mostly from the north to north-west. T_{2m} dropped from 269 K during the day on 26 March to 243 K at the end of the night on 27 March, while for the 48 m height this was 267.5 K during the day which dropped to just over 252 K at night. Therefore during the night a temperature inversion of over 9 K was reached between 2 and 48 m.

The observed snow depth was 62 cm. The snow heat flux G in this case was determined using the equation as for the Cabauw case, but on basis of temperatures at the snow surface and at 60 cm snow depth above the soil (2 cm below the snow-atmosphere interface). For the conductivity λ the value 0.084 W m^{-1} K^{-1} for snow with a density of 200 kg m^{-3} was used following Stull (1988).

4.2.3 Halley

The third study location is the Halley research station of the British Antarctic Survey (75.58° S, 26.65° W) at the Brunt ice shelf in Antarctica. A micro-meteorological mast provided temperature, relative humidity and wind speed and direction data at 1, 2, 4, 8, 16 and 32 m height. Also the components of the radiation budget at the surface were available, as well as daily radiosonde data with information on temperature, relative humidity and wind speed and direction. For more information on the measurement site and observations, see e.g. King and Anderson (1988, 1994).

The study covered the cloud free period starting at 8h on the 18th of May 2003 when a strong stratification of 11 K between 1 and 32 m height was observed, and which increased to 14 K after 9h. A low pressure system was located North-East of Halley, with a small high pressure system to the West of Halley and another low pressure system just over the Antarctic Peninsula (Figure 4.1c). Wind directions close to the surface ranged from the South to South-East. Low wind speeds of 0 - 1.1 m s^{-1} at the 1 m level and 2.1 - 4.7 m s^{-1} at the 32 m level were observed.

Sonic anemometer data at 4, 16 and 32 m was available for the sensible heat flux. The latent heat flux ($L_v E$) was lacking, though this is usually very small at this site. The $L_v E$ derived from bulk transfer relations (Garratt, 1992) was also around zero (not shown here).

The snow depth estimation was more difficult than for the two other sites. As there is practically no snow melt, the snow density (ρ_{snow}) increases with depth and gradually transforms to ice due to pressure. For the SCM simulations, the snow depth as modelled by WRF-3D (6.2 cm) was applied.

The soil heat flux G was determined as for the Cabauw and Sodankylä cases, but now $\mathrm{d}T/\mathrm{d}z$ was calculated using the surface temperature and a thermal diffusion model tuned to the buried thermometers. A conductivity $\lambda = 0.21$ W m^{-1} K^{-1} was used which follows from the measured snow surface diffusivity ($2.9 \cdot 10^{-7}$ m^2 s^{-1}) and snow density (350 kg m^{-3}) and the heat capacity of the ice (2108 J kg^{-1} K^{-1}).

4.3 Model description and set-up

To evaluate the WRF single-column model (SCM), the full 3D model provided meteorological fields for the initial input files, and the time dependent advective forcings. This particular 3D run will be evaluated as well. In all cases version 3.2.1 of the model was used.

4.3.1 3D WRF

The WRF model is a mesoscale meteorological model, which uses a vertically stretched σ coordinate with the model top set at a constant pressure. Sixty vertical levels were applied here, with the highest resolution close to the surface. We used a nested approach with horizontally 81 x 81 and 106 x 106 grid cells for the first and second domain respectively, and a spatial resolution of respectively 12 and 4 km. The center points of the domains were set at the coordinates of the observational sites described in the section of the observational data. The domains are shown in Figure 4.1. Furthermore, for the Sodankylä and Halley case, polar stereographic projections were used, while a Lambert projection was used for Cabauw. Boundary conditions were provided by the ECMWF operational analysis. The cases were run with a time step of 60 seconds.

For the 3D runs, the parametrization schemes were selected following the operational Antarctic Mesoscale Prediction System (NCAR UCAR, 2013). The BL physics were represented with the Mellor-Yamada-Janjic local, 1.5 order scheme (MYJ, Mellor and Yamada, 1982), for which the eddy diffusivities are determined utilizing the turbulent kinetic energy. The MYJ-BL scheme runs in conjunction with the Eta-similarity surface-layer scheme (Skamarock *et al.*, 2008; Tastula and Vihma, 2011). For the long wave and short wave radiation the Rapid Radiative Transfer Model for GCMs (RRTMG, Iacono *et al.*, 2008) and Goddard scheme (Chou and Suarez, 1994) were used respectively. For the micro-physics, the WSM 5-class scheme was employed, while for the cumulus parametrization the Kain-Fritsch scheme was used (Skamarock *et al.*, 2008). Finally, the 4-layer Noah land-surface model (LSM) was applied (Chen and Dudhia, 2001; Ek *et al.*, 2003). Note that different layer thicknesses in the WRF model are applied for land surfaces and sea-ice surfaces (Figure 4.2).

Considering that the thermal coupling is relatively important in the SBL for calm wind regimes (e.g. Sterk *et al.*, 2013), the surface characteristics should be captured accurately. To improve on the dominating land-surface characteristics of the particular cases, we adjusted the threshold snow depth (*SNUP*, a threshold value in meter snow water equivalent, Ek *et al.*, 2003), which determines 100% snow cover, such that the modelled albedo matched the observed albedo. This is necessary because with standard WRF settings, the snow cover remained unrealistically low for grassland, while this remained unrealistically high for an evergreen needle-leaf forest for example. E.g. with the standard settings and 200 kg m^{-3} snow density (ρ_{snow}), 20 cm of snow is needed for a 100% snow cover over grass, while 40 cm of snow is sufficient to have 100% snow cover over forest (Ek *et al.*, 2003). In reality, though the ground will be totally covered with snow, trees will stick through this snow cover (see Figure 4.2). By adjusting *SNUP*, a more realistic snow cover and albedo were obtained.

For the Cabauw case, we altered the *SNUP* value from 0.04 to 0.005 m such that

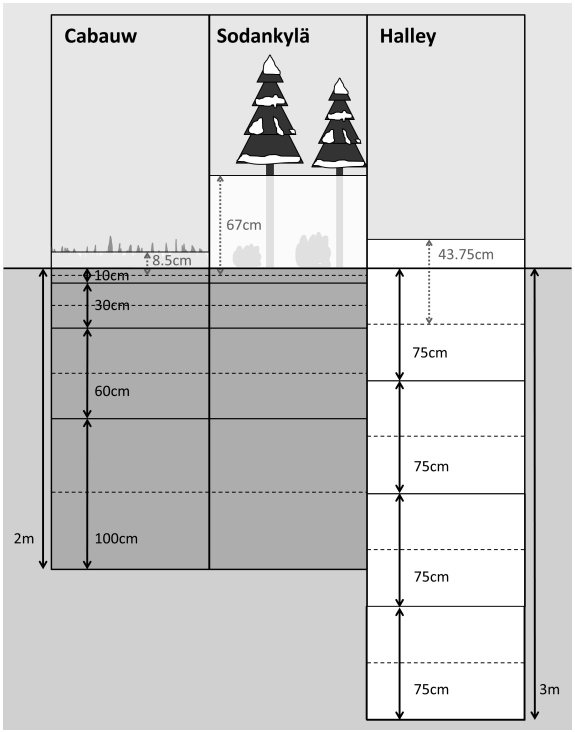

Figure 4.2: Illustration of the soil/ice layers in the Noah LSM for the three sites (not on scale). The black arrows indicate the standard thickness of the individual layers. The actual depth of this layer for which calculations are performed are indicated with the dashed lines. The grey dashed arrows indicate the top soil/ice layer when snow is present.

the resulting snow fraction obtained an albedo of around 0.63, as was observed. This *SNUP* value indicates that a snow layer of 5 cm is necessary to obtain 100% snow cover with a ρ_{snow} of about 100 kg m^{-3} which was indeed found in the 3D model with the fresh snow. The obtained snow cover was almost 80%. For the Sodankylä case study, the *SNUP* in 3D WRF was changed from 0.08 to 0.7 m which resulted in an albedo of $\sim$ 0.42 and a snow cover of $\sim$ 0.54. For the Halley case we could not retrieve the observed albedo due to the fact that the short wave radiation was absent during this part of winter. However, when sea ice is prescribed in the WRF-SCM runs, the snow cover is automatically set to 100%, so there was no need to change SNUP for this site.

Figure 4.3 shows the impact of the adjusted *SNUP* for both Cabauw (top figures) and Sodankylä (middle figures) for the WRF-3D runs in thick lines. For Cabauw, where the albedo with the old SNUP was about 0.3 with a snow cover of about 16%, there is a smaller isolating effect (larger snow-heat flux G) of the snow layer which results in higher 2 m temperature (T_{2m}) compared to the new SNUP run. For Sodankylä, with the old SNUP simulation, the albedo was about 0.67 with a snow cover of 98% (the maximum value with snow over land in WRF). This snow cover

is unrealistically high when trees are present, and results in too low T_{2m} during the day. During the night the old SNUP run actually is in better agreement with the observations regarding T_{2m} than the new SNUP run, though for the wrong reason due to the unrealistically high snow cover.

4.3.2 WRF-SCM

The WRF-SCM is based on the WRF-3D model and uses the same physics and dynamics. Again a vertically stretched σ coordinate was used for the vertical levels, but now 200 levels were applied, again with the highest resolution close to the surface, up to the model top at ≈ 12 km. We performed runs with similar physics as in WRF-3D, but did additional runs with different BL and long wave radiation schemes to test which scheme is more appropriate for the SBL modelling in the different case studies.

In addition to the MYJ-BL scheme, we applied the YSU-BL scheme (Hong *et al.*, 2006; Skamarock *et al.*, 2008; Hong, 2010) which is a first-order scheme (similar to Holtslag and Boville, 1993) where for stable conditions the eddy diffusivities are determined using the height, the boundary layer depth, and a velocity scale determined from the friction velocity and the stability function (Brost and Wyngaard, 1978; Troen and Mahrt, 1986). The YSU-BL scheme runs in conjunction with the MM5 surface-layer scheme (Skamarock *et al.*, 2008). Note that in the original WRF version 3.2.1 the stability function ϕ in YSU was erroneously implemented, and this was corrected in the WRF 3.2.1 version that we use (Sukanta Basu and Wayne Angevine, personal communications, summer 2012, see also Sterk *et al.*, 2013; Hu *et al.*, 2013). In this approach mixing is reduced, though there are indications that in some cases the modelled BL has now become too stable (Sun and Barros, 2013). Furthermore, the limitation on the friction velocity (u_*) of 0.1 m s^{-1} to keep the heat flux from going to zero in very stable conditions, has been lowered to 0.001 m s^{-1} following Jiménez *et al.* (2012).

In addition to the RRTMG LW radiation scheme, the GFDL and CAM schemes were used. The differences between the LW radiation schemes are mostly in the amount of bands that they use and the molecular species that they treat (see Skamarock *et al.*, 2008).

Also for the WRF-SCM runs, we altered the value of *SNUP* (see Section 4.3.1) for the Cabauw and Sodankylä cases. We did not use the same value as for the WRF-3D runs for the Cabauw case, because we applied a similar snow depth as was observed (3.5 cm) which is a bit more than was found in WRF-3D (2.7 cm). This was due to the fact that the system in 3D WRF was located more westerly ($\sim$ 50 km) than observed. We did use a similar ρ_{snow} of about 100 kg m^{-3} as was approximately modelled in WRF-3D (based on snow temperature and time, Ek *et al.*, 2003; Wang and Zeng, 2009) for the fresh snow at the start of the WRF-SCM study period. Then, with a *SNUP* of 0.006 m we obtained a similar albedo as observed, with a snow cover of around 0.83. Furthermore, for Cabauw the roughness length z_0 was adjusted from the grass/cropland value to the value of snow as used by WRF, i.e. 1 mm.

The new *SNUP* for Sodankylä amounted to 0.43 m resulting in a snow cover of 0.55. A ρ_{snow} of 200 kg m^{-3} was now used, as was modelled approximately with WRF-3D at the WRF-SCM starting time. WRF-3D modelled a higher snow depth

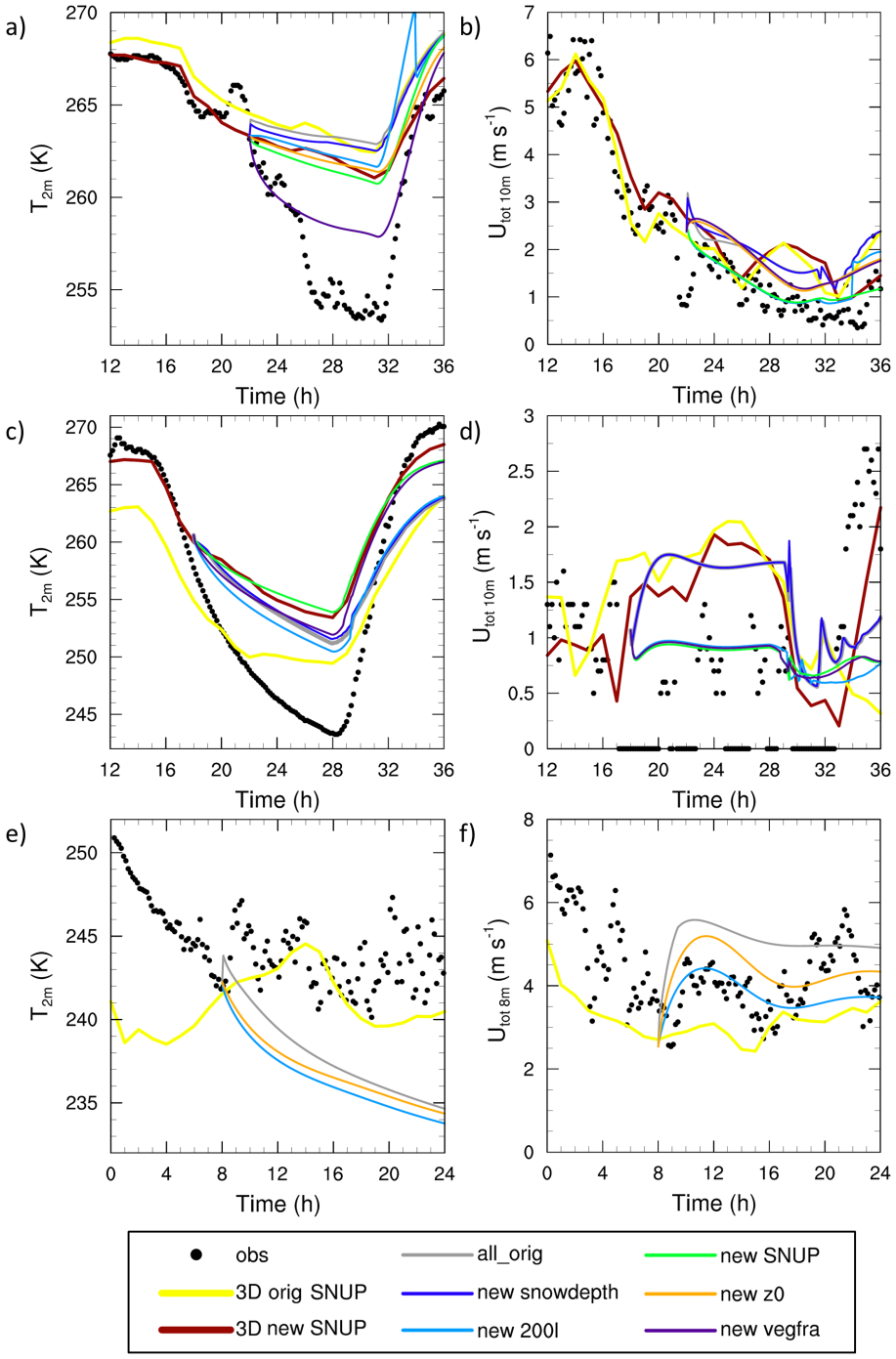

Figure 4.3: See next page.

(97 cm compared to the observed 62 cm), but this bias was already present at the start of the run and originated from the boundary conditions provided by the ECMWF. The z_0 for evergreen needleleaf forest remained unchanged (0.5 m), which is equal to the regional roughness length calculated for a 2 by 2 km area surrounding Sodankylä at the end of winter (Batchvarova *et al.*, 2001).

For the Halley case, also a ρ_{snow} of $\sim$ 200 kg m^{-3} was modelled, which was implied in the WRF-SCM as well. For z_0, the value of $5.6 \cdot 10^{-5}$ m was used as was measured at Halley for the momentum roughness length (King and Anderson, 1994).

Finally, we adjusted the vegetation fraction in the SCM. In WRF-3D this was only 27.8% at Cabauw, and 1% at Sodankylä. This vegetation fraction was determined from a spatially and monthly varying green vegetation fraction dataset determined with the satellite derived global fields, which is interpolated to the correct day (Gutman and Ignatov, 1998; Ek *et al.*, 2003). However, we lack confidence in these values, since they are unrealistically low for the studied sites. On the contrary, the ECMWF IFS applies a more realistic vegetation fraction of 0.85 for short grass, and 0.9 for crops and mixed farming. Therefore we used a vegetation fraction of 0.85 in the WRF-SCM runs for Cabauw. At Sodankylä, according to Batchvarova *et al.* (2001), about 49% of the surrounding land is coniferous and deciduous forest. Though the IFS of the ECMWF operational model applies a vegetation cover of 90% for evergreen needle-leaf trees (ECMWF, 2013), we decided to use 49% in the current SCM runs, following Batchvarova *et al.* (2001), representing the heterogeneous nature of the Sodankylä environment.

Figure 4.3 depicts the effects of all the above mentioned changes per step for the three sites. For the SCM no advection was prescribed, and the WRF-3D new SNUP run was used to determine the initial profiles (see Section 4.4, for Halley SNUP was not changed, so the WRF-3D with the original SNUP was used for the SCM forcings). The grey lines in Figure 4.3 give the model results when all original values are used: snow depth from WRF-3D, 60 vertical levels, original SNUP, original z_0, and the original WRF-3D vegetation fraction. Note that the other SCM runs have each time an additional (new) change, counting from top to bottom, left to right in the legend.

For Cabauw (Figure 4.3a and b) we find that the original SCM run is close to the WRF-3D runs, as the initial profiles from WRF-3D new SNUP were used, but with the original SNUP value. When the snow depth is increased to the observed value (dark blue line), G decreases, and T_{2m} decreases and comes closer to observations

Figure 4.3: *(Preceding page)* Time series for a,c,e) 2 m temperature T_{2m} (K), and b,d,f) 10/8 m wind speed $U_{tot\ 10/8m}$ (m s^{-1}) for the Cabauw (top figures), Sodankylä (middle figures) and Halley (bottom figures) cases. Time series are given for the observations (obs), the WRF-3D run with both original and new SNUP values, and the SCM runs with all original settings using the WRF-3D new SNUP run for the forcings (all_orig). For the other SCM runs every time a new adjustment is added, starting with renewed snow depth following observations (new snowdepth, not for Halley), additionally increasing the vertical levels from 60 to 200 (new 200l), additionally adjusting SNUP (new SNUP, not for Halley), additionally adjusting the roughness length (new z0, not for Sodankylä), and additionally adjusting the vegetation fraction (new vegfra, not for Halley). All SCM runs are without advection, only using the initial profiles from the WRF-3D run with new SNUP values. See also the text for further explanation.

while wind speeds increase slightly with the higher snow cover. When additionally the amount of vertical levels is increased from 60 to 200 (light blue line), T_{2m} decreases and improves even more (0.8 K lower at the end of the SCM study period (31h)), while additionally the 10 m wind ($U_{tot\ 10m}$) decreases and comes in close agreement with the observations. The sudden peak in T_{2m} just after sunrise (32h) is explained by moisture distribution in a thinner layer with the increased vertical resolution which then increases the incoming long wave radiation. The peak dissolves at 34h, likely due to the increased wind speed at that time. The next step is to adjust SNUP for a more realistic higher snow cover (green line). This again reduces G, and leads to an extra 1 K lower T_{2m} at 31h. When z_0 is adjusted to better fit a snow cover (orange line), T_{2m} increases somewhat (0.6 K), though a lower skin temperature (T_{skin}) is found and thus a stronger temperature gradient close to the surface. Unfortunately $U_{tot\ 10m}$ increases slightly (0.2 - 0.7 m s^{-1}) and is therefore less in agreement with observations due to a stronger decoupling effect with smaller friction velocity (u_*). The last modification of increasing the vegetation fraction (purple line), has a strong impact on the SCM simulations. Due to the stronger isolating effect of the vegetation and hence smaller G, T_{2m} decreases strongly (an additional 3.5 K compared to the orange line) and comes closer in agreement with the observations.

For Sodankylä (Figure 4.3c and d), at first sight the adjusted parameters do not improve the SCM simulations and the original run (grey line) regarding T_{2m} is one of the better SCM runs compared with observations (though still almost 8 K too high at the end of the SCM study period (27h)). However, this is due to the unrealistically high 98% snow cover. When now the snow depth is lowered to 62 cm which is observed (dark blue line), G increases and T_{2m} increases slightly further away from observations. When additionally the amount of vertical levels is increased (light blue line), as with Cabauw, T_{2m} decreases (an additional 1 K at 27h), and $U_{tot\ 10m}$ decreases and especially the latter resembles observations more. Still, the snow cover is unrealistically high. To decrease the snow cover, the threshold value SNUP that determines 100% snow cover must be increased (green line) (while this had to be decreased for Cabauw). The decreased snow cover causes an increased G and again a higher T_{2m} (3.2 K higher at 27h). Though this is now again further from observations, it does represent a more realistic snow surface for Sodankylä. As with Cabauw, an increase in vegetation (purple line) again has a positive effect on T_{2m}, as this decreases an extra 1.9 K at 27h with the smaller G and becomes more in agreement with observations.

Finally, for Halley (bottom figures) increasing the amount of levels leads to similar model behaviour as with the other cases: T_{2m} and $U_{tot\ 8m}$ decrease. Additionally lowering z_0 again increases T_{2m} and decreases T_{skin}, enhancing the temperature gradient at the surface, while with a smaller u_* which is closer to observations, $U_{tot\ 8m}$ increases as for Cabauw.

4.4 Methodology

This study emphasizes the evaluation of the WRF-SCM over a snow-covered surface for stable conditions. To compare SCM results with observations, we needed realistic input for the SCM. Studies often use a blend of observations and 3D model output to

make an independent estimate of the required forcings (Baas *et al.*, 2010; Bosveld *et al.*, 2014a). Complete measurements to retrieve the atmospheric state are not always available, and therefore we test whether the available set of WRF-3D fields provide reasonable forcings. Hence we will also evaluate one WRF-3D run per study case.

Regarding the SCM runs, we first performed a run without lateral forcings (set A). Next, we repeated the SCM runs where first only the geostrophic wind speed (U_g) changed in time (set B), secondly where advection of momentum was added to the forcings in set B, otherwise known as the horizontal dynamical tendency of momentum (set C), and thirdly advection of θ and q was included in addition to set C (set D). Furthermore, SCM runs were performed where a form of data-assimilation was applied above the BL height (set E). All time varying parameters were updated every hour. For an overview of the various forcings, see Table 4.2.

In this evaluation, we only used 3D model output with the new SNUP value for Cabauw and Sodankylä, and the output with standard SNUP for Halley (see Section 4.3.1) to determine the forcings. Hereto, the thermodynamic profiles were linearly interpolated to the levels which serve as input for the SCM runs. The temperature and moisture profiles in the soil layers were taken from the 3D output directly, though the snow depth was taken from the observations to ascertain that surface characteristics are in better agreement with observations compared to the modelled snow depth.

U_g is generally a good approximation to the actual wind speed above the BL in extra-tropical synoptic-scale disturbances (Stull, 1988; Holton, 2004). Therefore, above a threshold height, we defined U_g as the actual wind speed modelled with WRF-3D. Note that with $U_g = \frac{1}{\rho f}\left|\frac{dp}{dn}\right|$ approximately the same values were obtained. Below this threshold, the geostrophic wind speed was kept constant to the wind speed at the threshold height. The threshold height has to be higher than the modelled BL height and should also not be located in the nose of the low-level jet (LLJ) to avoid a too strong U_g close to the surface and therefore strong inertial oscillations. The BL height was determined following Troen and Mahrt (1986) when the bulk Richardson number reaches the critical value of 0.33 as used by Wetzel (1982)

Table 4.2: Overview of the particular forcing methods for the WRF-SCM runs.

Label	**BL scheme**	**LW$_{rad}$ scheme**	**Forcing**
A	MYJ	RRTMG	no lateral forcings
B	MYJ	RRTMG	varying U_g in time
C	MYJ	RRTMG	varying U_g in time + momentum adv.
D	MYJ	RRTMG	varying U_g in time + θ, q, momentum adv.
E	MYJ	RRTMG	force to WRF-3D field above threshold height
D + YSU	YSU	RRTMG	varying U_g in time + θ, q, momentum adv.
D + GFDL	MYJ	GFDL	varying U_g in time + θ, q, momentum adv.
D + CAM	MYJ	CAM	varying U_g in time + θ, q, momentum adv.

mainly for radiation dominated BLs (Vogelezang and Holtslag, 1996).

The advection prescribed in this study was determined by making use of the prognostic equations where we neglected the molecular diffusion terms and applied the Boussinesq approximations (Stull, 1988):

$$\frac{\partial \overline{\theta}}{\partial t} = -\overline{U_j}\frac{\partial \overline{\theta}}{\partial x_j} - \frac{1}{\overline{\rho} c_p}\frac{\partial \overline{Q_j^*}}{\partial x_j} - \frac{L_v E}{\overline{\rho} c_p} - \frac{\partial(\overline{U_j'\theta'})}{\partial x_j}\,, \tag{4.1}$$

$$\frac{\partial \overline{q}}{\partial t} = -\overline{U_j}\frac{\partial \overline{q}}{\partial x_j} + \frac{S_q}{\overline{\rho}} - \frac{\partial(\overline{U_j'q'})}{\partial x_j}\,, \tag{4.2}$$

$$\frac{\partial \overline{u}}{\partial t} = -\overline{U_j}\frac{\partial \overline{u}}{\partial x_j} - f_c(\overline{v_g} - \overline{v}) - \frac{\partial(\overline{U_j'u'})}{\partial x_j}\,, \tag{4.3}$$

$$\frac{\partial \overline{v}}{\partial t} = -\overline{U_j}\frac{\partial \overline{v}}{\partial x_j} + f_c(\overline{u_g} - \overline{u}) - \frac{\partial(\overline{U_j'v'})}{\partial x_j}\,, \tag{4.4}$$

where θ is the potential temperature, U_j represents the component of the wind speed vector in direction j, ρ the air density, c_p the specific heat for dry air, Q^* the net radiation, $L_v E$ the latent heat, q the specific humidity, S_q the net moisture source term for the remaining processes not already in the equation, u and v the u- and v-component of the wind speed respectively, f_c the Coriolis parameter and u_g and v_g the u- and v-components of the geostrophic wind speed respectively. The variables with a bar indicate a mean value, the variables with a prime indicate the turbulent fluctuation.

Here the term on the l.h.s. represents the tendency, the first term on the r.h.s. represents advection and the last term on the r.h.s. represents the turbulent flux divergence. The second and third term on the r.h.s. in equation 4.1 represent the radiative flux divergence and the change in temperature associated with latent heat release respectively. In equation 4.2, $S_q/\overline{\rho}$ is the net source term for extra moisture processes. The second term on the right for the u and v equations is the geostrophic departure and is a combination of the terms for the influence of the earth's rotation and the pressure gradient forces. Above the before mentioned threshold height this is equal to zero. Note that in stationary conditions, the advections are known to approximately balance the geostrophic departure term in the free atmosphere. Though in our case conditions are not stationary, it is clear that the u and v tendencies are very sensitive to all terms in the momentum equation, and hence to the way they are prescribed for the SCM simulations.

Here we determined the advection terms as a residual term from the other terms in the equation, using the WRF-3D results. We neglected the source term for additional moisture processes, because there was hardly any precipitation present (0.002 mm for Cabauw, 0.05 mm for Sodankylä and nothing for Halley in total for 9 h, as WRF-3D did in some hours simulate some clouds, see also the sections on the WRF-3D results). The tendencies at hour $\mathrm{T_n}$ were calculated based on 3D results 1h preceding ($\mathrm{T_{n-1}}$) and 1h following ($\mathrm{T_{n+1}}$) hour $\mathrm{T_n}$. For the other required terms on the r.h.s. we took the average of the preceding, the current and the following hour.

In the additional set E, a form of data-assimilation was applied above the BL

height. This was achieved by relaxing the SCM state above the BL towards a prescribed 3D state on the advection time scale (Ghan *et al.*, 1999; Rostkier-Edelstein and Hacker, 2010). In other words: the horizontal advective tendencies were obtained by the difference between the prescribed 3D field and the simulated SCM values over the advective time scale to nudge the SCM simulation towards the WRF-3D field. The relaxation was only applied from a certain height above the BL upwards to ascertain that the parametrizations in the BL are not affected. We used the same threshold height as for U_g mentioned above. We applied a smooth advective time scale profile to not stop the nudging at this height too abruptly. Above the threshold level this was a small advective time scale of 600s, while this increased tangentially to 10 days over a range of 250 m below this threshold level.

4.5 Results

This section describes the model results for the three case studies over different terrains. For each case, we first discuss the WRF-3D results that formed the basis for the WRF-SCM forcing files (with adjusted SNUP for Cabauw and Sodankylä). Hereafter the WRF-SCM results are evaluated for set A-E as well as the runs with different BL and LW radiation schemes.

4.5.1 Cabauw

WRF-3D

The WRF-3D model was started at 0 UTC on the 3$^{\text{rd}}$ of February, 2012. The first 12h were considered spin up time and are not shown here. The 3D run represented T_{2m}, $U_{tot\ 10m}$ and 2 m specific humidity (q_{2m}) well for the first 10 hours (see Figure 4.4). However, WRF-3D was unable to capture the strong T_{2m} drop after this time and remained too warm. Since wind speeds close to the surface were only slightly overestimated, we do not expect too large mixing due to excessive wind speeds to be the cause of this temperature bias. The WRF-3D runs did simulate some clouds at 24 and 25h at around 400 - 800 m, however, we did not see an increase in the long wave downward radiation ($LW\downarrow$), which therefore may also not explain the warm bias at the surface. Furthermore, $LW\downarrow$ was actually underestimated by $\sim$ 3 - 28 W m^{-2} during the SCM study period with WRF-3D. Note that the estimated accuracy of the measured $LW\downarrow$ is $\sim$ 4 W m^{-2} (Vihma *et al.*, 2009), though errors can be larger when frost, snow, rain, or liquid condensate is present on the domes. Temperatures at 200 m deviated at most 1 K from the observations and the wind speed variations at this same height were followed nicely as well though slightly underestimated by 2 m s^{-1} at the end of the night (not shown).

Concerning u_*, WRF-3D followed the available data rather well, but with an underestimation of about 0.05 - 0.1 m s^{-1}. The values were rather small which is typical during calm winds. The wind speed profiles were simulated reasonably well at most time steps (Figure 4.5). This also held for θ, but after 22h only for the higher tower levels because WRF-3D failed in reproducing the observed strong inversion.

The WRF-3D model produced a snowfall pattern that was located to the west (about 50 km) of the observed pattern which showed a band of snow fall with a maximum depth generally in north-south direction over the middle of the Netherlands.

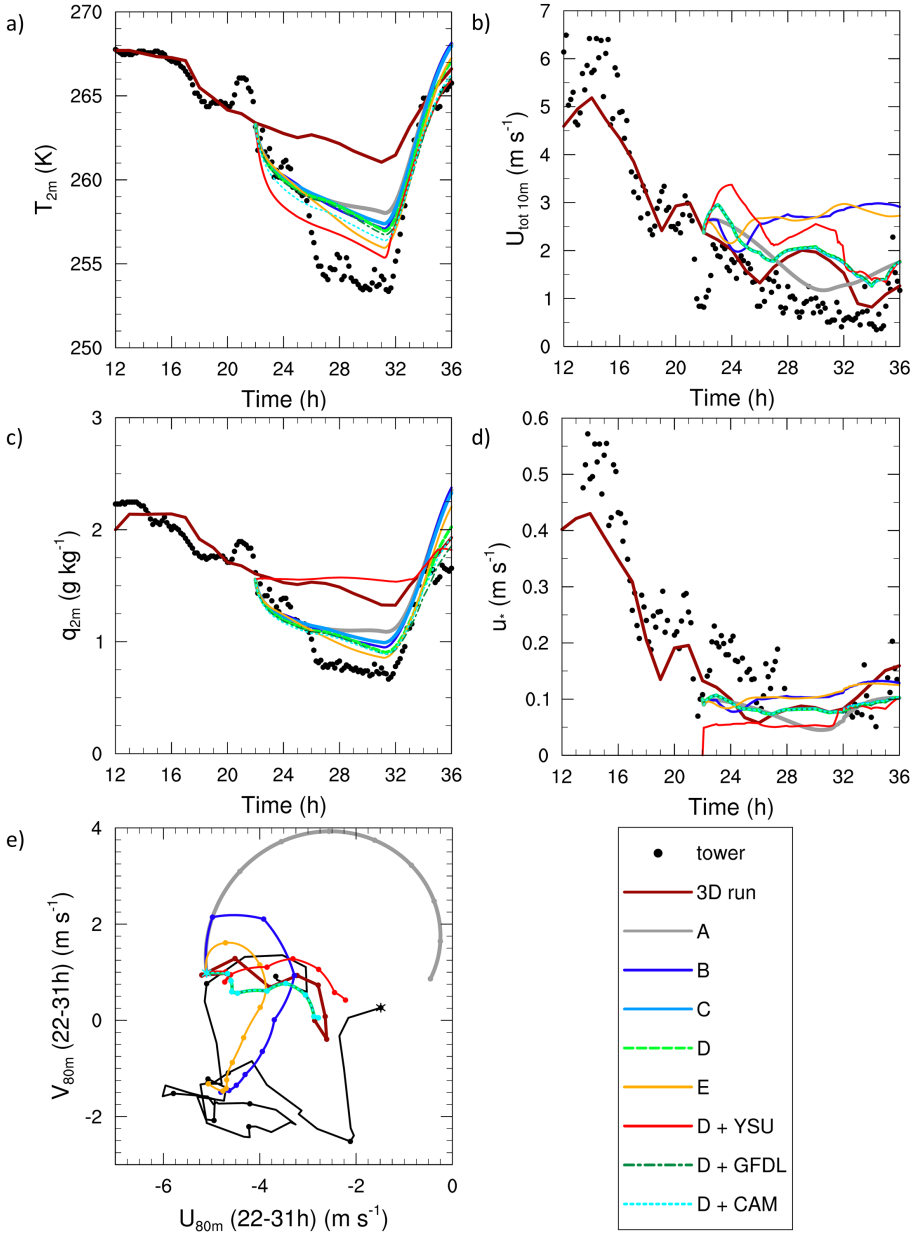

Figure 4.4: See next page

This partly explained the smaller snowfall than was observed at Cabauw (2.7 cm vs 3.5 cm), which affected the simulation of the near surface temperature.

The BL modelled with WRF-3D was very shallow and always below 100 m for the SCM research period between 22-31h. However, the threshold height to determine U_g should not only be above the BL, but also sufficiently high above the LLJ to not generate a unrealistic inertial oscillation when using this wind speed as U_g for the underlying model levels. A threshold depth of 400 m nicely fulfilled the criteria. The observed surface U_g (Section 4.2.1, Table 4.1) is in good agreement with this derived U_g, thus supporting this method.

WRF-SCM

Here, results of our WRF-SCM experiments formulated in sets A-E are presented, followed by the experiment results with other BL and radiation schemes. All runs are with the snow depth as observed, 200 vertical levels, adjusted SNUP and z_0 and increased vegetation fraction (Section 4.3.2). The runs were started at 22h, when the situation became cloud free, which is beneficial for the development of a very stable BL. Since we are mostly interested in the model performance during the stable conditions, we will evaluate the WRF-SCM performance between 22 and 31h (7UTC in the morning, just before sunrise).

The time series and vertical profiles after 31h (the end of the night) in Figure 4.4 and 4.5 for the different forcing methods are indicated with set A-E. The same parametrization schemes as in the WRF-3D run were used. Clearly, the 3D and SCM runs differ substantially for T_{2m} and q_{2m}. Mostly this was explained by the underlying medium and not as much the atmospheric forcings, as was explained in Section 4.3.2. Due to the stronger and more realistic insulating effect accompanying the increased vegetation fraction, all these runs simulated a colder T_{2m} than WRF-3D, and closer to the observed T_{2m}, though the WRF-SCM was unable to capture the strong temperature drop around 26h.

The differences for the T_{2m} simulations between sets A-E were rather small. Better results for T_{2m} were obtained when temperature and moisture advection were included (set D), decreasing the bias with about 1 K at 31h compared to neglected advection (set A), while for the higher levels, a slightly higher θ was simulated (up to about 0.5 K at 200 m), decreasing the bias here as well. Therefore, with set D, larger θ gradients were modelled. The temperature profiles showed that a varying U_g in time (set B) as well as momentum advection (set C) did not influence the temperature profile substantially. Interesting also, was the profile of set E where the profile above 400 m was nudged towards the WRF-3D field. Indeed the higher levels

Figure 4.4: *(Preceding page)* Time series for the Cabauw case for a) 2 m temperature T_{2m} (K), b) 10 m wind speed $U_{tot\ 10m}$ (m s^{-1}), c) 2 m specific humidity q_{2m} (g kg^{-1}), d) friction velocity u_* (m s^{-1}), and e) the hodograph at 80 m (wind speeds in m s^{-1}), where the asterisk indicates the time of the start of the WRF-SCM simulations (22h). As the measurements are performed every 10 minutes, the SCM output is provided every 5 minutes, and the WRF-3D output is provided hourly, only the full hours since the starting time are indicated with the dots to show the progression in time. Time series are given for the observations (obs), the WRF-3D run (3D run), the WRF-SCM simulations for the different forcing methods (set A-E), WRF-SCM with YSU-BL scheme (D + YSU), and with various LW radiation schemes (D + GFDL, and D + CAM).

followed the WRF-3D profiles, but this also influenced the profile below 400 m, where it appeared that the cold air could not be transported upwards and was therefore captured in the layer below, resulting in a stronger capping inversion just below 400 m which was not seen in the other runs. This trapping indeed appears to be caused by the nudging, as with an altered threshold height a similar model behaviour was found just below the altered threshold height (not shown).

The 10 m wind speed, $U_{tot\ 10m}$, was modelled reasonably well, especially for set A. However at higher levels the run went immediately through an inertial oscillation that disagreed with the higher level tower observations. This was especially clear with the hodograph at 80 m (Figure 4.4e), which was approximately the LLJ altitude of the observations, but also at other levels. Also when U_g only was altered in time (set B), the modelled wind speed profiles deviated a lot from reality, especially in the first few hours, though better agreement was found at hour 28-30. This also follows

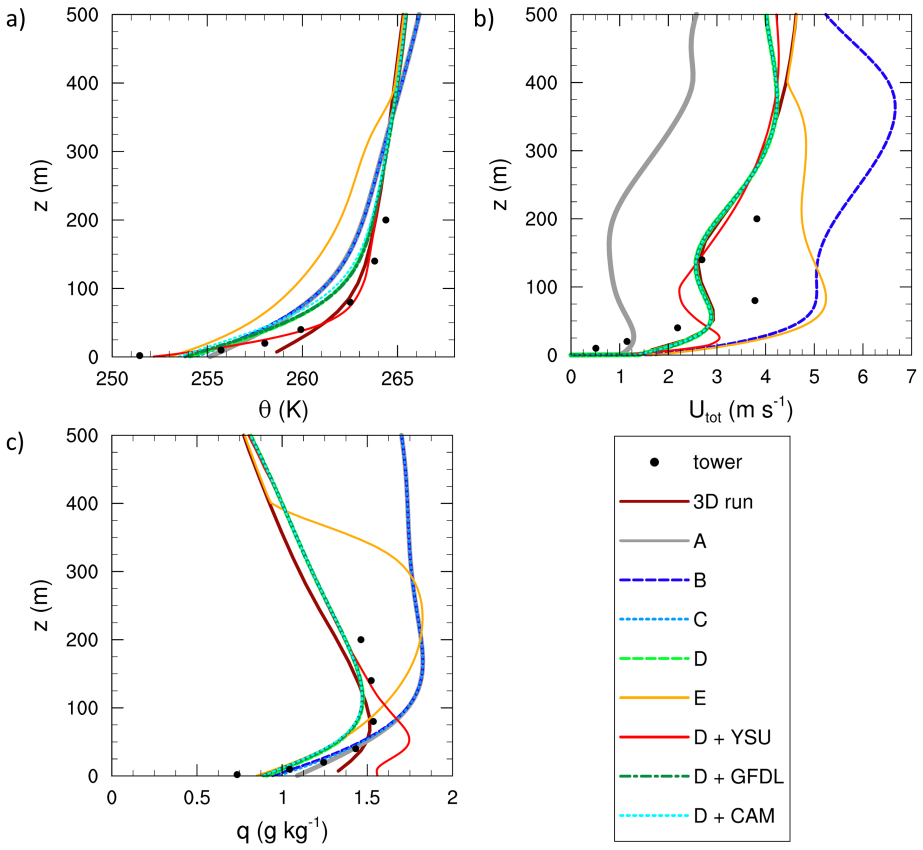

Figure 4.5: Vertical profiles for the Cabauw case at 31h, after 9h of WRF-SCM simulation, for a) the potential temperature θ (K), b) the total wind speed U_{tot} (m s^{-1}), and c) the specific humidity q (g kg^{-1}). (For an explanation of the legend, see Figure 4.4.)

from the reduced mean bias error at 200 m (Table 4.3), though the biases increase at 10 m. Even further improvements were found when momentum advection was included as well (set C-D) when compared to set A, biased were halved at 200 m. After 27h, $U_{tot\ 10m}$ remained slightly too high for sets C-D, though with $\sim$ 1.1 m s^{-1} this was reduced compared to $\sim$ 2-2.7 m s^{-1} of set B. Note that the set C and D runs overlapped mostly for the wind speed simulations, indicating that θ and q advection did not really influence the wind simulations in this case. This was confirmed by the wind speed profile at 31h (and other hours, not shown here). These profiles also indicated that the momentum advection was very important in modelling the correct wind speed, though we must keep in mind that the LLJ is a dynamical phenomenon and hence simulations and observations may be in a different phase at the time of the profile. However, studying the profiles at other hours by eye indicated that overall the sets with momentum advection were giving better wind speed profiles (not shown). From the hodograph in Figure 4.4e we find that the observations do follow some inertial oscillation at 80 m. As mentioned before, this also holds for set A, though this is not at the correct magnitude. Set B and set E also go through an oscillation. This is not as clear for the runs with prescribed momentum advection which more follow the WRF-3D results at 80 m, which shows that the model is very sensitive to the advection term in eqs. 4.3 and 4.4. The oscillation is more clear with set C-D at other levels. Finally, with set E, also for wind speed, the nudging above the 400 m threshold level is felt by the underlying air, where an oscillation occurred right below this threshold height, possibly due to that this layer could not transport its momentum upwards properly.

An analogous effect was found for the specific humidity (q) profiles (Figure 4.5), where with set E, the SCM was forced to a state with less q above 400 m, while in this way the moisture was kept in the layer below this height. The runs without any moisture advection corresponded with the tower data up to the 80 m level, though above that they remained too humid. With set D, the surface specific humidity was simulated better, but the run became somewhat too dry at the higher levels up to 80 m, though the bias was decreased compared to sets A-C for the even higher tower levels.

Regarding u_*, the WRF-SCM simulations resembled those modelled by WRF-3D during the night. Values were a bit lower than observed at the start of the run, and in the lower range of what was observed after sunrise.

In summary, when we compare the runs with different forcings for this case over snow-covered grass in Cabauw for low wind speeds, it appeared that some form of advection is important. Without any advection, or only changing U_g in time, the runs deviate strongly from the observations and the WRF-3D field (though the latter is not free from errors either). This appeared to be very important for wind speed. Due to the fact that this was a low wind speed case, turbulence is relatively weak and thus the turbulent flux divergence becomes relatively small and the other terms in eqs. 4.1-4.4 become relatively more important (Savijärvi, 2006, 2013). Also when we compare the radiative flux divergence to the turbulent flux divergence in equation 4.1 for set D, we find for Cabauw close to the surface a turbulent flux divergence varying from -0.4 K h^{-1} at the first hour to 0.3 K h^{-1} at the end of the night, while the radiative flux divergence has a more continuous value of $\sim$ -0.85 K h^{-1}, indicating

Table 4.3: Mean bias error (MBE), root mean square error (RMSE) and median of the absolute error between model simulations and observations, for the period of 22h - 31h, for the Cabauw case for variables: 2 and 200 m temperature in K (T_{2m} and T_{200m}), 10 and 200 m wind speed in m s^{-1} ($U_{tot\ 10m}$ and $U_{tot\ 200m}$), 2 and 200 m specific humidity in g kg^{-1} (q_{2m} and q_{200m}), sensible (H), and soil heat flux (G) in W m^{-2}, net radiation in W m^{-2} (Q_{net}), and downward ($LW\downarrow$) and upward ($LW\uparrow$) long wave radiation in W m^{-2}. Note for H this is only 22h - 26h due to erroneous measurements at later times. Measurements for L_vE were faulty for the entire period, and therefore errors are omitted here. Numbers in red are for the run with the smallest bias between runs with various forcing methods (set A-D), in bold for the run with lowest bias between all WRF-SCM runs (based on multiple decimals). Note that set E is omitted here, due to the non-physical behaviour below the threshold-height for the relaxation towards the 3D field.

		A	**B**	**C**	**D**	**D + YSU**	**D + GFDL**	**D + CAM**
MBE	T_{2m}	2.3	2.0	2.1	2.0	**0.4**	1.9	1.4
	T_{200m}	−0.6	−0.6	−0.6	−0.3	**−0.3**	−0.3	−0.4
	M_{10m}	**0.7**	1.3	0.9	0.9	1.4	0.9	0.9
	M_{200m}	−1.7	−0.9	−0.8	−0.8	**−0.7**	−0.8	−0.8
	q_{2m}	0.16	0.12	0.14	0.10	0.56	0.09	**0.08**
	q_{200m}	0.18	0.18	0.18	0.05	**0.05**	0.05	0.05
	H	−16.4	−16.2	−16.4	−16.4	**−5.8**	−16.9	−16.5
	G	−25.4	**−24.4**	−24.7	−25.6	−28.2	−26.3	−26.8
	$Qnet$	−28.1	−29.4	−29.0	−30.2	**−26.9**	−31.7	−31.2
	$LW\downarrow$	**−16.5**	−16.7	−16.6	−18.9	−19.1	−21.4	−21.6
	$LW\uparrow$	11.6	12.7	12.4	11.3	**7.7**	10.3	9.5
RMSE	T_{2m}	3.2	2.8	3.0	2.9	**2.0**	2.7	2.4
	T_{200m}	0.8	0.8	0.8	0.5	**0.4**	0.5	0.5
	M_{10m}	**0.7**	1.4	1.0	1.0	1.4	1.0	1.0
	M_{200m}	1.9	2.1	1.0	1.0	**0.9**	1.0	1.0
	q_{2m}	0.26	0.20	0.23	0.20	0.62	0.19	**0.19**
	q_{200m}	0.20	0.20	0.20	0.10	**0.10**	0.10	0.10
	H	16.9	16.7	16.9	16.9	**6.9**	17.5	17.0
	G	25.4	**24.4**	24.8	25.6	28.2	26.4	26.9
	$Qnet$	28.5	29.7	29.3	30.6	**27.3**	32.0	31.5
	$LW\downarrow$	**17.6**	17.8	17.7	19.8	20.0	22.2	22.4
	$LW\uparrow$	12.2	13.5	13.1	12.0	**8.8**	11.1	10.4
median	T_{2m}	3.2	2.7	2.9	2.8	**1.9**	2.6	2.2
	T_{200m}	0.7	0.7	0.7	0.5	**0.4**	0.5	0.5
	M_{10m}	**0.6**	1.4	1.0	1.0	1.4	1.0	1.0
	M_{200m}	1.8	1.3	0.9	0.9	**0.8**	0.9	0.9
	q_{2m}	0.29	0.21	0.24	0.21	0.74	0.20	**0.20**
	q_{200m}	0.16	0.16	0.16	0.09	**0.09**	0.09	0.09
	H	17.7	16.9	17.8	17.8	**6.5**	18.3	17.7
	G	25.9	**24.4**	24.8	26.0	27.9	26.8	27.2
	$Qnet$	27.6	29.2	28.5	29.7	**26.2**	30.9	30.4
	$LW\downarrow$	**16.4**	16.7	16.7	18.4	18.4	21.1	21.1
	$LW\uparrow$	12.6	13.8	13.7	12.5	**8.9**	11.5	10.7

the importance of the radiative processes at these low wind speeds (Savijärvi, 2006, 2013). As found in Tjemkes and Duynkerke (1989), the turbulent flux divergence can be positive. This is due to that turbulence has to warm the layer close to the surface when the radiative cooling is much larger than the total cooling rate in the BL. Indeed at higher levels, negative values for both components are found. The advection is rather small close to the surface, but becomes relatively more important higher up. Moreover, we confirm that the moisture advection was very important as well, therefore we recommend to apply advection for all variables, e.g. θ, q, and momentum.

The SCM runs were repeated with the revised YSU-BL scheme (Section 4.3.2). We performed the runs with all permutations (set A-E) as with the MYJ-BL scheme, however, the results for the 5 sets were similar to what we saw earlier. Thus we only show the YSU run with changing U_g and momentum, q and θ advection here (set D + YSU).

The T_{2m} is also simulated rather well with YSU, even lower temperatures were reached compared with MYJ. This increased the bias before 26h and decreased the bias after this time. The stratification was represented better with a stronger exponential, or concave up, shaped profile (though this was too strong at the start of the run (not shown here)). This is interesting since $U_{tot\ 10m}$ was overestimated more than with MYJ and it could be expected that this excessive wind speed mixes the BL more efficiently, leading to a weaker stratification. The LLJ was located at a lower altitude than with MYJ, and too low compared to observations, though the observed S-shape in the wind speed profiles was simulated as well (also with MYJ, this S-shape vanished an hour later). Also u_* was somewhat lower compared to the other SCM runs, hinting at a possible decoupling effect. The magnitude of the sensible heat flux (H) decreased strongly compared to the MYJ runs, and was closer to the observations which also followed from the reduced bias (Table 4.3). Possibly the simulation was in the very stable regime where H decreases with an increasing stratification close to the surface (Holtslag *et al.*, 2007), which would again indicate a decoupling effect between the BL and the surface. Then the weaker turbulence would lead to a reduced momentum loss to the surface, explaining the too high wind speeds (Rinke *et al.*, 2012).

The latent heat flux (L_vE) towards the surface on the other hand increased compared to the other SCM runs (around -10 compared to -5 W m^{-2}). This is explained by the larger amount of atmospheric moisture present within YSU, as was also found in the q profile and q_{2m} time series for which it is seen that a humidity inversion does not really develop. Since q above $\sim$ 170 m was equal to q in set D, it is unlikely that this enhanced amount of q below this level for YSU is due to entrainment from higher levels. Since a clear temperature inversion does develop, a similar behaviour would be expected for humidity because the exchange coefficients in the surface layer and the eddy diffusivities in the boundary layer are the same for both heat and humidity. This will be investigated in a future study.

The increase in L_vE with YSU was likely due to the increased wind speeds close to the surface in combination with the larger moisture gradient between the surface and the 2 m level. The conductive heat flux (G) was a bit stronger at the start of the run ($\sim$ -36 W m^{-2} with YSU compared to $\sim$ -30 W m^{-2} with MYJ) due to the

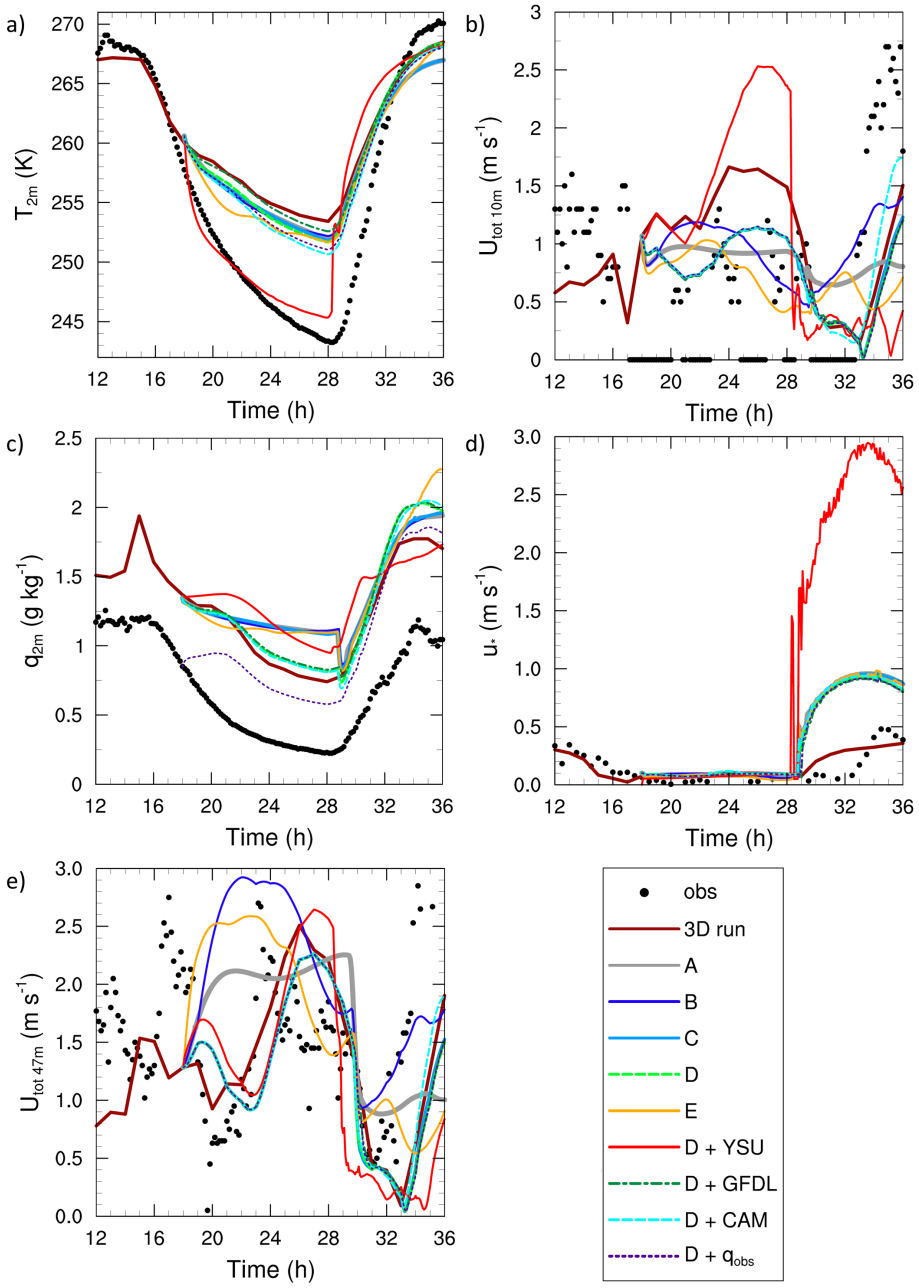

Figure 4.6: See next page

lower T_{skin} and comparable to the other SCM runs from 26h onwards.

Regarding the LW radiation schemes, both GFDL and CAM improved on the simulation of T_{2m} and q_{2m} by decreasing these values. However, this also resulted in slightly lower values higher up, increasing the biases there (only slightly). Unfortunately, the LW downward radiation ($LW\downarrow$) that was already underestimated, was now underestimated even more (Table 4.3). Therefore it appears that RRTMG performed best here. Similar results were seen for different LW radiation schemes in combination with YSU (not shown). Varying the radiation scheme did not seem to affect the wind field.

Overall, as long as the forcings are prescribed properly, both the MYJ and YSU-BL schemes perform reasonably well in simulating the SBL for this case over snow covered grass. With YSU the θ profiles are better forecasted than with MYJ, while with MYJ better wind profiles can be simulated. In a companion paper, we perform a sensitivity analysis to study if we can obtain similar improvements by adjusting the intensity of some of the governing processes in the SBL. Varying the LW radiation schemes led to smaller differences between the simulations, but RRTMG seems the better LW radiation scheme in that it underestimates $LW\downarrow$ the least.

4.5.2 Sodankylä

WRF-3D

The WRF-3D model was started at 0 UTC on the 26th of March, 2009. The 3D run performed very well for the first few hours (after the 12h spin-up period) regarding T_{2m} and $U_{tot\ 10m}$ (Figure 4.6), but as for the Cabauw case, it remained too warm when the sun set. At this time also the observed $U_{tot\ 10m}$ vanished which was not captured by WRF-3D, though the modelled wind speed was mostly below 1.3 m s^{-1}. Compared with sounding observations at 0UTC on the 27th of March (6h into the SCM simulation, Figure 4.7), near surface temperatures remained too high, with strongest biases close to the surface, and temperatures above 60 m were too low. This underlines that, as with Cabauw, the stratification was not strong enough. The LLJ was modelled at about the correct height at this time and with only a slightly lower magnitude, later the LLJ was located a bit too high with slightly stronger wind speeds than observed ($\sim$ 0.5 m s^{-1} too high). WRF-3D followed the sounding data above 100 m nicely for wind speed and was in good agreement with the tower data, though it missed the observed vanished winds at the lowest tower level.

The warm bias during night time could be partly explained by the overestimated q (Figures 4.6c and 4.7c). Though q was also overestimated before night time, the bias increased somewhat during the night. This also resulted in an overestimated

Figure 4.6: *(Preceding page)* Time series for the Sodankylä case for a) 2 m temperature T_{2m} (K), b) 10 m wind speed $U_{tot\ 10m}$ (m s^{-1}), c) 2 m specific humidity q_{2m} (g kg^{-1}), d) friction velocity u_* (m s^{-1}), and e) 47 m wind speed $U_{tot\ 47m}$ (m s^{-1}). Time series are given for the observations (obs), the WRF-3D run (3D run), the WRF-SCM simulations for the different forcing methods (set A-E), the WRF-SCM simulation with initial specific humidity profile based on observations (D + q_{obs}), WRF-SCM with YSU-BL scheme (D + YSU), and with various LW radiation schemes (D + GFDL, and D + CAM).

$LW\downarrow$ ($\sim$ 1.5 W m^{-2} at the start till $\sim$ 7 W m^{-2} at the end of the SCM study period), while for Cabauw this was underestimated. This overestimated $LW\downarrow$ can also be related to low clouds that were modelled for the lowest model levels for 20 - 23 UTC, and 2 UTC the next day. For other time steps the cloud fraction was 0 or below a fraction of 0.1. We see a slight increase in $LW\downarrow$ at 20h, but this decreases again right after that. However, for clear skies, $LW\downarrow$ was also overestimated ($\sim$ 1.5 - 5 W m^{-2} in the 6 hours prior to the SCM study period), making it unlikely that the present clouds are the main contributor to the overestimated temperatures close to the surface, as these were modelled better in the 6h prior to the SCM study (Figure 4.6a).

The BL was very shallow during the night as the critical Richardson number was already reached below the first model level. The friction velocity u_* was around 0.1 m s^{-1}, and slightly higher than the available measurements. As a threshold height for U_g for the SCM runs, the 300 m height was chosen, which is located sufficiently above the LLJ and the BL height.

WRF-SCM

Next, WRF-SCM results are presented for the Sodankylä case for sets A-E and the runs with different BL and radiation schemes (Figures 4.6 and 4.7). All runs are with the snow depth as observed, 200 vertical levels, adjusted SNUP and increased vegetation fraction (see Section 4.3.2). The period of interest was from 18UTC on the 26th of March 2009, which was the first hour after sunset, until 3UTC (27h) the next day which was just before sunrise. During this time stable conditions were observed along the tower.

T_{2m} modelled with the WRF-SCM was improved compared with WRF-3D by a few K, depending on the forcings, resulting in a stronger θ gradient. Differences between sets A-D were small close to the surface, though higher up in the θ profile slightly lower temperatures ($\sim$ 0.7 K at 60 m) were found for set D compared to sets A-C. Even better T_{2m} was obtained with set E, however, the artificial inversion below the threshold height of 300 m was again present as with the Cabauw case, though less strong.

For wind again differences close to the surface were small (Figure 4.6b), though now large differences between the sets were found at higher levels (Figure 4.6e, 4.7b). As for Cabauw, prescribing advection strongly impacts the simulated wind speed. Regarding the profiles in Figure 4.7b at 0UTC, results from sets C-D were in better agreement with the sounding data compared to sets A-B. At least between 100 and 400 m the biases between set C-D and observations were within 0.25 m s^{-1}, while this was up to 1.2 m s^{-1} for set A, and up to even 2.5 m s^{-1} for set B, supporting that prescribing proper momentum advection was necessary. At this particular time, sets C-D underestimate the higher level tower data compared to the other sets, though the general bias over 9h at 47 m decreases somewhat (Table 4.4) and indeed a better agreement with the tower data for sets C-D is seen at other times (not shown).

For Sodankylä, information about the wind direction and thus on the wind components was unavailable for the tower levels. To evaluate the model skills for higher level wind speeds, the 47 m wind speed ($U_{tot\ 47m}$) time series are shown in Figure 4.6e instead of the hodograph. This figure also indicates that prescribing momentum

advection was beneficial for the WRF-SCM simulation, especially for the first hours of the simulation, which already followed from the decreased biases between model runs and observations at 47 m (Table 4.4).

Part of the explanation for the overestimated temperature is the overestimated q, as already found with WRF-3D. Interesting is that lower temperatures were found with WRF-SCM compared to WRF-3D, but that q was overestimated even more. This lower temperature could be explained by the smaller G found with the WRF-SCM compared to WRF-3D due to the adjusted surface characteristics, such that heat was less easily transported from the deeper soil layers to the surface. Prescribing moisture advection was beneficial for q_{2m} and the q profiles compared to not prescribing this.

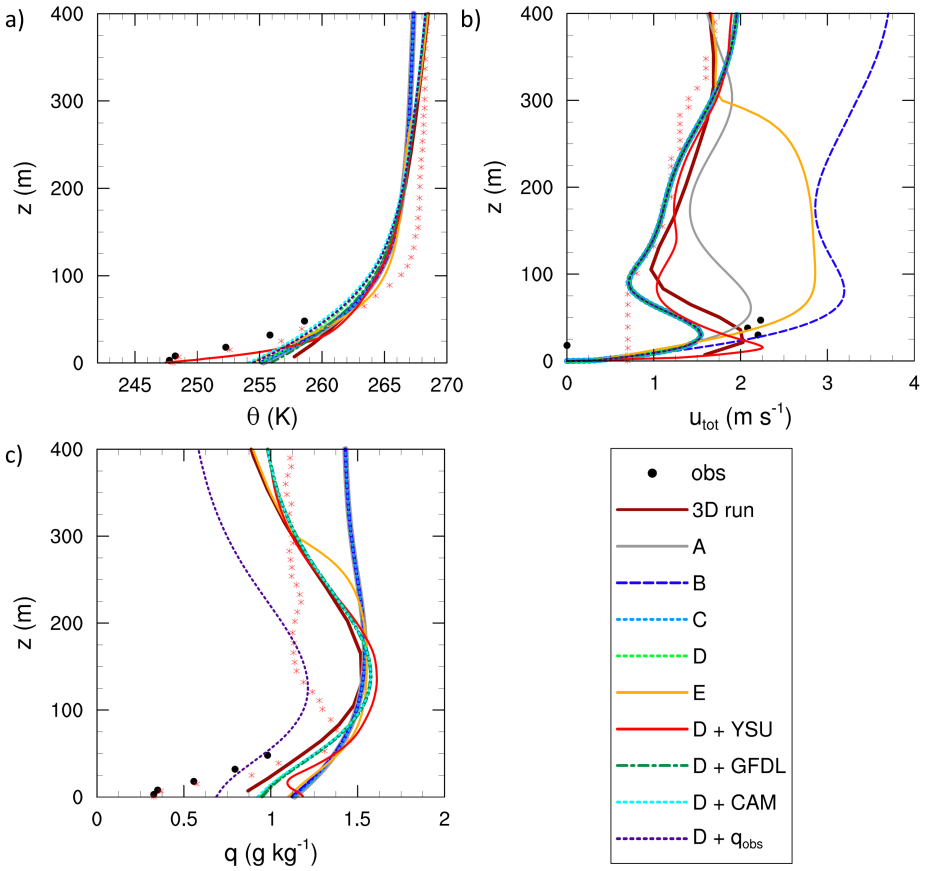

Figure 4.7: Vertical profiles for the Sodankylä case at 0UTC, 6h into the WRF-SCM simulation when sounding data was available, for a) the potential temperature θ (K), b) the total wind speed U_{tot} (m s^{-1}), and c) the specific humidity q (g kg^{-1}). (For an explanation of the legend, see Figure 4.6, sounding data is indicated with the red asterisks.)

Table 4.4: Mean bias error (MBE), root mean square error (RMSE) and median of the absolute error between model simulations and observations, for the period of 18h - 27h, for the Sodankylä case for variables: 2 and 48 m temperature in K (T_{2m} and T_{48m}), 10 and 47 m wind speed in m s^{-1} ($U_{tot\ 10m}$ and $U_{tot\ 47m}$), 2 and 48 m specific humidity in g kg^{-1} (q_{2m} and q_{48m}), sensible (H), latent ($L_v E$) and soil heat flux (G) in W m^{-2}, net radiation in W m^{-2} (Q_{net}), and downward ($LW\downarrow$) and upward ($LW\uparrow$) long wave radiation in W m^{-2}. Numbers in red are for the run with the smallest bias between runs with various forcing methods (set A-D), in bold for the run with lowest bias between all WRF-SCM runs (based on multiple decimals, D + q_{obs} is not included). Note that set E is omitted here, due to the non-physical behaviour below the threshold-height for the relaxation towards the 3D field.

		A	**B**	**C**	**D**	**D + q_{obs}**	**D + YSU**	**D + GFDL**	**D + CAM**
MBE	T_{2m}	6.4	6.3	6.4	6.4	5.9	**0.2**	7.1	5.7
	T_{48m}	0.7	0.7	0.7	**0.1**	−0.1	1.1	0.4	−0.3
	$U_{tot\ 10m}$	0.6	0.7	0.6	0.6	0.6	1.4	**0.6**	0.6
	$U_{tot\ 47m}$	0.6	1.1	0.1	0.1	0.1	0.2	**0.1**	0.1
	q_{2m}	0.75	0.74	0.75	0.64	0.36	0.81	0.65	**0.63**
	q_{48m}	−3.45	−3.45	−3.45	−3.51	−3.80	**−3.44**	−3.51	−3.52
	H	−16.7	−17.0	−16.8	−16.8	−18.0	**−13.8**	−15.8	−17.4
	$L_v E$	−2.1	−2.1	−2.1	−1.9	−1.4	−5.8	**−1.8**	−2.0
	G	−1.0	−1.0	−1.0	−1.0	−1.7	−1.5	**−0.2**	−1.5
	$Qnet$	18.1	17.8	18.0	18.2	16.5	18.2	20.4	**16.9**
	$LW\downarrow$	4.3	4.2	4.3	4.5	−1.1	1.9	11.5	**0.5**
	$LW\uparrow$	−12.6	−12.5	−12.5	−12.6	−16.5	−15.1	**−7.7**	−15.3
RMSE	T_{2m}	6.6	6.5	6.6	6.6	6.1	**1.1**	7.4	5.8
	T_{48m}	2.0	1.9	2.0	1.7	1.6	2.3	1.9	**1.5**
	$U_{tot\ 10m}$	**0.8**	0.9	0.8	0.8	0.8	1.5	0.8	0.8
	$U_{tot\ 47m}$	0.9	1.4	0.7	0.7	0.7	0.8	**0.7**	0.7
	q_{2m}	0.76	0.75	0.76	0.64	0.37	0.82	0.66	**0.64**
	q_{48m}	3.66	3.66	3.66	3.68	3.95	**3.62**	3.68	3.69
	H	16.9	17.2	17.0	17.0	18.2	**14.3**	16.0	17.7
	$L_v E$	2.1	2.2	2.2	1.9	1.5	5.8	**1.8**	2.0
	G	4.2	4.2	4.3	4.2	4.3	4.1	**4.0**	4.3
	$Qnet$	19.2	18.9	19.2	19.4	17.8	19.2	21.7	**18.2**
	$LW\downarrow$	4.5	4.4	4.5	4.6	1.6	2.1	11.6	**1.1**
	$LW\uparrow$	14.7	14.5	14.8	14.5	17.9	16.3	**10.2**	16.9
median	T_{2m}	6.8	6.6	6.9	7.0	6.6	**0.9**	7.9	6.2
	T_{48m}	1.7	1.7	1.8	1.4	1.3	2.3	1.7	**1.2**
	$U_{tot\ 10m}$	0.9	0.9	0.7	0.7	0.8	1.2	**0.7**	0.7
	$U_{tot\ 47m}$	0.7	1.1	0.6	0.6	0.6	**0.5**	0.6	0.6
	q_{2m}	0.80	0.79	0.81	0.62	0.37	0.83	0.64	**0.62**
	q_{48m}	3.27	3.28	3.27	3.33	3.62	**3.23**	3.32	3.33
	H	16.3	17.1	16.5	16.5	17.7	**13.1**	15.5	17.5
	$L_v E$	2.2	2.2	2.2	1.9	1.5	5.8	**1.8**	2.0
	G	3.0	3.0	3.1	3.0	2.8	**2.8**	3.2	2.8
	$Qnet$	16.6	16.0	16.8	16.7	15.1	16.6	18.9	**15.8**
	$LW\downarrow$	4.4	4.3	4.4	4.8	0.7	2.0	11.5	**1.0**
	$LW\uparrow$	10.6	10.1	10.7	10.9	14.8	13.6	**5.8**	13.9

Interestingly, $LW\downarrow$ was not too far off with an MBE of $\sim$ 4.3 W m^{-2} (slightly overestimated, for Cabauw this was underestimated), even though q was strongly overestimated. This again may point to a deficiency in the LW radiation scheme. According to Zhang *et al.* (2001) and Svensson and Karlsson (2011), the clear-air $LW\downarrow$ for cold and dry conditions is relatively more sensitive to a small change in the q-profile than a small change in the temperature profile. Consequently, q is very important for the radiation balance at the surface. When we prescribed the initial moisture profile from the average of the soundings at 11.30 and 23.30h on the 26th of March and the lower tower levels to test the sensitivity of the WRF-SCM runs to the initial set up of the moisture, the run started with a correct q_{2m}, but immediately tried to regain a balance by increasing q_{2m}. Furthermore, q was underestimated at higher levels compared to the sounding data (Figure 4.7c). We did see a positive effect of lower q in the decreased θ and about 1 K lower T_{2m} at the end of the night. Also now the $LW\downarrow$ bias has decreased compared to the D run and has become very small (Table 4.4). Again, we point out that this may be for the wrong reason, since q was overestimated below about 40 m and underestimated at the higher levels.

When we again compare the radiative and turbulent flux divergence from equation 4.1 for set D to study the effect of the radiative processes, we see that the radiative flux divergence can reach up to -4 K h^{-1} at the start of the run which decreases to $\sim$ -2.3 K h^{-1} at 9h. For the turbulent flux divergence this is $\sim$ 2.4 - 1.9 K h^{-1} at 1h and 9h respectively. Both processes are of comparable magnitude, which again shows the importance of the radiative processes.

Runs were repeated with the revised YSU-BL scheme with time-changing U_g and momentum, q and θ advection. Strong differences are seen compared with MYJ. With YSU, T_{2m} biases were greatly reduced (despite the even stronger overestimated q), while temperature biases increased for the highest 2 tower levels, with too high simulated temperatures. Therefore, YSU was able to generate a very stably stratified BL, which in fact became somewhat too stable as was found for the first few hours with the Cabauw case and in previous research (Sun and Barros, 2013, Kleczek *et al.*, 2014). As for Cabauw, stronger near-surface wind speeds were simulated with YSU and biases increased. Again a stronger LLJ at a lower altitude was modelled, which was for most time steps too strong and at a too low altitude (up to 1.5 m s^{-1} too fast and up to 20 - 40 m too low), but the sharpness of the LLJ nose was more in agreement with observations than with the SCM runs with MYJ. Furthermore, a strong shift was observed around 28h, where T_{2m} increased strongly and wind speeds decreased strongly. At this time the sun rises, resulting in a lot of mixing and a dilution of the strong stratification, which is more efficient with YSU. This also explained the increase in u_* after this time.

The runs with set D were also repeated with 2 different LW radiation schemes (D + GFDL and D + CAM). With GFDL and CAM higher and lower temperatures were obtained respectively than with set D and the RRTMG LW radiation scheme, while for the Cabauw case both schemes simulated lower temperatures. Apparently these schemes handle these challenging conditions with low temperatures and q differently than for the Cabauw case. Very minor differences were found in q_{2m} and the q profile, however, the $LW\downarrow$ bias increased and decreased for GFDL and CAM respectively compared to when RRTMG was used. In fact, $LW\downarrow$ modelled with CAM was in

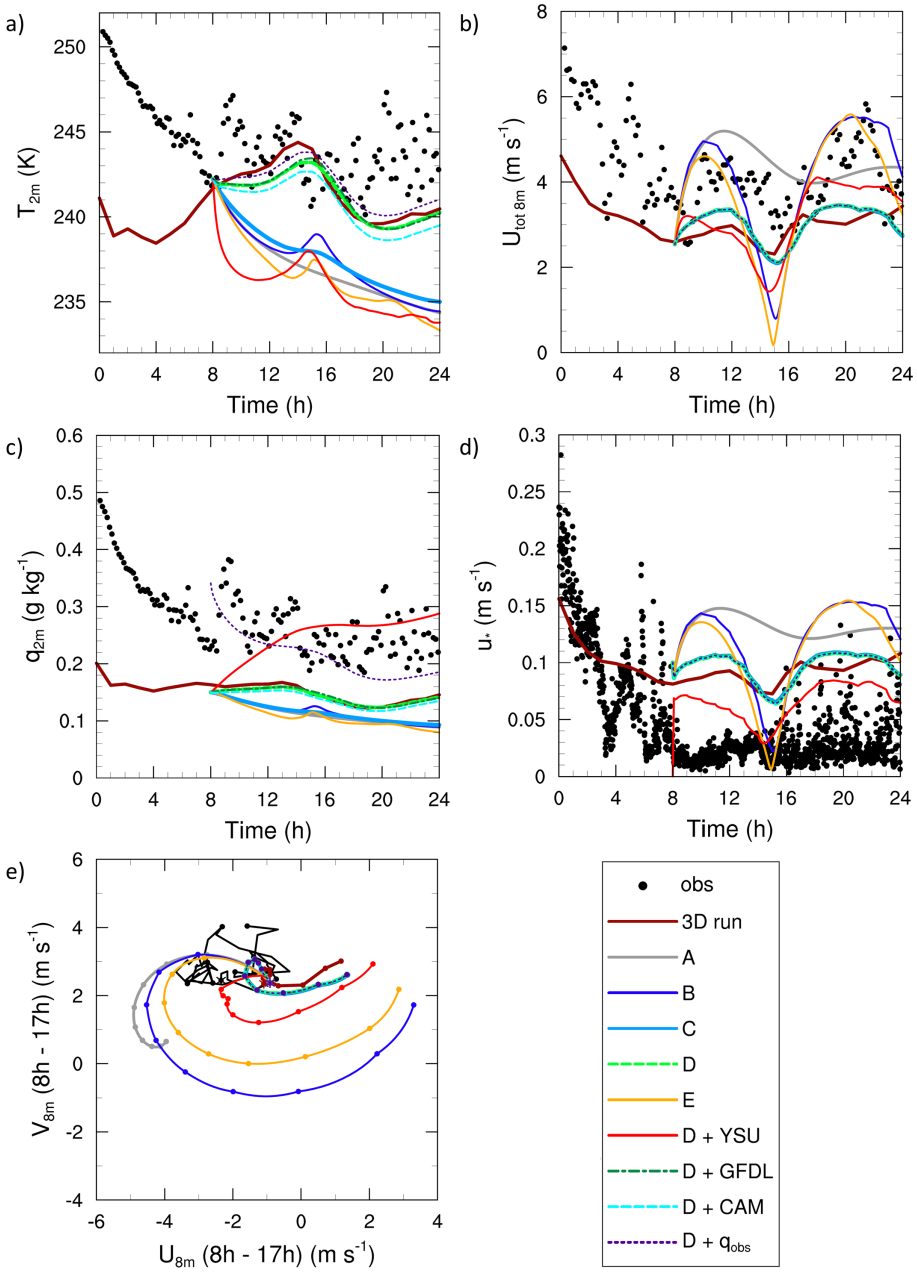

Figure 4.8: See next page.

good agreement with the observations during the night, though overestimated after sunrise, despite the already overestimated q. The influence of the LW radiation scheme on the wind speed simulations was again negligible.

4.5.3 Halley

WRF-3D

The WRF-3D model was started at 0UTC on the 15th of May 2003. The SCM study started at 8h on the 18th of May 2003, therefore the spin-up time for the Halley case was longer than for Cabauw and Sodankylä. However, this may be necessary due to the limited observations in this area and thus limited influence of the observations on the ECMWF boundary conditions, so that the model may require more time to reach equilibrium with the underlying medium. Timeseries are shown from 0h on May 18th 2003 onwards, assuming 72h spin-up.

Initially, WRF-3D underestimated T_{2m} (Figure 4.8), though from the starting time of the WRF-SCM simulations onwards this recovered and observations were followed better though underestimations of up to $\sim$ 5 K were found. The wind speed variation at the 8 m level ($U_{tot\ 8m}$) was followed accurately by the WRF-3D model as well, but $U_{tot\ 8m}$ was slightly underestimated with 0 - 3 m s^{-1}.

Modelled profiles after 9h of simulation (Figure 4.9) indicated for Halley an underestimation of the temperature inversion, consistent with the results for Cabauw and Sodankylä. The near surface θ matched well, but θ at 32 m was modelled almost 8 K too low. Regarding the wind speed profiles, we found that the order of magnitude was in agreement with the observations, although the LLJ observed at 10 m height was not reproduced with WRF-3D at this time step. At other time steps the LLJ was reproduced (not shown) but at a too high altitude (about 30 - 60 m).

The cold bias may be explained, amongst others, by the too low q_{2m} (0.05 - 0.2 g kg^{-1}) and q at the higher levels. With a modelled amount of 0.18 g kg^{-1} at 32 m, the model did not even contain half of the observed q (0.43 g kg^{-1}). Note that the sounding at 3h after the start of the WRF-SCM simulation indicated a q of $\sim$ 0.35 g kg^{-1} at around 150 m which decreased to 0.31 g kg^{-1} at 500 m, for which the WRF-3D run simulated 0.23 and 0.29 g kg^{-1} respectively, hinting at a better representation higher up. Unfortunately, only 1 sounding per day was available, so that we could not compare model results with observations higher than 32 m at other time steps. Though there were some clouds modelled at around 5 and 8 km, $LW\downarrow$ was underestimated with $\sim$ 23 - 30 W m^{-2}. We expect the clouds to have a minor

Figure 4.8: *(Preceding page)* Time series for the Halley case for a) 2 m temperature T_{2m} (K), b) 8 m wind speed $U_{tot\ 8m}$ (m s^{-1}), c) 2 m specific humidity q_{2m} (g kg^{-1}), d) friction velocity u_* (m s^{-1}), and e) the hodograph at 8 m (wind speeds in m s^{-1}), where the asterisk indicates the time of the start of the WRF-SCM simulations (8h). As the measurements are performed every 10 minutes, the SCM output is provided every 5 minutes, and the WRF-3D output is provided hourly, only the full hours since the starting time are indicated with the dots to show the progression in time. Time series are given for the observations (obs), the WRF-3D run (3D run), the WRF-SCM simulations for the different forcing methods (set A-E), the WRF-SCM simulation with the initial q profile based on observations (D + q_{obs}), WRF-SCM with YSU-BL scheme (D + YSU), and with various LW radiation schemes (D + GFDL, and D + CAM).

influence on the SCM simulations in this case, since SCM results in which clouds were kept absent, had a similar amount of $LW\downarrow$.

The modelled BL was very shallow and varied between 20 and 40 m during the WRF-SCM study period. The modelled u_* followed the observed decrease accurately just before the start of the WRF-SCM simulations, but remained too high later on (0.07 - 0.11 m s^{-1} versus the observed 0.01 - 0.08 m s^{-1} (excluding some spikes)). As a threshold height for U_g used in the WRF-SCM simulations, the 300 m height was chosen, which again was located sufficiently above the BL height and the LLJ.

WRF-SCM

Here WRF-SCM results for Halley, for sets A-E and the runs with different BL and radiation schemes are described (Figure 4.8 and 4.9). The evaluation period ranged from 8h - 17h on the 18th of May 2003 and was characterized by stable conditions

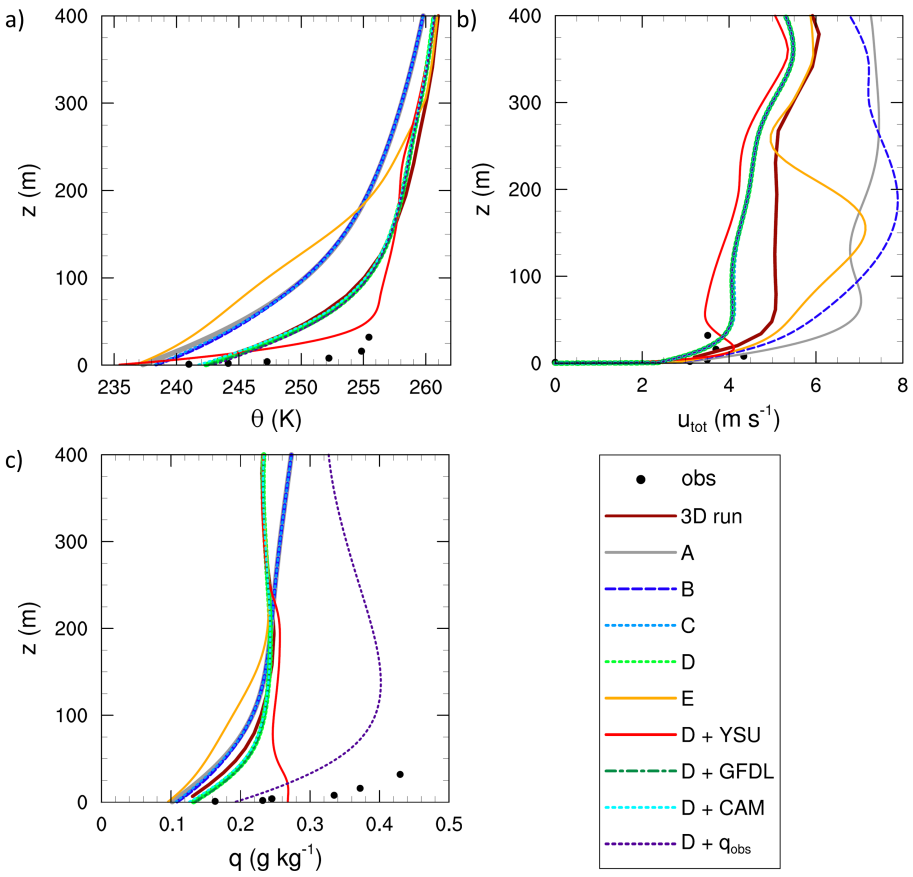

Figure 4.9: Vertical profiles for the Halley case at 17h on the 18th of May 2003, 9h into the WRF-SCM simulation, for a) the potential temperature θ (K), b) the total wind speed U_{tot} (m s^{-1}), and c) the specific humidity q (g kg^{-1}). (For an explanation of the legend, see Figure 4.8.)

and low wind speeds. Since the episode covered a polar night, we decided to keep the study period 9h, i.e. equal as for Cabauw and Sodankylä.

WRF-3D modelled the surface conditions as sea ice with 100 % snow cover for 6.2 cm of snow, which had a $\rho_{snow} \approx 200$ kg m^{-3}. This was applied in the WRF-SCM as well, since it is difficult to determine the actual observed snow depth due to the gradual transition from snow to firn to ice in those regions. Though Halley is in reality located on an ice shelf of about 100 m, we do not expect a large influence of the underlying ocean boundary at 3 m depth (the standard sea-ice depth used in WRF) at this time scale. We furthermore adjusted the z_0 of the snow to $5.6 \cdot 10^{-5}$ m, as was measured at the Halley location (King and Anderson, 1994).

Contrary to results for Cabauw and Sodankylä, the T_{2m} results deteriorated with the WRF-SCM for Halley. The cold bias already modelled with WRF-3D, increased even more, the extent depending on the forcing type. Without temperature advection (set A-C), we noticed a runaway cooling effect for which the simulated T_{2m} deviated more and more from reality, up to 6 K after 9h. When temperature advection was prescribed (set D), T_{2m} was fairly similar to the 3D output, though about 1 K lower for the first few hours. The θ profiles also benefited from the prescribed θ advection since the near-surface θ of set D was more in agreement with observations. At the highest tower level θ remained underestimated with $\sim$ 8 K with set D, though this bias was reduced from an underestimation of $\sim$ 13 K with set A-C. For all forcing types the θ inversion remained too weak compared to the observations, though with set D the inversion became slightly stronger. Also with set E T_{2m} remained too low, and as for the other cases, the artificial inversion was modelled in the θ profile.

For wind speed, similar results as for WRF-3D were found with set D in the $U_{tot\ 8m}$ time series, and for set B and E strong oscillations were simulated, which after around 17h actually matched the order of magnitude of the observed $U_{tot\ 8m}$ nicely, though in our study period the strong decrease was not observed. Though biases did not differ much at 8 m (Table 4.5), they greatly decreased at 32 m (and 2 m, not shown) with prescribed momentum advection. This was confirmed by the wind profiles (Figure 4.9b, and at other hours, not shown), and by the hodograph for 8 m which is approximately the LLJ height of the observations (Figure 4.8e), where the wind speed magnitude for set C-D was in the range of what was observed. This holds even more so for 2 m and 32 m (not shown). Again for set E, the model felt the restriction at the 300 m level in the wind speed profile.

Considering q_{2m}, the WRF-SCM was too dry, and the deficiency increased when moisture advection was absent. The q profile also showed a strong underestimation, and too weak moisture inversion. Slightly higher q values were found up to 130 m for set D, not prescribing q advection lead to even lower q compared to WRF-3D. To test the sensitivity of the WRF-SCM to the initial q profile, we performed an additional simulation with an initial q profile based on a linear interpolation in time between the soundings on the 17$^{\text{th}}$ and 18$^{\text{th}}$ of May 2003, combined with the tower data. This showed a clear improvement in q_{2m} (mean bias error decreased from -0.11 to -0.03 g kg^{-1}, see Table 4.5), and a slight improvement for T_{2m} (mean bias error decreased from -1.4 to -0.9 K). Although the moisture inversion strength was still underestimated, it was modelled better than when using the WRF-3D initial q profile. Biases in Table 4.5 also indicated improvements on temperature and humidity along

Table 4.5: Mean bias error (MBE), root mean square error (RMSE) and median of the absolute error between model simulations and observations, for the period of 8h - 17h, for the Halley case for variables: 2 and 32 m temperature in K (T_{2m} and T_{32m}), 8 and 32 m wind speed in m s^{-1} ($U_{tot\ 8m}$ and $U_{tot\ 32m}$), 2 and 32 m specific humidity in g kg^{-1} (q_{2m} and q_{32m}), sensible (H), and soil heat flux (G) in W m^{-2}, net radiation in W m^{-2} (Q_{net}), and downward ($LW\downarrow$) and upward ($LW\uparrow$) long wave radiation in W m^{-2}. Numbers in red are for the run with the smallest bias between runs with various forcing methods (set A-D), in bold for the run with lowest bias between all WRF-SCM runs (based on multiple decimals, D + q_{obs} is not included). Note that set E is omitted here, due to the non-physical behaviour below the threshold-height for the relaxation towards the 3D field.

		A	**B**	**C**	**D**	**D + q_{obs}**	**D + YSU**	**D + GFDL**	**D + CAM**
MBE	T_{2m}	−5.5	−4.9	−4.8	−1.4	−0.9	−6.8	**−1.3**	−1.9
	T_{32m}	−9.5	−9.4	−9.3	−4.8	−4.6	**−1.0**	−4.7	−5.1
	$U_{tot\ 8m}$	0.9	**−0.3**	−0.9	−0.9	−0.9	−1.1	−0.9	−0.9
	$U_{tot\ 32m}$	3.8	1.8	0.3	0.4	0.4	**−0.1**	0.4	0.4
	q_{2m}	−0.14	−0.14	−0.14	−0.11	−0.03	**−0.04**	−0.11	−0.12
	q_{32m}	−0.27	−0.27	−0.27	−0.23	−0.08	**−0.19**	−0.23	−0.24
	H	−25.2	−22.2	−22.6	−26.8	−25.0	**−12.5**	−26.5	−27.7
	G	2.2	1.8	1.8	2.9	3.4	**0.8**	3.0	2.6
	$Qnet$	−32.8	−30.4	−30.7	−34.2	−32.9	**−22.5**	−33.9	−35.6
	$LW\downarrow$	−34.3	−34.1	−34.0	−31.2	−27.0	−31.8	**−30.2**	−34.5
	$LW\uparrow$	**−1.1**	−3.2	−2.9	3.5	6.4	−8.8	4.1	1.5
RMSE	T_{2m}	5.8	5.2	5.1	2.2	2.0	7.0	**2.2**	2.5
	T_{32m}	9.8	9.6	9.5	4.9	4.7	**1.7**	4.8	5.1
	$U_{tot\ 8m}$	1.0	1.2	1.0	1.0	1.0	1.4	1.0	**1.0**
	$U_{tot\ 32m}$	3.9	2.5	**0.5**	0.5	0.5	0.6	0.5	0.5
	q_{2m}	0.15	0.14	0.15	0.12	0.05	**0.08**	0.12	0.13
	q_{32m}	0.27	0.27	0.27	0.24	0.09	**0.20**	0.23	0.24
	H	25.5	23.3	23.0	27.0	25.2	**13.1**	26.8	27.9
	G	4.1	4.1	3.9	4.4	4.7	**3.4**	4.5	4.2
	$Qnet$	32.9	**30.8**	30.8	34.4	33.1	22.7	34.0	35.7
	$LW\downarrow$	34.3	34.1	34.1	31.3	27.2	31.9	**30.4**	34.6
	$LW\uparrow$	**1.8**	4.9	3.3	4.5	7.1	9.1	5.1	3.0
median	T_{2m}	5.5	5.0	4.9	1.5	1.5	7.1	**1.4**	1.9
	T_{32m}	10.0	10.0	9.8	4.9	4.7	**1.1**	4.9	5.0
	$U_{tot\ 8m}$	1.0	**0.9**	0.9	0.9	0.9	1.3	0.9	0.9
	$U_{tot\ 32m}$	4.1	1.9	0.4	0.4	0.4	**0.3**	0.4	0.4
	q_{2m}	0.14	0.13	0.13	0.10	0.03	**0.05**	0.10	0.11
	q_{32m}	0.27	0.27	0.27	0.23	0.08	**0.17**	0.23	0.24
	H	25.2	24.3	22.8	27.9	26.1	**12.5**	27.9	29.0
	G	3.1	3.1	3.0	3.7	4.1	**2.3**	3.7	3.4
	$Qnet$	31.7	31.1	30.1	33.9	32.5	**22.6**	33.7	35.2
	$LW\downarrow$	34.0	33.6	33.8	31.0	26.9	31.6	**30.6**	34.4
	$LW\uparrow$	**1.7**	1.9	3.0	3.8	6.8	8.6	5.2	2.2

the tower. Changes in the wind simulations were negligible.

Also for Halley we compared the radiative and turbulent flux divergence with set D. As for Sodankylä we found a positive turbulent heat flux divergence of $\sim$ 0.46 - 1.3 K h^{-1}, though this decreased to a negative value of -0.64 K h^{-1} at 9h. The radiative heat flux varied from -0.5 to -0.93 K h^{-1} throughout the 9h, again being of comparable size to the turbulent heat flux divergence.

We repeated the runs with the YSU-BL scheme in combination with set D forcings. Now, T_{2m} became up to 7 K too low. Temperatures aloft were simulated better with YSU than with MYJ as illustrated by the strongly reduced biases (Table 4.5) and the θ profile (Figure 4.9). Also the temperature inversion improved substantially. A slightly larger bias was found for $U_{tot\ 8m}$, where also stronger oscillations are simulated than for set D with MYJ, though a strong overestimated wind speed as was found for Cabauw and Sodankylä was not found for Halley. The wind speed profile resembled the observations nicely, with a LLJ of the correct order of magnitude and only 10 m too high after 9h into the WRF-SCM simulation.

Large differences for q were found between MYJ and YSU. Right from the start q_{2m} increased with YSU and followed the observed values nicely. The q profile was now totally different, with an almost well-mixed profile shape, which was not in agreement with the observed strong inversion. This higher amount of q was also seen with the Cabauw case.

Runs with set D were repeated with varying LW radiation schemes (D + GFDL and D + CAM). Differences between RRTMG and GFDL were very small, but with CAM a slightly lower T_{2m} (about 0.6 K) was found compared to RRTMG and the $LW\downarrow$ was underestimated more (Table 4.5). The $LW\uparrow$ did improve when applying the CAM scheme, but overall $LW\uparrow$-biases were very small. As with the two previous studied cases, the choice of the LW radiation scheme did not influence the wind speed simulations.

4.6 Conclusion and discussion

Many numerical weather prediction and climate models experience difficulties with simulating stratified conditions, especially over snow and when low wind speeds are observed (e.g. Edwards *et al.*, 2011; Atlaskin and Vihma, 2012; Holtslag *et al.*, 2013). In this study, the WRF-3D and SCM, employed with the MYJ boundary-layer scheme, are evaluated for these conditions for three contrasting terrains with snow cover, being Cabauw in the Netherlands (snow over grass/crop-land), Sodankylä in Northern Finland (snow over a needle-leaf forest), and Halley in Antarctica (snow over an ice shelf). Though atmospheric conditions for all sites are not exactly equal, all cases are characterized by clear-skies, stable stratification, and near surface wind speeds below 5 m s^{-1}.

For Cabauw and Sodankylä, WRF-3D experiments demonstrated that the default land-use settings gave incorrect output regarding the snow cover and vegetation fraction. This greatly influenced the soil heat flux and thus surface temperatures. Adjusting these settings with site specific information improved the results.

Overall the performance of 3D WRF was quite good, especially regarding the wind speed simulations. Close to the surface, wind speeds were modelled correctly or

with a very small overestimation for Cabauw and Sodankylä, while this was correct or slightly underestimated for Halley. Modelling the near surface temperature appeared to be (more) challenging. T_{2m} was strongly overestimated up to 7 K and 11 K for Cabauw and Sodankylä respectively at the end of the night, while the model performed better at higher tower levels. For Halley, T_{2m} was modelled more accurately during the SCM study period, while they were too low during the previous 8h (5 - 10 K). Also at higher levels temperatures remained too low for Halley. The three cases shared an underestimation of the modelled temperature gradient.

The WRF-3D fields were used to construct the SCM forcings where we distinguished between: A) not prescribing any lateral forcings, B) prescribing only time-varying geostrophic wind speed, C) prescribing momentum advection in addition to B, D) prescribing temperature and moisture advection in addition to C, and E) nudging the SCM to the 3D field at a height sufficiently above the BL. For all cases we found that runs without lateral forcings and constant geostrophic wind speeds, lead to a substantial bias for wind speed. Prescribing momentum advection improved the modelled wind speed substantially, while model results for temperature, stratification and specific humidity improved considerably with set D. The nudging approach provided a deterioration of the model results and is therefore not advised. Hence, we conclude that prescribing time-varying geostrophic wind speed and momentum, temperature and humidity advection provides the best results for all sites.

Moreover, we conclude that model results are only marginally sensitive to the selected long wave radiation schemes. Model simulations did show contrasting results between the MYJ and YSU boundary-layer schemes. YSU simulated a more stably stratified boundary layer than MYJ. For Sodankylä the stratification became even too strong, as reported by Sun and Barros (2013) and Kleczek *et al.* (2014) for other sites. With YSU, T_{2m} was better simulated for Cabauw and Sodankylä, but strongly underestimated for Halley. Using YSU did degrade the simulated near-surface wind speed, which now remained too high, and simulated a LLJ at a too low altitude, consistent with the enhanced decoupling. The skill for q also decreased and values remained too high for Cabauw and Sodankylä. For Halley q close to the surface improved, but the profile became more mixed than found in observations.

Note that in this study we determined the advection at hour $\mathrm{T_n}$ as a residual term from the prognostic equations for which the individual terms are based on WRF-3D results of the interval 1h preceding ($\mathrm{T_{n-1}}$) and 1h following ($\mathrm{T_{n+1}}$) hour $\mathrm{T_n}$. Of course, one can also calculate the advection directly from the WRF-3D field (e.g. for temperature with $-\bar{\mathrm{U}} \cdot \nabla\theta$). Then the advection is somewhat dependent on the order of the numerical spatial derivatives, while additionally the calculation of the advection close to the surface is hampered by varying terrain heights in the adjacent grid cells. Furthermore, this method provides more instantaneous fields, while the method applied here uses information of the previous and following hour and is in that respect more smooth.

Observations of the surface energy budget, revealed a significant imbalance for all three sites. Surface energy balance closure is very challenging, especially over snow covered surfaces and/or in stable conditions (Sánchez *et al.*, 2010; Chen *et al.*, 2011; Knowles *et al.*, 2012; Helgason and Pomeroy, 2012). Understanding the nature of this problem is beyond the scope of this paper and a study area in itself (e.g. Heusinkveld

et al., 2004; Foken, 2008b; Aubinet, 2008). However, it must be kept in mind when comparing the model results with the observed energy balance terms.

Possibly improvements can be achieved in the representation of the snow pack. The Noah land-surface model has a bulk layer of snow and soil (Niu *et al.*, 2011) in which it adds the total snow depth as part of the first soil layer, making the resolution in the snow rather poor (Figure 4.2). Especially for Sodankylä where the snow depth is 62 cm, this may have an effect. Moreover, when using the standard settings of WRF over sea ice, a constant snow conductivity in depth (though varying slightly in time with increasing density) is used, while a smooth transition from snow conductivity to ice conductivity would be more realistic when snow is gradually pressed to firn and ice.

It must also be mentioned that model results are grid averaged, making a comparison against a local observation more difficult (Atlaskin and Vihma, 2012). According to Atlaskin and Vihma (2012), therefore the comparison should be made against observations that are averaged in that particular grid cell. However, such extensive measurements are uncommon for sites over snow.

All in all, the study shows that quite good results can be obtained for WRF-SCM runs for low wind speeds and three contrasting terrains for the studied cases, as long as a proper advection of momentum, temperature and moisture is prescribed. This confirms the study of Steeneveld *et al.* (2006a) and Baas *et al.* (2010) and extends these findings for SBLs over snow. Additionally, we recommend a detailed prescription of the snow cover and vegetation fraction since these variables influence the energy balance.

Though a perfect match between the model simulations and the observations has not been obtained, significant improvements were made with the right forcings. From this reference, the SCM can be used as a tool to study the small scale processes in SBL modelling to improve our understanding of the SBL processes. In part 2 of this study we will perform a sensitivity analysis with the WRF-SCM on the three cases of this particular study, where we focus on the processes of snow-surface coupling, radiation and turbulent mixing. In this way we study their impact on the SBL evolution of the 3 cases and explore if further agreement with observations can be achieved.

Acknowledgements

The authors are grateful to the KNMI (Royal Netherlands Meteorological Institute), the FMI (Finnish Meteorological Institute) and the BAS (British Antarctic Survey) for the measurement data that was used in this study. We thank ECMWF for the necessary boundary conditions for the WRF-3D runs that have been obtained from their data server. We also thank Tiina Nygård for the discussions on the Halley data. We acknowledge the support from NWO (The Dutch Science Foundation) with grant 829.09.005 ("Quantifying contributions of surface climate feedbacks to the Arctic amplification of greenhouse warming" in the Sustainable Earth program). The contribution by G.J. Steeneveld has partly been sponsored by the NWO contract 863.10.010 (Lifting the fog) and the work of T. Vihma was supported by the Academy of Finland (contracts 259537 and 263918). Finally, we thank the two anonymous reviewers for their valuable suggestions.

Chapter 5

Clear-sky stable boundary layers with low winds over snow-covered surfaces. Part 2: Process sensitivity

Abstract

This study evaluates the relative impact of snow-surface coupling, downward long wave radiation, and turbulent mixing on the development of the stable boundary layer (SBL) over snow using the WRF single-column model (SCM), and compares these model simulations with observations. We consider three contrasting sites with snow-covered surfaces at Cabauw (Netherlands, grass), Sodankylä (Finland, needle-leaf forest) and Halley (Antarctica, ice shelf). All cases are characterized by stable, clear-sky, and calm conditions. Part 1 of this study determined the optimal SCM forcing strategy. From that reference, the intensities of the three governing processes are adjusted.

The analysis reveals a large variety of the modelled atmospheric state and surface variables. Overall, the temperature and moisture gradients, which were mostly underestimated with the reference cases, improve by decreasing the process intensities. The impact is strongest with reduced mixing, though then the model overestimates the near-surface wind speed.

To study the surface energy balance terms, we use so-called process diagrams. The achieved variation between the sensitivity runs, shows the relative orientation of the model sensitivity to each process. The overall orientation of each sensitivity is similar for the three sites. However, the relative positioning of the sensitivity runs with respect to the observations, varies for the three locations. This makes a general recommendation for model improvement not as straightforward. Furthermore, sometimes meaningful interpretation of observations is troublesome, which hampers the comparison with model results. The sensitivity analysis reveals that radiation is relatively more important at Cabauw and Sodankylä, while coupling plays a more important role at Halley.

The sensitivity analysis is performed with 2 boundary-layer schemes (MYJ and YSU). YSU simulates a stronger atmospheric temperature gradient, while MYJ simulates the humidity and wind speed better. A non-linear behaviour, where the 2 m temperature increases with decreased mixing, is most obvious with YSU.

This Chapter has been submitted to *Q. J. R. Meteorol. Soc.* as Sterk HAM, Steeneveld GJ, Bosveld FC, Vihma T, Anderson PS, Holtslag AAM, Clear-sky stable boundary layers with low winds over snow-covered surfaces, Part II: Process sensitivity, and is now pending for revisions.

5.1 Introduction

A single-column model (SCM) is a convenient tool to study the physical processes that are omnipresent in the boundary layer (BL, Baas *et al.*, 2010, Bosveld *et al.*, 2014b) and can thus be used to improve our understanding of the stable boundary layer (SBL). SBL modelling is challenging due to the multiplicity of relatively small-scale processes that may act simultaneously in the SBL, e.g. land-surface coupling, radiative effects, turbulent mixing, the presence of clouds or fog, subsidence, advection, gravity waves, and drainage and katabatic flows (Delage, 1997; Mahrt *et al.*, 1998; Mahrt, 1999; Steeneveld *et al.*, 2006a; Williams *et al.*, 2013; Mahrt, 2014). Moreover, the physical processes and their interactions are either not completely understood, and/or are represented incompletely in models. Also, different SBL arche-types can be distinguished, i.e. the flow can be continuously or intermittently turbulent, or even virtually absent (Van de Wiel *et al.*, 2002; Steeneveld *et al.*, 2006a; Van de Wiel *et al.*, 2012; Mahrt, 2014). This affects the SBL evolution and the vertical and horizontal exchanges of quantities for example (Holtslag *et al.*, 2006, 2013).

In Part 1 of the current study, the WRF model was evaluated for stable conditions over snow over three contrasting land surfaces in low wind regimes, since many models have difficulties for these circumstances (Edwards *et al.*, 2011, Atlaskin and Vihma, 2012, Holtslag *et al.*, 2013). The first case was selected from the Cabauw dataset in the Netherlands (snow over grass/crop-land), the second case from the Sodankylä dataset in Northern Finland (snow over a needle-leaf forest) and the third case from the Halley dataset in Antarctica (snow over an ice shelf). For all three sites, we selected a case with predominantly cloud-free conditions. We required the selected cases to be stably stratified and to have low wind speeds (less than 5 m s^{-1}) at the 10 / 8 m mast level, and relatively low wind speeds higher up. In all cases a so-called type I type of SBL was selected, where under very stable circumstances and low wind speeds, radiative cooling is very important and the shape of the potential temperature (θ) profile is approximately exponential, or concave up ($\partial^2\theta/\partial z^2 < 0$) (Van Ulden and Holtslag, 1985; Vogelezang and Holtslag, 1996). A more detailed description of the cases is given in Part 1 of this study (Sterk *et al.*, 2015).

To validate the SCM performance, the model needs to be driven by realistic forcings of the 3D atmosphere (Baas *et al.*, 2010). Part 1 mainly focused on the influence of various prescribed forcings on the model performance, where we distinguished between strategies that A) do not prescribe any lateral forcings, B) prescribe a varying geostrophic wind speed (U_g) in time, C) prescribe momentum advection on top of B, D) prescribe θ and specific humidity (q) advection on top of C, and E) force the SCM to the 3D field above a threshold height sufficiently above the BL. Since observations of the forcings are in general not available at sufficiently high resolution in time and space, we decided to rely on WRF-3D runs to define the forcings. The WRF-3D runs were also evaluated in Part 1. Furthermore, we learned that model skill depends on subtle differences in land-surface properties regarding snow cover and vegetation fraction. Especially in calm conditions, the model is sensitive to land-surface coupling (e.g. Sterk *et al.*, 2013, henceforth SSH13). More accurate land-use prescriptions clearly improved SCM results. Besides studying the influence of the different forcings on the SCM performance, the impact of different BL and

long wave radiation schemes was investigated.

Overall, WRF-3D simulated the evolution of the near-surface wind speed surprisingly well, but for Cabauw and Sodankylä the near-surface θ and q were substantially overestimated, while these were underestimated for Halley. Best SCM results were found with the set D forcings: varying U_g in time and prescribing momentum, θ and q advection obtained by WRF-3D. Therefore the results corresponded to the WRF-3D results, and were in closer agreement with observations than when neglecting this advection. For all sites, the SCM underestimated the θ and q inversion strength. With the YSU BL scheme, stronger θ inversions were found, which were closer in agreement with observations than with the MYJ BL scheme used previously. Unfortunately, then the skill for wind speed and q deteriorated such that better results were obtained with MYJ. Differences between the simulations with various long wave radiation schemes were small.

By having defined more or less optimal forcings for the three cases, we are now in a position to perform a systematic sensitivity analysis using the WRF-SCM, which is the aim of this Part 2. The particular emphasis is on the processes of snow-surface coupling, long wave radiation and turbulent mixing as these processes are most important for the SBL development and its structure (André and Mahrt, 1982; Beljaars and Holtslag, 1991; Steeneveld *et al.*, 2006b; Bosveld *et al.* 2014b). SSH13 studied the relative importance of these three processes for different geostrophic wind regimes. They found that for high wind speeds, the turbulent mixing was most important while the other processes were of minor importance. With decreasing geostrophic wind regimes, long wave radiation and especially surface coupling became relatively more important. However, their study was performed for an idealized case. The goal here is to study the relative significance of the processes for real cases with low wind speeds to see if this is similar. This is done using the SCM simulations with set D forcings as a reference, and adjusting the intensity of the three processes. Secondly, it is of interest to investigate how these sensitivity runs compare with observations. The process sensitivity is shown in so-called process diagrams, following SSH13 and Bosveld *et al.* (2014b). The variation between the sensitivity runs for each site indicates the relative importance of the process. Thirdly, by comparing the process sensitivity over different terrain types, possible variations in relative importance of the governing processes can be identified. In this way we aim to gain insight from this sensitivity analysis in possible future research fields.

The methodology of this analysis is described in Section 5.3, after a short section on the model description in Section 5.2. Results regarding the time series and vertical profiles are presented in Section 5.4, while results regarding the process diagrams are presented in Section 5.5. The discussion and conclusions follow in Section 5.6.

5.2 Model description

The single-column model (SCM) used in our study, is based on the Weather Research and Forecasting (WRF, Skamarock *et al.*, 2008) mesoscale meteorological model version 3.2.1, and applies the same physics and dynamics as the full WRF-3D model. A vertically stretched σ coordinate is used to determine the vertical levels, with the model top at a constant pressure level at $\approx$ 12 km. To minimize vertical resolution

as a limiting factor, we apply 200 vertical levels, with the highest resolution close to the surface, and the first model level at about 0.55 m.

WRF offers many options for the parametrizations of the physical processes, which differ in their degree of complexity and computational efficiency. The forcings for the WRF-SCM are determined with WRF-3D. For the 3D and SCM runs similar parametrizations were used as in the operational Antarctic Mesoscale Prediction System (NCAR UCAR, 2013), see also Part 1. In the SCM simulations we switched off the micro-physics, since our focus is on clear skies and the observations during our study periods indicated mostly cloud-free conditions as well. The used parametrization schemes of turbulent mixing, snow-surface coupling and long wave radiation are described below, as these represent the processes of interest in this study.

The BL physics are represented with the Mellor-Yamada-Janjic BL scheme (MYJ, Mellor and Yamada, 1982) which is a local, 1.5 order scheme that runs together with the Eta-similarity surface-layer scheme (Tastula and Vihma, 2011). This combination is considered appropriate for stable and slightly unstable flows, though in more convective situations, model biases can increase (Hu *et al.*, 2010). As an alternative we apply the YSU-BL scheme (Hong *et al.*, 2006; Hong, 2010) which is a first order, non-local scheme which runs together with the MM5-similarity surface-layer scheme (Skamarock *et al.*, 2008). The incorrect implementation of the stability function ϕ in WRF 3.2.1 was corrected in our study (Sukanta Basu and Wayne Angevine, personal communications, summer 2012, see also SSH13; Hu *et al.*, 2013). Mixing is now reduced, which in some cases results in too stable SBLs (Sun and Barros, 2013; Kleczek *et al.*, 2014). Also the minimum friction velocity (u_*) is lowered from 0.1 to 0.001 m s^{-1} (Jiménez *et al.*, 2012). This prevents a vanishing heat flux in very stable conditions, but gives the BL has more freedom to represent mixing than with the more strict limitation.

We utilize the Noah land-surface model (LSM, Chen and Dudhia, 2001; Ek *et al.*, 2003), which uses 4 layers to represent the soil dynamics and takes soil, ice, and fractional snow cover effects into account, as well as surface emissivity properties (Skamarock *et al.*, 2008). The snow layer is included in the top soil layer (Figure 4.2 in Part 1).

The atmospheric heating/cooling due to radiative flux divergence and the surface downward long wave radiation is represented by the Rapid Radiative Transfer Model for GCMs (RRTMG). This scheme is a modification of the RRTM long wave radiation scheme (Iacono *et al.*, 2008) and is a spectral-band scheme which uses 16 different bands.

5.3 Methodology

This section describes three parts of the methodology. The first part summarizes the general simulation setup for all SCM experiments (see also Part 1). The second part explains the strategy that was applied for the sensitivity analyses. The third part comments on the uncertainties in observations.

5.3.1 General simulation setup

Part 1 already reported on the different forcing methods that were used for the SCM simulations. The advection was determined as the residual term from the tendency equations for the respective quantities, where for example for θ advection the radiative flux divergence, the temperature tendency due to latent heat release and the turbulent flux divergence were subtracted from the total tendency term.

The geostrophic wind speed U_g is assumed to be equal to the actual wind speed that was modelled with WRF-3D above a certain height, since the actual wind speed is usually a good approximation of U_g in extra-tropical synoptic-scale disturbances (Stull, 1988; Holton, 2004). This threshold height should be located sufficiently above the BL height and the nose of the low-level jet (LLJ) to avoid an unrealistically strong U_g and consequently too strong inertial oscillations. For Cabauw this threshold height was 400 m, while for Sodankylä and Halley this was 300 m. Below the threshold height, U_g equals U_g at the threshold height.

In calm winds, the WRF model results are relatively sensitive to the snow-surface coupling (SSH13), which requires a thoughtful prescription of the surface characteristics. Hence, though the atmospheric forcings for the SCM as well as the snow/soil temperature and moisture are determined with WRF-3D, the snow depth is set equal to the observed snow depth. Furthermore, with the standard WRF-3D set-up, the snow cover remained unrealistically low for the Cabauw case and unrealistically high for the Sodankylä case. To improve on the surface characteristics, we adjusted the threshold snow depth above which there is 100% snow cover for both WRF-3D and the WRF-SCM, such that the modelled albedo matches the observed albedo. As the SCM simulations are performed during night time, it is not of interest to obtain a more realistic albedo (though this is beneficial for the longer 3D runs which may run during day time), but the main goal is to improve on the snow surface characteristics.

5.3.2 Sensitivity analysis strategy

To quantify the sensitivity of the WRF-SCM to the parametrization of turbulent mixing, snow-surface coupling and long wave radiation, we follow SSH13 (see below), but we extend their idealised study and compare results with observations. A similar sensitivity analysis was already carried out by Bosveld *et al.* (2014b) for the GABLS3 case (no snow and higher wind speeds). The runs obtained in Part 1 when advection was prescribed for θ, q, and momentum, are taken as a reference here.

In this sensitivity analysis, we adjust the intensity of the three physical processes, and compare the results with the reference runs and the observations. Apart from comparing representative thermodynamic profiles, we discuss so-called 'process diagrams' as introduced by Bosveld *et al.* (2014b) and as applied in SSH13. In a process diagram, two variables are plotted against each other, for which the variable is, in our case, either a time average over 9h, or a change in 9h time. By drawing lines from the reference run to the simulations with adjusted process intensity, we can systematically compare the orientation and length of the sensitivity for the three processes.

The amount of turbulent mixing is adjusted by multiplying the eddy diffusivities for momentum, heat, and moisture (K_m, K_h and K_q respectively) in the BL scheme with a certain factor. Simultaneously, a similar adjustment in the exchange coeffi-

cients (C_m, C_h and C_q respectively) in the surface-layer scheme is made. Especially in conditions with low wind speeds, the model is more sensitive to also adjusting the turbulent mixing in the surface layer (SSH13) since the strongest temperature gradients are found close to the surface. C_m is not directly determined in WRF. Therefore we adjusted the friction velocity u_* such that effectively C_m was altered in the same way as C_h and C_q. With the YSU scheme, u_* is also used to determine the eddy-diffusivity coefficients, for which we made a correction to avoid a double multiplication in the sensitivity study. Multiplication factors as in SSH13 have been used, being 0.25, 0.5, 2.0 and 4.0. This range has been inspired by Cuxart *et al.* (2006) who showed that the maximum K_m and K_h vary roughly between 1 - 5 m^2 s^{-1}, so that the range chosen here captures the typical uncertainty in K. These runs are referred to as *mixing*.

The same multiplication factors are used for the snow thermal conductivity (λ_{snow}) (referred to as *coupling* runs). Observations indicate a large range of uncertainties in the snow/ice conductivity as this can vary in space (both horizontally and vertically) and time due to various densities and/or texture differences. Several λ_{snow} values have been reported, e.g. 0.078 - 0.574 W m^{-1} K^{-1} for various snow densities (Sturm *et al.*, 2002), hourly values of 0.1 - 1.0 W m^{-1} K^{-1} with average values of 0.4 - 0.5 W m^{-1} K^{-1} for various sites (Huwald *et al.*, 2005), 0.02 - 0.3 W m^{-1} K^{-1} for various sites (Gouttevin *et al.*, 2012) and 0.06 - 0.4 W m^{-1} K^{-1} for various depths (Domine *et al.*, 2012). With the multiplication factors used in our modelling study, λ_{snow} varies from 0.032 - 0.51 W m^{-1} K^{-1} for Cabauw and from 0.054 - 0.86 W m^{-1} K^{-1} for Sodankylä and Halley.

The amount of incoming long wave radiation ($L\downarrow$) is adjusted by altering the initial q profile, since Svensson and Karlsson (2011) showed that $L\downarrow$ in very cold and dry clear-sky conditions is more sensitive to a small change in the q profile than a small change in the temperature profile. This was also shown by Zhang *et al.* (2001). A smaller range of multiplication factors was used in this case, being 0.5, 0.67, 1.5 and 2.0, because a multiplication with a larger factor could lead to unrealistic amounts of atmospheric q. We find a range of 0.79 - 11.3 g kg^{-1} for cloud-free conditions in the winter months (DJF) of years 1951 - 2014 for measurements at De Bilt (about 25 km North-East of Cabauw). With an initial q of 1.6 g kg^{-1} for the Cabauw case, we remain in the range of realistic q with these multiplication factors. Cloud-free, DJF data for Sodankylä from December 2006 - December 2013, show a range for observed q between 0.08 - 4.66 g kg^{-1}. With an initial q of 1.37 g kg^{-1} this is also in the observed range after applying the multiplication factors. Studies at Halley indicated a range of monthly averages of 0.4 - 0.5 g kg^{-1} for the winter months (King and Anderson, 1999), and a median of about 0.34 g kg^{-1} for a 10-year winter climatology (2000-2009) (Nygård *et al.*, 2013). Since the initial q in our case (0.16 g kg^{-1}) is already below this range, decreasing q might be not as realistic, however, we will include all permutations for completeness. The variation of initial $L\downarrow$ that we obtain by applying the permutation factors is about 178.6 - 205.6 W m^{-2} for Cabauw (191.0 W m^{-2} for the reference case), about 166.2 - 192.3 W m^{-2} for Sodankylä (reference = 178.1 W m^{-2}) and about 124.2 - 143.6 W m^{-2} for Halley (reference = 133.9 W m^{-2}). Svensson and Karlsson (2011) also found a variation of over 20 W m^{-2} for $L\downarrow$ for clear-sky conditions in their study with nine global

climate models during the Arctic winter (DJF), which is comparable to the range found here. The simulations with adjusted q will be referred to as $q - radiation$.

Besides that a change in q has an impact on $L\downarrow$, it may also change the surface evaporation and thus the surface energy balance and temperature in the air. Therefore, a change in model behaviour may not only be due to the $L\downarrow$ impact. $L\downarrow$ can alternatively be forced by adjusting the CO_2 gas concentration, as in McNider *et al.* (2012) and Bosveld *et al.* (2014b). In these simulations we use 50 and 1500 ppmv instead of the reference 379 ppmv (as in Bosveld *et al.*, 2014b). We are aware that these numbers are somewhat extreme, however, we only want to focus on the difference in behaviour/orientation compared to the altered q runs. As such only 2 runs are performed. The ranges of realized $L\downarrow$ values are 183.0 - 197.4, 169.5 - 184.8 and 126.0 - 138.4 W m^{-2} for Cabauw, Sodankylä and Halley respectively. These runs will be referred to as $CO_2 - radiation$.

5.3.3 Observation uncertainties

Model results may vary substantially due to uncertainties in parametrizations and/or initial conditions. When comparing the model simulations with observations, one also needs to consider the reliability, the measurement uncertainty and the representativeness of the observations. Especially in cold and/or very stable conditions, measuring atmospheric variables may be challenging (e.g. Tjernström *et al.*, 2014). Equipment is more suspect to failure, and turbulence is weak which hampers accurate flux measurements (Jacobs *et al.*, 2008; Lazzara *et al.*, 2012; Mikolajczyk *et al.*, 2012).

The measurement uncertainties in the process diagrams are shown with a small black line through the observation point. To estimate the measurement uncertainties, we assume for the 2 m temperature (T_{2m}) and the sensible heat flux (H) similar uncertainties as were found to be typical for the SHEBA measurements over Arctic sea ice (Andreas *et al.*, 2010). For the air temperature, they found an uncertainty of $\pm$ 0.2 °C, while for H the uncertainty is of the order of 20%.

Westermann *et al.* (2009) found an uncertainty for the conductive heat flux (G) of $\approx$ 30% at Svalbard, which we will also use, while Town *et al.* (2008) found an uncertainty of $\pm$ 2.6 W m^{-2} - $\pm$ 3.8 W m^{-2} for snow at the South Pole for a 9-year dataset. These error margins are within the 30% of the G found in our study. Marty *et al.* (2003) found an absolute uncertainty of $\pm$ 2 W m^{-2} for the measured $L\downarrow$ under Arctic winter conditions, while Persson *et al.* (2002) and Vihma *et al.* (2009) report an uncertainty in radiation components of $\pm$ 4 W m^{-2} for the net long wave radiation. For the skin temperature (T_{skin}) Andreas *et al.* (2010) quantified an uncertainty of $\pm$ 0.5 °C, while Langer *et al.* (2011) report an uncertainty of $\pm$ 1 °C for the T_{skin} in North Siberian winter, which will also be adopted here.

In the process diagrams, the measurement uncertainty of the T_{2m} difference in time is taken as twice the uncertainty in T_{2m} ($\pm$ 0.4 °C), as that is the maximum uncertainty that can occur. The measurement uncertainty of the average difference between T_{2m} and T_{skin} is maximum $\pm$ 1.2 °C, taking into account both uncertainties of T_{2m} and T_{skin}.

Besides the measurement uncertainties, the comparison of model results with observations is subject to 'representation errors' when observations are not representative for the model average grid cells. Tolk *et al.* (2008) state that representation

errors in the SBL are relatively large due to unresolved topography with coarse model resolutions (for CO_2 in their case). Though this will not have a major role in our SCM simulations, we must keep in mind that observations can be influenced strongly by local processes, which are not captured in the model average grid cells. Furthermore, this could play a role in the WRF-3D simulations from which the advection was determined, though a relatively high resolution of 4 by 4 km grid boxes was used for that.

Measurements may also suffer from equipment failure. For our SCM study period at the Cabauw site, only a limited amount of observations was available for the sensible heat flux (H), therefore we present H only for the first 4h.

5.4 Time series and vertical profiles

In this section, we study the time series (Figure 5.1) of T_{2m}, the humidity at 2 m (q_{2m}) and the total 10 m wind speed ($U_{tot\ 10m}$) and the profiles after 9h of simulation (Figure 5.2) of θ, wind speed magnitude U_{tot} and q. To limit the number of lines, only the findings with the maximum perturbation from the reference are shown (i.e. 0.25 and 4.0 for mixing and coupling, 0.5 and 2.0 for q-radiation, and the 50 and 1500 ppmv for CO_2-radiation). Note that the time series are only depicted for Cabauw, since in general analogous model behaviour was found for Sodankylä and Halley. The process diagrams (Section 5.5) provide information on the surface variables for all sites.

As is clear from Figures 5.1 and 5.2, a large range of model solutions can be obtained with the various process intensities. The goal of this section is to explain the model behaviour for these runs. Also, since Part 1 indicated that overall the θ and q stratification remained underestimated, it is interesting to study the effect of the process strengths on these gradients, as the vertical profiles of the variables strongly influence the SBL state.

5.4.1 Temperature

Increasing the mixing intensity (dark blue lines in Figure 5.1 and 5.2), results in a more efficient downward mixing of warm air and upward mixing of cold air, providing weaker concave up shaped θ profiles, and higher T_{2m}, for all 3 locations. With YSU (dotted dark blue) even somewhat better-mixed, or concave down, profiles are simulated close to the surface.

Decreased mixing (light blue lines) results in a stronger concave up shaped θ profile. Furthermore, we find that the near-surface air temperatures decrease with MYJ (full lines, $\approx$ 0.9 K lower at 2 m, 31h, at Cabauw), and with YSU at Cabauw (dashed lines, $\approx$ 0.5 K lower at 2 m, 31h) but increase with YSU at the other sites (Figure 5.2d and 5.2g), compared to their own reference run, as is also the case at the start of the simulation for Cabauw. Due to the low amount of mixing, the BL becomes very weak and shallow. Then, taking the lowest mixing intensity simulation as a reference, extra mixing will result in relatively more upward mixed cold air which is insufficiently compensated for by downward mixed warm air. This happens with small eddy sizes and a stronger θ gradient close to the surface compared to higher up. Thus indeed T_{2m} is higher for a lower amount of mixing. T_{skin} does decrease

with reduced mixing for both MYJ and YSU as we would expect. This non-linear behaviour regarding near-surface temperatures was also modelled by McNider *et al.* (2012) and SSH13 and found in observations (Acevedo and Fitzjarrald, 2003; Lüpkes *et al.*, 2008; Rinke *et al.*, 2012). For Halley at the very end of the study period T_{2m} also increases slightly with the $0.25K$ run with MYJ, while T_{skin} decreases.

Enhanced coupling (dark grey lines), also results in higher T_{2m} ($\approx$ 1.6 K higher at 31h, Cabauw), higher θ and weaker concave up shaped θ profiles. With increased λ_{snow}, heat from the underlying medium is more effectively brought towards the sur-

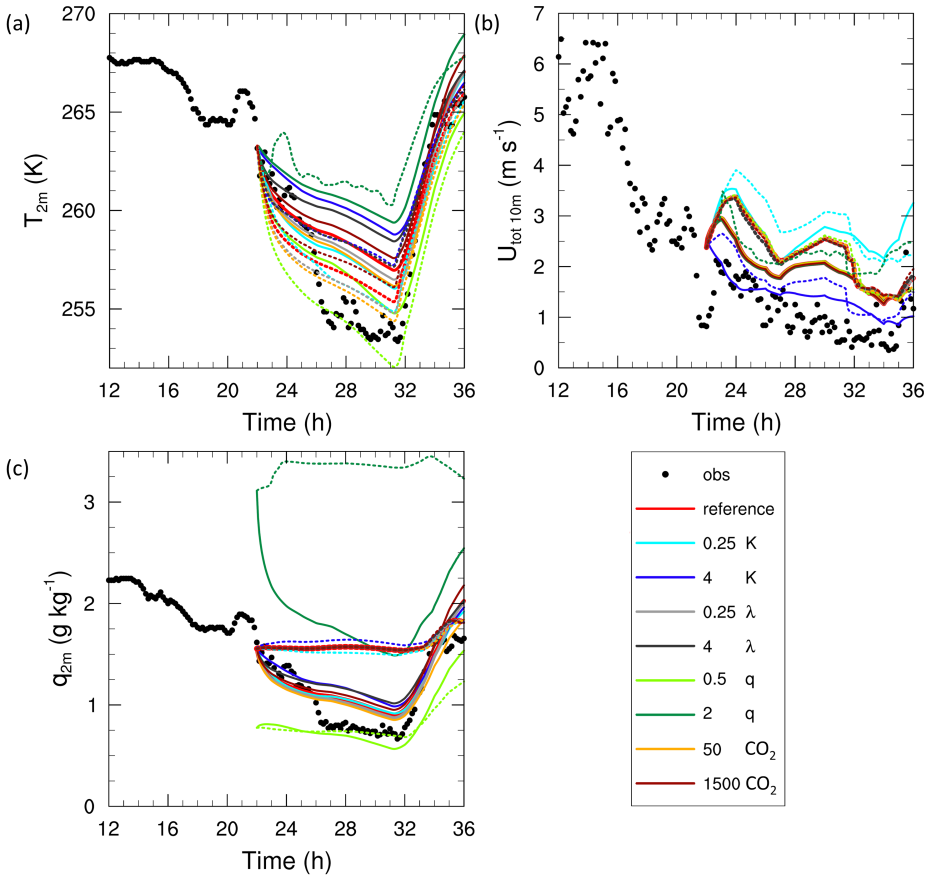

Figure 5.1: Time series of the WRF-SCM simulations and observations for the 2 m temperature (T_{2m} (K)) and specific humidity (q_{2m} (g kg^{-1})), and the total 10 m wind speed ($U_{tot\ 10m}$ (m s^{-1})) for Cabauw. Time is since 3 February 2012, 0 UTC. Full lines are for simulations with the MYJ-BL scheme, dotted lines for simulations with YSU. K represents the change in mixing in both boundary and surface layer, λ represents the ice conductivity and thus the coupling, q represents the specific humidity profile and therefore the incoming long wave radiation, and CO_2 represents the amount of CO_2 in ppmv and therefore also the incoming long wave radiation. The observations are represented by the black dots.

face. This temperature signal is transferred to the atmosphere leading to less strong stratifications. The opposite occurs with reduced coupling (light grey lines) and T_{2m}

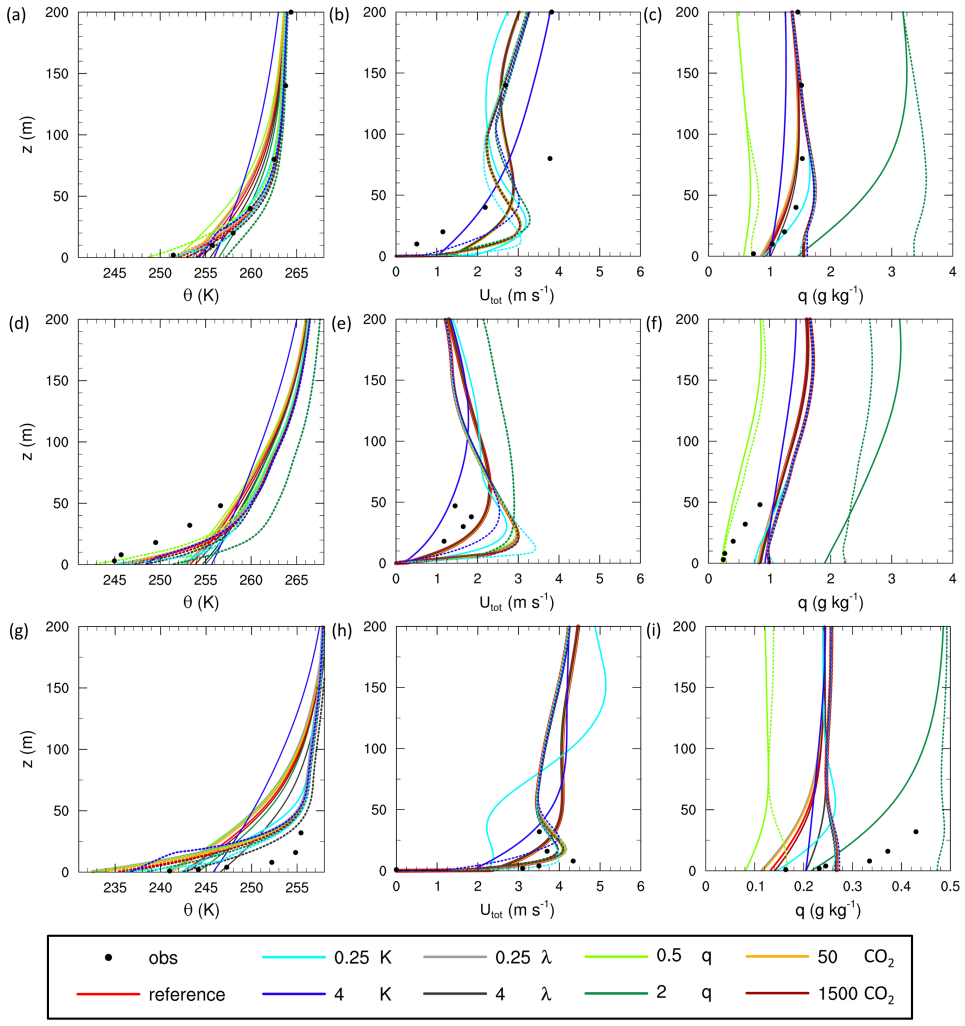

Figure 5.2: Vertical structure after 9h of WRF-SCM simulation of the potential temperature θ (K), the total wind speed U_{tot} (m s^{-1}), and the specific humidity q (g kg^{-1}) for Cabauw (top figures), Sodankylä (middle figures) and Halley (bottom figures). The axes range is kept similar per variable for straightforward comparison, except for q at Halley since these values are considerably smaller than at the other sites. Full lines are for simulations with the MYJ-BL scheme, dotted lines for simulations with YSU. K represents the change in mixing in both boundary and surface layer, λ represents the ice conductivity and thus the coupling, q represents the specific humidity profile and therefore the incoming long wave radiation, and CO_2 represents the amount of CO_2 in ppmv and therefore also the incoming long wave radiation. The observations are represented by the black dots.

decreases ($\approx$ 0.5 K at 31h at Cabauw) accompanied by stronger stratifications. Note that the impact of coupling is stronger at Halley compared to the other locations. At Halley, the snow cover is 100% such that the impact of a change in λ_{snow} is maximal, while Cabauw and Sodankylä have a smaller snow cover such that there is relatively more influence of the unaltered λ of the underlying medium. Furthermore, in the sea-ice part of the model, the conductivity of the underlying layers is set equal to λ_{snow}. Therefore the conductivity of the entire underlying medium is altered. We did test whether setting the conductivity of the layers below the first layer to the conductivity of ice (2.2 W m^{-1} K^{-1} as specified in WRF) changed this, but due to the coarse resolution in the sea ice in WRF (see also Figure 4.2 in Part 1), this impact was negligible.

Finally, an increase in $L\downarrow$ either by amplifying the initial q (dark green lines) or CO_2 (dark red lines) also leads to higher T_{skin} of which the signal is again transported into the atmosphere. This leads to higher temperatures and a weaker stratification. The opposite occurs when $L\downarrow$ is decreased (light green (q) and orange (CO_2) lines).

Besides the non-linear behaviour regarding near-surface temperatures found with YSU and not with MYJ, other differences between these BL schemes are that overall stronger stratifications and lower temperatures close to the surface are found when using YSU. This was also the case in Part 1 and in Kleczek *et al.* (2014).

Comparing the model simulations with observations, shows that decreasing the process intensities gives better θ profiles for Cabauw, as the near-surface inversion strength (e.g. up to 30 m) increases. However, decreasing $L\downarrow$ is not a preferred solution since $L\downarrow$ was already underestimated (not shown). The YSU simulations perform best, and especially the $0.25K$ run follows the observations accurately, though they underestimate T_{2m} at the start of the run up to almost 2.5 K at 24 h. For Sodankylä also improved results are obtained with lowered process intensities. Temperatures close to the surface are better forecasted with YSU, though the overall inversion strength along the tower then remains too strong. Inversion strengths along the tower also improve for Halley with decreased process intensities, and the best θ shapes are again obtained with YSU, though the inflection point in the simulated θ profile is at a too high level (around 50 m while in the observations this appears to be just below 20 m) and in general the θ values are too low. The $0.25K$ run predicts the θ better than the reference run, though then the near-surface temperature is even more underestimated. For Halley the atmospheric temperatures are also predicted accurately with YSU and increased coupling, though then near-surface temperatures remain slightly too high.

5.4.2 Wind speed

The model sensitivity on the simulated wind fields is most clear with an altered mixing process (Figure 5.1b, and 5.2b, e and h). With enhanced mixing (dark blue lines) the LLJ disappears with MYJ (full lines, also at other hours), while these are located at at higher altitude with YSU (dotted lines, also at other hours). At the 10 m level (Figure 5.1b) the strengthened mixing leads to lower wind speeds (up to 1 m s^{-1} lower for both BL schemes at Cabauw). For Sodankylä and Halley also lower wind speeds are found than the reference case. This improves the agreement with observations for Cabauw and Sodankylä, though at Halley $U_{tot\ 8m}$ is now underestimated

by $\approx$ 1 - 2.4 m s^{-1}.

A reduced mixing strength (light blue lines) leads to less exchange between the layers and therefore higher $U_{tot\ 10m}$ than the reference case (up to 0.8 and 0.7 m s^{-1} higher with MYJ and YSU respectively). Similar results are found for Sodankylä and Halley, though at Halley slightly lower wind speeds than the reference case are simulated at the end of the study period. The wind speed profiles indicate that the LLJ is now located at a lower altitude and is intensified for all cases except at Halley. At Halley the LLJ is also at a lower height, but does become slightly less intense, though it is more intense earlier in the simulation (not shown).

The impact of reduced $L\downarrow$ (light green for q runs, orange for CO_2 runs) on wind speed is very small. A slightly higher $U_{tot\ 10m}$ is found (Figure 5.1b, up to 0.1 m s^{-1} for decreased q with YSU, smaller with CO_2 and for MYJ) which is explained by the slightly stronger stratification and smaller exchange between the layers, while the opposite is found with increased $L\downarrow$ (dark green for q runs, dark red for CO_2 runs). Differences are more clear when $L\downarrow$ is adjusted by altering q, due to the stronger perturbations in $L\downarrow$ compared to with the adjusted CO_2 simulations. The effect of increased $L\downarrow$ with a doubling of q for YSU (dark green) is more profound at Cabauw and Sodankylä. In these cases an unstable stratification just at the start of the simulation is modelled and was in fact also seen in a sudden peak in the T_{2m} time series (Figure 5.1a), T_{skin} and the surface fluxes (not shown). This again starts to follow the general tendency of the other simulations after about 2h of simulation.

The effect of altered coupling on wind speed is also very small, and remains somewhat hidden by the radiation simulation lines (Figures 5.1 and 5.2). As with the modified $L\downarrow$, increased and decreased coupling result in decreased and increased stratification and slightly less and more exchange with the surface respectively. At Halley this is seen in the weaker LLJ with YSU with increased coupling.

Overall, the wind speed profiles and $U_{tot\ 10m}$ are most sensitive to the mixing intensity compared to the other studied processes, since a change in K_m and C_m have a more direct impact on the wind field. Also, the impacts of altered coupling and radiation are larger with YSU than with MYJ.

While decreasing mixing resulted in more accurate temperature simulations compared to observations, this deteriorates the wind speed forecast close to the surface as they increase more than what observations suggest. Only with YSU at Halley, the modelled wind speed profile improves with the $0.25K$ run.

5.4.3 Specific humidity

The strongest response on q_{2m} (Figure 5.1c) and the q profiles (Figure 5.2 c, f and i) is clearly obtained by the radiation-q simulations (green lines), as this is a direct result from the modified initial q profile. A smaller impact of similar sign is found when $L\downarrow$ is increased with higher CO_2 concentrations (dark red lines). Then q increases slightly ($\approx$ 0.05 g kg^{-1} higher with MYJ at Cabauw, very small increase with YSU). This is also the case with enhanced coupling (dark grey lines, similar deviations as for CO_2-radiation). Due to the higher temperatures the air is able to hold more moisture than in the reference case, and dew formation is slightly smaller. The opposite occurs for reduced CO_2-radiation and coupling (orange and light grey lines respectively) such that q decreases. The impact of coupling and CO_2-radiation

is most visible with MYJ and not as clear with YSU. However, with YSU more moisture is held in the atmosphere and the relative humidity is already close to or at 100%, and no more moisture can be contained. This also follows from the somewhat more negative L_vE with YSU than with MYJ.

Strengthened mixing (dark blue lines), also leads to more q_{2m} (up to ≈ 0.08 g kg^{-1} more with YSU at Cabauw, and up to ≈ 0.14 g kg^{-1} with MYJ) and more q in the profiles close to the surface, with lower amounts for MYJ aloft. Due to the more effective mixing, moisture is more evenly redistributed, leading to weaker q inversions. Simultaneously more moisture can be held in the atmosphere with higher temperatures. Only at Sodankylä, a very small decrease in near-surface q is seen with enhanced mixing in YSU.

The behaviour of the weaker mixing runs (light blue lines) is not as straightforward as for the enhanced mixing and differs per site and per BL scheme. With YSU we find a decrease in q_{2m} at Cabauw and Halley, but an increase at Sodankylä. With MYJ, q_{2m} at Cabauw and Halley decreases at first after which it increases slightly compared to the reference run, while for Sodankylä less q_{2m} is found. Regarding that more q_{2m} was simulated with increased mixing with MYJ, a non-linear effect analogous for temperature with YSU regarding the near-surface q is found. Hence, with less mixing, water vapour is less easily transported to the surface, which results in higher atmospheric q values with a stronger gradient close to the surface. This non-linear effect is most profound at Halley. It is however interesting, that for temperature this was mostly visible with YSU, while for moisture this is mostly visible with MYJ. Only at Sodankylä is this effect seen for YSU, but there it is not seen with MYJ. Apparently the way the schemes simulate temperature and moisture is different.

When we compare the q simulations with observations, the MYJ reference case (red full lines) captures the shape of the q inversion along the tower better than YSU for all sites. With the YSU reference case (red dotted lines) the q profile remains more well-mixed. Decreasing the mixing with MYJ (full light blue lines) does improve the modelled profile shape, though at Cabauw and Sodankylä q is somewhat overestimated, while q remains underestimated at Halley (except at the surface where better predictions are found). Decreasing CO_2-radiation and coupling also leads to stronger q inversions, when q decreases with the lower temperatures, but then for Cabauw skills at higher levels decrease, while at Halley the skill deteriorates for all levels with MYJ by modelling a too low q. Decreasing q-radiation improves q at the surface for Cabauw and Sodankylä and with YSU at Halley, but then the profile shape again is wrongly forecasted. Increasing q-radiation does seem to improve the q profile at Halley with MYJ, since observations higher up are better simulated and the stratification is developed better.

5.5 Process diagrams

In this section the process diagrams as described in the section 5.3.2 will be analysed. These show selected variables for coupling, radiation and mixing, and each will be studied separately in the following subsections.

The process diagrams show 2 sets of sensitivity lines, the first with the green dot as

reference simulation, which represents the run with the MYJ-BL scheme, from which the full lines are drawn indicating the altered intensities for the three processes. The second set of lines is with the red dot in the center which is the reference run performed with the YSU-BL scheme, from which the dotted lines indicate the sensitivity analysis.

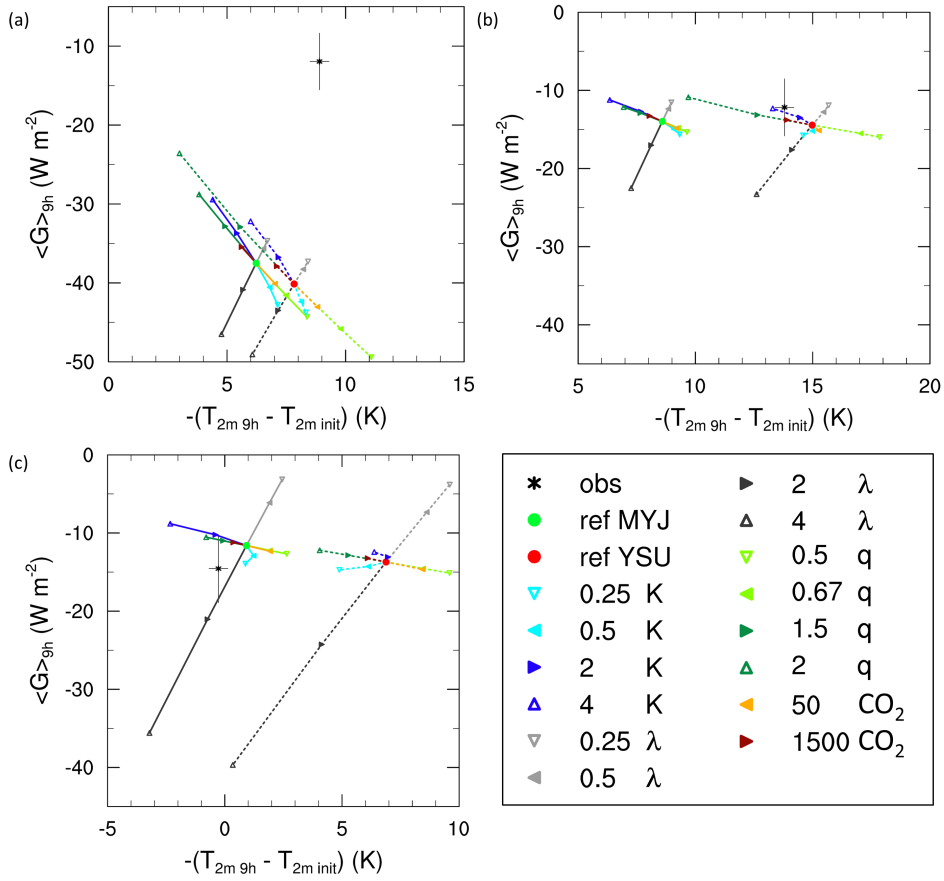

Figure 5.3: Cooling of the 2 m temperature (-($T_{2m\ 9h} - T_{2m\ init}$) (K)) over 9h versus the soil heat flux ($< G >_{9h}$ (W m^{-2})) averaged over 9h for a) Cabauw, b) Sodankylä and c) Halley. K represents the change in mixing in both boundary and surface layer, λ represents the ice conductivity and thus the coupling, q represents the specific humidity profile and therefore the incoming long wave radiation, and CO_2 represents the amount of CO_2 in ppmv and therefore also the incoming long wave radiation. std MYJ is the reference for the simulations with the MYJ-BL scheme (full lines) and std YSU is the reference for the simulations with the YSU-BL scheme (dashed lines). The asterisk with error bars represents the observation with its measurement uncertainties in the error bar.

5.5.1 Snow-surface coupling

First we focus on the process diagram representing the snow-surface coupling in Figure 5.3. Here the amount of cooling at 2 m during the 9h simulation is presented versus the average G to examine the time integrated interaction between the surface and the atmosphere. The general orientation of the observations for Cabauw and Sodankylä indicates that with stronger cooling, a stronger conductive heat flux is found. When the atmosphere close to the surface cools more, T_{skin} has also lowered more, resulting in a larger temperature gradient through the snow layer. For Halley, we find that there is actually some heating at the 2 m level in time, while the snow heat flux remains negative. For this case we noticed a strong advection (see Part 1 where differences between the no-advection and prescribed advection runs were substantial), which explains a small increase in T_{2m}, while T_{skin} does decrease.

Overall, we find that the processes of altered mixing and $L\downarrow$ follow the orientation of decreased G with decreased cooling in time for all locations. E.g. with increased mixing, more warm air from higher levels is brought towards the surface and cold air is brought upwards, such that the temperature gradient decreases and G becomes smaller. Also with enhanced $L\downarrow$, T_{skin} increases, leading to smaller G. The orientation of the coupling runs is perpendicular to this due to that λ_{snow} is adjusted to alter the coupling intensity. When λ_{snow} is increased, G increases, though at the same time more heat from the underlying medium is transported to the surface leading to less cooling in time which counteracts the stronger λ_{snow}.

Note that the general orientation of the process sensitivities as shown here, apart from the T_{2m} non-linearity with YSU (next subsection), is similar as was found with the RACMO-SCM in Bosveld *et al.* (2014b) for the Cabauw site without snow and with higher wind speeds. The relative contributions differ, but this makes sense since different multiplication factors have been applied, while additionally the conductivity of the soil was also adjusted which is not applied in our study. The general orientation is also comparable to the idealized case study in SSH13, which reassures that their findings for an idealized case are also applicable for real cases.

MYJ vs YSU

We find some differences between the two sensitivity analysis sets from the default MYJ (full lines) and YSU (dotted lines) simulations. The overall orientation for coupling and radiation is similar, but differences are found for the mixing behaviour. In the YSU runs, a non-linearity for T_{2m} is seen most clearly for Sodankylä and Halley, as was found by McNider *et al.* (2012) and SSH13. In these studies decreased mixing resulted in less cooling at the 2 m level. The mechanism for this was already explained in Section 5.4.1. Interestingly, this non-linear behaviour is only captured with the YSU-BL scheme and not as clearly with MYJ. With MYJ, T_{2m} did increase slightly at the very end of the study period at Halley when wind speeds also drop strongly, so that for the T_{2m} difference over 9h this non-linearity is clear. This is no longer visible for the average T_{2m} over the entire 9h study period, as seen later in Figure 5.4. This non-linear behaviour in models mostly occurred with light winds and low mixing (McNider *et al.*, 2012; SSH13). Therefore, a possible explanation for the non-linear behaviour occurring more clearly with YSU is that this scheme produces a stronger stratified BL than MYJ (Figure 5.2). Also mixing in the BL is less efficient

for the YSU reference case with a smaller eddy diffusivity in the BL (not shown). Evidently, this is related to the minimum background diffusivity present in WRF with MYJ, as reducing this amount lead to a more clear non-linearity with MYJ, and eddy diffusivities that were of comparable magnitude as with YSU (not shown). Since also observations indicate the existence of this non-linearity, it is promising that in essence both schemes can simulate this.

Moreover, with YSU a stronger impact of radiation variations is found than with MYJ (green and brown/orange lines), as is seen by the longer lines in the process diagrams. Though actually $L\downarrow$ between the MYJ and YSU runs do not differ much (apparently the extra q with YSU compensates for the lower temperatures close to the surface), the impact of a change in $L\downarrow$ is larger when T_{skin} is lower, as is the case with YSU compared to MYJ.

Also we find that the impact of coupling is larger with YSU than with MYJ, this is most clear for Halley. At Halley T_{skin} is already about 4 K lower with the reference YSU than with the reference MYJ run, and therefore a change in λ_{snow} has a stronger influence on T_{skin} due to the larger temperature gradient through the top snow layer. For Cabauw and Sodankylä the differences in coupling-line length are smaller, possibly due to the smaller impact of the snow-surface coupling due to the smaller snow cover and, in the case of Cabauw, smaller snow depth. Furthermore, the coupling lines of YSU have a smaller slope: e.g. a larger change in cooling for a fixed change in G such that the coupling impact seems to be larger here.

Site intercomparison

The general direction of the process orientation for the three sites is comparable (e.g. with increased mixing, less cooling and a weaker G is found). Interestingly, the strength of the sensitivity varies per station. Firstly, for the mixing and radiation processes, the change in G per change of cooling is a lot more profound for Cabauw than for the other sites, i.e. the lines are more steep. This could be related to the method of determining G in the WRF model:

$$G = -\lambda \frac{\Delta T}{\Delta z_{tot}}\,, \tag{5.1}$$

where ΔT is the temperature difference along the total depth of the top layer (Δz_{tot}) being the sum of the snow cover (Δz_{snow}) and the top soil layer (Δz_{soil}). The conductivity of the top layer, λ, is composed as follows (Ek *et al.*, 2003):

$$\lambda = \sigma_{snow}\lambda_{snow+soil+veg} + (1-\sigma_{snow})\lambda_{soil+veg}\,, \tag{5.2}$$

$$\lambda_{snow+soil+veg} = \frac{\Delta z_{snow}}{\Delta z_{tot}}\lambda_{snow} + \frac{\Delta z_{soil}}{\Delta z_{tot}}\lambda_{soil+veg}\,, \tag{5.3}$$

$$\lambda_{soil+veg} = \lambda_{soil} exp(-\beta_{veg}\sigma_{veg})\,, \tag{5.4}$$

where σ_{snow} is the snow cover fraction. $\lambda_{snow+soil+veg}$ is the conductivity of the soil with vegetation and snow cover and determined as in equation 5.3. λ_{snow} depends on the snow density which also changes in time. $\lambda_{soil+veg}$ is the conductivity of the soil with vegetation without snow cover, which is determined with the bare soil

conductivity λ_{soil} in combination with an empirical coefficient β_{veg} and the vegetation fraction σ_{veg} in equation 5.4.

All parameters in equation 5.1 vary for the three locations, since Δz_{tot} amounts to 8.5, 67 and 43.75 cm for Cabauw, Sodankylä and Halley respectively (as illustrated in Figure 4.2 in Part 1). As a consequence the resolution in the underlying medium is not the same for each site, making a comparison less straightforward.

Furthermore, λ differs between the sites due to the different snow cover and vegetation fractions. For Cabauw with 83% snow cover and 85% vegetation, a λ of ≈ 0.27 W m^{-1} K^{-1} is simulated. For Sodankylä with 55% snow cover and 49% vegetation, this is ≈ 0.42 W m^{-1} K^{-1}. For Halley with snow over sea-ice, WRF sets the snow-cover to 100% while additionally the conductivity of the underlying layers is set to the snow conductivity, such that λ is ≈ 0.21 W m^{-1} K^{-1}. Therefore, the relative impact of altering λ_{snow} on the total λ is most relevant for Halley, since at Cabauw and Sodankylä the relative impact of the underlying and unchanged $\lambda_{soil+veg}$ is larger due to the smaller snow-cover and the relatively large λ_{soil}. This stronger coupling impact at Halley compared to other site is also clearly visible with the longer coupling lines in Figure 5.4. Though actually ΔT throughout the first soil layer and λ are smaller for Cabauw than for Sodankylä, this is divided by a smaller Δz, so that the impact of a change in ΔT on G is expected to be largest at Cabauw.

In addition, the length of the radiation lines differs between sites: they are largest for Cabauw and smallest for Halley. This is explained by the higher q at Cabauw and hence larger $L\downarrow$ changes (Section 5.3.2) when equal multiplication factors are applied for the three sites. The effect of mixing seems to be a bit larger at Halley than at Sodankylä, but this could be related to the somewhat stronger wind speeds present in this particular Halley case.

Comparison with observations

At Cabauw G is greatly overestimated, which is partly explained by that WRF applies an equation for λ_{snow} which gives higher values for a certain snow density compared to what we used to estimate the observed values. E.g. for fresh snow with a density of 100 kg m^{-3}, a λ_{snow} of 0.128 W m^{-1} K^{-1} is utilized by WRF (where we used 0.021 W m^{-1} K^{-1} at Cabauw), while for snow with density 200 kg m^{-3}, a λ_{snow} of 0.215 W m^{-1} K^{-1} is modelled (we used 0.084 W m^{-1} K^{-1} for Sodankylä). Figure 5.3 confirms that reducing λ_{snow} brings the model results closer to the observations for Cabauw and Sodankylä, though for the latter G is only slightly overestimated. On the other hand, it must be noted that the Sodankylä measurement site is more heterogeneous than the other two sites. G is determined through the top 2 cm of the snow layer which implies that G is determined for a full snow cover, while there are also trees present, so that G representative for the entire site could be larger. The same holds for Cabauw, where some grass may still stick through the snow cover. For Halley the simulated λ_{snow} equals λ_{snow} used for observations, but now G is slightly underestimated, so apparently $\Delta T/\Delta z$ is too small in the model.

Furthermore, the model formulation for G is not identical to the way that the observed G was determined, which can cause some differences between observed and modelled G. We expect the differences to be smaller when the relative contribution of the snow depth is larger.

Regarding the cooling in time, we see that for Cabauw and Sodankylä better results are found with YSU. Also for Halley more cooling was found with YSU, but now the temperature is strongly underestimated. This is also seen in the profiles in Figure 5.2.

Temporal evolution

So far we have discussed the process diagrams that are obtained after 9h of simulations. However, sometimes a variable changes very rapidly in time at the start of the simulation which is now averaged out over the 9h. Therefore it is also interesting to see the development of the process diagrams in time. The process diagrams throughout the first hours of the night are shown in the supplementary material (end of this chapter). We find most clearly in the first few hours for Cabauw and Sodankylä that the change in G per change in cooling becomes smaller in time, e.g. the slope of the lines decreases, both for observations, as for the sensitivity analysis lines (for the latter also for Halley). Just after the start of the simulation a relatively stronger drop in T_{skin} is found, which causes a relatively stronger $\Delta T/\Delta z$ in the soil, while it takes a bit more time to transfer this signal to the 2 m level. Therefore initially the change in G is larger with a similar cooling at 2 m.

5.5.2 Long wave radiation

The process diagrams in Figure 5.4 represent the process of radiation where the net radiation ($Q*$) versus the 2 m temperature (T_{2m}) is depicted, both averaged over 9h. $Q*$ is defined as $L\downarrow$ minus $L\uparrow$ at the surface. Therefore, with higher surface temperatures, $L\uparrow$ will be larger, and with higher air temperatures and/or specific humidity, $L\downarrow$ will be larger.

In general, with strengthened mixing, T_{2m} increases due to the enhanced downward transport of warm air. This results in a larger $L\uparrow$ which dominates over the slightly larger $L\downarrow$ which thus results in a more negative $Q*$. For MYJ the opposite occurs when mixing weakens, while for YSU we find again the non-linear behaviour in T_{2m} as described in the previous sections. The coupling process follows the same orientation as the increased mixing process. When λ_{snow} is amplified, more heat from the underlying medium is transported to the surface which is reflected in a higher T_{2m}. Therefore again $L\uparrow$ increases which causes a more negative $Q*$, and the opposite is found for decreased coupling. For the radiation process, we influenced the amount of $L\downarrow$ by adjusting q and CO_2. When $L\downarrow$ is reduced, less energy reaches the surface leading to lower T_{2m}. This also results in less $L\uparrow$, however, since $Q*$ becomes more negative, the decreased $L\downarrow$ dominates over the decreased $L\uparrow$. With enhanced CO_2-radiation the opposite is found. This is also the case with increased q-radiation for MYJ and for YSU at Halley. However, with YSU at Cabauw and Sodankylä, a non-linear effect is reproduced, where indeed T_{2m} increases as we would expect, but also a more negative $Q*$ is found. So apparently here the extra $L\uparrow$ due to the higher temperatures dominates over the extra $L\downarrow$. This non-linearity is not found with higher CO_2. Then the increase in T_{2m} is a lot smaller than with more q so that $L\uparrow$ will not increase as much and $L\downarrow$ is still the dominant term for $Q*$.

MYJ vs YSU

Next, we again study the differences between the two sensitivity analysis sets. The non-linear orientation of mixing and radiation was already explained, but also the radiation lines with a similar direction are more 'flat' with YSU than with MYJ. Considering that the differences in $L\downarrow$ between MYJ and YSU are not that large, this means that $L\uparrow$ plays a relatively more important role in the YSU runs than in the MYJ runs, which is of course also seen from the non-linear behaviour with increased q runs at Cabauw and Sodankylä. The stronger changes in $L\uparrow$ also follow from the stronger changes in T_{2m}.

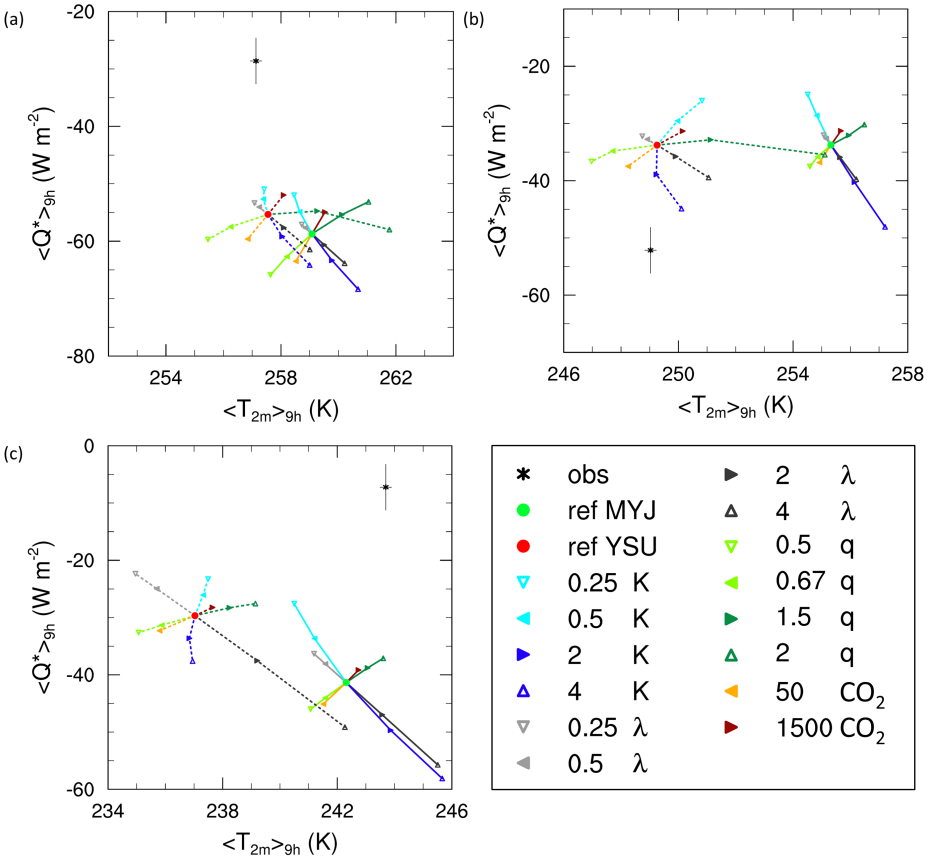

Figure 5.4: The 2 m temperature ($< T_{2m} >_{9h}$ (K)) versus the net radiation ($< Q^* >_{9h}$ (W m^{-2})), both averaged over 9h for a) Cabauw, b) Sodankylä and c) Halley. K represents the change in mixing in both boundary and surface layer, λ represents the ice conductivity and thus the coupling, q represents the specific humidity profile and therefore the incoming long wave radiation, and CO_2 represents the amount of CO_2 in ppmv and therefore also the incoming long wave radiation. std MYJ is the reference for the simulations with the MYJ-BL scheme (full lines) and std YSU is the reference for the simulations with the YSU-BL scheme (dashed lines). The asterisk with error bars represents the observation with its measurement uncertainties in the error bar.

As with the coupling process diagrams (Figure 5.3), the YSU runs also are more sensitive to coupling than MYJ, which is seen from the longer lines. Due to the larger temperature gradient through the top layer, the impact of an altered λ_{snow} on the surface temperature is more profound. Also (most clear at Sodankylä and Halley), the coupling line is more 'flat' with YSU compared to MYJ, since again $L\downarrow$ is comparable, but with lower temperatures, the impact on $L\uparrow$ is smaller for a similar change in T_{skin}.

Site intercomparison

When we compare the process diagrams of the different sites, we see that the impact of mixing is larger for Sodankylä compared to Cabauw, and even larger for Halley since the orientation is similar, but the lines are longer. This is related to the stronger θ stratification at Halley (Figure 5.2). Then when mixing is altered, the temperature change becomes more efficient compared to cases with weaker stratification. Furthermore, the near-surface wind speed is highest for Halley, which can also partly explain the more efficient mixing. This is not valid for explaining the difference in mixing efficiency between Cabauw and Sodankylä since wind speeds at Sodankylä are a bit lower than at Cabauw. Then differences in mixing sensitivity are most likely due to the stronger temperature stratifications at Sodankylä. Again we see for Halley a stronger impact of the coupling process as found before.

Comparison with observations

Comparing the model results with the observations, learns us that for Cabauw and Halley $Q*$ is substantially overestimated. Temperatures close to the surface are overestimated for Cabauw in most simulations, though for Halley these temperatures are mostly underestimated. Reducing T_{2m} with less mixing and less coupling brings the modelled $Q*$ closer to the observed value, but especially for Halley then too low temperatures are found. Lowering T_{2m} by reducing $L\downarrow$ is not advised, because $L\downarrow$ is already strongly underestimated for Cabauw and Halley (up to about 30 W m^{-2} for both cases). Note that at Cabauw, when θ is predicted nicely and q is somewhat overestimated with the $0.25K$ YSU simulation (top Figures 5.2, light blue dotted lines), $L\downarrow$ is still underestimated, which indicates an in-correctness in the radiation schemes. This was also recognized by Wild *et al.* (2001), who found that $L\downarrow$ was mostly underestimated in global circulation models, especially in cold and dry climates. In our study, different radiation schemes gave similar results, as was shown in Part 1. For Sodankylä an overestimation of $L\downarrow$ was found, up to 8 W m^{-2} for the reference case with MYJ and smaller for YSU. Though the T_{2m} and $L\downarrow$ for YSU are simulated almost correctly for Sodankylä, still $Q*$ is underestimated. With a too strong stratification with YSU, T_{skin} becomes too low (especially at the start of the simulation, not as clear in the profiles after 9h in Figure 5.2), leading to an underestimated $L\uparrow$ on average.

For Cabauw and Sodankylä a closer agreement with observations is found with YSU than with MYJ when looking at the variables of T_{2m} and $Q*$. Due to the weaker connection with the surface with YSU (smaller H and a lower eddy diffusivity in the BL), a stronger stratification is found explaining the better performance for T_{2m} and $Q*$.

Regarding the relative contribution of the processes, it appears that for this set of

variables, mixing is relatively more important for the sites with stronger temperature stratification, than with the variables from Figure 5.3. Again, coupling seems to be relatively more important at Halley, while radiation plays a bigger role at Cabauw.

Temporal evolution

The supplementary material (end of this chapter) shows the process diagrams for radiation through time. For Cabauw and Sodankylä we see that both for the observations and the simulations, the general trend in time is that T_{2m} decreases, and $Q*$ becomes less negative, as we would expect. For Halley this is not the case for the observations. Here, the position of the observation remains the same, due to the strong advection in combination with the already present polar night (see also Part 1, T_{2m} stayed around 244 K). For MYJ at Halley, T_{2m} and $Q*$ also stay rather similar. For YSU there was indeed a stronger decrease in T_{2m}, as was also seen in Part 1 with the reference case, combined with a less negative $Q*$ due to a smaller $L\uparrow$.

The change in $Q*$ becomes smaller in time with a similar variation in T_{2m}, so a 'flattening' of the lines, for all sites and each process. This is due to that at the start of the simulation the strongest impact is at the surface to which $L\uparrow$ is directly linked, while it takes some time before this signal is transferred to the 2 m level. Indeed throughout time the jump in the sensitivity analysis sets is largest in the first time interval, and more in the direction of less negative $Q*$ than in the direction of lower T_{2m}, while later the changes are smaller, and not as strongly in the less negative $Q*$ direction.

5.5.3 Turbulent mixing

The last process diagrams represent the process of atmospheric mixing where H versus the temperature difference between 2 m and the surface are displayed, both averaged over 9h of simulation (Figure 5.5). Overall, when coupling and radiation strengthen, more energy is available at the surface resulting in a smaller temperature difference, causing H to decline. The opposite for weaker coupling and radiation intensities occurs. For modified mixing, we see a line perpendicular to this orientation. Mixing is modified by multiplying the eddy diffusivities and exchange coefficients with a certain factor, thereby automatically altering H. So when mixing increases, a larger H is found and vice versa. More mixing does result in a more efficient exchange of heat close to the surface, resulting in a smaller temperature difference close to the surface (which somewhat counteracts the increase in H) and vice versa.

MYJ vs YSU

Comparing the mixing lines of MYJ and YSU (blue full and dotted lines respectively), the change in H is smaller for a similar temperature difference with YSU, i.e. the line is more 'flat'. So apparently, the counteracting process of reduced temperature gradient with enhanced mixing is relatively stronger with YSU than with MYJ, while also eddy diffusivities are larger with MYJ than YSU which reflects directly in H when multiplying K.

As with the mixing process, the orientations of radiation and coupling are also more 'flat' with YSU compared to MYJ for Cabauw and Halley, while for the orientation at Sodankylä this is the other way around. However, also the relative orientation

of the reference point to the origin in the plot (when dT and H are 0) is different: for Cabauw and Halley then the reference YSU is more flat, while at Sodankylä the MYJ-reference is more flat. The coupling and radiation processes more or less follow this reference orientation (for YSU this deviates more than for MYJ).

Interesting is the YSU line for Sodankylä for a radiation increase with q using multiplication factor 2 (dark green dotted line). At the start of the run, this simulation became unstably stratified with positive values for H. This explains a smaller H for the 9h average. Also, the surface seems to 'recover' from this unstable stratification

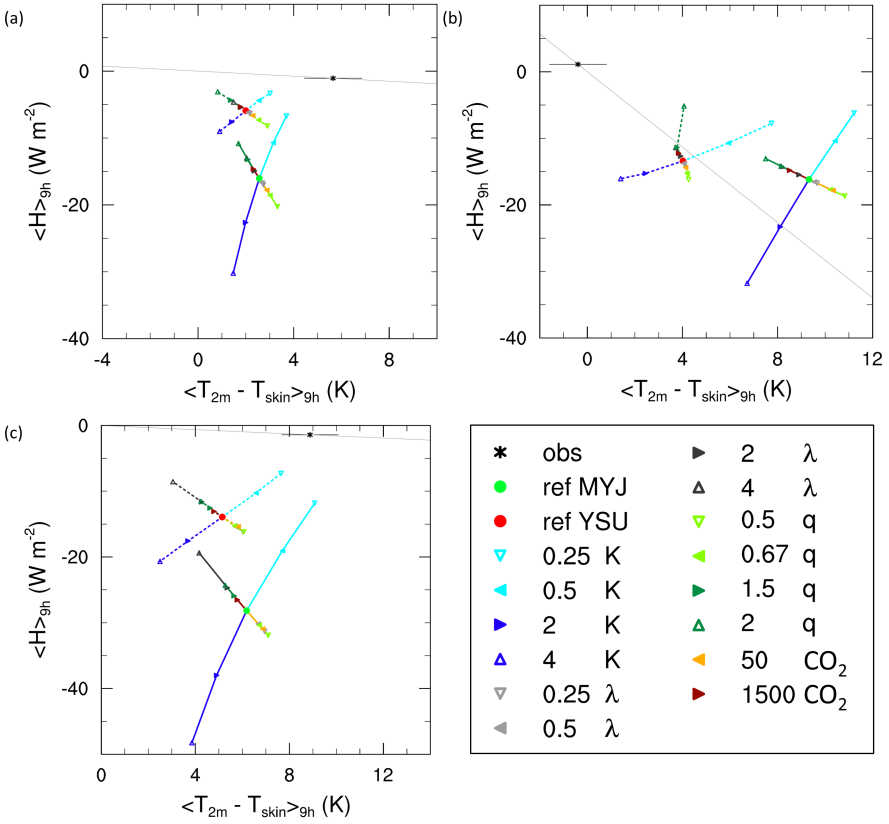

Figure 5.5: The temperature difference between the 2 m level and the surface ($< T_{2m} - T_{skin} >_{9h}$ (K)) versus the sensible heat flux ($< H >_{9h}$ (W m^{-2})), both averaged over 9h for a) Cabauw (then the observed H is averaged over only the first 4h due to an incomplete dataset), b) Sodankylä and c) Halley. K represents the change in mixing in both boundary and surface layer, λ represents the ice conductivity and thus the coupling, q represents the specific humidity profile and therefore the incoming long wave radiation, and CO_2 represents the amount of CO_2 in ppmv and therefore also the incoming long wave radiation. std MYJ is the reference for the simulations with the MYJ-BL scheme (full lines) and std YSU is the reference for the simulations with the YSU-BL scheme (dashed lines). The asterisk with error bars represents the observation with its measurement uncertainties in the error bars. The lines through the observational points and the origin, connect all points with a similar mixing as observed.

sooner than the 2 m level which explains the increase in temperature difference.

What is remarkable, is that for all sites, the atmospheric θ stratification seems smaller with MYJ than with YSU (Figure 5.2). However, the process diagrams indicate a larger temperature difference between 2 m and the surface for MYJ for all locations (most obvious for Sodankylä). This is explained by the relatively larger eddy diffusivities K with MYJ compared to YSU, in combination with relatively small exchange coefficients C, e.g. the ratio K/C is larger with MYJ than with YSU. Then the BL is able to mix e.g. heat more efficiently in the BL with the larger K giving relatively higher temperatures in the BL, but the surface layer cannot keep up with this efficient mixing with the smaller C, and thus the temperature difference between the surface and the first model level becomes rather large. Thus it seems that YSU has a more consistent transition from the surface-layer exchange coefficients to BL eddy diffusivities than MYJ. As mentioned by Svensson and Holtslag (2009) one should be careful in matching the surface layer and BL parametrizations. This deficiency in MYJ may be enhanced by the imposed background diffusivity in the BL that may not match with the lower limit on the exchange coefficients in the surface layer.

Site intercomparison

When we compare the three sites, we find again a change in the strength of the sensitivity. Regarding the mixing lines: for both BL schemes these are steepest for Cabauw (e.g. strongest change in H per $\mathrm{d}T$), and flattest at Sodankylä (weakest change in H per $\mathrm{d}T$). The other process sensitivities are not as straightforward: with YSU radiation and coupling are flattest at Cabauw and steepest at Sodankylä, while with MYJ this is opposite. As mentioned earlier, also the relative position of the reference points in the process diagram compared to the origin is different. E.g. the reference point compared to the origin is already flatter with YSU at Cabauw and Halley, and flatter with MYJ at Sodankylä, so that when radiation and coupling lines follow more or less the same mixing strength as the reference run, this results in flatter lines respectively as well.

Again, we find that the impact of radiation is larger for Cabauw and Sodankylä than for Halley, while for Halley the impact of coupling is stronger. Mixing seems also somewhat more important for this set of variables for Sodankylä and Halley, possibly due to the stronger stratifications found here and hence the stronger impact on temperatures close to the surface when the mixing intensity is modified.

Comparison with observations

In these stable conditions, the magnitude of H is not very large. For Cabauw, the dataset of H was incomplete for the duration of the night and is therefore averaged over only the first 4h (black asterisk). The model simulations overestimate H, though the temperature gradient remains underestimated. Decreased mixing brings the model simulations closer in agreement with the measured H, and also improves the temperature gradient.

The observed H at Sodankylä is slightly positive with a positive temperature gradient between the surface and the 2 m level, though the uncertainty indicates that this could be negative. Though the lowest two model levels in the θ profile indicate a stable stratification, the gradient is a bit smaller than for the higher tower

levels, due to that the lower part of the tower is in between the trees. Furthermore, H in time has very small values around zero, which explains that the average can be positive. It should be noted that the Sodankylä site is rather heterogeneous. Measurements of T_{2m} and the radiation components and hence T_{skin} are from a more open site than H measured along the tower in between trees. The WRF-SCM simulations overestimate the magnitude of H en $\mathrm{d}T$. With YSU a slightly smaller H magnitude is forecasted, combined with a smaller temperature gradient, compared to MYJ. For both BL schemes, decreasing the mixing does give a smaller H, though this overestimates the temperature gradients even more.

For Halley we also find small fluxes for H, which are overestimated by the model together with an underestimated ΔT. YSU shows simulations closer in agreement with the observed H, while MYJ has simulations closer in agreement with the observed ΔT. Reducing mixing brings the simulations closer to observations.

Finally, we must note that the eddy-covariance measurements at the different sites are not located directly at the surface, but some meters above it (3 m at Cabauw, 8 m at Sodankylä and 4 m at Halley). With these strongly stable conditions, it is questionable whether these measurements then occur in the constant flux layer (Foken, 2008a), or the lower 10% of the BL. As is seen in Figure 5.2, the observed LLJ at Halley is at around 8 m, which suggests the BL height to be at around the same height. For Sodankylä the LLJ is somewhat higher, but clearly below 80 m. Thus the measured H could be underestimating H closer to the surface.

Temporal evolution

The supplementary material (end of this chapter) also presents the process diagrams for turbulent mixing through time. At Cabauw, the orientation of the observed lines stays similar in time, with a smaller temperature gradient and H. At Sodankylä the observations turn around the origin, thus changing the orientation. Since both variables are very close to zero, the observations are very sensitive to measurement uncertainties regarding the sign. At Halley, the orientation changes slightly with an increase in altered H per $\mathrm{d}T$ (line steepens).

Regarding the orientation of the radiation and coupling process with YSU through time, we find the same orientation at Cabauw, a larger change in H per $\mathrm{d}T$ (steeper line) at Sodankylä, and a smaller change per $\mathrm{d}T$ (flatter line) at Halley. The YSU mixing line becomes more flat in time for all sites (smaller change in H per $\mathrm{d}T$). The MYJ mixing line on the other hand, shows a steepening of the line. The MYJ radiation and coupling orientations stay about similar in time for all locations. Furthermore, for all sites the impact of radiation with MYJ and YSU becomes smaller in time (line length decreases). This also holds for the mixing process with YSU at Cabauw and Sodankylä. It could be that the relative impact of the processes decreases in time due to that the strongest changes in e.g. T_{skin} are found in the beginning of the runs. Therefore, the impact averages out after more hours, when changes in time are not as strong.

5.6 Discussion and conclusions

This study analyses the relative impact of snow-surface coupling, downward long wave radiation, and turbulent mixing on the development of the stable boundary

layer (SBL) over snow, using the WRF single-column model as a research tool. The focus is on clear-sky conditions with low wind speeds. Three contrasting snow-cases over grass (Cabauw, The Netherlands), forest (Sodankylä, Finland) and an ice shelf (Halley, Antarctica, modelled as sea ice in WRF) were studied. Part 1 covered an evaluation of the SCM simulations for varying forcings. The sensitivity analysis presented here, is performed by varying the intensity of the three processes, for the simulation with optimized forcings from Part 1. For mixing, the boundary-layer eddy diffusivities and surface-layer exchange coefficients were adjusted, while for coupling the snow conductivity was adjusted. The incoming long wave radiation ($L\downarrow$) was altered by varying the initial specific humidity profile (q) and secondly by varying the amount of CO_2.

The sensitivity analysis is performed for both MYJ and YSU boundary-layer (BL) schemes. With increased mixing, the magnitude of the sensible heat flux (H) increased, and potential temperature (θ) and q inversions weakened. The low-level jet is less developed and at a higher altitude. The resulting smaller surface cooling leads to smaller conductive snow-heat fluxes (G), larger outgoing long wave radiation ($L\uparrow$), and a more negative net radiation ($Q*$). With increased snow conductivity, we find less cooling in time at the 2 m level and a more negative $Q*$. The impact of coupling on the q profile is very small (except for Halley), while the impact is negligible for wind speed. With increased $L\downarrow$, also θ and q inversions weakened, resulting in smaller G and H. The wind profiles are not very sensitive to the altered $L\downarrow$.

Concerning differences between the MYJ and YSU-BL schemes, we find:

- stronger atmospheric θ stratifications with YSU than with MYJ, while stratifications over the surface layer are strongest for MYJ. Furthermore, weaker q inversions are simulated with YSU than with MYJ, while the moisture surface inversions must be higher with YSU due to the lower T_{skin} and higher q in the atmosphere. Therefore, temperature and moisture are simulated differently between these schemes and/or their accompanying surface-layer schemes.

- H changes more profoundly for MYJ than for YSU for a certain T_{2m} - T_{skin}, which implies a more efficient eddy diffusivity in MYJ, and a stronger counteracting behaviour of reduced temperature gradient with enhanced mixing for YSU.

- a non-linearity with YSU for very low mixing intensities regarding temperature: T_{2m} increased for both increased and decreased mixing. With very light turbulence, cold air is not mixed upward sufficiently. Therefore, T_{2m} remains warmer than when mixing is increased. MYJ captured this behaviour only weakly at Halley. Reducing the background diffusivity did show the non-linearity with MYJ.

- a non-linearity clearest with MYJ at Halley for moisture: q_{2m} increased for both increased and decreased mixing, indicating a different treatment of moisture and temperature in both schemes.

- a non-linearity for $Q*$ with YSU at Cabauw and Sodankylä with the q-simulations: $Q*$ increased in magnitude for both increased and decreased q.

Overall, we conclude that:

- the radiation impact was relatively large for Cabauw and Sodankylä, most obviously so when q is adjusted. For these cases a higher humidity was present and therefore a larger impact on $L\downarrow$ is obtained.

- coupling is relatively more important at Halley. In the sea-ice coding in WRF the entire underlying medium is set to the snow conductivity which thus causes a higher impact of changing this variable. Furthermore, at Halley the snow cover is 100%, while this is about 83% at Cabauw (some grass sticks through the snow cover) and 55% at Sodankylä (though the ground was entirely covered by snow, trees still stick through). Therefore the influence of the unchanged underlying medium is larger at the last two sites, reducing the impact of the modified snow conductivity.

Note that some differences between the sites could also occur due to that atmospheric conditions are not exactly equal. Furthermore, the resolution of the top layer differs for the three sites, because it is a composite of the snow depth and the first soil layer in the WRF model. For the comparison between the three locations, a similar resolution would be desirable. However, in this study we aimed to compare the WRF model behaviour as is, without making too many modifications in the code.

Besides studying the processes sensitivities, we aim to quantify whether altered process intensities improve the model results compared to observations. We find that:

- G is greatly overestimated for Cabauw due to a higher snow conductivity in the model than was applied for the observed G. Also, G was determined through the (top) snow layer, assuming full snow cover (which is not true for Cabauw and Sodankylä), while WRF determines G from the snow layer and half of the top soil layer. We recommend to revise the determination of the snow conductivity in the WRF model, because now for fresh snow rather large values are applied.

- $Q*$ is strongly too negative for Cabauw and Halley. The simulation at Cabauw with YSU and 0.25 mixing, gave good results for the θ profiles and somewhat too high q profiles, but still $L\downarrow$ was underestimated, hinting at a deficiency in the long wave radiation scheme. Wild *et al.* (2001) attribute this to a problem in the simulation of the thermal emission from cold, dry and cloud-free atmospheres.

- the magnitude of H is overestimated by the WRF-SCM simulations. It could be that the measured H is underestimated when the eddy covariance is located above the constant flux layer.

- the θ stratification at the surface is underestimated for Cabauw and Halley. At Sodankylä the temperature stratification between the surface and the 2 m level is overestimated using data from the automatic weather station in a more open land. The Sodankylä tower located in a forested area, indicated that the stratification is underestimated with MYJ and overestimated with YSU.

Overall, we conclude that for most variables the WRF-SCM skill improves when mixing is decreased, mostly so for the YSU-BL scheme due to the stronger θ inversion along the tower (though still temperatures are strongly underestimated at Halley), while for MYJ then also q clearly improves. Unfortunately, apart from at Halley with YSU, the wind speed skill deteriorates with decreased mixing. Decreasing the coupling also improves the temperature and moisture gradients without strongly affecting the wind field, though the impact is less strong than reducing mixing. Decreasing $L\downarrow$ also gives stronger gradients, but this is not recommended due to the already underestimated $L\downarrow$.

Though the model results are not always in agreement with the observations, we must keep in mind that measurements can be uncertain due to technical and representation issues. Indeed measuring under these extreme conditions is challenging (Lazzara *et al.*, 2012; Mikolajczyk *et al.*, 2012; Tjernström *et al.*, 2014). Moreover, we noticed that the observed energy balance did not close, though we did not take into account the additional terms as in Heusinkveld *et al.* (2004). Though often the observed energy balance does not close with eddy covariance (Foken, 2008b; De Roode *et al.*, 2010; Steeneveld *et al.*, 2011) and the fluxes combined are not totally able to explain the available energy, uncertainties in the fluxes could be larger than the error bars in the presented process diagrams. Therefore it is difficult to make firm conclusions of the model results in comparison with observations from these particular cases. All in all, it is clear from this study, that not only different schemes, but also different process intensities have a great influence on the performance of the WRF-SCM.

A last point of discussion is that we prescribed advection for temperature, humidity and momentum, which followed from WRF-3D simulations with normal process intensities, as described in Part 1. Here in Part 2, the same advection is prescribed for the simulations with modified process strengths, but with a certain adjusted process strength, the advection amount needed, could change. We recommend an analogous study in a 3D model, when the advection would adjust itself accordingly.

Acknowledgements

We thank Dr. Reinder Ronda (Wageningen University) for his valuable discussions regarding WRF-related issues. Furthermore, we would like to thank the KNMI (Royal Netherlands Meteorological Institute), the FMI (Finnish Meteorological Institute) and the BAS (British Antarctic Survey) for the measurement data that was used in this study. We also thank the ECMWF for the boundary conditions that were used in the WRF-3D simulations. We acknowledge the support from NWO (The Dutch Science Foundation) with grant 829.09.005 ("Quantifying contributions of surface climate feedbacks to the Arctic amplification of greenhouse warming" in the Sustainable Earth program). The contribution by G.J. Steeneveld has partly been sponsored by the NWO contract 863.10.010 (Lifting the fog).

A1. Supplementary figures

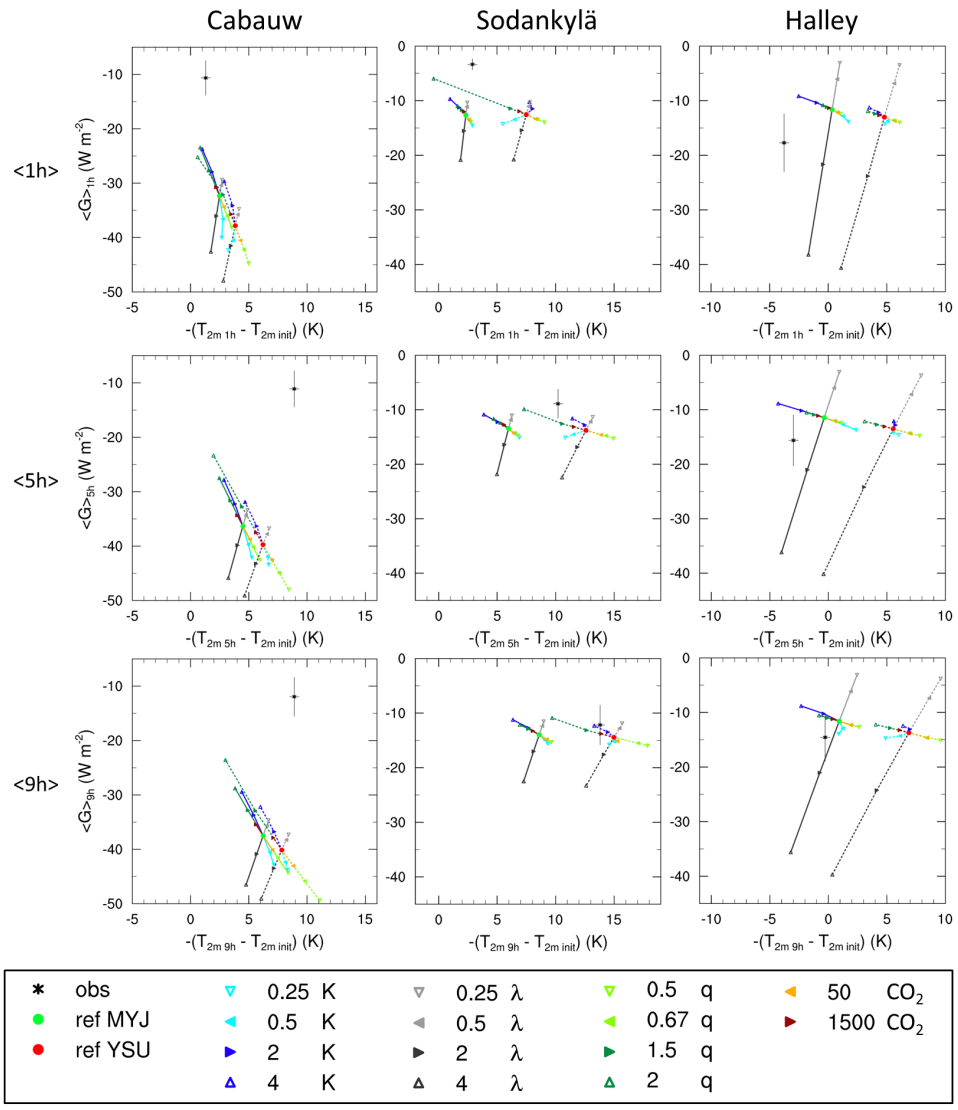

Figure 5.6: Cooling of the 2 m temperature (-($T_{2m\ xh} - T_{2m\ init}$) (K)) over xh versus the soil heat flux ($< G >_{xh}$ (W m^{-2})) averaged over xh for Cabauw (left column), Sodankylä (middle column) and Halley (right column) for various averaging times < xh > since the start of the simulation, i.e. an averaging time of 1h for the top row, 5h for the middle row, and 9h for the bottom row. K represents the change in mixing in both boundary and surface layer, λ represents the ice conductivity and thus the coupling, q represents the specific humidity profile and therefore the incoming long wave radiation, and CO_2 represents the amount of CO_2 in ppmv and therefore also the incoming long wave radiation. ref MYJ and ref YSU are the reference for the simulations with the MYJ-BL (full lines) and YSU-BL (dashed lines) scheme respectively. The asterisk with error bars represents the observation with its measurement uncertainties in the error bar.

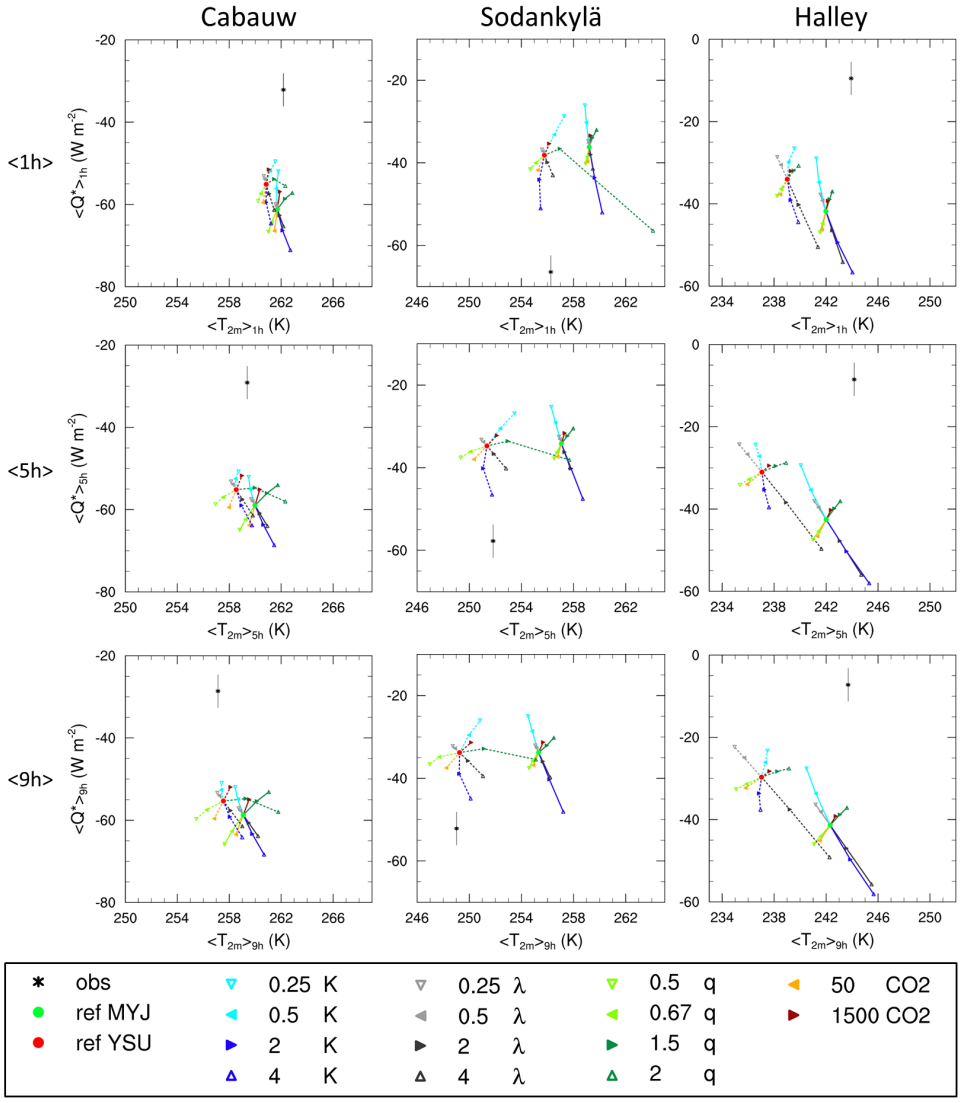

Figure 5.7: The 2 m temperature ($< T_{2m} >_{xh}$ (K)) versus the net radiation ($< Q^* >_{xh}$ (W m^{-2})), both averaged over xh for Cabauw (left column), Sodankylä (middle column) and Halley (right column) for various averaging times < xh > since the start of the simulation, i.e. an averaging time of 1h for the top row, 5h for the middle row, and 9h for the bottom row. K represents the change in mixing in both boundary and surface layer, λ represents the ice conductivity and thus the coupling, q represents the specific humidity profile and therefore the incoming long wave radiation, and CO_2 represents the amount of CO_2 in ppmv and therefore also the incoming long wave radiation. ref MYJ and ref YSU are the reference for the simulations with the MYJ-BL (full lines) and YSU-BL (dashed lines) scheme respectively. The asterisk with error bars represents the observation with its measurement uncertainties in the error bar.

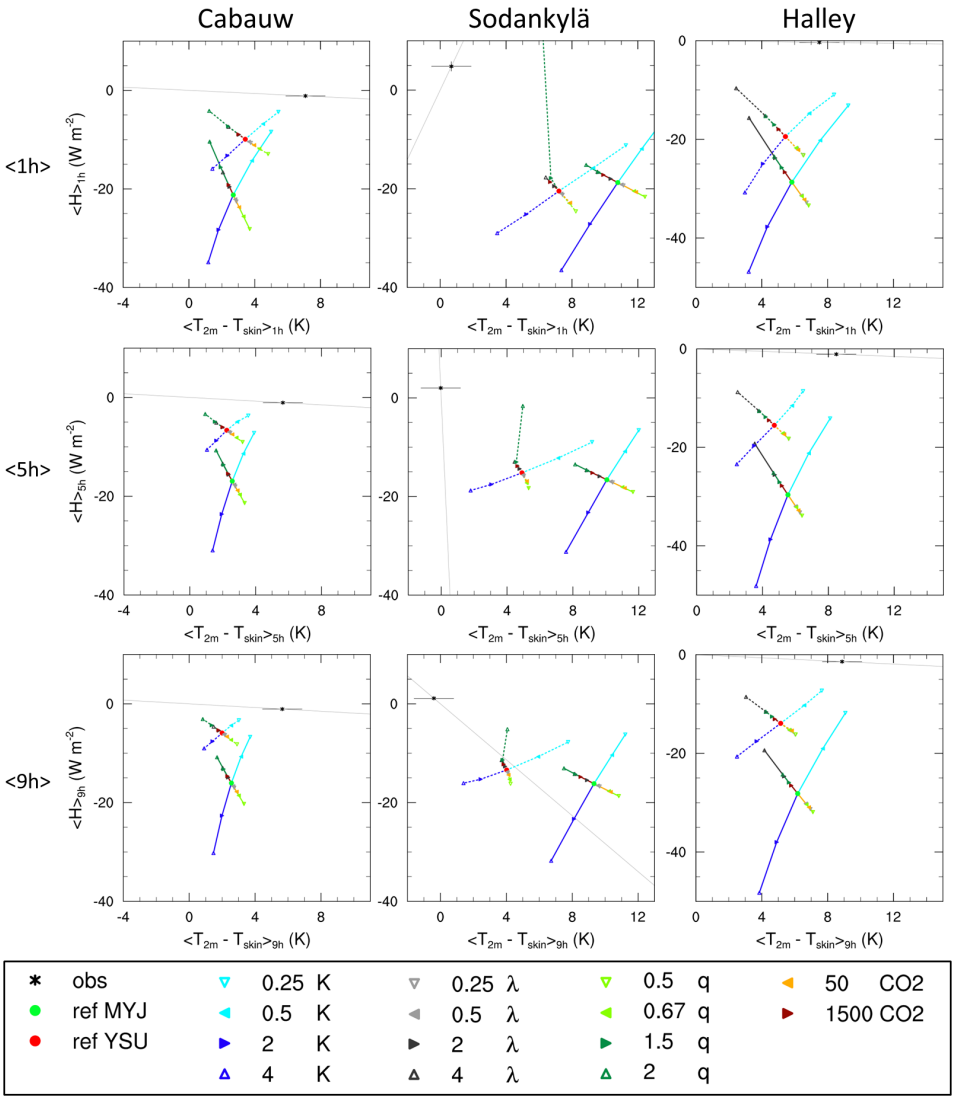

Figure 5.8: The temperature difference between the 2 m level and the surface ($< T_{2m} - T_{skin} >_{\mathrm{xh}}$ (K)) versus the sensible heat flux ($< H >_{\mathrm{xh}}$ (W m^{-2})), both averaged over xh for Cabauw (left column, observed H only averaged over 4h for the 5 and 9h figures due to missing data), Sodankylä (middle column) and Halley (right column) for various averaging times < xh > since the start of the simulation, i.e. an averaging time of 1h for the top row, 5h for the middle row, and 9h for the bottom row. K represents the change in mixing in both boundary and surface layer, λ represents the ice conductivity and thus the coupling, q represents the specific humidity profile and therefore the incoming long wave radiation, and CO_2 represents the amount of CO_2 in ppmv and thus also the incoming long wave radiation. ref MYJ and ref YSU are the reference for the simulations with the MYJ-BL (full lines) and YSU-BL (dashed lines) scheme respectively. The asterisk with error bars represents the observation with its measurement uncertainties in the error bars. The lines through the observational points and the origin, connect all points with a similar mixing as observed.

Chapter 6

Summary

The emphasis of this thesis is on the understanding and forecasting of the Stable Boundary Layer (SBL) over snow-covered surfaces. SBLs typically form at night and in polar regions (especially in winter), when radiative cooling at the surface causes a cooler surface than the overlying atmosphere and a stable stratification develops. This means that potential temperature increases with height and buoyancy effects suppress turbulence. Turbulence is then dominated by mechanical origin. If sufficient wind shear can be maintained, turbulence remains active, otherwise it will cease.

A proper representation of SBLs in numerical weather prediction models is critical, since many parties rely on these forecasts. For example, weather prediction is needed for wind energy resources, agricultural purposes, air-quality studies, and aviation and road traffic. Knowledge on SBLs is also essential for climate modelling. In the Arctic regions, climate change is most pronounced due to stronger changes in near-surface temperature compared to other latitudes. Though this 'Arctic amplification' is not yet fully understood, possible responsible processes are the ice-albedo feedback, alterations in cloud cover and water vapour, different atmospheric and oceanic circulations, and the weak vertical mixing in the lower atmosphere. However, many interactions exist between these processes. With positive feedbacks, changes are even further enhanced. This could have worldwide consequences, i.e. due to affected atmospheric circulations and sea level rise with Greenland's melting ice-sheets.

Scientists try to explain the observed climate changes, as well as provide outlooks for future changes in climate and weather. However, the understanding is hampered by the fact that many model output variables (e.g. regarding the 2 m temperature) vary substantially between models on the one hand, and from observations on the other hand. Modelling the SBL remains difficult, because the physical processes at hand are represented in a simplified way, and the understanding of the processes may be incomplete. Furthermore, since processes can play a role at a very small scale, the resolutions in models may be too poor to represent the SBL correctly. Additionally, there are many different archetypes of the SBL. Turbulence can be continuous, practically absent, or intermittent, and vary in strength which affects the efficiency of the exchange of quantities horizontally and vertically.

Processes that are considered critical for the SBL evolution are e.g. turbulent mixing, radiative effects, the coupling between the atmosphere and the underlying surface, the presence of clouds or fog, subsidence, advection, gravity waves, and drainage and katabatic flows. In this thesis, the focus is on the first three processes,

as these are most dominant for the evolution of the SBL (e.g. Bosveld *et al.*, 2014b).

In Chapter 3 an idealized clear-sky case over sea-ice was studied based on the GABLS1 benchmark study (e.g. Cuxart *et al.*, 2006), but extended by including radiative effects and thermal coupling with the surface. Hence the following research questions were posed:

> ***Question 1:*** *What is the variety in model outcome regarding potential temperature and wind speed profiles that can be simulated with one model by using different parametrization schemes?*
>
> ***Question 2:*** *Which of the three governing processes is most critical in determining the SBL state in various wind regimes?*
>
> ***Question 3:*** *Can we identify compensation mechanisms between schemes, and thus identify where possible compensating model errors may be concealed?*

From the analysis with different parametrization schemes performed with the WRF single-column model (SCM, Question 1), it followed that quite different types of SBLs were found. Some schemes forecasted a somewhat better mixed potential temperature profile where stratification increased with height, while another scheme produced profiles with the strongest stratification close to the surface and stratification decreased with height. After only 9 h of simulation time, a difference in temperature of almost 2 K was found near the surface. Regarding the wind speed profile, some variation was found in the simulated low-level jet speed and height. Mainly the difference in atmospheric boundary-layer (BL) schemes which parametrize the turbulent mixing are responsible for these model output variations. A variation in long wave parametrization schemes hardly affected the model results.

Question 2 addresses the problem whether other processes than turbulent mixing may be responsible for a similar spread in model results. A sensitivity analysis was performed where for one set of reference parametrization schemes the intensity of the processes was adjusted. The relative sensitivity of the three processes for different wind regimes was analysed using 'process diagrams'. In a process diagram, two physically related variables are plotted against each other, which in this case represent either a time average or a difference over time of the variable. A line connects the reference state with the state for which the process intensity is modified. By comparing the length and orientation of the lines, the relative significance of the individual processes for the different wind speeds can be studied. Overlapping line directions identify possible compensating errors.

Geostrophic wind speeds of 3, 8 and 20 m s^{-1} were selected representing low, medium and high wind speeds, capturing the range of wind speeds frequently occurring in the Arctic north of 75°N according to the ERA-Interim reanalysis dataset. Overall, a shift in relative importance was detected for the various wind regimes. With high geostrophic wind speeds, the model output is most sensitive to turbulent mixing. On the contrary, with low geostrophic wind speeds the model is most sensitive to the radiation and especially the snow-surface coupling. The impact of turbulent mixing is then minor, unless when mixing in both boundary layer and surface layer is adjusted. This stresses that proper linking between these two layers is essential.

Also with one set of parametrization schemes different SBL types were simulated. Potential temperature profiles were better mixed (increasing stratification with height) for high geostrophic wind speeds, and this tended to develop to profiles with the strongest stratification near the surface (decreasing stratification with height) for low geostrophic wind speeds. However, a variety in types was also found when keeping the same wind regime, but by varying the mixing strength. With enhanced mixing, the profile became better mixed, also when the reference profile showed the strongest stratification near the surface. With decreased mixing, profiles with a stronger stratification were found, again shaped with the strongest stratification near the surface. Thus a different mixing formulation has a strong impact on the vertical profiles, even when it may not necessarily strongly affect the surface variables. Therefore, it is recommended that when a model is evaluated and optimized, the vertical structure is also regarded in this process, since near-surface variables may be well represented, strong deviations aloft are still possible.

Furthermore, the process diagrams showed overlap in sensitivity to some processes. Therefore errors within the parametrizations of these processes could compensate each other and thus remain hidden (Question 3), making the model formulation possibly physically less realistic. This study did not reveal an unambiguous indication for the compensating processes regarding the various sets of variables, though overlap for single variables is seen.

This study also revealed a non-linear behaviour regarding the 2 m temperature, which is also found in observations (e.g. Lüpkes *et al.*, 2008) and in a model study by McNider *et al.* (2012). Here the 2 m temperature decreased with enhanced mixing strength and increased with a lower mixing intensity. This counter-intuitive behaviour is explained by that mixing only occurs in a shallow layer close to the surface. Cold air that is mixed up by the enhanced mixing, is insufficiently compensated by the downward mixed relatively warm air. This behaviour was found mostly for low wind speeds or with decreased mixing at the medium wind regime, when the potential temperature profile showed the strongest stratification near the surface.

The study proceeds with a model evaluation against observations in low wind speed regimes. Three stably stratified cloud-free study cases with near-surface wind speeds below 5 m s^{-1} were selected with each a different surface: Cabauw in the Netherlands with snow over grass, Sodankylä in northern Finland with snow in a needle-leaf forest, and Halley in Antarctica with snow on an ice shelf.

Chapter 4 presents the evaluation of the WRF-3D and SCM for these cases. In this study, the WRF-3D model was used to determine the forcings, as often not all the required observations at high resolution in time and space are available. Hence the following questions were formulated:

> ***Question 4:*** *What is the performance of WRF in stable conditions with low wind speeds for three contrasting snow-covered sites?*
>
> ***Question 5:*** *How should we prescribe the single-column model forcings, using WRF-3D?*

The standard WRF-3D simulation had an incorrect representation of the snow-cover and vegetation fraction, which deteriorates the conductive heat flux, the surface

temperatures and the SBL evolution. Indeed, Chapter 3 highlighted the critical role of the land-surface coupling representation. Adjusting the settings with site specific information, improved model simulations compared with the observations.

In general, the performance of WRF-3D was quite good for the selected cases, especially regarding the wind speed simulations. The temperature forecast proved to be more challenging. For Cabauw and Sodankylä, 2 m temperatures were strongly overestimated, though a better simulation was seen at higher tower levels. For Halley a better representation of the 2 m temperature was found, though aloft potential temperatures were underestimated. Hence, the three cases had an underestimated modelled temperature gradient in common.

This study also investigated how the forcing fields for the SCM should be prescribed. Model results for the three study cases all showed a significant deviation from the observed wind field without lateral forcings and time-invariant geostrophic wind speed. Including only a time-varying geostrophic wind speed did not improve the results. Prescribing additional momentum advection did have a positive impact on the modelled wind speed. The results regarding temperature, specific humidity and their stratification improved when temperature and humidity advection was also taken into account. Forcing the SCM field towards a prescribed 3D atmospheric state is not recommended, since unrealistic profiles were found below the threshold forcing height.

Having established the optimal model set-up, the SCM can be used as a tool to further study the small-scale processes for the three study cases, addressing the following questions:

> ***Question 6:*** *How do the model results with various process intensities compare with observations?*
>
> ***Question 7:*** *Are any differences in relative process impacts found for the three contrasting sites?*
>
> ***Question 8:*** *Does the model sensitivity vary between two different BL schemes?*

The sensitivity analysis was performed with the WRF-SCM and repeated for two BL schemes. In general, the temperature and humidity stratifications intensified by decreasing the process strengths and hence were in better agreement with observations than the reference cases. The wind field was most sensitive to turbulent mixing, with a weaker low-level jet at a higher altitude for enhanced mixing and the opposite for less mixing, while the impact of the other processes was small. Contrary to the temperature profiles, a better agreement with wind observations was found with amplified mixing, except for Halley where results improved with reduced mixing.

Regarding the surface energy budget, the conductive heat flux was greatly overestimated at Cabauw due to an overestimated snow conductivity, while better agreements were found for the other sites. A revision of the definition for snow conductivity in the model is recommended, because rather large values were assumed for fresh snow, and indeed results improved when the coupling strength was reduced for Cabauw and Sodankylä. For Halley almost the same snow conductivity was modelled as was used to determine the observed conductive heat flux, however, then the

temperature gradient through the first soil/snow layer was underestimated leaving the flux too small.

The net radiation was strongly too negative for the Cabauw and Halley case-studies. This is likely due to an underestimation of the incoming long wave radiation as part of a deficiency in the long wave radiation scheme. For all sites the sensible heat flux was overestimated, and decreased mixing improved the results. However, the eddy covariance measurements may have been made outside the constant flux layer, which hampers the model evaluation.

Though Question 6 aims to obtain understanding in which processes are most responsible for simulating model results that are in closer agreement with observations, measuring in these cold and dry circumstances is especially challenging. Furthermore, the measurements are mostly point measurements while the model grid represents a larger area, such that the measurements may be influenced by local features which are not captured in the model. These issues hinders a clear comparison of the model results with observations, and the observation uncertainties may be greater than what was represented in the process diagrams.

When comparing the process sensitivity for the different sites (Question 7), we found some distinct variations in relative process significance. The radiation impact was relatively large at Cabauw and Sodankylä where the specific humidity was higher such that a larger impact on the incoming long wave radiation can be obtained. The snow-surface coupling is more important at Halley. This is related to the higher snow cover at Halley compared to the other sites. Additionally, the conductivity of the underlying medium at Halley is set equal to that of snow. These two factors ensure that the impact of an altered snow conductivity is greater.

From the comparison of the sensitivity analyses for the two BL schemes (MYJ and YSU, Question 8), it followed that the overall direction of the sensitivity orientation is similar. However, stronger BL temperature stratifications were found with YSU, though between the surface and the first model level stronger stratifications were simulated with MYJ. This is related to the relatively high ratio of mixing in the boundary layer versus the surface layer with MYJ. Therefore the mixing in the BL is relatively more efficient and the surface layer cannot keep up the mixing to keep a smooth profile at the surface-layer / boundary-layer interface. This indicates the importance of a consistent transition between the BL and surface layer, as also pointed out by Svensson and Holtslag (2009). Furthermore, the non-linearity concerning the 2 m temperature behaviour discussed earlier is most profound with YSU, and not as obvious with MYJ due to a stronger implemented minimum diffusivity.

The results point towards the direction of focus for future research. This could be achieved by e.g. re-evaluating the snow representation, as well as investigating the long-standing problem of the underestimated long wave radiation. Additionally, the mixing seems to be too high in some of the simulations. As such, care should be taken in choosing the BL scheme and its constraints on the mixing, as these may hamper the development of the observed behaviour on non-linear near-surface temperature evolution for example.

Chapter 7

General discussion and outlook

The previous chapter summarized the findings of this thesis. This chapter describes some general discussions and some issues that were encountered during this thesis work which require further explanation and/or further research. This mostly concerns further model improvements, though the necessity of a good measurement network also became apparent which will be discussed below.

7.1 Generality of the results

In the previous chapters the relative importance of the turbulent mixing, the snow-surface thermal coupling, and the incoming long wave radiation was identified for night-time conditions. However, in Chapter 3 this was done for an idealized case with various wind speeds, such that it was not known how this compares with observations. When the sensitivity analysis was repeated in Chapter 5 for observed low-wind speed cases, in general a similar sensitivity was found, which gives confidence in the results found earlier. Furthermore, the general orientation of the sensitivity was comparable for different terrains, such that it is expected that the stable boundary layer will be affected similarly in other regions with comparable conditions. An extension of the sensitivity analysis could be to combine the altered process intensities (e.g. combining enhanced mixing with decreased coupling), and see how this impacts the state of the stable boundary layer, such that the feedbacks can be identified.

Regarding research question 7, differences in sensitivity analyses were studied for the various sites. However, we must keep in mind that the atmospheric conditions were not exactly equal, though we did try to ensure of several similarities such as clear-skies, relatively low wind speeds and stable stratifications. Furthermore, due to the representation of the snow pack on top of the soil in the model, different soil resolutions are applied for the three cases, which indeed occurs in practise as well for e.g. operational weather forecasts, but makes a straightforward comparison between the different sites more cumbersome. An extension of this research would be to vary the vertical resolution in the underlying snow pack for an identical case, to study the impact of the resolution on these cases.

To refrain from the more difficult interference with clouds and to enhance the probability of the development of a relatively stronger stably stratified boundary layer increases, only clear-sky conditions have been studied. Therefore it is recom-

mended that the process sensitivity is also analysed in cloudy conditions. As cloud radiation effects strongly impact the energy balance at the surface (e.g. Intrieri *et al.*, 2002; Pithan *et al.*, 2013) and interact with the temperature and specific humidity inversions (Vihma *et al.*, 2014), a different sensitivity to the processes could be found. The set-up of such a study needs care, as the variations in process strengths also affect the cloud development such that the individual simulations may consist of varying cloud characteristics, which impedes a straightforward comparison.

In fact, this difficulty is slightly similar to differences in surface forcing which followed from the process sensitivity carried out in Chapters 3 and 5. A doubling of the eddy diffusivity may not necessarily have the same impact as the doubling of thermal coupling. Therefore in Chapter 3 the sensitivity analysis was repeated for which the process strengths were adjusted such that the change in net radiation between the start and end of the simulation was similar for the different simulations. Comparable conclusions regarding the relative process sensitivity for various wind regimes were drawn. This approach might also be applied when a cloudy case is analysed. Alternatively, prescribing a certain cloud cover would assist in a more straightforward comparison. The drawback is that then physically realistic interactions are ignored, which may hamper further stable boundary layer understanding, as was found to be the case with prescribed surface temperatures (e.g. Van de Wiel, 2002; Holtslag *et al.*, 2007).

Pithan *et al.* (2013) performed a comparable process sensitivity analysis regarding turbulent mixing and snow-surface thermal coupling as in this thesis for a case with clouds. They studied the impact of various process strengths on the sensible heat flux and low-level stability for all time steps after the transition from cloudy to clear-sky conditions with a net long wave radiation being below -20 W m^{-2}, such that in effect only the process sensitivity on the clear state is considered. A similar approach with bounded conditions for cloudy cases could be applied to study the process sensitivity in cloudy conditions.

Besides that the sensitivity analyses in this thesis were restrained to clear-sky conditions, they were only performed with a single-column model. It remains a question how these findings will be affected when integrated in a 3D model with all the accompanying feedbacks and interactions known to us and that are included in the model. Figure 7.1 shows the 2 m temperature difference between a WRF-3D run where the snow conductivity is halved and a WRF-3D run using the standard snow conductivity, for the Sodanyklä case as described in Chapter 4. The simulations started on 0 UTC on the 26th of March, 2009, and the results are shown for 3 UTC on the 27th of March, 2009, which is at the end of the night. Micro-physics were still inactive, to prevent influence of clouds. For most of the area the 2 m temperature decreases, as was also found by the SCM studies performed in Chapter 3 and 5. However, some small areas also indicate an increase in temperature. Hence, the 3D picture seems not to be as straightforward as what was found with the SCM, and thus the sensitivity analysis study should be extended to the 3D field.

Intriguing would also be to see how this sensitivity holds on the longer time scales which is necessary for instance to study the Arctic's melting ice (Van den Broeke *et al.*, 2009; Graversen *et al.*, 2011) or the changes in atmospheric circulations (Lu *et al.*, 2004; Overland and Wang, 2010; Vihma, 2014; Walsh, 2014). The sensitivity

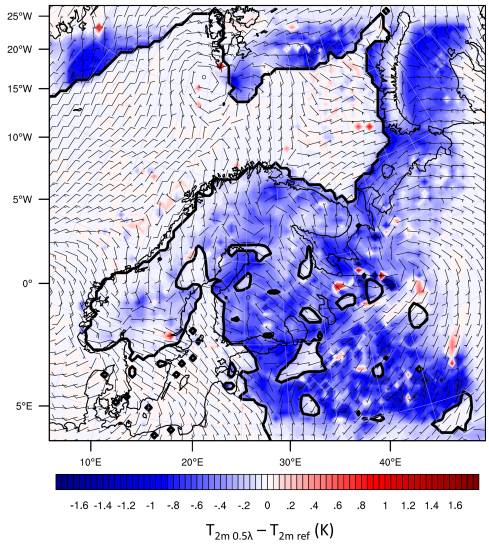

Figure 7.1: a) The difference in 2 m temperature between WRF-3D simulations with halved snow conductivity ($T_{2m\ 0.5\lambda}$) and the reference snow conductivity ($T_{2m\ ref}$). The thick black line indicates the area with more than 50% snow cover (present over most of Scandinavia, Russia and the Arctic regions).

analysis can be repeated with climate models. However, in that case it would be more difficult to attribute the cause of an event to a certain process, since the entire system is interconnected and many feedbacks are occurring for a long time.

Another aspect of the generality of the results regards the method of determining advection from the WRF-3D model. For all our three study cases, including this advection had a positive impact on the WRF-SCM simulations as was also found by Baas *et al.* (2010) and Bosveld *et al.* (2014a). However, the study was limited to cloud-free night-time conditions with low wind speeds over snow, and more extensive research for a wider range of conditions would be desirable to assess the more general applicability of the WRF-3D based advection, or other model based advections. The importance of quantifying the advection is also recognized by Vihma *et al.* (2014) as the Arctic's vertical structure is strongly affected by advective effects.

The flux-profile relations that were used for the turbulent transfer in the WRF model are based on Monin-Obukhov similarity theory (MOST). For this theory, homogeneous and stationary conditions are assumed. However, in very stable conditions the impact of local features on the flow may be relatively large compared to unstable conditions where small-scale heterogeneity disappears due to large eddies, such that MOST is no longer valid (Mahrt, 1999). Moreover, the existence of a constant-flux layer to ascertain the independence of the fluxes with height is assumed, but it remains questionable whether a constant-flux layer exists for very stable conditions (Mahrt, 1999; Sun *et al.*, 2003).

Besides of the validity of Monin-Obukhov similarity, there is also uncertainty in

the determination of the flux-profile relations that are used to determine the turbulent transfer (Mahrt, 1999; Yagüe *et al.*, 2006; Grachev *et al.*, 2007). Reasons for this could be that in very stable conditions the flux-measurements which are needed to determine the flux-profile relations from observations (Mahrt, 1999) become more difficult to measure. Also, in non-stationary and heterogeneous conditions, the contribution of non-stationary mesoscale motions on the flux becomes relatively large, such that the measurement results are sensitive to the choice of the averaging time (Vickers and Mahrt, 2006). Additionally, the problem of self-correlation exists between the flux-profile relation and the stability parameter z/L, as they have common variables (Baas *et al.*, 2006; Mauritsen and Svensson, 2007), such that measurement errors in these variables (i.e. u_*) can strongly affect the estimation of the flux-profile relationships. Flux-profile relations derived by Yagüe *et al.* (2006) and Grachev *et al.* (2007) indicate a levelling-off of the profile relations for increasing stability compared to the often used relation of $\phi_m = \phi_h = 1 + 5z/L$ (Businger *et al.*, 1971; Dyer, 1974). This would imply an underestimation of the flux with the Businger-Dyer function for strong stability (Yagüe *et al.*, 2006). Possibly implementing better validated flux-profile relations also for the very stable regime, would imply that less background diffusion is necessary. Mauritsen and Svensson (2007) and Grachev *et al.* (2012) demonstrated that flux-profile relations based on the gradient Richardson number instead of z/L may be more suitable for moderately and very stable conditions, as the vertical gradients are large and as such their errors relatively small, while furthermore self-correlation is avoided.

Further advances may also be obtained from higher resolution models, such as Large Eddy Simulation (LES) models. With LES, a higher resolution can be applied compared to numerical weather prediction models. Though then a smaller spatial domain can be simulated, relatively smaller eddies can be resolved such that it is less dependent on the parametrizations. With LES models, the weakly stably stratified boundary layer is simulated in agreement with observations (Beare *et al.*, 2006). However, with increasing stratification, LES models become more sensitive to the sub-grid-scale model within LES that parametrizes the smaller scale motions, such that these should be developed further for more reliable LES simulations as these were developed primarily for neutral and unstable flows (Poulos *et al.*, 2002; Beare *et al.*, 2006; Basu and Porté-Agel, 2006). Interestingly, LES results for the GABLS3 benchmark study, showed less sensitivity to the sub-grid-scale models (Basu *et al.*, 2012). Since radiative processes and land-surface coupling become more important for very stable conditions, it is essential that these processes are included in LES models (Basu and Porté-Agel, 2006). With simultaneously higher resolutions, more insight can be gained in for example the impact of heterogeneity on SBL structure and mixing efficiency (Mironov and Sullivan, 2012).

An even finer resolution is obtained with Direct Numerical Simulation (DNS) models for which also the turbulence scales are resolved. With DNS models valuable information regarding SBL processes can be obtained as well, e.g. regarding intermittency and collapsing turbulence (Ansorge and Mellado, 2014), though simulations are limited by the current space-time resolution that can be achieved in computers (Fernando and Weil, 2010). However, what is learned from LES and DNS studies, can also be applied on further development of numerical weather prediction model

parametrization schemes (Poulos *et al.*, 2002). With future increases in computational power, the issue of computational costs will become less apparent.

7.2 Observational challenges

Carrying out measurements in the polar regions is a difficult task (Lazzara *et al.*, 2012; Mikolajczyk *et al.*, 2012). With the extreme weather conditions that may occur, measurements may be impacted and equipment can break down from e.g. strong wind speeds, or freeze up when covered in rime/frost. Furthermore, snow may accumulate, such that the sensors are no longer at a fixed height above the surface, or become even entirely buried. Therefore it is important to visit the measurement stations on a routine basis. This is difficult as these areas are remote and not easily accessible, and weather conditions can swiftly change. Intensive measurement campaigns carried out with a ship for example are also challenging as influence of ship and humans on the measurements should be minimized, and ice drift complicates measurements that are connected to the ship for i.e. power supply (Tjernström *et al.*, 2014).

Due to the above mentioned challenges, in situ observations in the polar regions are relatively scarce, and often confined to the (near-)surface. In the Arctic, soundings that are available are mostly from coastal sounding stations and not as much from the Arctic Ocean (Tjernström and Graversen, 2009). Soundings may be launched in these areas during extensive measurement campaigns aboard ships for example (Uttal *et al.*, 2002; Tjernström *et al.*, 2014), though these are only available for relatively short-term periods. This lack of observations, hampers the further understanding of the (future) Arctic climate. Observations are also necessary to evaluate models and to possibly improve the representation of processes in models. Also for this thesis, more frequent information of the vertical structure of the atmosphere would have been desirable, i.e. for the model evaluation in Chapter 4.

From the model evaluation in this thesis, it followed that sometimes a meaningful interpretation of the observations is difficult. First of all, the sensible heat flux measurements at all sites were performed with the eddy covariance method. However, for this method it is assumed that the measurements take place in the constant flux layer, also seen as the lower 10% of the boundary layer. Especially at Sodankylä and Halley it remains questionable whether this condition is met since the atmospheric conditions are very stable and a low-level jet is found close to the surface, which implies a very thin boundary layer and thus the presence of a constant flux at a height below the measurement height. As such, the sensible heat flux may be measured incorrectly.

Further research is necessary on alternative methods to determine the sensible heat flux when the assumption of a constant flux layer at eddy-covariance measurement height is no longer valid. This is likely an often occurring problem when considering the very thin stable boundary layer. Simply measuring the eddy-covariance closer to the surface is not always a solution, as with a certain path length always a certain distance towards the surface should be maintained (Foken, 2008a) which could still be too high for the very stable boundary layer. However, for the Sodankylä site especially the eddy-covariance measurements are at a relatively high altitude of 8 m, such that better fluxes could be measured at a lower level in the open field

adjacent to the forest as well.

Furthermore, routine weather data can be used to estimate the fluxes instead of using eddy covariance measurements (Holtslag and Van Ulden, 1982; Van Ulden and Holtslag, 1985; Holtslag and De Bruin, 1988; Van den Broeke *et al.*, 2005; Van de Boer *et al.*, 2014). For example, Holtslag and Van Ulden (1982) found an almost constant value of the temperature scale θ_* of 0.1 K for clear-sky conditions. With the set of equations for the Obukhov length L being a function of θ_* and the friction velocity u_*, and an equation for u_* being a function of wind speed and L, the sensible heat flux could be determined. Also for other cloud conditions a dependence between u_* and θ_* was observed, such that semi-empirical relations could be obtained to derive the fluxes for more general cases. Holtslag and De Bruin (1988) determined a semi-emperical relation between u_* and θ_* which depends on the cloud cover and the conductive heat flux. Van de Wiel (2002) proposed to make this functional dependence explicit. This method could possibly be explored further. A drawback however, is that for these methods also use is made of the Monin-Obukhov similarity functions, for which it remains questionable whether these are valid for the stable conditions studied in this thesis, as discussed in the previous Section.

A second issue regarding the implementation of observations, is that the conductive heat flux that was calculated using observations, may not be representative for the average area, as this was determined from the temperature gradient through the snow pack assuming a certain conductivity. However, this flux then only represents the snow surface, while in fact for Cabauw and Sodankylä vegetation sticks through the surface such that the area average flux will be different. As such, this estimated observation is very local, while e.g. the sensible heat flux is measured at a greater height, such that it is representative of a slightly larger area or has a larger footprint than measurements closer to the surface. As will be discussed below, also the measured sensible heat flux is likely not representative for the model grid size area. Moreover, as found by e.g. Calonne *et al.* (2011) the conductivity varies both in horizontal and vertical direction, which is not taken into account. Also for a certain snow density, strong variations in conductivity are found (Calonne *et al.*, 2011; Domine *et al.*, 2012; Gouttevin *et al.* 2012). Possible advances could be obtained using remote sensing data. Tsuang (2005) showed that skin temperatures obtained from remote sensing techniques on-board satellites could be used to determine the conductive heat flux. With future techniques at higher resolution, more information on the spatial distribution of skin temperatures could be obtained. High resolution snow cover and vegetation / soil data would then also be required to determine the proper heat diffusion of the underlying medium needed to estimate the conductive heat flux.

Another constraint on the comparison between model results and measurements, is that measurements are mostly point measurements, while model results represent a larger grid. For example, Batchvarova *et al.* (2001) demonstrated that the area-averaged sensible heat flux for the Sodankylä region is about 30 - 50% of the measured sensible heat flux in the forest for near-neutral atmospheric conditions at the end of winter. Also in stable conditions with weak winds and small advection, there is a stronger influence of the local terrain on the surface energy balance and hence on e.g. the 2 m temperature (Atlaskin and Vihma, 2012). As such, the measurements

are representative of an area typically smaller than the model grid size (Hanna and Yang, 2001). Therefore a dense spatial network of observations should be applied to obtain a better area averaged comparison of observations with models (Fernando and Weil, 2010; Atlaskin and Vihma, 2012; Vihma *et al.*, 2014), though these type of high spatial resolution measurements are uncommon. In addition, scintillometry may provide useful spatial averages for turbulent fluxes, although these measurements again depend on Monin Obukhov Similarity Theory (Hartogensis et al., 2002).

The difficulties presented above make a straightforward comparison of the model results with observations more cumbersome. This also implies that the flux uncertainties may be larger than presented by the error bars in the process diagrams of Chapter 5. Regarding the Sodankylä area in particular, this is a rather heterogeneous terrain and sensible heat flux measurements are performed along the mast in the forest, while radiation measurements were performed in an open field. When comparing the sensible heat flux with the temperature gradient close to the surface determined from the radiation based skin temperature and 2 m temperature measurements as in the process diagram in Chapter 5, there may be a mismatch between the two, as the measurements are not representative of the same location.

The relatively small amount of measurements available in the polar areas, calls for a broader network of observations. As at one observational site often not all required variables may be measured at all or correctly, care should be given to fully equip observational sites. Since for example the atmospheric state is strongly linked to the surface processes, information on surface fluxes and e.g. near-surface temperature, wind speed and humidity as well as vertical profiles of these variables would be desirable at the same location. It is difficult to realize this extensive observational set-up though, due to the difficulties explained earlier and probably the high costs involved. Advances are likely to be gained from remote sensing data, e.g. regarding temperature and humidity inversions with atmospheric infra-red sounder data (Devasthale *et al.*, 2010; 2011), such that a higher spatial coverage is obtained. Also unmanned aerospace vehicles, or drones, could come to play a more important role in measuring atmospheric data (Stephens *et al.*, 2000; Houston *et al.*, 2012).

Besides for fundamental research, a more complete network of observations would also be useful for operational forecasting and to learn more about a sustainable exploration of the Arctic routing. Furthermore, the observations can be used to improve reanalysis data. Reanalysis data is created from data assimilation of observations on model simulations, which makes that the model influence with its possible physical deficiencies, is stronger in regions with limited observations. As reanalysis data is often used as a representation of the observed atmosphere in space and time (e.g. Screen and Simmonds, 2011; Svensson and Karlsson, 2011; Esau *et al.*, 2012), it is worthwhile to invest more in observations in observation scarce areas.

7.3 Dealing with the humidity problem in YSU

The results in Chapters 3 - 5 using the YSU boundary-layer scheme, show that a temperature inversion develops over time in stable conditions. However, in such cases hardly any change was seen in the humidity profile throughout time, nor in the time series of the specific humidity at 2 m. This is contrary to what would be expected, in

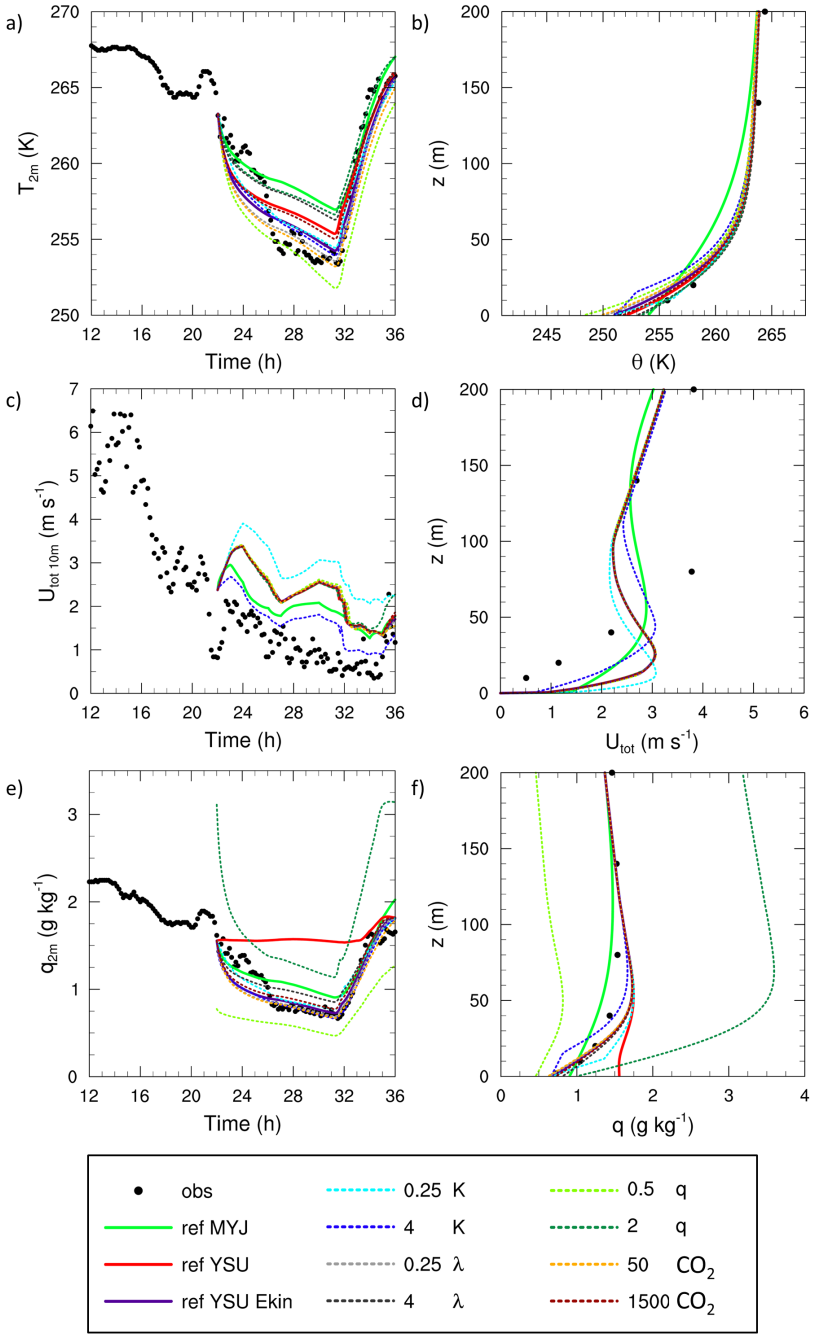

Figure 7.2: See next page.

the sense that in the Noah land-surface model, the same exchange coefficient is used for both heat and moisture, as was explained in Section 2.2.1. If heat is exchanged to the surface, humidity should also be exchanged. Furthermore, as is described in Section 2.1.1, the eddy diffusivity of heat and moisture are equal as well, so that also mixing in the BL should be comparable for heat and momentum.

This section investigates this humidity behaviour in YSU in closer detail. It turned out that this is a WRF specific problem for certain schemes. As such, this is a rather technical section. However, it is included in this outlook since the specific humidity profiles improved significantly after this issue was addressed and updated. This also somewhat affects the results shown in the previous chapters, though the general conclusions remain the same. Interestingly, when using MYJ, this peculiar behaviour for humidity does not occur. Now a humidity inversion does develop in time which is more as expected.

It is also noteworthy to see that the magnitude of the sensible heat flux H is larger with MYJ due to a larger exchange coefficient in combination with a larger temperature gradient. Despite that the same coefficient is used for the latent heat flux LE, the latter is larger with YSU. For H there is a direct dependence on the exchange coefficient C_h and the temperature difference, while this is a bit more complicated with LE as seen in equation 2.51. Likely, because of the high humidity concentration at the first model level in combination with the low surface temperature with YSU and hence low surface humidity, the humidity gradient must be very large, explaining the larger LE. However, then it would be expected that more moisture is extracted from the BL and transported towards the surface, and this appears not to be the case.

A closer investigation of the WRF code shows that the moisture flux that is provided to the YSU-BL scheme (*qfx*), equals zero. This is rather surprising, since the actual LE calculated in the land-surface model is not equal to zero, but has a negative value. However, it would explain why the humidity inversion does not develop.

It appears that the moisture flux read into the YSU-BL is equal to the latent heat flux in kg m^{-2} s^{-1} (E_{kin}, *ETA_KINEMATIC* in the code) calculated in the Noah land-surface model. When snow is present, E_{kin} is equal to:

$$E_{kin} = E_{snow}\sigma_{snow} + (E_{dir} + E_c + E_{tt})\,(1 - \sigma_{snow}) \tag{7.1}$$

Figure 7.2: *(Preceding page)* Timeseries of a) the 2 m temperature (T_{2m} (K)), c) the 10 m total wind speed ($U_{tot\ 10m}$ (m s^{-1}), and e) the 2 m specific humidity (q_{2m} (g kg^{-1}), and vertical profiles of b) the potential temperature (θ (K)), d) the total wind speed (U_{tot} (m s^{-1}), and f) the specific humidity (q (g kg^{-1})). All results are for the Cabauw case as described in Chapter 4 and 5 using the WRF-SCM. The profiles are at 9h after the start of the SCM simulation. ref MYJ is the reference for the simulations with the MYJ-BL scheme, ref YSU is the reference for the simulations with the YSU-BL scheme, and ref YSU Ekin is the simulation with the YSU-BL scheme when the moisture flux is read into the BL scheme. The sensitivity analysis lines are only shown for the YSU scheme with the moisture flux read into the BL scheme. K represents the change in mixing in both boundary and surface layer, λ represents the ice conductivity and thus the coupling, q represents the specific humidity profile and therefore the incoming long wave radiation, and CO_2 represents the amount of CO_2 in ppmv and therefore also the incoming long wave radiation.

Here E_{snow} represents the sublimation from the snow pack, with σ_{snow} being the snow cover fraction, and E_{dir}, E_c, and E_{tt} representing the direct soil evaporation, the canopy water evaporation, and the total plant transpiration respectively. However, all these terms are only calculated when the potential evaporation E_p is larger than 0, so for an upward moisture flux. Indeed it calculates LE in the form of dew-fall (or frost-fall) when $E_p \leq 0$, but not the actual terms needed for E_{kin} as indicated in Equation 7.1, and therefore this term remains zero. When snow is absent, E_{kin} is equal to the actual latent heat flux, which is equal to $E_{dir} + E_c + E_{tt}$ for the case that $E_p > 0$, and equal to E_p otherwise. Indeed, when we perform a simulation with YSU without snow being present, a humidity inversion does develop as we would expect.

As a first try for a solution to the problem with YSU, E_{kin} is overwritten with E_p. Note that this solution is only valid for downward transport of moisture. For upward transport, E_{kin} as in Equation 7.1 should be applied. By overwriting E_{kin} with E_p, the moisture flux calculated in the Noah land-surface model is read into the YSU-BL scheme. With this set-up, another set of simulations was performed for the Cabauw case as described in Chapter 4 and 5 prescribing advection for temperature, humidity and momentum. The results are shown in Figures 7.2 and 7.3. When analysing only the reference cases, a clear impact is found regarding the temperature and humidity when including the moisture flux in the YSU-BL scheme, while the impact on the wind field is negligible. The 2 m humidity decreases to almost the observed values during the night, while additionally lower temperatures at the 2 m level are reached. Indeed the potential temperature gradient develops stronger compared to the reference YSU, while furthermore the humidity inversion is much better in agreement with observations. The unrealistic almost well-mixed profile is no longer found.

The sensitivity analyses runs are also shown in Figure 7.2 for the reference case with the moisture flux read into the YSU-BL scheme, and compared with the sensitivity analyses of the standard MYJ and YSU-BL schemes in the process diagrams in Figure 7.3. Now the 2 m temperature non-linearity as discussed in Chapter 3 and 5 is even more profoundly present compared to the standard YSU case, which is likely due to the stronger concave up shaped potential temperature profile. Moreover, as was found with MYJ in Chapter 5, this non-linearity is now also present for the near-surface humidity when the moisture flux is read into YSU (Figure 7.2e). With enhanced mixing, lower humidity amounts are found while with decreased mixing this amount remains higher than the reference case. A similar explanation as for the near-surface temperature non-linearity is valid. In these low wind speed conditions, only a small amount of mixing exists, such that only a small amount of moisture is mixed away from the first model level towards the surface. When mixing increases, this transport becomes more efficient such that relatively dryer air is mixed away from the surface, while this is insufficiently compensated for by downward mixing of relatively moist air from the higher levels in the BL.

A stronger surface cooling also results in a larger temperature gradient through the underlying medium, explaining the stronger ground heat flux (Figure 7.3a) which is now less in agreement with the observed snow heat flux. Though with the reduced atmospheric humidity the amount of incoming long wave radiation is further reduced

(which was already underestimated), the amount of outgoing long wave radiation also becomes less with lower surface temperatures. As such the simulated net radiation is now more in agreement with the observations.

It is clear that when the latent heat flux calculated in the land-surface model is properly signalled to the YSU-BL, a great impact of the model simulations is found. Though the impact on the wind field is negligible, the temperature and even more

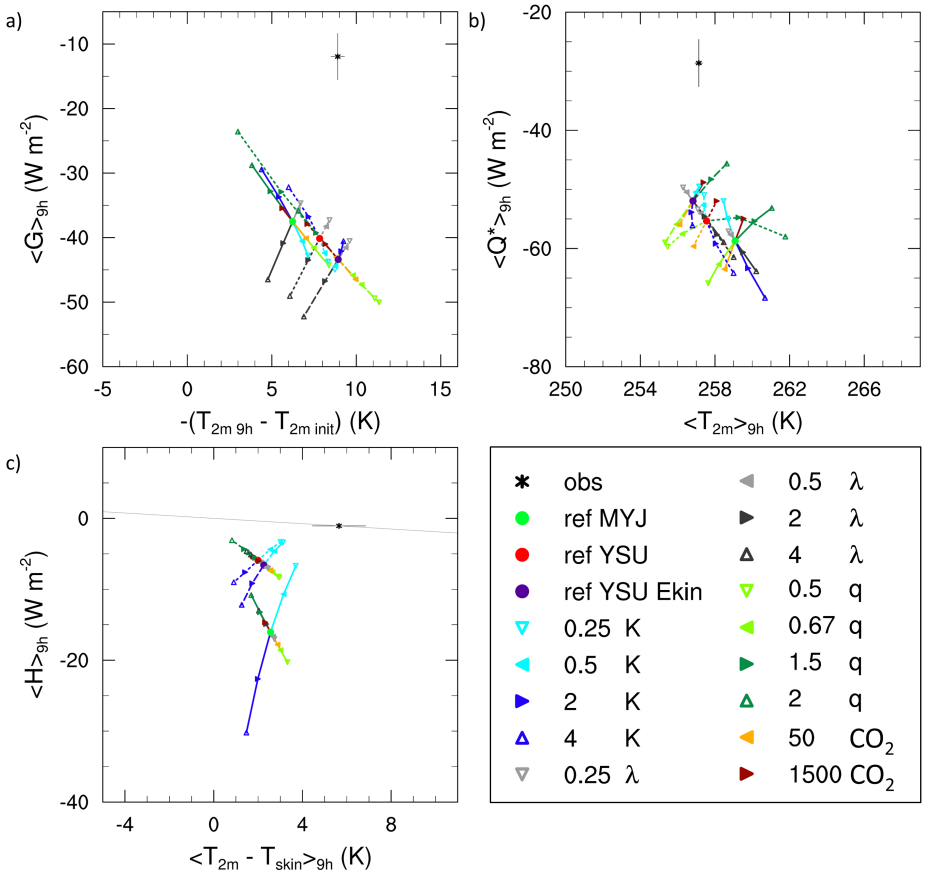

Figure 7.3: Process diagrams for the Cabauw case as described in Chapters 4 and 5 using the WRF-SCM for a) the cooling of the 2 m temperature ($-(T_{2m\ 9h} - T_{2m\ init})$ (K)) over 9h versus the soil heat flux ($< G >_{9h}$ (W m^{-2})) averaged over 9h, b) the 2 m temperature ($< T_{2m} >_{9h}$ (K)) versus the net radiation ($< Q^* >_{9h}$ (W m^{-2})), both averaged over 9h, and c) the temperature difference between the 2 m level and the surface ($< T_{2m} - T_{skin} >_{9h}$ (K)) versus the sensible heat flux ($< H >_{9h}$ (W m^{-2})), both averaged over 9h. For an explanation of the legend, see Figure 7.2. The sensitivity analysis is performed three times, first for the MYJ reference (full lines), secondly for the YSU reference (dotted lines), and thirdly for the YSU reference which has the moisture flux read into the BL scheme (dashed lines). The asterisk with error bars represents the observation with its measurement uncertainties in the error bars. The lines through the observational points and the origin in c), connect all points with a similar mixing as observed.

so the humidity are strongly impacted, which has in return an impact on the energy balance. Furthermore, in the case that clouds are allowed to develop, excessive fog formation would be expected when humidity is not transported away to the surface while the atmosphere is allowed to cool.

Note that YSU is not the only scheme for which E_{kin} is read into the BL. Therefore this humidity problem is also expected with the MRF, GFS, ACM, BOULAC and MYNN schemes for stable conditions over snow-covered surfaces. With MYJ not E_{kin} is read into the BL-scheme to determine the moisture flux from/towards the surface, but LE, and this is still equal to the potential latent heat flux in W m^{-2}, LE_p. Therefore this problem does not occur with MYJ and humidity transport towards the surface does take place in the BL-scheme, regardless of snow being present.

On basis of the findings above, the WRF support group has decided to update the code, starting from version 3.7 (Jimi Dudhia, personal communication).

7.4 Further model development recommendations

The findings of this thesis result in several recommendations regarding the WRF model. Note that these are not necessarily only valid for WRF, but should be considered carefully in other models as well.

First of all, the representation of the surface has a strong influence on the state of the stable boundary layer, an should be properly represented. However, it was clear from Chapter 4 that there are several issues regarding the representation of the surface with WRF. The vegetation fraction proved to be too low compared to what is seen in reality for the cases studied here. As such, a better database regarding the vegetation cover is advised, for example the CORINE land-use data which has a resolution of 250 by 250 m (Kim *et al.*, 2013) compared to the 15 by 15 km resolution currently used in the USGS land-use data (Ek *et al.*, 2003). Also, Kumar *et al.* (2014) recently studied the impact of using the 1 by 1 km resolution MODIS (Moderate resolution Imaging Spectroradiometer) vegetation data versus the USGS data, and noticed improvements in surface fluxes and temperature as well as the soil parameters.

Furthermore, the snow cover is simulated incorrectly, e.g. when 40 cm of snow is simulated, this is seen as a full snow cover in a forest, while in fact trees will stick through this snow layer. For grass on the other hand, 20 cm of snow is required to obtain a full snow cover, while often less snow will suffice. Therefore it is recommended to reconsider the method to determine the snow cover, e.g. by adjusting the depths for which 100% snow cover would be achieved for the various vegetation types.

Further improvements can also be made on the representation of the snow characteristics. As was shown in Chapter 5 the conductivity of snow is quite low compared to what literature based on observations suggests for a certain snow density which impacts the simulated heat flux trough the underlying medium. Moreover, for sea-ice a constant conductivity is assumed for the entire ice thickness, though a variation in time is seen due to temporal evolution of snow density. A more realistic approach would be to have a more smooth transition from snow conductivity to firn conductivity to ice conductivity. The equation for snow conductivity should therefore be

revised such that a more realistic conductivity is used in the model simulations. Additionally, the snow layer is now taken as one big slab on top of the first soil level, which together is then taken as the first level of the underlying medium. Especially in cases with a thick snow cover, the resolution of the underlying medium becomes very poor. A multi-layer snow pack would thus be preferable. In fact, the new Noah land-surface model with multiparametrization options (Noah-MP) already has three snow layers independent of the underlying soil layers, as well as a separated energy balance regarding snow covered and vegetated area, amongst other updates (Niu *et al.*, 2011).

Since WRF currently only addresses one dominant land cover type, a possible improvement for this could be to implement different tiles in the land-surface model, as is already the case in e.g. the ECMWF model (Van den Hurk *et al.*, 2000; Beljaars *et al.*, 2006). Though in the 3.2.1 WRF version used in this thesis, separation between snow covered surface and snow free surface is allowed, only a single vegetation type is used in combination with its fraction to find the accompanying conductivity of the soil and vegetation combined. Therefore in regions with multiple vegetation types, the non-dominant vegetation types are ignored, while this would also impact the area-average energy balance. Li *et al.* (2013) implemented a tiling approach into the WRF model and compared this with the standard Noah land-surface model approach. They showed that the tiled method had in general a better performance for a heterogeneous urban/suburban area. It would be interesting to repeat this implementation for other areas.

When representing the atmosphere in the model, it is important that a high resolution near the surface is applied (Byrkjedal *et al.*, 2008; Svensson and Holtslag, 2009; Savijärvi, 2013). Especially in the very stable boundary layer, temperature gradients can be very strong close to the surface. With a too coarse resolution, the curvature of e.g. the potential temperature is simulated incorrectly which can have an impact on the radiative flux divergence for example (Ha and Mahrt, 2003), while also the near-surface temperature gradient is used to determine the sensible heat flux. Furthermore, Svensson and Holtslag (2009) have already shown that having the first model level relatively close to the surface is beneficial for the wind turning with height, as then the curvature in the momentum profile is better represented.

With the WRF-SCM a high resolution was implemented by applying 200 vertical levels. With WRF-3D however only 60 vertical levels were applied. Though implementing 200 levels in the WRF-3D simulation would be computationally be very expensive, increasing the amount of vertical levels somewhat, would likely improve the 3D forecasts as well. Furthermore, this could be beneficial for determining the advection field for the WRF-SCM simulations, as this was now only based on a simulation with 60 levels.

It was shown that reducing the amount of turbulent mixing amongst others is an effective way to increase the simulated potential temperature inversion. However, we also noticed that a minimum eddy diffusivity was imposed in the YSU and MYJ boundary-layer schemes which was largest for MYJ. Especially for MYJ, this has implications on the consistency of mixing between the surface layer and the boundary layer. It followed from the simulations in Chapter 5 that the eddy diffusivity / exchange coefficient ratio is much larger with MYJ than with YSU. Therefore with

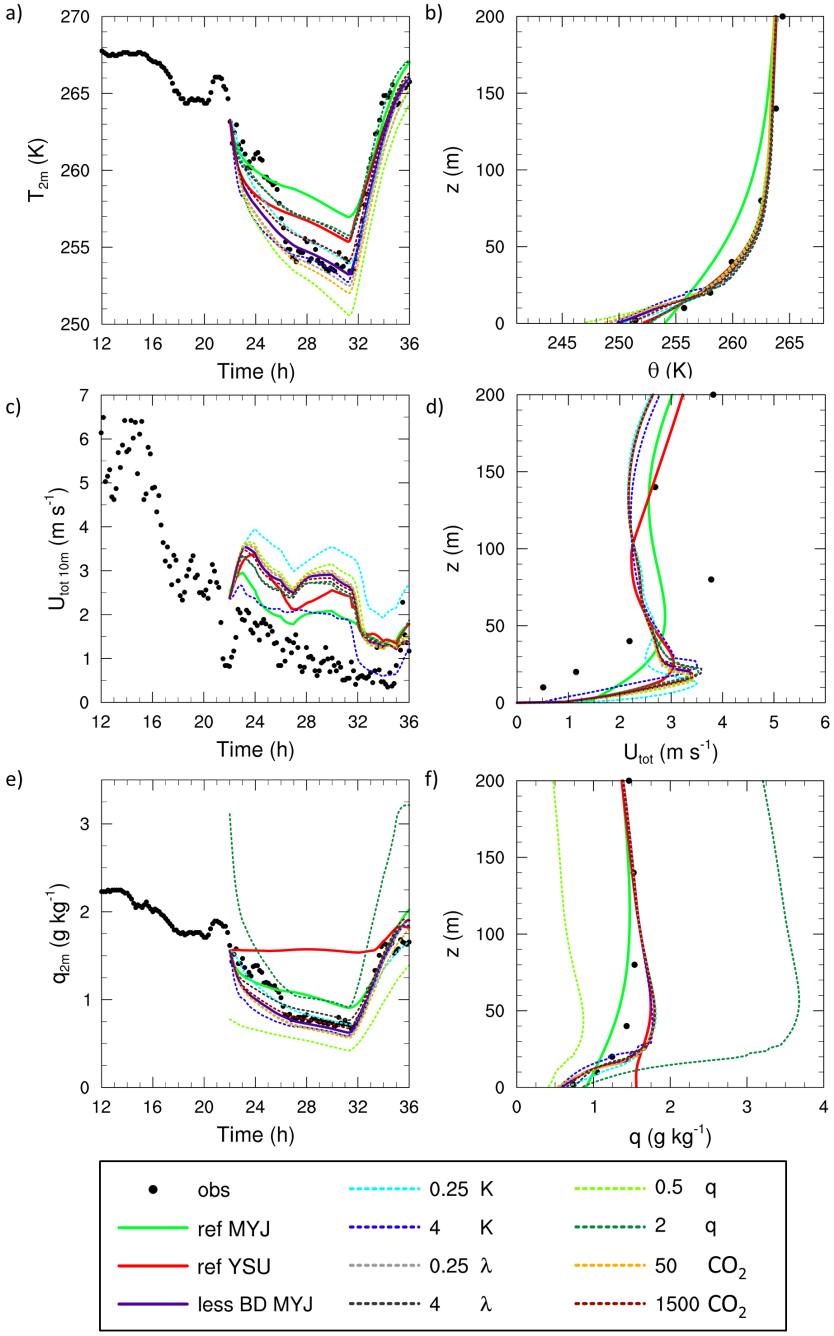

Figure 7.4: See next page.

MYJ a strong transition in temperature gradient was found between these two layers, due to that the mixing in the boundary-layer scheme is relatively efficient and the mixing in the surface-layer scheme cannot keep up with this mixing. As such, a very strong temperature gradient between the surface and the first model level is simulated and this is not consistent with the temperature gradient between the first and second model level. This transition is more smooth with YSU.

Figure 7.4 shows the SCM results regarding some time series and profiles for the Cabauw case for the simulations with the reference MYJ and YSU as already shown in Chapters 4 and 5. The reference line is added for which the limitation for the background eddy diffusivity (or actually a minimum TKE of 0.2 m^2 s^{-2} which resulted in a minimum eddy diffusivity of about 0.09 m^2 s^{-1}) with MYJ is lowered by a factor 100, as well as the sensitivity analysis lines for this case. Obviously, adjusting this minimum eddy diffusivity has a great impact on the simulations. The minimum temperatures and specific humidity are more easily reached, and the profile shape for the potential temperature is more in agreement with observations. Unfortunately, as with YSU, the wind speed skill deteriorates. The wind speed is now too strong close to the surface with a low-level jet too close to the surface.

With the reduced minimum mixing, MYJ is able to simulate the non-linear behaviour regarding near surface temperatures, a feature which is also seen in observations. This also follows from the turned orientation in the process diagrams in Figure 7.5, which show the same sensitivity analyses sets for the normal MYJ and YSU as already shown in Chapter 5, but with the additional sensitivity analysis for the reduced background mixing with MYJ. Where for the Cabauw case the non-linearity with YSU was not as obvious as for the other sites, this is very obvious with the adjusted MYJ boundary-layer scheme. This indicates that one should be careful with prescribing fixed minima regarding mixing, as it can strongly influence certain physics as shown here.

When comparing the potential temperature profiles in Figure 7.4, it is found that the profile shape for the enhanced mixing run is somewhat concave down, though still the 2 m temperature decreases compared to the reference run. Evidently the non-linearity is not only governed by the potential profile shape, but is also affected by the mixing efficiency e.g. due to the wind speed and the eddy size. This was also discussed in Chapter 3, where in Figure 3.5 for the decreased run with higher wind speeds, the non-linearity was no longer seen but the potential temperature profile

Figure 7.4: *(Preceding page)* Timeseries of a) the 2 m temperature (T_{2m} (K)), c) the 10 m total wind speed ($U_{tot\ 10m}$ (m s^{-1}), and e) the 2 m specific humidity (q_{2m} (g kg^{-1}), and vertical profiles of b) the potential temperature (θ (K)), d) the total wind speed (U_{tot} (m s^{-1}), and f) the specific humidity (q (g kg^{-1})). All results are for the Cabauw case as described in Chapter 4 and 5 using the WRF-SCM. The profiles are at 9h after the start of the SCM simulation. ref MYJ is the reference for the simulations with the MYJ-BL scheme, ref YSU is the reference for the simulations with the YSU-BL scheme, and less BD MYJ is the simulation with the MYJ-BL scheme but with reduced background diffusivity. The lines in the figure indicate the sensitivity results for the reduced background diffusivity simulations with MYJ. K represents the change in mixing in both boundary and surface layer, λ represents the ice conductivity and thus the coupling, q represents the specific humidity profile and therefore the incoming long wave radiation, and CO_2 represents the amount of CO_2 in ppmv and therefore also the incoming long wave radiation.

remained concave up.

Besides the turbulent mixing issues, it was apparent from the studies performed in this thesis that a deficiency exists in the long wave radiation scheme, as was also recognized by others with other models (e.g. Wild *et al.*, 2001; Niemelä *et al.*, 2001; Barton *et al.*, 2014). Especially in cold and dry conditions, the incoming long wave radiation is underestimated, and as was also shown in this thesis, even with a

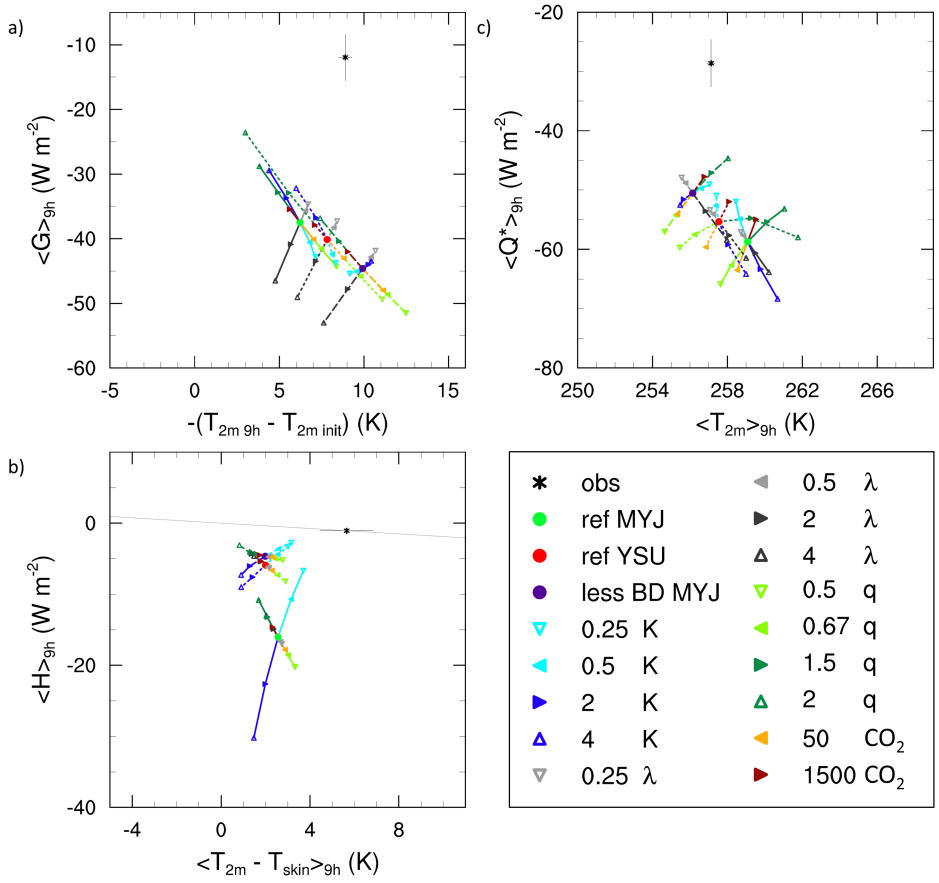

Figure 7.5: Process diagrams for the Cabauw case as described in Chapters 4 and 5 using the WRF-SCM for a) the cooling of the 2 m temperature ($-(T_{2m\ 9h} - T_{2m\ init})$ (K)) over 9h versus the soil heat flux ($< G >_{9h}$ (W m^{-2})) averaged over 9h, b) the 2 m temperature ($< T_{2m} >_{9h}$ (K)) versus the net radiation ($< Q^* >_{9h}$ (W m^{-2})), both averaged over 9h, and c) the temperature difference between the 2 m level and the surface ($< T_{2m} - T_{skin} >_{9h}$ (K)) versus the sensible heat flux ($< H >_{9h}$ (W m^{-2})), both averaged over 9h. For an explanation of the legend, see Figure 7.4. The sensitivity analysis is performed three times, first for the MYJ reference (full lines), secondly for the YSU reference (dotted lines), and thirdly for the MYJ reference which uses a lower limitation on the background diffusivity (dashed lines). The asterisk with error bars represents the observation with its measurement uncertainties in the error bars. The lines through the observational points and the origin in c), connect all points with a similar mixing as observed.

properly forecasted temperature and specific humidity profile, this remains too low. This strongly affects the surface energy balance. As demonstrated by Zhang *et al.*, (2001), Persson (2012), and Maksimovich and Vihma (2012), the amount of incoming long wave radiation is important for the onset of snow melt on the Arctic sea ice and should be modelled correctly.

As explained in Section 2.4, the RRTM long-wave radiation scheme uses a look-up table with stored reference absorption coefficients for a range of pressures in combination with a set of reference temperatures. Then the actual absorption coefficients needed for the simulated atmospheric layer are interpolated. When the pressure or temperature is not in the range of the stored values, extrapolation is applied (Mlawer *et al.*, 1997). Possibly, linear extrapolation is not suitable for these cold and dry conditions, such that another form of extrapolation should be investigated. Additionally, a mid-latitude summer profile was used to determine the reference absorption values. Maybe improvements could be made when a reference set of absorption values is made for an Arctic profile. Even though enhancing the incoming long wave radiation may lead to weaker temperature inversions which are less in agreement with observations according to the evaluations that were performed in this thesis, this would be physically more realistic.

Also, working from a more realistic reference point, may pinpoint more easily where compensating errors remain hidden. Furthermore, then other more realistic model adjustments may become more apparent as the compensating errors then stop balancing each other out (Vihma *et al.*, 2014). This also points out the potential for performing 2-way (or more-way) sensitivity analyses as mentioned earlier in Section 7.1, where various process intensities are combined for a set of processes. Where a stand-alone model adjustment may deteriorate the model skill, advances may be gained by combining this with other model adjustments. This should be investigated additionally to stand-alone changes, as then we really learn more about the feedbacks.

References

Acevedo OC, Fitzjarrald DR. 2003. In the core of the night - Effects of intermittent mixing on a horizontally heterogeneous surface. *Bound.-Layer Meteorol.* **106**: 1-33

ACIA. 2005. *Arctic Climate Impact Assessment*, Cambridge Univ. Press, Cambridge, U.K., 1042 pp.

Alexeev VA, Langen PL, Bates JR. 2005. Polar amplification of surface warming on an aquaplanet in "ghost forcing" experiments without sea ice feedbacks. *Clim. Dyn.* **24**: 655-666

André JC, Mahrt L. 1982. The nocturnal surface inversion and influence of clear-air radiative cooling. *J. Atmos. Sci.* **39**: 864-878

Andreas EL, Persson POG, Jordan RE, Horst TW, Guest PS, Grachev AA, Fairall CW. 2010. Parameterizing Turbulent Exchange over Sea Ice in Winter. *J. Hydrometeorol.* **11**: 87-104

Ansorge C, Mellado JP. 2014. Global Intermittency and Collapsing Turbulence in the Stratified Planetary Boundary Layer. *Bound.-Layer Meteorol.* **153**: 89-116

Atlaskin E, Vihma T. 2012. Evaluation of NWP results for wintertime nocturnal boundary-layer temperatures over Europe and Finland. *Q. J. R. Meteorol. Soc.* **138**: 1440-1451

Aubinet M. 2008. Eddy covariance CO_2 flux measurements in nocturnal conditions: an analysis of the problem. *Ecol. Appl.* **18**: 1368–1378

Baas P, Steeneveld GJ, Van de Wiel BJH, Holtslag AAM. 2006. Exploring Self-Correlation in Flux-Gradient Relationships for Stably Stratified Conditions. *J. Atmos. Sci.* **63**: 3045-3054

Baas P. 2009. *Turbulence and Low-Level Jets in the Stable Boundary Layer. PhD thesis.* Wageningen University, Wageningen, 152 pp.

Baas P, Bosveld FC, Lenderink G, Van Meijgaard E, Holtslag AAM. 2010. How to design single-column model experiments for comparison with observed nocturnal low-level jets. *Q. J. R. Meteorol. Soc.* **136**: 671-684

Balsamo G, Viterbo P, Beljaars A, Van den Hurk B, Betts AK, Scipal K. 2009. Revised Hydrology for the ECMWF Model: Verification from Field Site to Terrestrial Water Storage and Impact in the Integrated Forecast System. *J. Hydrometeorol.* **10**: 623-643

Balsamo G, Agustì-Panareda A, Albergel C, Beljaars A, Boussetta S, Dutra E, Komori T, Lang S, Muñoz-Sabater J, Pappenberger F, de Rosnay P, Sandu I, Wedi N, Weisheimer A, Wetterhal F, Zsoter E. 2014. *Representing the Earth surfaces in the Integrated Forecasting System: Recent advances and future challenges.* ECMWF Technical Memorandum, 729, 50 pp.

Barton NP, Klein SA, Boyle JS. 2014. On the Contribution of Longwave Radiation to Global Climate Model Biases in Arctic Lower Tropospheric Stability. *J. Clim.* **27**: 7250-7269

Basu S, Porté-Agel F. 2006. Large-Eddy Simulation of Stably Stratified Atmospheric Boundary Layer Turbulence: A Scale-Dependent Dynamic Modeling Approach. *J. Atmos. Sci.* **63**: 2074-2091

Basu S, Holtslag AAM, Bosveld FC. 2012. GABLS3-LES Intercomparison Study. *Proceedings of the Workshop on Diurnal cycles and the stable boundary layer, 7-10 November, 2011*, Reading, U.K., pp. 75-82

Batchvarova E, Gryning SE, Hasager CB. 2001. Regional fluxes of momentum and sensible heat over a sub-Arctic landscape during late winter. *Bound.-Layer Meteorol.* **99**: 489-507

Beare RJ, MacVean MK, Holtslag AAM, Cuxart J, Esau I, Golaz JC, Jimenez MA, Khairoutdinov M, Kosovic B, Lewellen D, Lund TS, Lundquist JK, McCabe A, Moene AF, Noh Y, Raasch S, Sullivan PP. 2006. An intercomparison of large-eddy simulations of the stable boundary layer. *Bound.-Layer Meteorol.* **118**: 247-272

Beljaars ACM, Holtslag AAM. 1991. Flux parameterization over land surfaces for atmospheric models. *J. Appl. Meteorol.* **30**: 327-341

Beljaars ACM, Bosveld FC. 1997. Cabauw Data for the Validation of Land Surface Parameterization Schemes. *J. Clim.* **10**: 1172-1193

Beljaars ACM, Viterbo P. 1998. Role of the Boundary Layer in a Numerical Weather Prediction Model, *Clear and Cloudy boundary layers*, AAM Holtslag and PG Duynkerke Eds, Royal Netherlands Academy of Arts and Sciences, Amsterdam, pp. 287-304

Beljaars A, Balsamo G, Betts A, Viterbo P. 2006. Atmosphere/surface interactions in the ECMWF model at high latitudes. *Proceedings of ECMWF Seminar on Polar Meteorology, 4-8 September, 2006*, ECMWF, Reading, U.K., pp. 153-168

Bergot T, Carrer D, Noilhan J, Bougeault P. 2005. Improved Site-Specific Numerical Prediction of Fog and Low Clouds: A Feasibility Study. *Weather Forecast.* **20**: 627-646

Bianco L, Bao JW, Fairall CW, Michelson SA. 2011. Impact of Sea-Spray on the Atmospheric Surface Layer. *Bound.-Layer Meteorol.* **140**: 361-381

Bintanja R, Graversen RG, Hazeleger W. 2011a. Arctic winter warming amplified by the thermal inversion and consequent low infrared cooling to space. *Nat. Geosci.* **4**: 758-761

Bintanja R, Van der Linden EC, Hazeleger W. 2011b. Boundary layer stability and Arctic climate change: a feedback study using EC-Earth. *Clim. Dyn.* **39**: 2659-2673

Blackadar AK. 1962. The Vertical Distribution of Wind and Turbulent Exchange in a Neutral Atmosphere. *J. Geophys. Res.* **67**, No. 8: 3095-3102

Boé J, Hall A, Qu X. 2009. Current GCMs' unrealistic negative feedback in the Arctic. *J. Clim.* **22**: 4682-4695

Bony S, Colman R, Kattsov VM, Allan RP, Bretherton CS, Dufresne JL, Hall A, Hallegatte S, Holland MM, Ingram W, Randall DA, Soden BJ, Tselioudis G, Webb MB. 2006. Review Article: How well do we understand and evaluate climate change feedback processes? *J. Clim.* **19**: 3445-3482

Bosveld FC, Baas P, Steeneveld GJ, Holtslag AAM. 2012. GABLS3 SCM intercomparison and evaluation: What did we learn? *Proceedings of the Workshop on Diurnal cycles and the stable boundary layer, 7-10 November, 2011*, Reading, U.K., pp. 91-102

Bosveld FC, Baas P, van Meijgaard E, de Bruijn EIF, Steeneveld GJ, Holtslag AAM. 2014a. The Third GABLS Intercomparison Case for Evaluation Studies of Boundary-Layer Models: Part A: Case Selection and Set-up. *Bound.-Layer Meteorol.* **152**: 133-156

Bosveld FC, Baas P, Steeneveld GJ, Holtslag AAM, Angevine WM, Bazile E, de Bruijn EIF, Deacu D, Edwards JM, Ek M, Larson VE, Plein JE, Raschendorfer M, Svensson G. 2014b. The Third GABLS Intercomparison Case for Evaluation Studies of Boundary-Layer Models: Part B: Results and Process Understanding. *Bound.-Layer Meteorol.* **152**: 157-187

Brost RA, Wyngaard JC. 1978. A Model Study of the Stably Stratified Planetary Boundary Layer. *J. Atmos. Sci.* **35**: 1427-1440

Businger JA, Wyngaard JC, Izumi Y, Bradley EF. 1971. Flux-Profile Relationships in the Atmospheric Surface Layer. *J. Atmos. Sci.* **28**: 181-189

Byrkjedal Ø, Esau I, Kvamstø NG. 2008. Sensitivity of simulated wintertime Arctic atmosphere to vertical resolution in the ARPEGE/IFS model. *Clim. Dyn.* **30**: 687-701

CESAR. 2013. Cabauw Experimental Site for Atmospheric Research. (http://www.cesar-observatory.nl)

Calonne N, Flin F, Morin S, Lesaffre B, Rolland du Roscoat S, Geindreau C. 2011. Numerical and experimental investigations of the effective thermal conductivity of snow. *Geophys. Res. Lett.* **38**, L23501

Carlson TN, Boland FE. 1978. Analysis of Urban-Rural Canopy Using a Surface Heat Flux / Temperature Model. *J. Appl. Meteorol.* **17**: 998-1013

Carlson MA, Stull RB. 1986. Subsidence in the Nocturnal Boundary Layer. *J. Clim. Appl. Meteorol.* **25**: 1088-1099

Chen F, Dudhia J. 2001. Coupling an advanced land surface-hydrology model with the Penn State-NCAR MM5 modelling system. Part I: Model implementation and sensitivity. *Mon. Weather Rev.* **129**: 569-585

Chen N, Guan D, Jin C, Wang A, Wu J, Yuan F. 2011. Influences of snow event on energy balance over temperate meadow in dormant season based on eddy covariance measurements. *J. Hydrol.* **399**: 100-107

Chou MD, Suarez MJ. 1994. *An efficient thermal infrared radiation parameterization for use in general circulation models.* NASA Technical Memorandum, 104606, 3, 85 pp. (https://archive.org/stream/nasa_techdoc_19950009331/19950009331#page/n0/mode/2up)

Claffey KJ, Andreas EL, Perovich DK, Fairall CW, Guest PS, Persson POG. 1999. Surface temperature measurements at SHEBA, *Preprints, Fifth Conference on Polar Meteorology and Oceanography*, American Meteorological Society, Dallas, Texas, pp. 327-332

Collins WD, Rash PJ, Boville BA, Hack JJ, McCaa JR, Williamson DL, Kiehl JT, Briegleb B, Bitz C, Lin SJ, Zhang M, Dai Y. 2004. *Description of the NCAR Community Atmosphere Model (CAM 3.0)*, NCAR Technical Note, Climate and Global Dynamics Division, National Center for Atmospheric Research (NCAR), Boulder, Colorado, 226 pp. (http://www.cesm.ucar.edu/models/atmcam/docs/description/description.pdf).

Comiso JC, Parkinson CL, Gertsen R, Stock L. 2008. Accelerated decline in the Arctic sea ice cover. *Geophys. Res. Lett.* **35**, L01703

Curry JA, Schramm JL, Ebert EE. 1995. Sea Ice-Albedo Climate Feedback Mechanism. *J. Clim.* **8**: 240-247

Cuxart J, Holtslag AAM, Beare RJ, Bazile E, Beljaars A, Cheng A, Conangla L, Ek M, Freedman F, Hamdi R, Kerstein A, Kitagawa H, Lenderink G, Lewellen D, Mailhot J, Mauritsen T, Perov V, Schayes G, Steeneveld GJ, Svensson G, Taylor P, Weng W, Wunsch S, Xu KM. 2006. Single-column model intercomparison for a stably stratified atmospheric boundary layer. *Bound.-Layer Meteorol.* **118**, 273-303

De Bruin HAR. 1998. *Micrometeorologie*. Vakgroep Meteorologie, Landbouwuniversiteit Wageningen. 156 pp.

Delage Y. 1974. A numerical study of the nocturnal atmospheric boundary layer. *Q. J. R. Meteorol. Soc.* **100**: 351-364

Delage Y. 1997. Parameterising sub-grid scale vertical transport in atmospheric models under statically stable conditions. *Bound.-Layer Meteorol.* **82**: 23-48

Derbyshire SH. 1999. Boundary-layer decoupling over cold surfaces as a physical boundary instability. *Bound.-Layer Meteorol.* **90**: 297-325

De Roode SR, Bosveld FC, Kroon PS. 2010. Dew Formation, Eddy-Correlation Latent Heat Fluxes, and the Surface Energy Imbalance at Cabauw During Stable Conditions. *Bound.-Layer Meteorol.* **135**: 369-383

Devasthale A, Willen U, Karlsson KG, Jones CG. 2010. Quantifying the clear-sky temperature inversion frequency and strength over the Arctic Ocean during summer and winter seasons from AIRS profiles. *Atmos. Chem. Phys.* **10**: 5565-5572

Devasthale A, Sedlar J, Tjernström M. 2011. Characteristics of water-vapour inversions observed over the Arctic by Atmospheric Infrared Sounder (AIRS) and radiosondes. *Atmos. Chem. Phys.* **11**: 9813-9823

Domine F, Gallet JC, Bock J, Morin S. 2012. Structure, specific surface area and thermal conductivity of the snowpack around Barrow, Alaska. *J. Geophys. Res.* **117**, D00R14

Dutra E, Balsamo G, Viterbo P, Miranda PMA, Beljaars A, Schär C, Elder K. 2010. An Improved Snow Scheme for the ECMWF Land Surface Model: Description and Offline Validation. *J. Hydrometeorol.* **11**: 899-916

Dutra E, Schär C, Viterbo P, Miranda PMA. 2011. Land-atmosphere coupling associated with snow cover. *Geophys. Res. Lett.* **38**, L15707

Duynkerke PG. 1991. Radiation fog: A comparison of model simulation with detailed observations. *Mon. Weather Rev.* **119**: 324-341

Duynkerke PG. 1999. Turbulence, radiation and fog in Dutch stable boundary layers. *Bound.-Layer Meteorol.* **90**: 447-477

Dyer AJ. 1974. A review of flux-profile relationships. *Bound.-Layer Meteorol.* **7**: 363-372

ECMWF (European Centre for Medium-Range Weather Forecasts). 2009. *IFS Documentation Cy33r1, Operational implementation 3 June 2008, Part IV: Physical Processes*, Reading, U.K., 162 pp. (http://old.ecmwf.int/research/ifsdocs/CY33r1/PHYSICS/IFSPart4.pdf)

ECMWF (European Centre for Medium-Range Weather Forecasts). 2012. *IFS Documentation Cy37r2, Operational implementation 18 May 2011, Part IV: Physical Processes*, Reading, U.K., 174 pp. (http://old.ecmwf.int/research/ifsdocs/CY37r2/IFSPart4.pdf)

ECMWF (European Centre for Medium-Range Weather Forecasts). 2013. *IFS Documentation Cy38r1, Operational implementation 19 June 2012, Part IV: Physical Processes*, Reading, U.K., 189 pp. (http://old.ecmwf.int/research/ifsdocs/CY38r1/IFSPart4.pdf)

Edwards JM. 2009a. Radiative Processes in the Stable Boundary Layer: Part I. Radiative Aspects. *Bound.-Layer Meteorol.* **131**: 105-126

Edwards JM. 2009b. Radiative Processes in the Stable Boundary Layer: Part II. The Development

of the Nocturnal Boundary Layer. *Bound.-Layer Meteorol.* **131**: 127-146
Edwards JM, McGregor JR, Bush MR, Bornemann FJ. 2011. Assessment of numerical weather forecasts against observations from Cardington: seasonal diurnal cycles of screen-level and surface temperatures and surface fluxes. *Q. J. R. Meteorol. Soc.* **137**: 656-672
Ek M, Mahrt L. 1991. *OSU 1-D PBL Model User's Guide version 1.0.4., A one-dimensional planetary boundary layer model with interactive soil layers and plant canopy.* Department of Atmospheric Sciences, Oregon State University, 126 pp.
Ek MB, Mitchell KE, Lin Y, Rogers E, Grunmann P, Koren V, Gayno G, Tarpley JD. 2003. Implementation of Noah land surface model advances in the National Centers for Environmental Prediction operational mesoscale Eta model. *J. Geophys. Res.* **108**: (D22), 8851
Esau I, Davy R, Outten S. 2012. Complementary explanation of temperature response in the lower atmosphere. *Environ. Res. Lett.* **7** (7pp), 044026
Fernando HJS, Weil JC. 2010. Whither the Stable Boundary Layer? A Shift in the Research Agenda. *Bull. Am. Meteorol. Soc.* **91**, 1475-1484
Floors R, Vincent CL, Gryning SE, Peña A, Batchvarova E. 2013. The Wind Profile in the Coastal Boundary Layer: Wind Lidar Measurements and Numerical Modelling. *Bound.-Layer Meteorol.* **147**: 469-491
FMI-ARC. 2013. Arctic Research Centre of the Finnish Meteorological Institute. (http://fmiarc.fmi.fi)
Foken, T. 2008a. *Micrometeorology.* Springer - Verlag Berlin Heidelberg, 308 pp.
Foken T. 2008b. The energy balance closure problem: an overview. *Ecol. Appl.* **18**: 1351-1367
Francis JA, Hunter E. 2007. Changes in the fabric of the Arctic's greenhouse blanket. *Environ. Res. Lett.*, 045011 (6pp)
Garratt JR, Brost RA. 1981. Radiative Cooling Effects within and above the Nocturnal Boundary Layer. *J. Atmos. Sci.* **38**: 2730-2746
Garratt JR. 1992. *The atmospheric boundary layer*, Cambridge University Press: Cambridge, UK; 316 pp.
Ghan SJ, Leung LR, McCaa J. 1999. A Comparison of Three Different Modeling Strategies for Evaluating Cloud and Radiation Parameterizations. *Mon. Weather Rev.* **127**: 1967-1984
Gouttevin I, Menegoz M, Dominé F, Krinner G, Koven C, Ciais P, Tarnocai C, Boike J. 2012. How the insulating properties of snow affect soil carbon distribution in the continental pan-Arctic area. *J. Geophys. Res.* **117** G02020
Grachev AA, Fairall CW, Persson POG, Andreas EL, Guest PS. 2005. Stable boundary-layer scaling regimes: the SHEBA data. *Bound.-Layer Meteorol.* **116**: 201-235
Grachev AA, Andreas EL, Fairall CW, Guest PS, Persson POG. 2007. SHEBA flux-profile relationships in the stable atmospheric boundary layer. *Bound.-Layer Meteorol.* **124**: 315-333
Grachev AA, Andreas EL, Fairall CW, Guest PS, Persson POG. 2012. Outlier Problem in Evaluating Similarity Functions in the Stable Atmospheric Boundary Layer. *Bound.-Layer Meteorol.* **144**: 137-155
Graversen RG. 2006. Do Changes in the Midlatitude Circulation Have Any Impact on the Arctic Surface Air Temperature Trend? *J. Clim.* **19**: 5422-5438
Graversen RG, Mauritsen T, Tjernström M, Källén E, Svensson G. 2008. Vertical structure of recent Arctic warming. *Nature* **451**: 53-56
Graversen RG, Wang M. 2009. Polar amplification in a coupled climate model with locked albedo. *Clim. Dyn.* **33**: 629-643
Graversen RG, Drijfhout S, Hazeleger W, Van de Wal R, Bintanja R, Helsen M. 2011. Greenland's contribution to global sea-level rise by the end of the 21st century. *Clim. Dyn.* **37**: 1427-1442
Grell GA, Dudhia J, Stauffer DR. 1994. *A Description of the Fifth-Generation Penn State/NCAR Mesoscale Model (MM5).* NCAR Technical Note, Mesoscale and Microscale Meteorology Division, National Center for Atmospheric Research (NCAR), Boulder, Colorado, 128 pp.
Gultepe I, Pearson G, Milbrandt JA, Hansen B, Platnick S, Taylor P, Gordon M, Oakley JP, Cober SG. 2009. The Fog Remote Sensing and Modeling Field Project. *Bull. Am. Meteorol. Soc.* **90**: 341-359
Gutman G, Ignatov A. 1998. The derivation of the green vegetation fraction from NOAA/AVHRR data for use in numerical weather prediction models. *Int. J. Remote Sens.* **19**: 1533-1543
Ha KJ, Mahrt L. 2003. Radiative and turbulent fluxes in the nocturnal boundary layer. *Tellus* **55A**: 317-327
Hanjalic K, Launder BE. 1972. Fully developed asymmetric flow in a plane channel. *J. Fluid Mech.*

51: 301- 335
Hanna SR, Yang R. 2001. Evaluations of Mesoscale Models' Simulations of Near-Surface winds, Temperature Gradients, and Mixing Depths. *J. Appl. Meteorol.* **40**: 1095-1104
Hartogensis OK, De Bruin HAR, Van de Wiel BJH. 2002. Displaced-Beam Small Aperture Scintillometer Test. Part II: Cases-99 Stable Boundary-Layer Experiment. *Bound.-Layer Meteorol.* **105**: 149-176
Helgason W, Pomeroy J. 2012. Problems Closing the Energy Balance over a Homogeneous Snow Cover during Midwinter. *J. Hydrometeorol.* **13**: 557-572
Heusinkveld BG, Jacobs AFG, Holtslag AAM, Berkowicz SM. 2004. Surface energy balance closure in an arid region: role of soil heat flux. *Agric. For. Meteorol.* **122**: 21-37
Hoch SW, Calanca P, Philipona R, Ohmura A. 2007. Year-Round Observation of Longwave Radiative Flux Divergence in Greenland. *J. Appl. Meteorol. Climatol.* **46**: 1469-1479
Holland MM, Bitz CM. 2003. Polar amplification of climate change in coupled models. *Clim. Dyn.* **21**: 221-232
Holt T, Raman S. 1988. A review and comparative evaluation of multilevel boundary layer parameterizations for first-order and turbulent kinetic energy closure schemes. *Rev. Geophys.* **26**: 761-780
Holton JR. 2004. *An introduction to dynamic meteorology* (4th Edn). Elsevier Academic Press; Burlington, MA. 535 pp.
Holtslag AAM, Van Ulden AP. 1982. Simple estimates of nighttime surface fluxes from routine weather data. *Scientific Report* **82-4**, Royal Netherlands Meteorological Institute (KNMI), De Bilt.
Holtslag AAM, De Bruin HAR. 1988. Applied modelling of the nighttime surface energy balance over land. *J. Appl. Meteorol.* **27**: 689-704
Holtslag AAM, Boville BA. 1993. Local Versus Nonlocal Boundary-Layer Diffusion in a Global Climate Model. *J. Clim.* **6**: 1825-1842
Holtslag AAM. 1998. Modelling of Atmospheric Boundary Layers. *Clear and Cloudy Boundary Layers*, Amsterdam, The Netherlands, pp. 85-110
Holtslag AAM. 2006. GEWEX atmospheric boundary-layer study (GABLS) on stable boundary layers. *Bound.-Layer Meteorol.* **118**: 243-246
Holtslag AAM, Steeneveld GJ, Van de Wiel BJH. 2007. Role of land-surface temperature feedback on model performance for the stable boundary layer. *Bound.-Layer Meteorol.* **125**: 361-376
Holtslag AAM, Svensson G, Basu S, Beare B, Bosveld FC, Cuxart J. 2012. Overview of the GEWEX Atmospheric Boundary Layer Study (GABLS), *Proceedings of the Workshop on Diurnal cycles and the stable boundary layer, 7-10 November 2011*, Reading, U.K., pp. 11-23 (http://www.ecmwf.int/publications/library/do/references/list/201111)
Holtslag AAM, Svensson G, Baas P, Basu S, Beare B, Beljaars ACM, Bosveld FC, Cuxart J, Lindvall J, Steeneveld GJ, Tjernström M, Van De Wiel BJH. 2013. Stable Atmospheric Boundary Layers and Diurnal Cycles - Challenges for Weather and Climate Models. *Bull. Am. Meteorol. Soc.* **94**: 1691-1706
Holtslag AAM. 2015. Modeling and Parameterization. *Encyclopedia of Atmospheric Sciences*, 2nd Edition, Volume 1: 265-273
Hong SY, Noh Y, Dudhia J. 2006. A new vertical diffusion package with an explicit treatment of entrainment processes. *Mon. Weather Rev.* **134**: 2318-2341
Hong SY, Kim SW. 2008. Stable boundary layer mixing in a vertical diffusion scheme. *18th Symposium on Boundary Layers and Turbulence*, Stockholm, Sweden, 9-13 June 2008, Amer. Meteorol. Soc., Boston, 16B.2
Hong SY. 2010. A new stable boundary-layer mixing scheme and its impact on the simulated East Asian summer monsoon. *Q. J. R. Meteorol. Soc.* **136**: 1481-1496
Houston AL, Argrow B, Elston J, Lahowetz J, Frew EW, Kennedy PC. 2012. The collaborative Colorado-Nebraska unmanned aircraft system experiment. *Bull. Am. Meteorol. Soc.* **93**: 39-54
Hu XM, Nielsen-Gammon JW, Zhang F. 2010. Evaluation of three planetary boundary layer schemes in the WRF model. *J. Appl. Meteorol. Climatol.* **49**: 1831-1844
Hu XM, Klein PM, Xue M. 2013. Evaluation of the updated YSU Planetary Boundary Layer Scheme within WRF for Wind Resource and Air Quality Assessments. *J. Geophys. Res. Atmos.* **118**: 10,490-10,505
Hunke H, Meier W. 2012. Polar Boundary Layer Processes: Important Factors for Investigating Biogeochemistry and Climate. *EOS, Trans. Am. Geophys. Union* **93**, No. 44, 441

Huwald H, Tremblay LB, Blatter H. 2005. Reconciling different observational data sets from Surface Heat Budget of the Arctic Ocean (SHEBA) for model validation purposes. *J. Geophys. Res.* **110**, C05009

Iacono MJ, Mlawer EJ, Clough SA, Morcrette JJ. 2000. Impact of an improved longwave radiation model, RRTM, on the energy budget and thermodynamic properties of the NCAR community climate model, CCM3. *J. Geophys. Res.* **105** D11: 14873-14890

Iacono MJ, Delamere JS, Mlawer EJ, Shephard MW, Clough SA, Collins WD. 2008. Radiative forcing by long-lived greenhouse gases: Calculations with the AER radiative transfer models. *J. Geophys. Res.* **113**: D13103

Iacono MJ. 2011. Final Technical Report for the Project: Application of Improved Radiation Modeling to General Circulation Models. *Atmospheric and Environmental Research, Inc.*

Inoue J, Liu J, Pinto JO, Curry JA. 2006. Intercomparison of Arctic regional climate models: Modeling clouds and radiation for SHEBA in May 1998. *J. Clim.* **19**: 4167-4178

Intrieri JM, Fairall CW, Shupe MD, Persson POG, Andreas EL, Guest PS, Moritz RE. 2002. An annual cycle of Arctic surface cloud forcing at SHEBA. *J. Geophys. Res.* **107** No. C10, 8039

Jacobs AFG, Heusinkveld BG, Wichink Kruit RJ, Berkowicz SM. 2006. Contribution of dew to the water budget of a grassland area in the Netherlands. *Water Resour. Res.* **42**, W03415

Jacobs AFG, Heusinkveld BG, Holtslag AAM. 2008. Towards Closing the Surface Energy Budget of a Mid-latitude Grassland. *Bound.-Layer Meteorol.* **126**: 125-136

Janjić ZI. 2001. *Nonsingular Implementation of the Mellor-Yamada Level 2.5 Scheme in the NCEP Meso model.* National Centers for Environmental Prediction (NCEP) Office Note, No. 437, 61 pp.

Jiménez PA, Dudhia J, Fidel González-Rouco J, Navarro J, Montávez JP, García-Bustamante E. 2012. A revised scheme for the WRF surface layer formulation. *Mon. Weather Rev.* **140**: 898-918

Johannessen OM, Bengtsson L, Miles MW, Kuzmina SI, Semenov VA, Alekseev GV, Nagurnyi AP, Zakharov VF, Bobylev LP, Pettersson LH, Hasselmann K, Cattle HP. 2004. Arctic climate change: observed and modelled temperature and sea-ice variability. *Tellus* **56A**: 328-341

Karppinen A, Joffre SM, Kukkonen J, Bremer P. 2001. Evaluation of inversion strengths and mixing heights during extremely stable atmospheric stratification. *Int. J. Environ. and Pollut.* **16**: 603-613

Kim J, Mahrt L. 1992. Simple formulation of turbulent mixing in the stable free atmosphere and nocturnal boundary layer. *Tellus* **44A**: 381-394

Kim Y, Sartelet K, Raut JC, Chazette P. 2013. Evaluation of the Weather Research and Forecast/Urban Model Over Greater Paris. *Bound.-Layer Meteorol.* **149**: 105-132

King JC, Anderson PS. 1988. Installation and performance of the stable instrumentation at Halley. *Brit. Antarct. Surv. B.* **79**: 65-77

King JC, Anderson PS. 1994. Heat and water vapour fluxes and scalar roughness lengths over an Antarctic ice shelf. *Bound.-Layer Meteorol.* **69**: 101-121

King JC, Anderson PS. 1999. A humidity climatology for Halley, Antarctica, based on frost-point hygrometer measurements. *Antarct. Sci.* **11**: 100-104

Kleczek MA, Steeneveld GJ, Holtslag AAM. 2014. Evaluation of the Weather Research and Forecasting mesoscale model for GABLS3: Impact of boundary-layer schemes, boundary conditions and spin-up. *Bound.-Layer Meteorol.* **152**: 213-243

Klemp, JB. 2006. Research community priorities for WRF-system development. WRF Research Applications Board (http://www.wrf-model.org/development/wrab/docs/RAB-plan-final.pdf)

KNMI. 2012. *Maandoverzicht van het Weer in Nederland.* Koninklijk Nederlands Meteorologisch Instituut. (http://www.knmi.nl/klimatologie/mow/pdf/mow_201202.pdf)

Knowles JF, Blanken PD, Williams MW, Chowanski KM. 2012. Energy and surface moisture seasonally limit evaporation and sublimation from snow-free alpine tundra. *Agric. For. Meteorol.* **157**: 106-115

Köhler M, Ahlgrimm M, Beljaars A. 2011. Unified treatment of dry convective and stratocumulus-topped boundary layers in the ECMWF model. *Q. J. R. Meteorol. Soc.* **137**: 43-57

Kondo J, Yamazawa H. 1986. Measurement of snow surface emissivity. *Bound.-Layer Meteorol.* **34**: 415-416

Kosovic B, Curry JA. 2000. A Large Eddy Simulation study of a quasi-steady, stably stratified atmospheric boundary layer. *J. Atmos. Sci.* **57**: 1052-1068

Kumar A, Chen F, Barlage M, Ek MB, Niyogi D. 2014. Assessing Impacts of Integrating MODIS

Vegetation Data in the Weather Research and Forecasting (WRF) Model Coupled to Two Different Canopy-Resistance Approaches. *J. Appl. Meteorol. Climatol.* **53**: 1362–1380
Langer M, Westermann S, Muster S, Piel K, Boike J. 2011. The surface energy balance of a polygonal tundra site in northern Siberia – Part 2: Winter. *The Cryosphere* **5**: 509–524
Lazzara MA, Weidner GA, Keller LM, Thom JE, Cassano JJ. 2012. Antarctic Automatic Weather Station Program, 30 Years of Polar Observations. *Bull. Am. Meteorol. Soc.* **93**: 1519–1537
Li D, Bou-Zeid E, Barlage M, Chen F, Smith JA. 2013. Development and evaluation of a mosaic approach in the WRFNoah framework. *J. Geophys. Res. Atmos.* **118**, 11918-11935
Liou KN. 2002. *An Introduction to Atmospheric Radiation.* Second Edition, Academic Press, USA, 583 pp.
Lu J, Greatbatch RJ, Peterson KA. 2004. Trend in Northern Hemisphere Winter Atmospheric Circulation during the Last Half of the Twentieth Century. *J. Clim.* **17**: 3745–3760
Luce CH, Tarboton DG. 2001. A modified force-restore approach to modeling snow-surface heat fluxes. In *Proceedings of the 69th Annual Meeting of the western Snow Conference*, Sun Valley, ID, 17-19 April 2001, 103-104
Lüpkes C, Vihma T, Birnbaum G, Wacker U. 2008. Influence of leads in sea ice on the temperature of the atmospheric boundary layer during polar night. *Geophys. Res. Lett.* **35**, L03805
Mäkiranta E, Vihma T, Sjöblom A, Tastula EM. 2011. Observations and modelling of the atmospheric boundary layer over sea-ice in a Svalbard fjord. *Bound.-Layer Meteorol.* **140**: 105-123
Mahrt L, Ek M. 1998. The Influence of Atmospheric Stability on Potential Evaporation. *J. Clim. Appl. Meteorol.* **23**: 222-234
Mahrt L, Sun J, Blumen W, Delany T, Oncley S. 1998. Nocturnal boundary-layer regimes. *Bound.-Layer Meteorol.* **88**: 255-278
Mahrt L. 1999. Stratified atmospheric boundary layers. *Bound.-Layer Meteorol.* **90**: 375-396
Mahrt L. 2014. Stably Stratified Atmospheric Boundary Layers. *Annu. Rev. Fluid Mech.* **46**: 23-45
Maksimovich E, Vihma T. 2012. The effect of surface heat fluxes on interannual variability in the spring onset of snow melt in the central Arctic Ocean. *J. Geophys. Res.* **117**, C07012
Marty C, Philipona R, Delamere J, Dutton EG, Michalsky J, Stamnes K, Storvold R, Stoffel T, Clough SA, Mlawer EJ. 2003. Downward longwave irradiance uncertainty under arctic atmospheres: Measurements and modeling. *J. Geophys. Res.* **108**(D12), 4358
Mauritsen T, Svensson G. 2007. Observations of Stably Stratified Shear-Driven Atmospheric Turbulence at Low and High Richardson Numbers. *J. Atmos. Sci.* **64**: 645–655
Mauritsen T, Svensson G, Zilitinkevich SS, Esau I, Enger L, Grisogono B. 2007. A total turbulent energy closure model for neutrally and stably stratified atmospheric boundary layers. *J. Atmos. Sci.* **64**: 4113-4126
McNider RT, Steeneveld GJ, Holtslag AAM, Pielke Sr. RA, Mackaro S, Pour-Biazar A, Walters J, Nair U, Christy J. 2012. Response and sensitivity of the nocturnal boundary layer over land to added longwave radiative forcing. *J. Geophys. Res.* **117**, D14106
Mellor GL. 1973. Analytic Prediction of the Properties of Stratified Planetary Surface Layers. *J. Atmos. Sci.* **30**: 1061-1069
Mellor GL, Yamada T. 1982. Development of a turbulence closure model for geophysical fluid problems. *Rev. Geophys. Space Phys.* **20**: No. 4, 851-875
Mikolajczyk DE, Lazzara MA, Welhouse LJ, Keller LM, Thom JE, Tsukernik M, Cassano JJ. 2012. The Antarctic Automatic Weather Station Network: The Challenges and Rewards of Making Polar Observations. *12th Conference on Polar Meteorology and Oceanography.* American Meteorological Society, Seattle, Washington, USA, p 1.3
Mironov DV, Sullivan PP. 2012. Mixing in the SBL over Temperature-Heterogeneous Surfaces: LES Findings and Some Parameterisation Ideas. *Proceedings of the Workshop on Diurnal cycles and the stable boundary layer, 7-10 November, 2011*, Reading, U.K., pp. 149-151
Mlawer EJ., Taubman SJ, Brown PD, Iacono MJ, Clough SA. 1997. Radiative transfer for inhomogeneous atmospheres: RRTM, a validated correlated-k model for the longwave. *J. Geophys. Res.* **102** D14: 16663-16682
Monin AS, Obukhov AM. 1954. Basic laws of turbulent mixing in the surface layer of the atmosphere. Originally published in *Tr. Akad. Nauk SSSR Geophiz. Inst.* **24**(151): 163-187 [Translated from Russian to English by John Miller, 1959]
Morcrette JJ, Mlawer EJ, Iacono MJ, Clough SA. 2001. Impact of the radiation-transfer scheme RRTM in the ECMWF forecasting system. *ECMWF Newsletter*, No. 91, Reading, U.K., pp. 2-9

NCAR UCAR. 2013. *Current AMPS Configuration.* (http://www2.mmm.ucar.edu/rt/amps/information/configuration/configuration.html)

NERC-BAS. 2014. Natural Environment Research Council, British Antarctic Survey. (http://www.antarctica.ac.uk/images/in_pictures/halley.php)

Niemelä S, Raisanen P, Savijärvi H. 2001. Comparison of surface radiative flux parameterizations Part I: Longwave radiation. *Atmos. Res.* **58**: 1-18

Nieuwstadt FTM, Driedonks AGM. 1979. The Nocturnal Boundary Layer: A Case Study Compared with Model Calculations. *J. Appl. Meteorol.* **18**: 1397-1405

Niu GY, Yang ZL, Mitchell KE, Chen F, Ek MB, Barlage M, Kumar A, Manning K, Niyogi D, Rosero E, Tewari M, Xia Y. 2011. The community Noah land surface model with multiparameterization options (Noah-MP): 1. Model description and evaluation with local-scale measurements. *J. Geophys. Res.* **116**, D12109

NOAA Climate.gov. 2014. Sea ice concentration map. The National Oceanic and Atmospheric Administration. (http://www.climate.gov./news-features/understanding-climate/2013-arctic-sea-ice-minimum-compared-new-normal)

NSIDC. 2014a. All About Arctic Climatology and Meteorology. National Snow and Ice Data Center (NSIDC). (http://nsidc.org/cryosphere/arctic-meteorology/)

NSIDC. 2014b. Data for the sea ice concentration map. National Snow and Ice Data Center (NSIDC). Boulder, Colorado (http://www.climate.gov./news-features/understanding-climate/2013-arctic-sea-ice-minimum-compared-new-normal)

Nygård T, Valkonen T. 2013. Antarctic Low-Tropospheric Humidity Inversions: 10-Yr Climatology. *J. Clim.* **26**: 5205-5219

Oldroyd HJ, Higgins CW, Huwald H, Selker JS, Parlange MB. 2013. Thermal diffusivity of seasonal snow determined from temperature profiles. *Adv. Water Resour.* **55**: 121-130

Overland J, Wang M. 2010. Large-scale atmospheric circulation changes are associated with the recent loss of Arctic sea ice. *Tellus* **62A**: 1-9

Panofsky HA. 1963. Determination of stress from wind and temperature measurements. *Q. J. R. Meteorol. Soc.* **89**: 85-94

Persson POG, Fairall CW, Andreas EL, Guest PS, Perovich DK. 2002. Measurements near the Atmospheric Surface Flux Group tower at SHEBA: Near-surface conditions and surface energy budget. *J. Geophys. Res.* **107**(C10), 8045

Persson POG. 2012. Onset and end of the summer melt season over sea ice: thermal structure and surface energy perspective from SHEBA. *Clim. Dyn.* **39**: 1349-1371

Pithan F, Medeiros B, Mauritsen T. 2013. Mixed-phase clouds cause climate model biases in Arctic wintertime temperature inversions. *Clim Dyn.* **43**: 289-303

Pithan F, Mauritsen T. 2014. Arctic amplification dominated by temperature feedbacks in contemporary climate models. *Nature Geosci.* **7**: 181-184

Pleacher D. 2014. Lesson #66 Concavity. (http://www.pleacher.com/mp/mlessons/calc2006/day66.html)

Poulos GS, Blumen W, Fritts DC, Lundquist JK, Sun J, Burns SP, Nappo C, Banta R, Newsom R, Cuxart J, Terradellas E, Balsley B, Jensen M. 2002. CASES-99: A Comprehensive Investigation of the Stable Nocturnal Boundary Layer. *Bull. Am. Meteorol. Soc.* **83**: 555–581

Prabha T, Hoogenboom G. 2008. Evaluation of the Weather Research and Forecasting model for two frost events. *Comput. Electron. Agric.* **64**: 234-247

Rinke A, Dethloff K, Cassano JJ, Christensen JH, Curry JA, Du P., Girard E, Haugen J-E, Jacob D, Jones CG, Køltzow M, Laprise R, Lynch AH, Pfeifer S, Serreze MC, Shaw MJ, Tjernström M, Wyser K, Žagar M. 2006. Evaluation of an ensemble of Arctic regional climate models: spatiotemporal fields during the SHEBA year. *Clim. Dyn.* **26**: 459-472

Rinke A, Ma Y, Bian L, Xin Y, Dethloff K, Persson POG, Lüpkes C, Xiao C. 2012. Evaluation of atmospheric boundary-layer surface process relationships in a regional climate model along an East Antarctic traverse. *J. Geophys. Res.* **117**: D09121

Rodgers CD. 1967. The use of emissivity in atmospheric radiation calculation. *Q. J. R. Meteorol. Soc.* **93**: 43-54

Roeckner E, Bäuml G, Bonaventura L, Brokop R, Esch M, Giorgetta M, Hagemann S, Kirchner I, Kornblueh L, Manzini E, Rhodin A, Schlese U, Schulzweida U, Tompkins A. 2003. *Report No. 349: The atmospheric general circulation model ECHAM5, Part 1, Model description.* Max Planck Institute for Meteorology, Hamburg, Germany, 140 pp. (http://www.mpimet.mpg.de/fileadmin/publikationen/Reports/max_scirep_349.pdf)

Ronda RJ, De Bruin HAR. 1999. A Note on the Concept of 'Effective' Bulk Exchange Coefficients for Determination of Surface Flux Densities. *Bound.-Layer Meteorol.* **93**: 155-162
Rostkier-Edelstein D, Hacker JP. 2010. The Roles of Surface-Observation Ensemble Assimilation and Model Complexity for Nowcasting of PBL Profiles: A Factor Separation Analysis. *Weather Forecast.* **25**: 1670-1690
Salmond JA, McKendry IG. 2005. A review of turbulence in the very stable nocturnal boundary layer and its implications for air quality. *Prog. Phys. Geogr.* **29**: 171-188
Sánchez JM, Caselles V, Rubio EM. 2010. Analysis of the energy balance closure over a FLUXNET boreal forest in Finland. *Hydrol. Earth Syst. Sci.* **14**: 1487-1497
Sandu I, Beljaars A, Bechtold P, Mauritsen T, Balsamo G. 2013. Why is it so difficult to represent stably stratified conditions in numerical weather prediction (NWP) models? *J. Adv. Model. Earth Syst.* **5**: 117–133
Savijärvi H. 2006. Radiative and turbulent heating rates in the clear-air boundary layer. *Q. J. R. Meteorol. Soc.* **132**: 147-161
Savijärvi H. 2013. High-resolution simulations of the night-time stable boundary layer over snow. *Q. J. R. Meteorol. Soc.* **140**: 1121-1128
Schröder D, Vihma T, Kerber A, Brümmer B. 2003. On the parameterization of turbulent surface fluxes over heterogeneous sea ice surfaces. *J. Geophys. Res.* **108** No. C6, 3195
Screen JA, Simmonds I. 2010. The central role of diminishing sea ice in recent Arctic temperature amplification. *Nature* **464**: 1334-1337
Screen JA, Simmonds I. 2011. Erroneous Arctic Temperature Trends in the ERA-40 Reanalysis: A Closer Look. *J. Clim.* **24**: 2620-2627
Serreze MC, Barry RG, Walsh JE. 1995. Atmospheric water vapor characteristics at 70°N. *J. Clim.* **8**: 719-731
Serreze MC, Francis JA. 2006. The Arctic amplification debate. *Clim. Chang.* **76**: 241-264
Serreze MC, Barrett AP, Stroeve JC, Kindig DN, Holland MM. 2009. The emergence of surface-based Arctic amplification. *The Cryosphere* **3**: 11-19
Serreze MC, Barrett AP, Cassano JJ. 2011. Circulation and surface controls on the lower tropospheric air temperature field of the Arctic. *J. Geophys. Res.* **116**, D07104
Shin HH, Hong SY. 2011. Intercomparison of planetary boundary-layer paramterizations in the WRF model for a single day from CASES-99. *Bound.-Layer Meteorol.* **139**: 261-281
Shupe MD, Intrieri JM. 2004. Cloud Radiative Forcing of the Arctic Surface: The Influence of Cloud Properties, Surface Albedo, and Solar Zenith Angle. *J. Clim.* **17**: 616-628
Skamarock WC, Klemp JB, Dudhia J, Gill DO, Barker DM, Duda MG, Huang XY, Wang W, Powers JG. 2008. *A Description of the Advanced Research WRF Version 3.* Mesoscale and Microscale Meteorology Division, National Center for Atmospheric Research (NCAR), Boulder, Colorado, U.S.A., 113 pp. (http://www2.mmm.ucar.edu/wrf/users/docs/arw_v3.pdf)
Spielhagen RF, Werner K, Sørensen SA, Zamelczyk K, Kandiano E, Budeus G, Husum K, Marchitto TM, Hald M. 2011. Enhanced Modern Heat Transfer to the Arctic by Warm Atlantic Water. *Science* **331**: 450-453
Steeneveld GJ, Van de Wiel BJH, Holtslag AAM. 2006a. Modelling the Arctic nocturnal stable boundary layer and its coupling to the surface. *Bound.-Layer Meteorol.* **118**: 357-378
Steeneveld GJ, Van de Wiel BJH, Holtslag AAM. 2006b. Modeling the Evolution of the Atmospheric Boundary Layer Coupled to the Land Surface for Three Contrasting Nights in CASES-99. *J. Atmos. Sci.* **63**: 920-935
Steeneveld GJ. 2007. *Understanding and Prediction of Stable Atmospheric Boundary Layers over Land.* PhD thesis, Wageningen University, Wageningen, 199 pp.
Steeneveld GJ, Wokke JJ, Groot Zwaaftink CD, Pijlman S, Heusinkveld BG, Jacobs AFG, Holtslag AAM. 2010. Observations of the radiation divergence in the surface layer and its implication for its parameterization in numerical weather prediction models. *J. Geophys. Res.* **115**: D06107
Steeneveld GJ, Tolk LF, Moene AF, Hartogensis OK, Peters W, Holtslag AAM. 2011. Confronting the WRF and RAMS mesoscale models with innovative observations in the Netherlands: Evaluating the boundary layer heat budget. *J. Geophys. Res.* **116**, D23114
Steeneveld GJ. 2014. Current challenges in understanding and forecasting stable boundary layers over land and ice. *Front. Environ. Sci.* **2**, No 41, 6 pp.
Stensrud DJ. 2007. *Parameterization Schemes: Keys to understanding numerical weather prediction models*, Cambridge University Press, Cambridge, 459 pp.
Stephens GL, Miller SD, Benedetti A, McCoy RB, McCoy Jr. RF, Ellingson RG, Vitko Jr. J,

Bolton W, Tooman TP, Valero FPJ, Minnis P, Pilewskie P, Phipps GS, Sekelsky S, Carswell JR, Lederbuhr A, Bambha R. 2000. The Department of Energy's Atmospheric Radiation Measurement (ARM) Unmanned Aerospace Vehicle (UAV) Program. *Bull. Am. Meteorol. Soc.* **81**: 2915-2938

Stoll R. 2012. The effect of surface heterogeneity on fluxes in the stable boundary layer. *Proceedings of the Workshop on Diurnal cycles and the stable boundary layer, 7-10 November, 2011*, Reading, U.K., pp. 187-196

Storm B, Dudhia J, Basu S, Swift A, Giammanco I. 2009. Evaluation of the Weather Research and Forecasting model on forecasting low-level jets: implications for wind energy. *Wind Energy* **12**: 81-90

Stramler K, Del Genio AD, Rossow WB. 2011. Synoptically Driven Arctic Winter States. *J. Clim.* **24**: 1747-1762

Stull RB. 1988. *An Introduction to Boundary-layer Meteorology.* Kluwer Academic Publishers: Dordrecht, 666 pp.

Stull RB. 2000. *Meteorology for Scientists and Engineers.* 2nd Editions, Brooks/Cole Thomson, Pacific Grove, USA, 502 pp.

Sturm M, Perovich DK, Holmgren J. 2002. Thermal conductivity and heat transfer through the snow on the ice of the Beaufort Sea. *J. Geophys. Res.* **107**: SHE 19-1 - SHE 19-17

Sukoriansky S, Galperin B, Perov V. 2006. A quasi-normal scale elimination model of turbulence and its application to stably stratified flows. *Nonlinear Process. Geophys.* **13**: 9-22

Sukoriansky S. 2008. *Implementation of the Quasi-Normal Scale Elimination (QNSE) Model of Stably Stratified Turbulence in WRF*, Report on WRF-DTC Visit, Developmental Testbed Center, 8 pp. (http://www.dtcenter.org/visitors/reports_07/Sukoriansky_report.pdf)

Sun J, Burns SP, Delany AC, Oncley SP, Horst TW, Lenschow DH. 2003. Heat Balance in the Nocturnal Boundary Layer during CASES-99. *J. Appl. Meteorol.* **42**: 1649-1666

Sun X, Barros AP. 2013. High resolution simulation of tropical storm Ivan (2004) in the Southern Appalachians: role of planetary boundary-layer schemes and cumulus parametrization. *Q. J. R. Meteorol. Soc.* **140**: 1847-1865

Svensson G, Holtslag AAM. 2009. Analysis of Model Results for the Turning of the Wind and Related Momentum Fluxes in the Stable Boundary Layer. *Bound.-Layer Meteorol.* **132**: 261-277

Svensson G, Karlsson J. 2011. On the Arctic wintertime climate in Global Climate Models. *J. Clim.* **24**: 5757-5771

Svensson G, Holtslag AAM, Kumar V, Mauritsen T, Steeneveld GJ, Angevine WM, Bazile E, Beljaars A, De Bruijn EIF, Cheng A, Conangla L, Cuxart J, Ek M, Falk MJ, Freedman F, Kitagawa H, Larson VE, Lock A, Mailhot J, Masson V, Park S, Plein J, Söderberg S, Weng W, Zampieri M. 2011. Evaluation of the Diurnal Cycle in the Atmospheric Boundary Layer Over Land as Represented by a Variety of Single-Column Models: The Second GABLS Experiment. *Bound.-Layer Meteorol.* **140**: 177-206

Tardif R, Hacker JP. 2006. *Description of the WRF-1d Planetary Boundary Layer Model.* National Center for Atmospheric Research (NCAR), Research Applications Laboratory. (http://sisla06.samsi.info/compmod/climate/group4/josh3.pdf)

Tardif R. 2007. The Impact of Vertical Resolution in the Explicit Numerical Forecasting of Radiation Fog: A Case Study. *Pure Appl. Geophys.* **164**: 1221-1240

Tastula EM, Vihma T. 2011. WRF model experiments on the Antarctic atmosphere in winter. *Mon. Weather Rev.* **139**: 1279-1291

Tjemkes SA, Duynkerke PG. 1989. The Nocturnal Boundary Layer: Model Calculations Compared with Observations. *J. Appl. Meteorol.* **28**: 161-175

Tjernström M, Zagar M, Svensson G, Cassano JJ, Pfeifer S, Rinke A, Wyser K, Dethloff K, Jones C, Semmler T, Shaw M. 2005. Modelling the Arctic boundary layer: An evaluation of six ARCMIP regional-scale models using data from the SHEBA project. *Bound.-Layer Meteorol.* **117**: 337-381

Tjernström M, Graversen RG. 2009. The vertical structure of the lower Arctic troposphere analysed from observations and the ERA-40 reanalysis. *Q. J. R. Meteorol. Soc.* **135**: 431–443

Tjernström M, Leck C, Birch CE, Bottenheim JW, Brooks BJ, Brooks IM, Bäcklin L, Chang RY-W, de Leeuw G, Di Liberto L, de la Rosa S, Granath E, Graus M, Hansel A, Heintzenberg J, Held A, Hind A, Johnston P, Knulst J, Martin M, Matrai PA, Mauritsen T, Müller M, Norris SJ, Orellana MV, Orsini DA, Paatero J, Persson POG, Gao Q, Rauschenberg C, Ristovski Z, Sedlar J, Shupe MD, Sierau B, Sirevaag A, Sjogren S, Stetzer O, Swietlicki E, Szczodrak M,

Vaattovaara P, Wahlberg N, Westberg M, Wheeler CR. 2014. The Arctic Summer Cloud Ocean Study (ASCOS): overview and experimental design. *Atmos. Chem. Phys.* **14**: 2823-2869

Tolk LF, Meesters AGCA, Dolman AJ, Peters W. 2008. Modelling representation errors of atmospheric CO_2 mixing ratios at a regional scale. *Atmos. Chem. Phys.* **8**: 6587-6596

Town MS, Waddington ED, Walden VP, Warren SG. 2008. Temperatures, heating rates and vapour pressures in near-surface snow at the South Pole. *J. Glaciol.* **54**: 487-498

Troen IB, Mahrt L. 1986. A simple model of the atmospheric boundary layer; sensitivity to surface evaporation. *Bound.-Layer Meteorol.* **37**: 129-148

Tsuang BJ. 2005. Ground Heat Flux Determination according to Land Skin Temperature Observations from In Situ Stations and Satellites. *J. Hydrometeorol.* **6**: 371–390

Uttal T, Curry JA, McPhee MG, Perovich DK, Moritz RE, Maslanik JA, Guest PS, Stern HL, Moore JA, Turenne R, Heiberg A, Serreze MC, Wylie DP, Persson POG, Paulson CA, Halle C, Morison JH, Wheeler PA, Makshtas A, Welch H, Shupe MD, Intrieri JM, Stamnes K, Lindsey RW, Pinkel R, Pegau WS, Stanton TP, Grenfeld TC. 2002. Surface Heat Budget of the Arctic Ocean. *Bull. Am. Meteorol. Soc.* **83**: 255-275

Valkonen T, Vihma T, Johansson MM, Launiainen J. 2013. Atmosphere–sea ice interaction in early summer in the Antarctic: evaluation and challenges of a regional atmospheric model. *Q. J. R. Meteorol. Soc.* **140**: 1536-1551

Van de Boer A, Moene AF, Graf A, Simmer C, Holtslag AAM. 2014. Estimation of the refractive index structure parameter from single-level daytime routine weather data. *Appl. Opt.* **53**: 5944-5960

Van de Wiel BJH. 2002. *Intermittent turbulence and oscillations in the stable boundary layer over land.* PhD thesis, Wageningen University, Wageningen, 130 pp.

Van de Wiel BJH, Ronda RJ, Moene AF, De Bruin HAR, Holtslag AAM. 2002. Intermittent Turbulence and Oscillations in the Stable Boundary Layer over Land. Part I: A Bulk Model. *J. Atmos. Sci.* **59**: 942-958

Van de Wiel BJH, Moene AF, Hartogensis OK, De Bruin HAR, Holtslag AAM. 2003. Intermittent turbulence and oscillations in the stable boundary layer over land, Part III : A classification for observations during CASES-99. *J. Atmos. Sci.* **60**: 2509-2522

Van de Wiel BJH, Moene AF, Steeneveld GJ, Hartogensis OK, Holtslag AAM. 2007. Predicting the Collapse of Turbulence in Stably Stratified Boundary Layers. *Flow Turbul. Combust.* **79**: 251-274

Van de Wiel BJH, Moene AF, Jonker HJJ, Baas P, Basu S, Donda JMM, Sun J, Holtslag AAM. 2012. The Minimum Wind Speed for Sustainable Turbulence in the Nocturnal Boundary Layer. *J. Atmos. Sci.* **69**: 3116-3127

Van den Broeke M, Van As D, Reijmer C, Van de Wal R. 2005. Sensible heat exchange at the Antarctic snow surface: a study with automatic weather stations. *Int. J. Climatol.* **25**: 1081-1101

Van den Broeke M, Bamber J, Ettema J, Rignot E, Schrama E, Van de Berg WJ, Van Meijgaard E, Velicogna I, Wouters B. 2009. Partitioning Recent Greenland Mass Loss. *Science* **326**: 984-986

Van den Hurk BJJM, Viterbo P, Beljaars ACM, Betts AK. 2000. *Offline validation of the ERA40 surface scheme.* ECMWF Technical Memorandum, 295, 43 pp.

Van der Velde IR, Steeneveld GJ, Wichers Schreur BGJ, Holtslag AAM. 2010. Modeling and Forecasting the Onset and Duration of Severe Radiation Fog under Frost Conditions. *Mon. Weather Rev.* **138**: 4237-4253

Van Dijk A, Moene AF, De Bruin HAR. 2004. *The principles of surface flux physics: theory, practice and description of the ECPACK library.* Internal Report 2004/1, Meteorology and Air Quality Group, Wageningen University, Wageningen, The Netherlands, 99 pp.

Van Dinther D, Hartogensis OK, Moene AF. 2013. Crosswinds from a Single-Aperture Scintillometer Using Spectral Techniques. *J. Atmos. Ocean. Tech.* **30**: 3–21

Van Ulden AP, Holtslag AAM. 1985. Estimation of atmospheric boundary layer parameters for diffusion applications. *J. Clim. Appl. Meteorol.* **24**: 1196-1207

Van Ulden AP, Wieringa J. 1996. Atmospheric boundary layer research at Cabauw. *Bound.-Layer Meteorol.* **78**: 39-69

Vickers D, Mahrt L. 2006. A solution for flux contamination by mesoscale motions with very weak turbulence. *Bound.-Layer Meteorol.* **118**: 431-447

Vihma T, Johansson MM, Launiainen J. 2009. Radiative and turbulent surface heat fluxes over sea ice in the western Weddell Sea in early summer. *J. Geophys. Res.*, **114**, C04019

Vihma T. 2014. Effects of Arctic Sea Ice Decline on Weather and Climate: A Review. *Surv. Geophys.* **35**: 1175-1214

Vihma T, Pirazzini R, Fer I, Renfrew IA, Sedlar J, Tjernström M, Lüpkes C, Nygård T, Notz D, Weiss J, Marsan D, Cheng B, Birnbaum G, Gerland S, Chechin D, Gascard JC. 2014. Advances in understanding and parameterization of small-scale physical processes in the marine Arctic climate system: a review. *Atmos. Chem. Phys.* **14**: 9403-9450

Viterbo P, Beljaars A, Mahfouf JF, Teixeira J. 1999. The representation of soil moisture freezing and its impact on the stable boundary layer. *Q. J. R. Meteorol. Soc.* **125**: 2401-2426

Vogelezang DHP, Holtslag AAM. 1996. Evaluation and model impacts of alternative boundary-layer height formulations. *Bound.-Layer Meteorol.* **81**: 245-269

Walsh JE, Chapman WL, Romanovsky V, Christensen JH, Stendel M. 2008. Global Climate Model Performance over Alaska and Greenland. *J. Clim.* **21**: 6156-6174

Walsh JE, 2014. Intensified warming of the Arctic: Causes and impacts on middle latitudes. *Glob. Planet. Chang.* **117**: 52–63

Wang Z, Zeng X. 2009. Using satellite and in situ data to evaluate snow albedo schemes in weather and climate models. *Extended Abstract, 16th Conference on Satellite Meteorology and Oceanography.* American Meteorological Society, Phoenix, Arizona, JP6.3

West R, Goody R, Chen L, Crisp D. 2010. The correlated-k method and related methods for broadband radiation calculations. *J. Quant. Spectrosc. Ra.* **111**: 1672-1673

Westermann S, Lüers J, Langer M, Piel K, Boike J. 2009. The annual surface energy budget of a high-arctic permafrost site on Svalbard, Norway. *The Cryosphere* **3**: 245-263

Wetzel PJ. 1982. Toward Parameterization of the Stable Boundary Layer. *J. Appl. Meteorol.* **21**: 7-13

Wild M, Ohmura A, Gilgen H, Morcrette JJ, Slingo A. 2001. Evaluation of Downward Longwave Radiation in General Circulation Models. *J. Clim.* **14**: 3227-3239

Williams AG, Chambers S, Griffiths A. 2013. Bulk Mixing and Decoupling of the Nocturnal Stable Boundary Layer Characterized Using a Ubiquitous Natural Tracer. *Bound.-Layer Meteorol.* **149**: 381-402

Xue L, Chu X, Rasmussen R, Breed D, Boe B, Geerts B. 2014. The Dispersion of Silver Iodide Particles from Ground-Based Generators over Complex Terrain. Part II: WRF Large-Eddy Simulations versus Observations. *J. Appl. Meteorol. Climatol.* **53**: 1342–1361

Yagüe C, Viana S, Maqueda G, Redondo JM. 2006. Influence of stability on the flux-profile relationships for wind speed, ϕ_{m}, and temperature, ϕ_{h}, for the stable atmospheric boundary layer. *Nonlinear Process. Geophys.* **13**: 185-203

Ylitalo R. 2014. Finnish Meteorological Institute (http://www.eu-interact.org/field-sites/observer-stations-37/finland-4/pallas-sodankyla/)

Zhang D, Anthes RA. 1982. A High-Resolution Model of the Planetary Boundary Layer—Sensitivity Tests and Comparisons with SESAME-79 Data. *J. Appl. Meteorol.* **21**: 1594–1609

Zhang T, Stamnes K, Bowling SA. 2001. Impact of the atmospheric thickness on the atmospheric downwelling longwave radiation and snowmelt under clear-sky conditions in the Arctic and Subarctic. *J. Clim.* **14**: 920-939

Zilitinkevich SS. 1995. Non-local turbulent transport: pollution dispersion aspects of coherent structure of connective flows. *Air pollution III, Volume I. Air Pollution Theory and Simulation*, Computational mechanics Publications, Boston, pp. 53-60

Zilitinkevich SS. 2002. Third-order transport due to internal waves and non-local turbulence in the stably stratified surface layer. *Q. J. R. Meteorol. Soc.* **128**: 913-925

Samenvatting

Het doel van dit proefschrift is het begrijpen en het beter modelleren van de stabiele grenslaag boven besneeuwde oppervlaktes. Stabiele grenslagen vormen zich gebruikelijk 's nachts en in polaire gebieden (vooral in de winter), wanneer door de stralingsafkoeling aan het aardoppervlak een lagere oppervlaktetemperatuur ontstaat dan de temperatuur van de bovenliggende atmosfeer en er zich een stabiele stratificatie ontwikkelt. Dit betekent dat de potentiële temperatuur toeneemt met de hoogte en dat de werking van dichtheidsverschillen (buoyancy) de turbulente bewegingen onderdrukt. Turbulentie wordt dan voornamelijk mechanisch gegenereerd. Wanneer er voldoende windschering is, kan turbulentie actief blijven, anders zal het afzwakken.

Een goede weergave van de stabiele grenslaag in numerieke weerverwachtingsmodellen is essentieel, aangezien velen belang hebben bij een goede verwachting. Zo is een goede weersverwachting bijvoorbeeld nodig voor de windenergie-industrie, voor agrarische doeleinden, luchtkwaliteitsstudies, en voor vlieg- en wegverkeer. Kennis over de stabiele grenslaag is ook nodig voor klimaatmodellering. In de Arctische gebieden is de temperatuurstijging door klimaatverandering sterker dan op andere breedtegraden. De fysische mechanismen achter deze 'Arctische Versterking' worden nog niet volledig begrepen. Waarschijnlijk zijn de volgende factoren en processen van belang: het ijs-albedo terugkoppelingsmechanisme, veranderingen in de wolkbedekkingsgraad en de hoeveelheid waterdamp, veranderde atmosferische en oceanische circulaties, en de zwakke verticale menging in de lagere atmosfeer. Er zijn echter vele interacties tussen deze processen. Door positieve terugkoppelingen kunnen mogelijke veranderingen zelfs verder versterkt worden. Dit kan wereldwijde consequenties hebben, zoals bijvoorbeeld volgt uit de invloed op atmosferische circulaties en de zeespiegelstijging door afsmelting van de Groenlandse ijskap.

Wetenschappers proberen de waargenomen klimaatveranderingen beter te begrijpen, en toekomstige veranderingen in het klimaat in te schatten. Het begrip wordt echter beperkt door het feit dat modeluitkomsten (zoals de 2 m temperatuur), substantieel variëren zowel tussen modellen, alsook ten opzichte van observaties. De oorzaak hangt samen met het feit dat de fysische processen gesimplificeerd weergegeven zijn en het begrip van de relevante processen nog onvolledig is. Bovendien kan de modelresolutie te beperkt zijn voor een correcte weergave van de stabiele grenslaag, aangezien de processen een rol kunnen spelen op hele kleine schaal. Daarnaast zijn er verschillende types stabiele grenslagen. Turbulentie kan onafgebroken zijn, vrijwel afwezig, of intermitterend, maar kan ook verschillen in sterkte wat het vermogen tot horizontale en verticale uitwisseling van stoffen en energie beïnvloedt.

De fysische processen die de ontwikkeling van de stabiele grenslaag bepalen, zijn bijvoorbeeld turbulente menging, stralingseffecten, de interactie tussen de atmosfeer

en het onderliggende oppervlak, de aanwezigheid van wolken of mist, subsidentie, advectie, zwaartekrachtsgolven, en katabatische stromingen. In dit proefschrift ligt de focus op de eerste drie processen aangezien deze als meest overheersend worden beschouwd voor de ontwikkeling van de stabiele grenslaag (bijv. Bosveld *et al.*, 2014b).

In Hoofdstuk 3 is een geïdealiseerde wolkenloze case boven zee-ijs gebaseerd op de GABLS1 referentiestudie (bijv. Cuxart *et al.*, 2006) bestudeerd, maar uitgebreid met stralingseffecten en thermische koppeling met het oppervlak. Zodoende zijn de volgende onderzoeksvragen opgesteld:

> ***Vraag 1:*** *Wat is de variëteit in modeluitkomsten voor potentiële temperatuur- en windsnelheidsprofielen die kan worden gesimuleerd met een enkel model, gebruikmakende van verschillende parameterizatieschema's?*
>
> ***Vraag 2:*** *Welke van de fysische processen is het meest essentieel voor de bepaling van de stabiele grenslaagtoestand bij verschillende windsnelheden?*
>
> ***Vraag 3:*** *Kunnen we compenserende mechanismes identificeren tussen de schema's, en zo aanwijzen waar mogelijke compenserende modelfouten verborgen kunnen zijn?*

Voor Vraag 1 werd een analyse met verschillende parameterizatieschema's uitgevoerd met het WRF een-kolomsmodel (single-column model, SCM). Hieruit volgde dat verschillende stabiele-grenslaag archetypes gevonden werden. Sommige schema's lieten een enigszins beter-gemengd potentieel temperatuurprofiel zien (stratificatie neemt toe met de hoogte), terwijl een ander schema een potentieel temperatuurprofiel simuleerde waarbij de sterkste stratificatie vlak boven het oppervlak ligt en de stratificatie afneemt met de hoogte. Na slechts 9 uur simulatietijd werd reeds een verschil van 2 K in temperatuur nabij het oppervlak gevonden. Daarnaast werd er wat variatie gevonden in de gemodelleerde windsnelheid en hoogte van de low-level jet (nachtelijk windmaximum). Vooral het verschil in de gebruikte grenslaagschema's die de turbulente menging parameterizeren, zijn verantwoordelijk voor de verschillen in modeluitkomsten. Een variatie in langgolvige straling-parameterisatieschema's daarentegen beïnvloedde de modelresultaten nauwelijks.

Vraag 2 onderzoekt welke andere processen dan turbulente menging verantwoordelijk kunnen zijn voor een soortgelijke variatie in modeluitkomst. Hiertoe is een gevoeligheidsanalyse uitgevoerd waarbij voor één set van referentie-parameterizatieschema's de intensiteit van de processen is gevarieerd. De relatieve gevoeligheid van de drie processen voor verschillende geostrofische windsnelheden is geanalyseerd met behulp van 'procesdiagrammen'. In een procesdiagram worden 2 fysisch gerelateerde grootheden tegen elkaar uitgezet, welke in dit geval óf een tijdsgemiddelde óf een verschil in de tijd weergeven. Een lijn verbindt de referentietoestand met de toestand waarvoor de procesintensiteit is aangepast. Door de lengte en oriëntatie van de lijnen met elkaar te vergelijken, kan de relatieve gevoeligheid van de individuele processen voor de verschillende windsnelheden bestudeerd worden. Overlappende lijnen identificeren mogelijke compenserende fouten.

Voor de gevoeligheidsanalyse zijn geostrofische windsnelheden van 3, 8 en 20 m s^{-1} geselecteerd om de spreiding van veel voorkomende windsnelheden in het Arc-

tische gebied ten noorden van 75°N in beschouwing te nemen. In het algemeen werd een verschuiving in de relatieve significantie aangetroffen voor de verschillende windregimes. Bij hoge geostrofische windsnelheden was de modeluitkomst het meest gevoelig voor de turbulente menging. Bij lage windsnelheden daarentegen, is het model het meest gevoelig voor de straling en met name voor de koppeling met het sneeuwoppervlak. Het effect van turbulente menging is dan klein, tenzij menging zowel in de grenslaag als in de oppervlaktelaag worden aangepast. Dit benadrukt het belang van een goede koppeling tussen deze twee lagen.

Ook met één set parameterizatieschema's werden verschillende stabiele grenslaagtypes gesimuleerd: potentiële temperatuurprofielen waren beter-gemengd met een toenemende stratificatie met de hoogte bij hoge geostrofische windsnelheden, terwijl de stratificatie afnam met de hoogte bij lage geostrofische windsnelheden. Echter, een verschil in grenslaagtypes werd ook gevonden bij dezelfde geostrofische windsnelheden, maar bij een variërende mengingsintensiteit. Bij versterkte menging nam de stratificatie van het potentiële temperatuurprofiel toe met de hoogte, ook wanneer de referentietoestand een profiel met een afname in stratificatie met de hoogte simuleerde. Bij afgezwakte menging lieten de profielen juist een snellere afname in stratificatie met de hoogte zien. Zodoende heeft een andere formulering van de menging een sterke invloed op de verticale profielen, ook al heeft dit niet noodzakelijk een grote invloed op de grootheden nabij het oppervlak. Daarom is het aan te bevelen dat wanneer een model geëvalueerd en geoptimaliseerd wordt, er ook rekening wordt gehouden met de verticale profielen. De grootheden nabij het oppervlak kunnen namelijk wel goed gerepresenteerd zijn, maar daarboven kunnen sterke afwijkingen mogelijk zijn.

Verder toonden de procesdiagrammen een overlap in gevoeligheid voor enkele processen. Zodoende kunnen fouten binnen de parameterizaties van deze processen elkaar compenseren en op die manier verborgen blijven (Vraag 3), waardoor de modelformulering fysisch mogelijk minder realistisch is. Deze studie liet niet een eenduidige aanwijzing zien voor compenserende processen met betrekking tot de verschillende combinaties van variabelen, maar een overlap voor een variabele op zichzelf is wel waargenomen.

Deze studie liet tevens een niet-lineair gedrag zien met betrekking tot de 2 m temperatuur, een gedrag dat ook waargenomen is in observaties (bijv. Lüpkes *et al.*, 2008) en in een modelstudie van McNider *et al.* (2012). Hier nam de 2 m temperatuur af met versterkte mengingsintensiteit, terwijl deze juist toenam met verzwakte mengingsintensiteit. Dit contra-intuïtieve gedrag kan verklaard worden doordat de menging alleen plaatsvindt in een dunne laag aan het oppervlak. De koude lucht die dan extra omhoog gemengd wordt bij versterkte menging, wordt onvoldoende gecompenseerd door de extra omlaag gemengde relatieve warme lucht. Dit gedrag werd het meest gevonden bij lage windsnelheden of met zwakkere menging bij middelmatige windsnelheden, wanneer de stratificatie in het potentiële temperatuurprofiel het grootst is aan het oppervlak.

Het onderzoek werd vervolgd door het model te evalueren met observaties bij lage windsnelheden. Drie stabiel-gestratificeerde wolkenloze weersituaties met windsnelheden nabij het oppervlak lager dan 5 m s^{-1} zijn geselecteerd. Deze zijn kenmerkend voor verschillende landgebruikstypes: Cabauw in Nederland met sneeuw op gras, So-

dankylä in noord-Finland met sneeuw in een naaldbos, en Halley in Antarctica met sneeuw op een ijskap.

Hoofdstuk 4 presenteert de evaluatie van het WRF-3D model en het SCM voor deze cases. In dit onderzoek is het WRF-3D model gebruikt om de forceringen voor het SCM te bepalen, aangezien vaak niet alle benodigde observaties hiervoor beschikbaar zijn met hoge resolutie in tijd en ruimte. De volgende onderzoeksvragen werden gesteld:

> ***Vraag 4:*** *Wat is de prestatie van WRF in stabiele omstandigheden met lage windsnelheden voor drie contrasterende besneeuwde terreinen?*
>
> ***Vraag 5:*** *Hoe moeten we de forceringen voor het een-kolomsmodel voorschrijven met behulp van WRF-3D?*

De WRF-3D simulatie had een incorrecte weergave van de sneeuwbedekking en de vegetatiefractie, wat een verslechterde bodemwarmtestroom, oppervlaktetemperatuur en stabiele-grenslaagontwikkeling tot gevolg had. Inderdaad benadrukte Hoofdstuk 3 reeds de cruciale rol van het correct representeren van de koppeling met het landoppervlak. Het aanpassen van deze instellingen met terrein-specifieke informatie, verbeterde de modelsimulaties vergeleken met de observaties.

Over het algemeen was de prestatie van WRF-3D behoorlijk goed voor de geselecteerde cases, met name voor de windsnelheid. Het voorspellen van de temperatuur bleek uitdagender. Voor Cabauw en Sodankylä werden de 2 m temperaturen sterk overschat, hoewel het model beter presteerde op grotere hoogte. Voor Halley werd een betere weergave van de 2 m temperatuur gevonden, terwijl hoger langs de mast potentiële temperatuur onderschat werd. Zodoende hadden de drie cases een onderschatte temperatuurgradiënt gemeen.

Deze studie onderzocht ook hoe de forceringsvelden voor het SCM idealiter voorgeschreven moeten worden. Modelresultaten zonder laterale forceringen en met constante geostrofische windsnelheid lieten voor alle drie de cases een aanzienlijke afwijking zien van het waargenomen windveld. Het voorschrijven van een tijdsafhankelijke geostrofische wind verbeterde de resultaten nauwelijks. Daarentegen had een aanvullende momentumadvectie een positieve invloed op de gemodelleerde windsnelheid. De resultaten voor temperatuur, specifieke vochtigheid en hun stratificatie verbeterde wanneer ook advectie van temperatuur en vocht werd meegenomen. Het forceren van het SCM veld naar voorgeschreven 3D atmosferische condities wordt niet aanbevolen, aangezien onrealistische profielen gevonden werden net onder de grenslijn van de forceringshoogte.

Met de vastgestelde optimale model-setup, kan het SCM gebruikt worden als een hulpmiddel om de kleinschalige processen voor de drie cases verder te bestuderen. Hierbij werden de volgende vragen gesteld:

> ***Vraag 6:*** *Hoe verhouden de modelresultaten met variërende procesintensiteiten zich tot de observaties?*
>
> ***Vraag 7:*** *Zijn er verschillen in relatieve procesgevoeligheid voor de drie contrasterende terreinen?*

Vraag 8: *Verandert de modelgevoeligheid voor twee verschillende grenslaagschema's?*

De gevoeligheidsanalyse is uitgevoerd met het WRF-SCM en herhaald voor twee grenslaagschema's. Over het algemeen werden de stratificaties van temperatuur en luchtvochtigheid sterker door de processterktes te verminderen, en zodoende waren deze resultaten beter in overeenstemming met de waarnemingen dan de referentiecases. Het windveld was het meest gevoelig voor de turbulente menging, met een zwakkere low-level jet op een grotere hoogte voor intensievere menging, en het tegenovergestelde voor zwakkere menging, terwijl het effect van de andere processen klein was. In tegenstelling tot de temperatuurprofielen werd een betere overeenkomst met windwaarnemingen gevonden bij sterkere menging, met uitzondering van Halley waar resultaten verbeterden met een lagere menging.

Betreffende het energiebudget aan het oppervlak, werd de bodemwarmtestroom sterk overschat bij Cabauw door een overschatte sneeuwgeleidingscoëfficiënt, terwijl betere overeenstemming werd gevonden voor de andere locaties. Het herzien van de definitie voor de sneeuwgeleiding wordt aangeraden, omdat behoorlijk hoge waardes worden aangenomen voor verse sneeuw, en inderdaad verbeterden de resultaten met een afgezwakte koppelingssterkte voor Cabauw en Sodankylä. Voor Halley werd vrijwel dezelfde sneeuwgeleiding gemodelleerd als werd gebruikt om de waargenomen geleidingswarmtestroom te bepalen, maar door een onderschatte temperatuurgradiënt door de bovenste bodem/sneeuwlaag bleef deze warmtestroom te klein.

De netto straling was sterk te negatief voor de Cabauw en Halley casestudies. Dit komt waarschijnlijk door een onderschatting van de inkomende langgolvige straling door een gebrek in het langgolvige-stralingsschema. Voor alle locaties werd de voelbare warmtestroom onderschat, wat werd verbeterd door minder menging. Echter, de eddy-covariantiemetingen kunnen mogelijk boven de constante fluxlaag genomen zijn, wat de modelevaluatie belemmert.

Hoewel Vraag 6 meer inzicht probeert te krijgen in welke processen verantwoordelijk zijn voor het verkrijgen van modelresultaten die dichter bij de waarnemingen liggen, is het verrichten van metingen in deze koude en droge condities erg moeilijk. Bovendien zijn de metingen voornamelijk puntmetingen terwijl het model grid een groter gebied representeert, zodat metingen beïnvloed kunnen worden door lokale kenmerken die niet meegenomen worden in het model. Deze kwesties belemmeren een duidelijke vergelijking van modelresultaten met observaties, en de waarnemingsonzekerheid kan groter zijn dan is weergegeven in de procesdiagrammen.

Wanneer de procesgevoeligheid voor de verschillende locaties vergeleken wordt (Vraag 7), zien we enige duidelijke variaties in relatieve significantie. Het stralingseffect was relatief groot voor Cabauw en Sodankylä waar de specifieke vochtigheid groter was zodat een grotere gevoeligheid voor de inkomende langgolvige straling verkregen kon worden. De sneeuwoppervlak-koppeling is belangrijker voor Halley. Dit is gerelateerd aan de hogere sneeuwbedekking bij Halley vergeleken met de andere locaties, alsook aan de geleiding van het onderliggend oppervlak aan Halley wat in het model gelijk gesteld wordt aan die van sneeuw. Deze twee factoren zorgen voor de grotere impact van de gewijzigde sneeuwgeleiding.

Uit de vergelijking van de gevoeligheidsanalyses voor de twee grenslaagschema's (MYJ en YSU, Vraag 8), volgde dat de algemene richting van de gevoeligheids-

oriëntatie hetzelfde is. Echter, met YSU werden sterker ontwikkelde temperatuurstratificaties gevonden, hoewel tussen het oppervlak en het eerste model niveau de stratificaties groter waren met MYJ. Dit komt door de relatief hoge verhouding van menging in de grenslaag ten opzichte van de menging in de oppervlaktelaag met MYJ. Hierdoor is de menging in de grenslaag relatief efficiënter en kan de oppervlaktelaag de hoeveelheid menging niet bijbenen zodat er geen gelijkmatige overgang is in de verticale profielen bij de overgang tussen oppervlaktelaag en grenslaag. Dit geeft aan dat de overgang tussen de oppervlaktelaag en de grenslaag erg belangrijk is, wat ook opgemerkt werd door Svensson en Holtslag (2009). Verder is de eerder genoemde niet-lineariteit met betrekking tot de 2 m temperatuur het meest ontwikkeld met YSU, en is dit niet zo duidelijk met MYJ doordat daar een hogere waarde voor de minimale diffusie is toegepast.

De resultaten wijzen op de richting van focus voor toekomstig onderzoek. Voorbeelden zijn het herzien van de sneeuwrepresentatie, alsook het onderzoeken van het langdurige probleem van de onderschatte inkomende langgolvige straling. Daarnaast lijkt de hoeveelheid menging te groot te zijn in veel simulaties. Zodoende moet zorg worden geboden in het formuleren van het grenslaagschema en diens beperkingen op de hoeveelheid menging, aangezien deze bijvoorbeeld de ontwikkeling van het niet-lineaire gedrag betreffende de temperatuur nabij het oppervlak kunnen belemmeren.

Dankwoord

Nu dit boekwerk af is, wil ik graag iedereen die mij de afgelopen jaren geholpen en/of gesteund heeft ontzettend bedanken. Velen hebben hieraan bijgedragen, maar ik wil graag een aantal in het bijzonder noemen.

Allereerst natuurlijk Gert-Jan, enorm bedankt voor je begeleiding de afgelopen jaren en voor alle tijd die je steeds weer voor me had. Ik vond het erg fijn dat ik altijd binnen kon komen lopen om problemen waar ik tegenaan liep te bespreken of gewoon om wat gedachten uit te wisselen. Jouw goede inzichten en schat aan kennis kwamen vaak van pas. Ongelofelijk hoe de bibliotheek zich in jouw hoofd geordend heeft! Sorry als ik soms een beetje gefoeterd heb op de hoeveelheid commentaar, ik weet zeker dat het de kwaliteit van dit proefschrift wel ten goede is gekomen. Ook heb ik veel geleerd van de tijd bij het geven van het vak 'Atmospheric Modelling' en vond ik het leuk om hieraan mee te mogen werken.

Daarnaast heb ik veel gehad aan mijn promotor Bert. Het was altijd interessant om over de stabiele grenslaag te discussiëren. Ook al gingen we soms wat rond in cirkels, de titels zijn er in ieder geval beter op geworden! Bedankt ook voor het vertrouwen dat je altijd in me gehouden hebt. Zeker meer naar het einde van mijn PhD toen ik me afvroeg of er ooit wel een einde aan zou komen, wist je me weer op te peppen.

Reinder, ook jij bent een grote hulp geweest. Hartstikke mooi hoe jij het advectieschema in WRF hebt omgebouwd, zodat we tenminste snappen wat er gebeurt en we de advectie op een fatsoenlijke manier kunnen voorschrijven. Ook bedankt voor het toelichten van dit alles in lange mails met verschillende kleuren voor de antwoorden op elkaars vragen toen ik in Finland zat. Maar ook de andere gesprekken heb ik erg gewaardeerd, zij het over WRF, of over lieve kattenbeestjes in het asiel. Ik hoop dat ik straks weer meer tijd heb om daar langs te gaan!

Furthermore, I would like to acknowledge my (former) colleagues at MAQ, for the good times both in and out of the office. Thanks for the tea and coffee breaks that we've had and for listening to my blowing off some steam sometimes. I also appreciated the support in the form of discussions and technical/organizational assistance that I've received from some of you. And of course thanks for the walks outside the office, the sports activities, the great music sessions both live and with the SingStar game, for trying to defeat Bowser (we came só close!), the holidays and the nice times during conferences, drinks and dinners, the fun of writing songs for the various PhD promotions, and the organizing of the BBOS spring symposium, but also for pointing out possible job opportunities for after my PhD. I also valued the good conversations that I've had with several of you during all these activities. I think I've grown a lot personally during my time at MAQ and I am truly grateful

for that.

I would like to thank my co-authors for their help with the data and useful comments on the articles. Also thanks to Timo, Tiina, Roberta and Rogier for the time at the Finnish Meteorological Institute. It was a very nice experience to do some research outside Wageningen, and great that some of the preliminary GABLS4 set-up could be applied for the work in this thesis. Fred, jij ook hartelijk bedankt voor de discussies over de procesdiagrammen die jij ontworpen hebt voor de GABLS3 studie. We hebben hier in deze thesis dankbaar gebruik van gemaakt om het begrip van de model-proces-gevoeligheid meer inzichtelijk te krijgen. Ook Richard, Eveline en Wilco van het QUASI project bedankt voor de leuke meetings.

Natuurlijk ben ik ook mijn paranimfen dankbaar. Brenda, leuk dat je mij wilt bijstaan op deze dag. Het is me een roller-coaster geweest de afgelopen jaren, allebei druk met onze PhD. Fijn dat we elkaar nog regelmatig bellen om alle frustraties weer even uit te spuien, en om elkaar over onze toekomstsplannen te kunnen vertellen. And of course thanks to my stable-boundary-layer-buddy Michał. It was great to have another PhD-student at MAQ on this topic who uses WRF as well, so we could relate on some of the weird findings that followed from our research. Also thanks for your help in the understanding of the revised YSU-scheme. Besides the work-related discussions, I appreciate all the other conversations that we've had. I am glad that we are still in touch now that you live in Schiedam, and I hope that we continue to do so in the future!

Verder wil ik graag al mijn kattenoppassers ontzettend danken voor hun goede zorgen voor Stoffer en Frunnik als ik weer eens op een conferentie, workshop of iets dergelijks was. Ik zal geen namen noemen omdat ik dan vast per ongeluk iemand vergeet, maar wil wel Laura expliciet noemen die soms zelfs weken in mijn huis bivakkeerde om de beestjes op hun wenken te bedienen. Maar ook alle anderen enorm bedankt, ik weet zeker dat Stoffer en Frunnik ook het eten uit jullie hand zeer waardeerden!

BWA-meiden, goed dat we zo nu en dan nog contact houden in de vorm van een lunch, een etentje, of een gezellige picknick in het park. En Suzanne, leuk dat wij ook nog af en toe afspreken, op Skype of voor een lekkere wandeling ergens.

Sanne, Stella, Coralien en Hanneke, ik vind het superleuk dat we nog regelmatig afspreken om bij te kletsen. Ik ben blij met hoe onze vriendschap zich verder heeft ontwikkeld zelfs al die jaren na de middelbare school.

Papa en mama, jullie ben ik natuurlijk ook ontzettend dankbaar voor alle steun, niet alleen van de afgelopen jaren, maar ook van daarvoor. Fijn dat ik altijd bij jullie terecht kan voor een luisterend oor, en dat jullie altijd achter me staan. Ellen en Harmen, jullie ook bedankt, misschien niet zozeer voor PhD-gerelateerde zaken, maar wel voor de afleiding daarvan.

En dan als laatste mijn lieve Thijs, dapper van je dat je het zowaar aandurfde in de laatste anderhalf jaar van mijn PhD-traject iets met me te beginnen! Je zal vast ook opgelucht zijn als het er straks op zit ;). Bedankt voor je hulp met het maken van het omslagdesign. Maar bovenal dank je wel voor al je liefde en dat je er voor me bent, zowel voor het aanhoren van de PhD highs en lows alsook voor alle andere dingen. Ik heb het echt getroffen met jou en hoop dat er nog vele jaren mogen volgen samen.

List of publications

Peer-reviewed papers

Sterk HAM, Steeneveld GJ, Holtslag AAM. 2013. The role of snow-surface coupling, radiation, and turbulent mixing in modeling a stable boundary layer over Arctic sea ice, *J. Geophys. Res. Atmos.* **118**: 1199-1217, doi: 10.1002/jgrd.50158.

Sterk HAM, Steeneveld GJ, Vihma T, Anderson PS, Bosveld FC, Holtslag AAM. 2015. Clear-sky stable boundary layers with low winds over snow-covered surfaces. Part 1: WRF model evaluation. *Q. J. R. Meteorol. Soc.*, doi: 10.1002/qj.2513.

Sterk HAM, Steeneveld GJ, Bosveld FC, Vihma T, Anderson PS, Holtslag AAM. Clear-sky stable boundary layers with low winds over snow-covered surfaces. Part 2: Process sensitivity. In preparation for resubmission to *Q. J. R. Meteorol. Soc.*.

Pithan F, Svensson G, Ackerman AS, Angevine WM, Hartung K, Ickes L, Mauritsen T, Medeiros B, Sandu I, Steeneveld GJ, Sterk HAM, Vaillancourt PA, Zadra A. Why models fail or succees in representing the Arctic winter boundary layer - a model intercomparison. In preparation.

Other papers

Sterk HAM, Steeneveld GJ, Holtslag AAM. 2012. Unravelling the role of turbulent mixing, land surface coupling and radiation in a coupled GABLS1 experiment. In *Proceedings of the Workshop on Diurnal cycles and the stable boundary layer, Reading, UK, 7-10 November 2011*, ECMWF (European Centre for Medium-Range Weather Forecasts), UK, p. 251.

Sterk HAM. 2012. Modelgevoeligheid voor de Arctische stabiele grenslaag. *Meteorologica*, **21(4)**: 24-25.

Sterk HAM. 2013. Een WRF 1D studie in stabiele omstandigheden boven sneeuw. *Meteorologica*, **22(4)**: 15.

Sterk HAM, Steeneveld GJ, Holtslag AAM. 2015. Modelling clear-sky atmospheric boundary layers over snow. In *Proceedings of the 1st Pan-Eurasian Experiment (PEEX) Conference and the 5th PEEX Meeting*, February 2015, Helsinki, Finland. Report series in aerosol science. No 163. pp. 429 - 434.

Netherlands Research School for the
Socio-Economic and Natural Sciences of the Environment

D I P L O M A

For specialised PhD training

The Netherlands Research School for the
Socio-Economic and Natural Sciences of the Environment
(SENSE) declares that

Hendrika Adriana Maria Sterk

born on 20 January 1986 in Gorinchem, The Netherlands

has successfully fulfilled all requirements of the
Educational Programme of SENSE.

Wageningen, 29 April 2015

the Chairman of the SENSE board	the SENSE Director of Education
Prof. dr. Huub Rijnaarts	Dr. Ad van Dommelen

The SENSE Research School has been accredited by the Royal Netherlands Academy of Arts and Sciences (KNAW)

K O N I N K L I J K E N E D E R L A N D S E

The SENSE Research School declares that **Ms Marina Sterk** has successfully fulfilled all requirements of the Educational PhD Programme of SENSE with a work load of 52.2 EC, including the following activities:

SENSE PhD Courses

- Environmental Research in Context (2010)
- Research in Context Activity: Organising BBOS Spring Symposium on Geo-engineering: Hack the Climate, Wageningen (2011)
- Bridging the gap between atmospheric scales (2012)

Other PhD and Advanced MSc Courses

- Atmospheric Gravity Waves (2011)
- Scientific Writing (2012)
- PhD Career Assessment (2013)
- Last Stretch of your PhD (2014)

External training at a foreign research institute

- Training Course module NWP-PA: Parametrization of subgrid physical processes, European Centre for Medium-Range Weather Forecasts (ECMWF), England (2010)
- Visiting scientist, Finnish Meteorological Institute, Finland (2012)

Management and Didactic Skills Training

- Teaching Assistant for the BSc course 'Inleiding Atmosfeer' (2010 and 2013)
- Teaching Assistant for the MSc course 'Mesoscale Meteorological Modelling' (2011)
- Supervision of BSc student: thesis entitled 'Using dimensional analysis in search of a stable boundary-layer height formulation' (2012)
- Teaching Assistant for the MSc course 'Atmospheric Modelling' (2014)

Selection of Oral Presentations

- *Unravelling the role of turbulent mixing, land surface coupling and radiation in a coupled GABLS1 experiment*. European Meteorological Society's 11th Annual Meeting, 12-16 September 2011, Berlin, Germany
- *Analysing the role of land-surface coupling, radiation and turbulent mixing in an Arctic stable boundary layer*. American Meteorological Society's 20th Symposium on Boundary Layers and Turbulence, 9-13 July 2012, Boston, United States
- *The role of snow-surface coupling, radiation and turbulent mixing in modelling a stable boundary layer over Arctic sea-ice*. American Meteorological Society's 12th Conference on Polar Meteorology and Oceanography, 29 April-1 May 2013, Seattle, United States *(Best presentation award)*
- *A WRF SCM study in stable conditions over snow*. Buys Ballot Research School (BBOS) Autumn Symposium, 30 October-1 November 2013, Kerkrade, The Netherlands

SENSE Coordinator PhD Education

Dr. ing. Monique Gulickx

This PhD project was funded by NWO (The Dutch Science Foundation) with grant 829.09.005 ("Quantifying contributions of surface climate feedbacks to the Arctic amplification of greenhouse warming" in the Sustainable Earth program).

Financial support from Wageningen University for printing this thesis is gratefully acknowledged.

Also thanks to Lynne Lancaster, aka Weirdvis, for the inspiration for the cover image (http://www.rgbstock.com/images/finlandia).